(千葉大学審査学位論文)

Studies on Low-Frequency Spectra of Ionic Liquids and Ionic Liquid Mixtures by Femtosecond Laser Spectroscopy

February 2023

Masatoshi Ando

Department of Chemistry

CHIBA UNIVERSITY

Contents

Chapter I. General Introduction ····· 1

I.1 Ionic Liquids ····· 2

I.2 Features of ILs ····· 3

I.3 Microscopic Pictures of ILs and IL Mixtures ····· 4

I.4 Measurement Methods of Intermolecular Vibrations of IL and IL Mixtures ····· 5

I.5 Preceding Reports of Low-Frequency Spectra of IL and IL Mixtures ····· 6

I.6 Purpose and Structure of This Study ····· 7

Chapter II. Experimental Section ····· 9

II.1 Synthesis Methods of Ionic Liquids ····· 10

II.2 Measurements of Liquid Properties ····· 10

II.3 Femtosecond Raman-Induced Kerr Effect Spectroscopy ····· 11

Chapter III. Low-Frequency Spectra of 1-Methyl-3-octylimidazolium Tetrafluoroborate Mixtures with Methanol, Acetonitrile, and Dimethyl Sulfoxide ····· 21

III.1 Introduction ····· 22

III.2 Experimental and Computational Methods ····· 23

III.3 Results ····· 25

III.4 Discussion ····· 39

III.5 Conclusions ····· 44

Chapter IV. Low-Frequency Spectra of 1-Methyl-3-octylimidazolium Tetrafluoroborate Mixtures with Formamide, *N*-Methylformamide, and *N*,*N*-Dimethylformamide ····· 45

IV.1 Introduction ····· 46

IV.2 Experimental and Computational Methods ····· 47

IV.3 Results ····· 49

IV.4 Discussion ····· 67

IV.5 Conclusions ····· 74

Chapter V. Low-Frequency Spectra of 1-Methyl-3-octylimidazolium Tetrafluoroborate Mixtures with Poly(Ethylene Glycol) ····· 75

V.1 Introduction ····· 76

V.2 Experimental Method ····· 77

V.3 Results ····· 78

V.4 Discussion ····· 89

V.5 Conclusions ····· 99

Chapter VI. Low-Frequency Spectra of Phosphonium Bis(fluorosulfonyl)amide Ionic Liquids with Pentyl, Ethoxyethyl, or 2-(Ethylthio)ethyl Group ····· 101

VI.1 Introduction ····· 102

VI.2 Experimental Methods and Computational Methods ····· 103

VI.3 Results ····· 106

VI.4 Discussion ····· 119

VI.5 Conclusions ····· 126

Chapter VII. Summary ····· 129

References ····· 133

Appendix ····· 145

Acknowledgements ····· 249

Publication Lists ····· 250

Chapter I.

General Introduction

I.1 Ionic Liquids

Typical salts have high melting points and are solids at room temperature due to strong Coulomb forces between cation and anion. However, some organic salts show low melting points and are liquids at near room temperature. These liquid salts are referred to as ionic liquids (ILs).[1-8] ILs are generally defined as having a melting point below 373 K and, especially, those with a melting point near room temperature are often called as room-temperature ionic liquids (RTILs).[1,9] The history of RTIL started about 100 years ago when Paul Walden, who is the inventor of Walden inversion, synthesized ethylammonium nitrate in 1914.[10] Still, ILs received little attention for the first several decades. After that, ILs were gradually received attentions. Some of them,[11-15] such as the mixtures of 1-alkyl-3-methylimidazolium chloride and aluminum chloride,[16] were investigated as electrolytes. However, ILs synthesized in the early days, such as chloroaluminate-based ILs, are unstable at ambient conditions because they react irreversibly with moisture in air. This is probably the reason why the research on ILs just developed a little. The breakthrough for IL research was the invention of 1-ethyl-3-methylimidazolium tetrafluoroborate, which is stable in air and water, by Wilkes and Zaworotko in 1992.[17] Thereafter, the unique properties of ILs have found and ILs have come into the limelight.

Figure I.1 illustrates typical examples of cations and anions for ILs. The cations in Figure I.1 are dialkylimidazolium, alkylpyridinium, quaternary phosphonium, quaternary ammonium, and dialkylpyrrolidinium. These cations are essentially organic compounds and possess a bulky structure due to their long alkyl group. The anions in Figure I.1 are halides, tetrafluoroborate, hexafluorophosphate, bis(trifluoromethylsulfonyl)amide, and dicyanamide. Unlike cations, IL anions include both organic and inorganic ones.

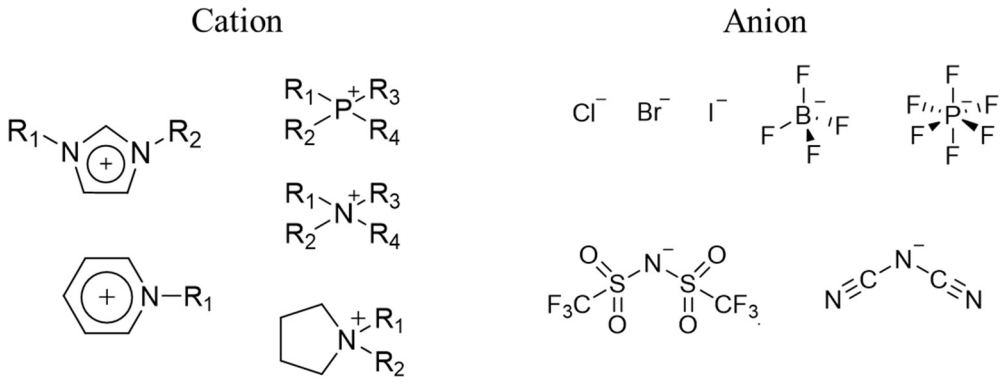

Figure I.1. Structural formulas for typical cations and anions in ILs. $R_{1\sim4}$ of cations represents various alkyl groups.

I.2 Features of ILs

ILs possess unique properties in comparison with common molecular liquids (MLs). For example, IL shows negligible vapor pressure in ambient conditions.[4,18] Therefore, it needs high temperature and low pressure to distill ILs.[19,20] Because of this low volatility, they are less flammable despite organic compounds. Furthermore, since they are purely composed of ions, they can be electrically conductive and have a wide electrochemical window without an addition of supporting electrolyte.[21-23] The above characteristics of ILs make them particularly suitable for use with battery solvents. The rechargeable battery solvents currently in use are organic solvents, which can cause ignition and explosions in the batteries.[24] Accordingly, ILs are attracting attentions as a safer electrolyte that can solve this problem.[25-27]

In addition, ILs have a different microscopic structural feature from common MLs. Canongia Lopes and Pádua reported the nanometer-scale structures of ILs by molecular dynamics (MD) simulations in 2006.[28] Their simulation results revealed that ILs had a microsegragated structure with polar and nonpolar regions, and the nonpolar domains became larger and the ionic network are more swollen with increasing alkyl chain length. Experimentally, Trioro and coworkers have made X-ray diffraction measurements of imidazolium-based ILs.[29] They found pre-peaks in a low-Q region and confirmed these pre-peaks are derived from the aggregation of alkyl groups of ILs. These results indicate that ILs have heterogeneous or microsegregation structures. This heterogeneous structure provides great solubility for a variety of substances,[30-35] and thus ILs are expected to be applied as extraction materials[36,37] and new solvents in organic synthetic reactions.[4,38,39]

As noted in the previous section, ILs have many attractive properties, but also some unfavorable ones. One of them is high viscosity[4,34] due to Coulombic force between cation and anion. The viscous nature of ILs is often a problem when using ILs. For example, application to electrolytes is required less viscous nature to enhance the electrical conductivity. Therefore, many researchers have tried to design and synthesize low-viscosity ILs.

The viscosity of IL depends strongly on both cation and anion species.[40-43] For example, IL with halide anion shows a high viscosity and IL with bis(trifluoromethylsulfonyl)amide shows a low viscosity.[41] Additionally, the length of the alkyl group of the cation also affects the viscosity of IL.[40-42,44-46] The shorter the length of the alkyl group, the lower the viscosity of IL (e.g. 1-butyl-3-methylimidazolium iodide: 1400 cP > 1-butyl-3-methylimidazolium bis(trifluoromethylsulfonyl)amide: 59.3 cP > 1-ethyl-3-methylimidazolium bis(trifluoromethylsulfonyl)amide: 35.7 cP).[41] Besides these, “heavy atom

substitution effect" also significantly affects the viscosity of ILs.[47-51] Usually, a substitution by heavy atom in neutral organic solvents increases the viscosity due to an increase in van der Waals' force.[52] In ILs, on the other hand, a heavy atom has a large volume. Therefore, a substitution by a heavy atom in ionic species makes lower viscosity, since the distance between cation and anion widens. This is very useful in the synthesis of low-viscosity ILs because this effect works for both cation and anion.

Another simple way to reduce the viscosity of ILs is to mix a low-viscosity ML with ILs.[33,53-56] For example, a number of IL mixtures with H_2O, which is the most typical solvent, have been studied and reductions in viscosity have been reported.[33,54,56]

I.3 Microscopic Pictures of ILs and IL Mixtures

The variations in liquid properties mentioned above are due to the changes in the microscopic intermolecular interactions and structures, and thus it is necessary to understand their microscopic pictures in order to obtain ILs and IL mixtures with the desired liquid properties. However, as explained in the previous section, it is not straightforward to understand their microscopic pictures since ILs have microheterogeneous structures due to amphiphilic cations.

An early study showing the complicated microscopic picture of ILs was reported by Schröder et al.[57] They estimated the diffusion coefficients of neutral (*N*,*N*,*N*′,*N*′-tetramethyl-*p*-phenylenediamine, TMPD), cationic (methyl viologen, MV_2^+), and anionic (hexacyanoferrate(III), $Fe(CN)_6^{3-}$) redox compounds in ILs and IL/H_2O mixtures using cyclic voltammetry. In neat ILs, the diffusion coefficients of TMPD were twice as large as those of MV_2^+ and $Fe(CN)_6^{3-}$. In a mixture of ionic liquids and water, however, the diffusion coefficients of MV_2^+ and $Fe(CN)_6^{3-}$ increased drastically. They suggested that MV_2^+ and $Fe(CN)_6^{3-}$ interacted with IL's cation and anion in neat ILs, making diffusion difficult in neat IL, but when the ILs mix with water, the water forms nanostructures in the ILs and MV_2^+ and $Fe(CN)_6^{3-}$ diffused through the polar region, resulting in the drastic increase in the diffusion coefficient.

After Schröder's study, there have been other studies on the influence of water nanostructures in ILs.[58-60] As one example, Takekiyo et al. measured the structural changes of chicken egg white lysozyme in aqueous 1-butyl-3-methylimidazolium nitrate ([BMIm][NO_3]) solutions (0-24 M of [BMIm][NO_3]) by Fourier transform infrared spectroscopy (FTIR), circular dichroism (CD) spectra and small-angle scattering (SAXS).[61] In pure water, lysozyme folded and became spherical (globule state). When [BMIm][NO_3] was added in water up to 6

M, the α-helix was destroyed by $[NO_3]^-$, causing lysozyme to unfold. However, when [BMIm][NO_3] was further added up to 10 M, the lysozyme became a partially globule state. They found that the 10 M [BMIm][NO_3] solution contained water aggregation structures (which they called "water pocket") by Raman spectroscopy and reported that lysozyme was partially folded by these water nanostructures.

Focusing on their structures, Canongia Lopes and coworkers calculated microscopic structures of 1-butyl-3-methylimidazolium hexafluoroborate ([BMIm][PF_6]) mixtures with hexane, acetonitrile, methanol, and H_2O by MD simulations.[62,63] Their results exhibited the microscopic structures of the [BMIm][PF_6] mixtures depend on the properties of the solutes. Hexane, which is a nonpolar molecule, located in the nonpolar alkyl region of the [BMIm][PF_6], while H_2O, which is a polar molecule, located in the polar ionic region of the [BMIm][PF_6]. Then, acetonitrile and methanol were dispersed in the boundary region between polar and nonpolar regions of [BMIm][PF_6], although they interacted with [BMIm][PF_6] cation and anion in different ways.

As these preceding studies have shown, the microscopic picture of ILs and IL mixtures is complicated. Therefore, it is important to understand the intermolecular interactions of ILs and IL mixtures for understanding the microscopic pictures of ILs and IL mixtures.

I.4 Measurement Methods of Intermolecular Vibrations of IL and IL Mixtures

Intermolecular interactions of condensed phases influence intermolecular vibrations. The time scale of intermolecular vibrations is about subpico- to picosecond, and thus the spectrum coming from intermolecular vibrations appears mainly in the region below 200 cm^{-1}. Therefore, measurements of low-frequency spectra are a very useful choice for understanding intermolecular interactions in condensed phases. However, conventional steady-state spectroscopies cannot accurately measure the entire low-frequency range. For example, in far-infrared (far-IR) spectroscopy, the energy of the light less than 200 cm^{-1} is close to the thermal energy at room temperature. Thus, the low-frequency IR spectra include the thermal noise as it is. Alternatively, in Raman spectroscopy, the strong Rayleigh scattering dominates the low-frequency Raman signal. Both spectroscopic techniques have been developed to measure low-frequency regions with high accuracy (the detector (bolometer) is cooled with liquid helium to reduce thermal noise in IR, and notch filters are used to remove the Rayleigh scattering in Raman), but it is still difficult to measure the entire low-frequency region accurately with these spectroscopic techniques.

On the other hand, time-domain spectroscopic techniques using a femtosecond laser, such as terahertz time-domain spectroscopy (THz-TDS)[64,65] and femtosecond Raman-induced Kerr effect spectroscopy (fs-RIKES)[66-70] are very effective. THz-TDS and fs-RIKES are complementary to each other like IR and Raman spectroscopies (THz-TDS observes changes in collective dipole moment and fs-RIKES observes those in collective polarizability). Our laboratory has built fs-RIKES and measured low-frequency spectra of liquids and solutions using a laboratory built-fs-RIKES. In this thesis, low-frequency spectra of the ILs and IL mixtures were measured using fs-RIKES.

I.5 Preceding Reports of Low-Frequency Spectra of IL and IL Mixtures

The first report on low-frequency spectra of ILs measured by fs-RIKES was done by Quitevis and coworkers in 2002.[71] They compared 1-alkyl-3-methylimidazolium-based ILs with different alkyl chain lengths in the cation. In subsequent years, they reported fs-RIKES measurements for many ILs.[72-74] Shirota and coworkers measured the low-frequency spectra of 40 aromatic-ILs[41] and 40 nonaromatic-ILs[42] and discussed the characteristics of the low-frequency spectra of ILs in a semi-exhaustive manner. The temperature dependences of low-frequency spectra for ILs were also reported by Quitevis,[72] Wynne,[75,76] and Kakinuma,[70,77-79] respectively. In particular, Kakinuma systematically measured the temperature dependence of low-frequency spectra for ILs and discussed the change in the vibrational dynamics of IL molecules with temperature change in detail.

While many low-frequency spectra of neat ILs have been reported as described above, there are few reports of low-frequency spectra of IL mixtures with ML. Quitevis et al. investigated the low-frequency spectra of imidazolium-based ILs with carbon disulfide[80,81] and acetonitrile.[82] Their results suggest that carbon disulfide, which is a nonpolar molecule, is distributed in the nonpolar region of ILs and acetonitrile, which is a polar molecule, is distributed at the boundary between the polar and nonpolar regions of ILs. Shirota also reported low-frequency spectra of 1-methyl-3-octylimidazolium tetrafluoroborate ([MOIm][BF_4]) mixtures with water[53] and benzene[55] by fs-RIKES. Shirota reported that water molecules do not disrupt the ionic network of [MOIm][BF_4] in the low water concentration, while benzene affects the ionic interaction from the low benzene concentration. However, to the best of my knowledge, low-frequency spectra of imidazolium-based ILs mixtures with MLs by fs-RIKES have only been reported for the mixtures with the four MLs (acetonitrile, carbon disulfide, H_2O, and benzene) mentioned above. Thus, the intermolecular interactions of IL mixtures have not yet

been fully understood. Therefore, it is of great significance to systematically discuss the low-frequency spectra of IL mixtures in this thesis.

I.6 Purpose and Structure of This Thesis

Recently, global warming has become a worldwide problem and is caused by the excessive use of fossil fuels. Therefore, the efficient use of renewable energy sources will become more important in the future. I believe that ILs are one of the options that can contribute to solving this global warming problem as new electrolyte materials. I have studied the intermolecular interactions of ILs and IL mixtures in this doctoral thesis to obtain fundamental knowledge for the reform of ILs.

So far, I have introduced the background of preceding researches about IL and IL mixtures in Chapter I.

In Chapter II, I will describe the details of experimental and analytical methods used in this thesis.

I will investigate the low-frequency spectra of [MOIm][BF_4] mixtures with typical solvent MLs, methanol (MeOH), acetonitrile (MeCN), and dimethyl sulfoxide (DMSO) and discuss the interaction between solvent MLs and [MOIm][BF_4] in Chapter III.

[MOIm][BF_4] mixtures with formamide (FA), *N*-methylformamide (NMF), and *N*,*N*-dimethylformamide (DMF), which have strong intermolecular interactions, will be discussed to clarify the effects of strong hydrogen bonding on the ionic interactions of [MOIm][BF_4] in Chapter IV.

In Chapter V, I will describe the first report on the low-frequency spectra of mixtures of polyethylene glycol (PEG) and [MOIm][BF_4]. PEG is one of the most common polymer electrolytes and IL/polymer mixtures are expected to be applied to solid battery electrolytes. Thus, I will examine the effects of polymer on the intermolecular interactions of the IL mixtures in this chapter.

Low-frequency spectra of neat phosphonium-based ILs with pentyl, ethoxyethyl, or 2-(ethylthio)ethyl group will be critically compared in Chapter VI. The IL whose cation has a thioether group showed higher viscosity than the IL including its comparable alkyl and ether groups in the previous results,[83] which contradict the previous heavy atom substitution effect on viscosity in ILs. I will investigate the effect of the heavy atom substitution on the intermolecular interactions of the ILs in detail to obtain new insights into the influence of ILs on the physical properties. Furthermore, I will compare the low-frequency spectra obtained not only by fs-RIKES but also THz-TDS. There are few reports comparing low-frequency spectra

of ILs using Raman and IR, and this comparison will allow us to examine how the combination of fs-RIKES and THz-TDS is useful in the systems with multiple components such as ILs and IL mixtures.

Chapter VII summarizes this thesis.

Chapter II.

Experimental Section

II.1 Synthesis of Samples

In Chapter III, IV, and VI, I used synthesized ILs. The ILs were synthesized by two typical ionic liquid synthesis processes: alkylation and anion exchange reactions.[4] To confirm that pure ILs have been synthesized, I checked the ILs by ^{1}H NMR and elemental analysis. The rates of the carbon, hydrogen, and nitrogen in elemental analysis were agreed with the calculated rates within ±0.4%. This error region is following the criterion in the Journal of Organic Chemistry. Additionally, in chapter V, I also synthesized 1-octylimidazole for comparison with [MOIm][BF_4]. The purity of 1-octylimidazole was confirmed by ^{1}H NMR and ^{13}H NMR. The detail of the synthesis procedure of the samples are summarized in Appendix.

II.2 Measurements of Liquid Properties

In this study, I measured liquid properties, such as density (ρ), viscosity (η), surface tension (γ), and electrical conductivity (σ) of samples. The ρ values of the mixtures and neat liquids were measured by a densitometer (Anton Paar, DMA 4100 M) at 293.0 ± 0.1 K. The η values of samples were estimated using a reciprocating electromagnetic piston viscometer (Cambridge Viscosity, ViscoLab 4100) equipped with a circulating water bath (Yamato, BB300) at 293.0 ± 0.2 K. The γ values of samples were determined by a contact angle meter (Kyowa Interface Science, DMs-401) at 293.0 ± 0.2 K with a circulating water bath (EYELA, NBC-1210). An electrical conductivity meter (Mettler Toledo, S470 SevenExcellence) which was equipped with a laboratory-built temperature controller based on a Peltier module (VICS, VPE35-5-20TS) used for measuring the σ values of the samples at 293.0 ± 0.2 K. The physical properties of neat [MOIm][BF_4] are measured independently in the three papers related to Chapters III, IV, and V, respectively and the values of the physical properties of neat [MOIm][BF_4] were averaged in this thesis.

In Chapter VI, I also measured melting points, T_m, and glass transition temperatures, T_g, of the samples by differential scanning calorimetry (DSC) measurements (Shimadzu, DSC-60 Plus) in Chapter VI. The liquid samples were cooled to 143 K and then heated to 323 K twice with a scanning rate of 5 K/min. In order to erase the thermal histories, T_m and T_g were determined during the second heating process.

II.3 Femtosecond Raman-Induced Kerr Effect Spectroscopy

II.3.1. Third-order Nonlinear Spectroscopy

Femtosecond Raman-Induced Kerr Effect Spectroscopy (fs-RIKES) is a third-order nonlinear spectroscopy technique based on the pump-and-probe method using a femtosecond laser pulse. Before the explanation of the principle of fs-RIKES, I will explain third-order nonlinear phenomenon.

In many common spectroscopies, optical phenomena (absorption, scattering, emission, diffraction, and so on) are linearly proportional to the electric field of light and called linear optical phenomena. On the other hand, a laser, which has a strong photoelectric field, can induce the nonlinear response of a material.[84,85] The response of a material to the light can be expressed by the polarization *P* as follows:

$$P = \varepsilon_0 \chi^{(1)} E + \varepsilon_0 \chi^{(2)} E^2 + \varepsilon_0 \chi^{(3)} E^3 + \cdots \quad \text{(II-1)}$$

where ε_0 is the vacuum permittivity, χ is the electrical susceptibility, and *E* is the electric field of incident light. The first term in Eq (II-1) is for linear optical phenomena, while the second and higher order terms represent nonlinear optical phenomena. Second-order nonlinear optical phenomena in the second term include the sum frequency generation, difference frequency generation, second-harmonic generation, and so on. Then the third term represents third-order nonlinear optical phenomena including fs-RIKES.

In the third-order nonlinear optical phenomena, three electric fields have an effect on the third-order nonlinear polarization. The incident electric field *E*(r, t), which is time-dependent and position-dependent and has angular frequency ω, is expressed as follows:[85-87]

$$E(r,t) = E_\omega \cos\left(\omega t - \vec{k}\vec{r}\right) \quad \text{(II-2)}$$

where E_ω is the maximum amplitude of the electric field which has angular frequency ω, $\vec{k}$ is the wavenumber vector, and $\vec{r}$ is the position vector. Since the third-order nonlinear polarization $P^{(3)}$ is caused by three electric fields, it can be rewritten as follows:

$$P^{(3)}(r,t) = \varepsilon_0 \chi^{(3)} E(r,t)^3 =$$
$$\varepsilon_0 \chi^{(3)} \left\{ E_{\omega_1} \cos\left(\omega_1 t - \vec{k}_1 \vec{r}\right) + E_{\omega_2} \cos\left(\omega_2 t - \vec{k}_2 \vec{r}\right) + E_{\omega_3} \cos\left(\omega_3 t - \vec{k}_3 \vec{r}\right) \right\}^3 \quad \text{(II-3)}$$

Expanding this Eq (II-3) reveals that $P^{(3)}(r,t)$ contains the different angular frequency components as shown below.[84]

$$3\omega_1, 3\omega_2, 3\omega_3, 2\omega_1 \pm \omega_2, 2\omega_2 \pm \omega_3, 2\omega_3 \pm \omega_1, \omega_1 \pm 2\omega_2, \omega_2 \pm 2\omega_3, \omega_3 \pm 2\omega_1,$$
$$\omega_1 + \omega_2 + \omega_3, \omega_1 + \omega_2 - \omega_3, \omega_1 - \omega_2 + \omega_3, -\omega_1 + \omega_2 + \omega_3, \omega_1, \omega_2, \omega_3 \quad \text{(II-4)}$$

There are nonlinear optical phenomena corresponding to each of these angular frequencies. For example, $3\omega_1$ is third harmonic generation and $\omega_1 + \omega_2 + \omega_3$ is four-wave mixing, and so on.

These nonlinear optical phenomena require the incident lights to satisfy phase matching conditions.[84,87,88] For example, the nonlinear polarization component of coherent anti-Stokes Raman scattering (CARS)[89,90] is

$$P^{(3)}_{2\omega_2-\omega_1}(r,t) = \frac{3}{4}\varepsilon_0\chi^{(3)}{E_{\omega_1}}{E_{\omega_2}}^2 \cos\left((2\omega_2 - \omega_1)t - (2\vec{k}_2 - \vec{k}_1)\vec{r}\right) \quad \text{(II-5)}$$

This equation indicates that the polarization of CARS generates the light with an angular frequency of $2\omega_2 - \omega_1$ and a wavenumber vector of $2\overrightarrow{k_2} - \overrightarrow{k_1}$. The relationship between k and ω is given by $k = \frac{n\omega}{c}$,[85,87] using the refractive index n of the medium and the light speed c. Thus, the phases of light and polarization are spatially aligned by selecting a wavenumber vector (angle of incidence) that satisfies the following equation.

$$\left|2\overrightarrow{k_2} - \overrightarrow{k_1}\right| = \frac{n}{c}(2\omega_2 - \omega_1) \quad \text{(II-6)}$$

This relation calls phase matching condition.

On the other hand, the nonlinear polarization component of induced Raman scattering including fs-RIKES[91,92] is

$$P^{(3)}_{\omega_1}(r,t) = \frac{3}{4}\varepsilon_0\chi^{(3)}({E_{\omega_1}}^2 + 2{E_{\omega_1}}{E_{\omega_2}}^2 + 2{E_{\omega_1}}^2{E_{\omega_2}}) \cos\left(\omega_1 t - \vec{k}_1\vec{r}\right) \quad \text{(II-7)}$$

In this case, it can be seen that the phase matching condition is automatically satisfied and the nonlinear polarization is generated in the same direction as the incident light. Thus, the nonlinear polarization component is reflected in the intensity change of the incident laser light.

II.3.2. Principle of fs-RIKES

II.3.2.1. Energy Diagram and Induced Raman Process of fs-RIKES

Figure II.1 shows a schematic energy diagram of fs-RIKES.[87] Since fs-RIKES observes both Stokes and anti-Stokes scattering simultaneously, Figure II.1 depicts the two processes. At first ($\tau = 0$), the vibrational state of the molecule is induced by the pump light.

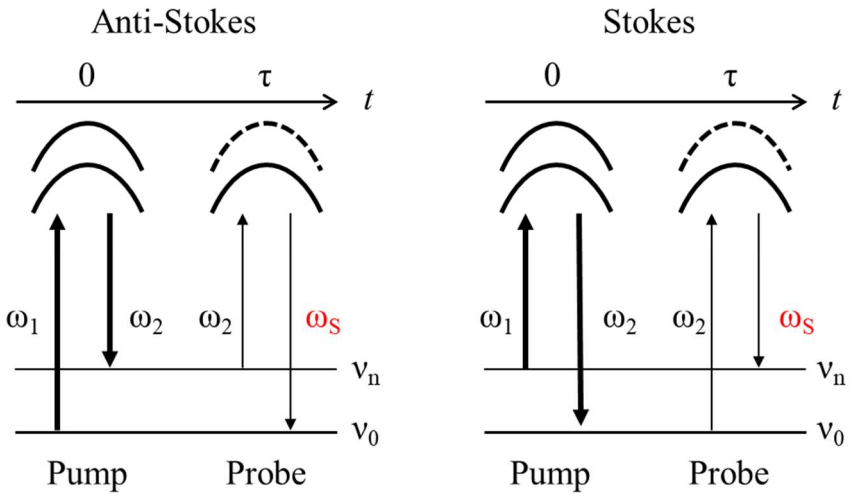

Figure II.1. Schematic energy diagram of fs-RIKES.

Now, I will explain why this induced process occurs, focusing on the polarizability of the molecule, α_{ij}. When a molecule with dipole moment p due to polarizability α_{ij} receives potential energy W from the electric fields of lights, $E_i(t)$ and $E_j(t)$, the equation of W is

$$W = -pE = -\sum_{ij} \alpha_{ij} E_i(t) E_j(t) \tag{II-8}$$

In the normal mode of the molecule, the molecule is vibrating with $q(t)$.[85]

$$q(t) = q_0 \cos(\omega t) = \frac{1}{2} q_0 \exp(-i\omega t) + cc \tag{II-9}$$

where q_0 is the amplitude of $q(t)$ and cc is the complex conjugate term. The α_{ij} is dependent on $q(t)$ and can be written as[87]

$$\alpha_{ij}(t) = (\alpha_0)_{ij} + \left[\frac{1}{2}\left(\frac{\partial \alpha_{ij}}{\partial q}\right)_0 q_0 \exp(-i\omega t) + cc\right] \tag{II-10}$$

where $(\alpha_0)_{ij}$ is the polarizability of the molecule when the nucleus is in equilibrium (time-independent polarizability component) and $(\frac{\partial \alpha_{ij}}{\partial q})_0$ is the Raman polarizability. The force F that a molecule receives from light is

$$F = -\frac{\partial W}{\partial q} = \sum_{ij}(\frac{\partial \alpha_{ij}}{\partial q})_0 E_i(t)E_j(t) \quad \text{(II-11)}$$

The component F' in Eq (II-11) which has a differential frequency ($\omega = \omega_1 - \omega_2$) that can resonate with the intermolecular vibrational modes is Eq (II-12).[87]

$$F' = \frac{1}{4}\sum_{ij}(\frac{\partial \alpha_{ij}}{\partial q})_0 \left\{E_{i,\omega_1}E_{j,\omega_2} \exp(-i(\omega_1 - \omega_2)t) + cc\right\} \quad \text{(II-12)}$$

The equation of motion of the molecule on the normal coordinate $q(t)$ is

$$F'' = m\frac{d^2q(t)}{dt^2} + 2m\Gamma\frac{dq(t)}{dt} + m{\omega_\nu}^2 q(t) \quad \text{(II-13)}$$

where m is the reduced mass of the molecule and ω_ν is the vibrational angular frequency of the molecule. The second term involving Γ on the right hand side is the frictional force that depends on the velocity of the molecules.[93] The steady-state solution to Eq (II-13) can be written using Eq (II-9) and (II-12) as follows:

$$q_0 = \frac{1}{2m[{\omega_\nu}^2 - (\omega_1 - \omega_2)^2 - 2i(\omega_1 - \omega_2)\Gamma]}\sum_{ij}(\frac{\partial \alpha_{ij}}{\partial q})_0 \left\{E_{i,\omega_1}E_{j,\omega_2}\right\} \quad \text{(II-14)}$$

Then, the polarizability is

$$\alpha_{ij}(t) = (\alpha_0)_{ij} + \left[\frac{1}{2}\left(\frac{\partial \alpha_{ij}}{\partial q}\right)_0 \frac{1}{2m[{\omega_\nu}^2 - (\omega_1 - \omega_2)^2 - 2i(\omega_1 - \omega_2)\Gamma]}\sum_{ij}(\frac{\partial \alpha_{ij}}{\partial q})_0 E_{i,\omega_1}E_{j,\omega_2} \exp(-i(\omega_1 - \omega_2)t) + cc\right] \quad \text{(II-15)}$$

When $\omega_\nu = \omega_1 - \omega_2$, the amplitude of $\alpha_{ij}(t)$ is maximized and $\alpha_{ij}(t)$ is expressed as follows:

$$\alpha_{ij}(t) = (\alpha_0)_{ij} + \left[\frac{i}{8m(\omega_1-\omega_2)\Gamma}\left(\frac{\partial\alpha_{ij}}{\partial q}\right)_0 \sum_{kl}(\frac{\partial\alpha_{ij}}{\partial q})_0 E_{i,\omega_1} E_{j,\omega_2} \exp(-i(\omega_1-\omega_2)t) + cc\right] \text{(II-16)}$$

Eq(II-16) shows that when the difference between ω_1 and ω_2 coincides with the vibrational mode, ω_v, of the molecule, the polarizability of the molecule is perturbed and excited coherently with the incident light. This process is called the induced Raman process. In the above series of explanations, two electric fields, E_{ω_1} and E_{ω_2}, are involved. In fs-RIKES, only a single pump pulse is enough to generate this induced Raman process, because a fs laser pulse has a wide frequency band due to its short time width.

The coherent vibrational state of the molecule gradually relaxes over time. By gradually changing the incident timing of the probe light pulse, fs-RIKES can measure this vibrational relaxation process.

II.3.2.2. Signal Detection of fs-RIKES

Figure II.2 shows a schematic diagram of signal detection corresponding to anisotropic molecular motion. In the apparatus used in this study, the polarization of the probe light is set to +45° relative to the polarization of the pump light, and the polarization of the detector is set to -45°. No signal is detected in the case of an isotropic sample as it is. When a pump pulse hit the sample, the Raman active mode of the sample molecule is induced and the sample become anisotropic due to the induced Raman active mode. As a result, the polarization of the probe light is tilted and a signal is detected on the polarization side of the detector. This phenomenon is called Raman-induced Kerr effect. This anisotropy returns to its original isotropic state over time. Femtosecond-RIKES observes the time variation of this process with the probe laser pulse.

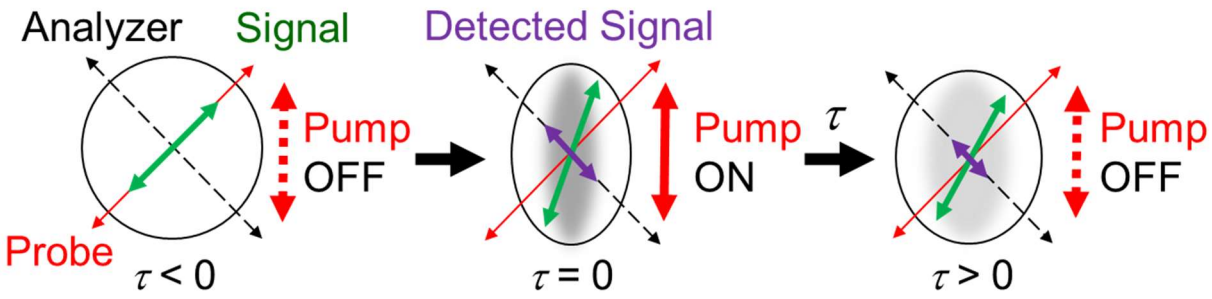

Figure II.2. Schematic of fs-RIKES signal detection.

However, homodyne detection, which is proportional to the square of the signal electric field (E_{Sig}), is difficult to provide accurate measurements because the signal intensity is small. Then, by tilting the polarization slightly (~1.5°) and using a quarter-wave plate to polarize the probe beam elliptically, a local oscillating electric field (E_{LO}) can be introduced. Since the E_{LO} mixes with E_{Sig} automatically, the intensity by the heterodyne detection[94] is

$$I_{Hetero} \propto \left|E_{Sig} + E_{LO}\right|^2 = \left|E_{Sig}\right|^2 + \left\{E_{Sig}E_{LO} + cc\right\} + \left|E_{LO}\right|^2 \qquad \text{(II-17)}$$

The $\left|E_{Sig}\right|^2$ term might be ignored by tuning $|E_{LO}|^2$ so that $|E_{LO}|^2 \gg \left|E_{Sig}\right|^2$. Only the second term can be taken out using the lock-in amplifier with good accuracy by modulating E_{Sig}. In the actual experiment, the signals are measured with the probe light's polarization tilted by about +1.5° or -1.5°. Both are added together to remove the homodyne signal contribution so that only the pure heterodyne signal is used in the discussion.

II.3.2.3 Setup of fs-RIKES

Figure II.2.3 exhibits the setup of the fs-RIKES and Ti:sapphire fs-pulse laser used in this thesis.[95,96] The fs-RIKES system was based on the setup reported by McMorrow and Lotshaw.[97] The fs-RIKES system used a Ti:sapphire laser (KMLabs Inc., Griffin). The Ti:sapphire has a very short fluorescence lifetime (3.15 μs) and can only be excited by an intense laser source. Since the absorption wavelength of Ti:sapphire is around 500 nm, the Ti:sapphire laser was pumped by a Nd:YVO_4 diode laser (Spectra Physics, Millennia Pro 5sJ).

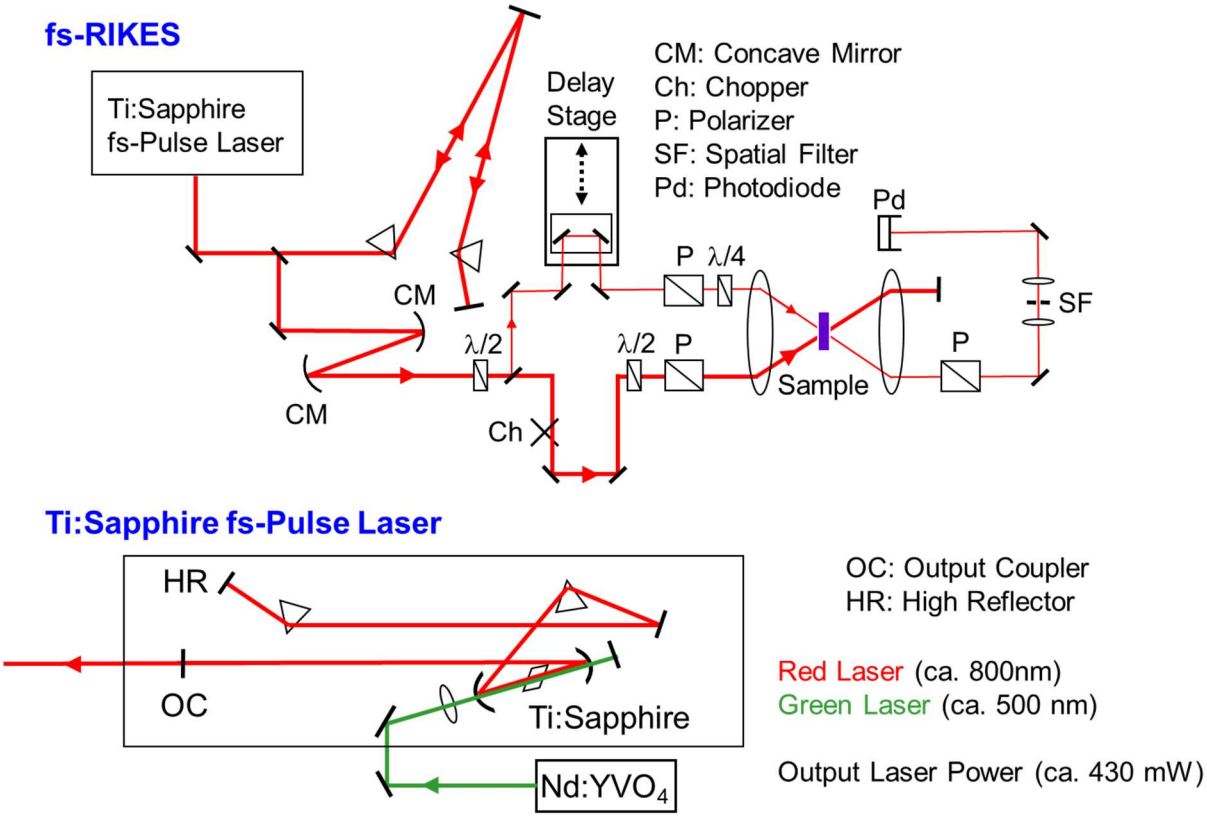

Figure II.2.3. Setup of the fs-RIKES device used in this study.

Femtosecond-RIKES is a spectroscopic technique in which polarization must be carefully controlled. Therefore, Glan-Thomson polarizers with a high extinction ratio (10^6 in our laboratory) were used to obtain data with a higher signal-noise ratio. However, the optical path length of such a polarizer with a high extinction ratio is quite long (1 inch). Thus, positive dispersion occurs when the laser passes through it, causing the light with longer wavelengths to travel faster and that with shorter wavelengths to travel slower. As a result, the time response of the device deteriorates. Therefore, a prism pair was used to increase the optical path length of the light on the long wavelength side and applied inverse dispersion to the laser pulse. This

prism pair is called a dispersion compensating element. These prisms are Brewster prisms. Therefore, when a p-polarized laser beam is injected into this prism at Brewster's angle, θ_B, the reflectance of the p-polarized laser beam becomes zero and no loss of laser intensity occurs. ($\theta_B = arctan(^{n_2}/_{n_1})$, where n_1 and n_2 are the refractive indexes of the incident and transmitted media, respectively.) The Ti:sapphire laser system also used a similar prism pair for phase compensation. By adjusting this prism pair in the resonator, the laser modes are combined in a mode-locked state to generate very short optical pulses. The time response of the fs-RIEKS used in this study was measured by inducing second harmonic generation by a pump light and a probe light on a nonlinear optical KDP crystal. This nonlinear optical crystal KDP has a phase matching type of Type-I (parallel polarization of the two light sources to be coupled) and a thickness of 200 μm. The time response of the fs-RIEKS was confirmed to be about 38 fs at half maximum.

The laser beam passing through the prism pair was narrowed by two concave mirrors. After that, the polarization of the laser was rotated 90° to become vertical by a half-wavelength plate and divided into a pump beam and a probe beam by a beam splitter. The intensity ratio of the pump light to the probe light was approximately 95:5. On the probe light side, there were a time delay stage, a Glan-Thompson polarizer, and a quarter-wavelength plate. The polarizer and quarter-wavelength plate are required for the heterodyne detection as described above and the polarization of the polarizer is +45°. Then, on the pump light side, there were a mechanical chopper (Stanford Research System), a half-wavelength plate, and a Glan-Thompson polarizer. The chopper applied a modulation of approximately 1000 Hz to the pump light and the polarization of the pump light remained vertical. The sample was sandwiched between achromatic lenses so that the pump and probe lights were focused on the sample. The probe light passing through the sample went through the polarizer which was quenched with respect to the polarization of the initial probe light. A spatial filter with a 250 μm pinhole was placed in front of the detector to improve the signal-to-noise ratio, and a PIN photodiode was used as the detector. A heterodyne signal was obtained from the detection signal using a lock-in amplifier (Stanford Research System, SR 830). The sample temperature was controlled by a Peltier temperature controller (Quantum Northwest, Luma 40).

II.3.2.4 Signal Analysis of fs-RIKES

In this thesis, the Kerr transient's data were scanned with an interval of 3.335 fs and the scan ranges were 12.3 ps (in Chapter III~V) and 13.7 ps (in Chapter VI). In Chapters IV and V, I also measured the Kerr transient's data for a long time window (~334 ps) with an interval of 0.167 or 0.133 ps to obtain the information of the slower relaxation processes. Figure II.2.4. shows the Kerr transient of MeCN measured in Chapter III. All Kerr transients were normalized by the intensity at $\tau = 0$, which is corresponding to the instantaneous electrical response. After the electrical response, the Kerr transient exhibits three different kinds of oscillating processes corresponding to the nuclear responses: First is an underdamped motion which is corresponding to the intermolecular vibrations, second is a small beat which is attributed from the intramolecular vibrations, and third is an overdamped motion which is derived from the reorientation process.

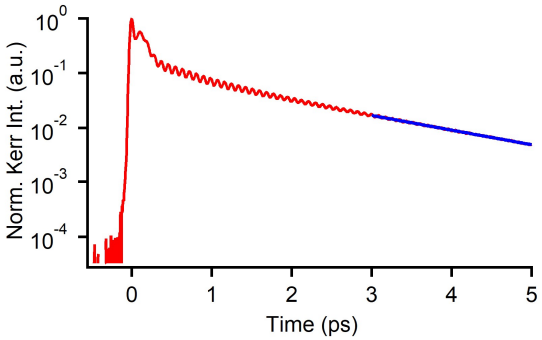

Figure II.2.4. Kerr transient of MeCN measured in Chapter III. Blue line is two exponencial fitting.

This Kerr signal response, $R(t)$, can be written in the following equation.[91]

$$R(t) = \sigma(t) + \sum_i r_i(t) \qquad \text{(II-18)}$$

where $\sigma(t)$ is the instantaneous electrical response (electrical hyperpolarizability), and $r_i(t)$ is the sum of the nuclear responses. In reality, the laser induction is not instantaneous, but takes the time of the laser pulse. Thus, the actual signal $T(t)$ obtained is as follows:

$$T(t) = \int_{-\infty}^{\infty} dt\, R(t-\tau) G_2(t) \qquad \text{(II-18)}$$

where $G_2(t)$ is the second-order autocorrelation function due to the laser pulse. The Fourier transform of the Kerr transient's data in this thesis is based on the procedure developed by Lotshaw and McMorrow. When the imaginary component of the nuclear response component in frequency range is obtained by Fourier transform, the $G_2(t)$ is removed by the deconvolution analysis:

$$\mathrm{Im}[R(\omega)] = \frac{F[T(\tau)]}{F[G_2(\tau)]} \tag{II-19}$$

This allows us to obtain spectra that do not include the instrument response and are derived only from sample response.

The obtained Kerr spectra are shown in Figure II.2.5. The fs-RIKES used in this thesis can measure the low-frequency region oof 0.3~700 cm^{-1}. The sharp peak appearing above 200 cm^{-1} (380 cm^{-1} in Figure II.2.5) is derived from the intramolecular vibration (bending mode of CH_3−C≡N) of MeCN, while the broad bands below 200 cm^{-1} originate from the intermolecular vibrations and reorientational motions. In this thesis, I focus on the intermolecular vibrations of liquid. Thus, I discuss the red spectrum, removing the contribution of the reorientational motion shown in the blue spectrum.

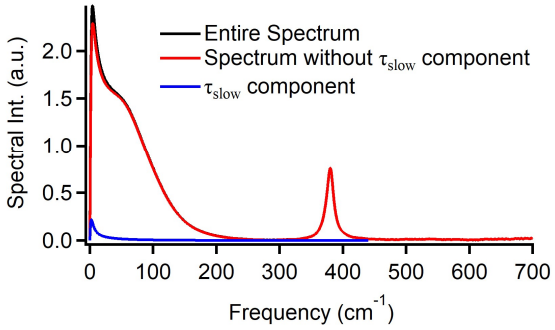

Figure II.2.5. Fourie transform Kerr spectrum of MeCN measured in Chapter III. Blue line is entire spectrum, blue line is the spectrum of the picosecond reorientational component, and red line is the spectrum without the picosecond reorientational component.

Chapter III.

Low-Frequency Spectra of 1-Methyl-3-octylimidazolium Tetrafluoroborate Mixtures with Methanol, Acetonitrile, and Dimethyl Sulfoxide

J. Phys. Chem. B **2020**, 124, 7857-7871.

III. 1. INTRODUCTION

As mentioned in Chapter I, low-frequency spectra of IL/ML mixtures have been reported,[53,55,80-82] but they are few and the influence of molecular liquids on the intermolecular interactions of IL has not been fully discussed. Therefore, in this chapter, I measured low-frequency spectra of [MOIm][BF_4], which possesses high microheterogeneity due to a long alkyl group, mixtures with typical solvent MLs, methanol (MeOH), acetonitrile (MeCN), and dimethyl sulfoxide (DMSO) via fs-RIKES to discuss the effect of ML on the low-frequency spectra of IL systematically.

Takamuku and co-workers measured 1-ethyl-3-methylimidazolium bis(trifluoromethanesulfonyl)amide mixtures with MeOH, MeCN, and DMSO by steady-state Raman spectroscopy, attenuated total reflection infrared spectroscopy (ATR-IR), ^1H and ^{13}C NMR.[98] They revealed that the C^2–H vibration mode of the imidazolium ring shows the largest redshift and deshielding than the other atoms of the cation or the anion and the amplitudes of the largest redshift and deshielding are in the order of DMSO $\gg$ MeOH > MeCN. These orders are consistent with the order of donor numbers (DN) in MLs (DN_{MeOH}: 19.0, DN_{MeCN}:14.1, DN_{DMSO}: 29.8), suggesting that these interactions are hydrogen-bonding interactions. From their results, I expected that these MLs have different effects on the low-frequency spectra, which reflect the intermolecular interactions, of the IL mixtures due to hydrogen-bonding abilities of MLs.

I also measured the liquid properties (density ρ, surface tension γ, viscosity η, and electrical conductivity σ) of the [MOIm][BF_4] mixtures with MeOH, MeCN, and DMSO. In addition, the density-of-states (DOS) spectra based on MD simulations were analyzed to understand the ML concentration dependence of the low-frequency spectra in detail.

III.2. EXPERIMENTAL AND COMPUTATIONAL METHODS

III.2.1. Reagents and Sample Mixtures

In this study, I chose [MOIm][BF_4] as a target IL and MeOH, MeCN, and DMSO as target MLs. [MOIm][BF_4] is one of the common ILs and has a microheterogeneous structure due to its long alkyl group. The MLs have different accepter numbers and donner numbers, each other. Therefore, I expected that the study of the intermolecular dynamics of these mixtures would provide insight into the effect of MLs on the intermolecular interactions of ILs, which are microheterogeneity. [MOIm][BF_4] was synthesized according to the previous synthesized method[99] (see Apendix). The synthesized [MOIm][BF_4] was checked by ^{1}H NMR and elemental analysis. The rates of the carbon, hydrogen, and nitrogen in elemental analysis were agreed with the calculated rates within ±0.4%, which was following the criterion in the Journal of Organic Chemistry. The synthesized [MOIm][BF_4] was used after drying in vacuo at 313 K over 36 h. The water content in [MOIm][BF_4] was measured by a Karl-Fischer coulometer (Hiranuma AQ-300) and the value of the water content was 97 ppm. MeOH (Kanto Chemical, dehydrated, >99.8%), MeCN (Wako Pure Chemicals, Infinity Pure, >99.8%), and DMSO (Wako Pure Chemicals, Infinity Pure, >99.5%), were dried with molecular sieves (3A, Kanto Chemical) before using. I weighed [MOIm][BF_4] and MeOH, MeCN, or DMSO at various ML mole fractions X_{ML} (0 (neat [MOIm][BF_4]), 0.2, 0.4, 0.6, 0.7, 0.8, 0.9, 0.95, 0.97, 0.99, 1 (neat ML)) and prepared all samples.

III.2.2. MD Simulations

The MD simulations were performed by the Takamuku's Laboratory at Saga University. MD simulations of neat [MOIm][BF_4] (X_{ML} = 0), neat MLs (X_{ML} = 1) and their mixture systems at X_{ML} = 0.6 and 0.9 were performed by the MD program package GROMACS 2018.7.[100-106] The compositions of the examined systems are summarized in Table III.1. The [MOIm][BF_4]'s force field developed by Lopes and Padua[28,107,108] was used and the simulations were performed for molecules in a cubic cell under a periodic boundary condition. The three ML models were constructed based on the OPLS-AA force field.[109-112] Table B1 listed the parameters of the present simulations and Figure B1−B4 exhibited the notation of the atoms within each molecule. The simulations considered the bending and torsion terms of the intramolecular interactions, the Lennard-Jones and Coulomb terms, while the LINCS algorithm[113] was used to constrain the bond stretching terms for all atoms. I integrated with 1 fs time step using the leapfrog method[114] and calculated the electrostatic interactions by a smooth particle mesh Ewald method with a real-space cutoff of 13.5 Å.[115] The van der Waals

interactions were decreased and reached null in the switching range (12.0–13.5 Å). The conditions of the simulations were at 1 atm (or 101.325 kPa) and 298.2 K controlled by the Parrinello–Rahman methods[116-118] and Nose–Hoover[119,120] with time constants of 1 ps and 0.5 ps, respectively.

Table III.1. Numbers of Molecules in MD Cell of [MOIm][BF_4]/MeOH, [MOIm][BF_4]/MeCN, and [MOIm][BF_4]/DMSO Systems. Densities Derived from MD Simulations, ρ_{MD}, and Experimentally Determined, ρ_{exp}, at 298.2 K. MD Cell Size l Represents the Length of One Side of the Cube.

	Numbers of molecules in an MD cell		ρ_{MD}	ρ_{exp}	Cell size, l
X_{MeOH}	$N_{[MOIm][BF4]}$	N_{MeOH}	(g cm^{-3})	(g cm^{-3})	(Å)
0	195		1.086	1.104	43.81
0.6	160	241	1.035	1.045	43.93
0.9	85	769	0.9137	0.9227	44.54
1		1367	0.7694	0.7867	45.56
X_{MeCN}	$N_{[MOIm][BF4]}$	N_{MeCN}			
0	195		1.086	1.104	43.81
0.6	160	241	1.024	1.035	44.69
0.9	85	769	0.8809	0.9023	47.13
1		1367	0.7408	0.7766	50.11
X_{DMSO}	$N_{[MOIm][BF4]}$	N_{DMSO}			
0	195		1.086	1.104	43.81
0.6	144	216	1.098	1.103	44.31
0.9	62	559	1.098	1.099	45.23
1		820	1.095	1.095	45.97

In this simulation, the NPT ensemble was used. First, the center of mass of the molecules was randomly placed in a cubic cell, and the molecules in the cell were stirred at 800.2 K and 1000 atm for the first 500 ps. After that, the system was equilibrated at 298.2K and 1 atm (or 101.325 kPa) for 1.5ns and continued running for 10ns. The density estimated by the MD simulation and the density of the real solution obtained experimentally at 298.2 ± 0.1 K are shown in Table III.1. The changes in density obtained from the MD calculation were within a deviation of 4.8% in the worst case, confirming the validity of the simulation (see Figure B5 in Appendix).

III.2.3. Quantum Chemistry Calculations

I used the Gaussian 16 program (Revision C.01)[121] for quantum chemistry calculations for the geometry optimizations of $[MOIm]^+$, $[BF_4]^-$, MeOH, MeCN, and DMSO. The density functional theory (DFT) calculations were based on the B3LYP/6-311+G(d.p) level of theory.[122,123] Table B2 of the Appendix listed the atom coordinates of the optimized structures of the ions and MLs.

III.3. RESULTS

III.3.1. Liquid Properties: Density, Surface Tension, Viscosity, and Electrical Conductivity

The X_{ML} dependences of ρ for the [MOIm][BF_4] mixtures with MeOH, MeCN, and DMSO are shown in Figure III.1. The measuring temperature is 293.0 K. The value of ρ for neat [MOIm][BF_4] shows almost similar to the values reported by previous studies[41,53,55] and those for neat MLs were also coincide with those in the CRC Handbook[52] within the experimental error ranges. Table B3 of the Appendix summarized the values of ρ for the mixtures. As shown in Figure III.1, the X_{ML} dependence of ρ for the [MOIm][BF_4] mixtures with MeOH and MeCN exhibited similar X_{ML} dependence. On the other hand, the ρ of the [MOIm][BF_4]/DMSO showed almost same values with increasing X_{ML}. This may be because the ρ of neat [MOIm][BF_4] (1.1075 g/mL) is almost like that of neat DMSO (1.1005 g/mL).

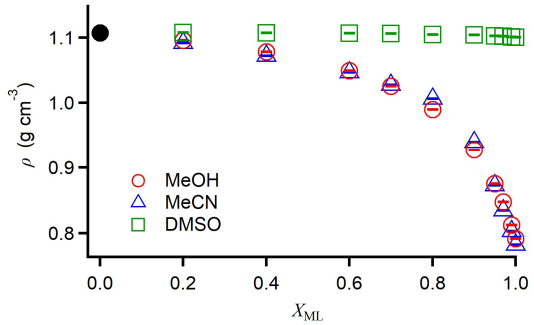

Figure III.1. Plots of ρ vs. X_{ML} for [MOIm][BF_4] mixtures with MeOH (red circles), MeCN (blue triangles), and DMSO (green squares). Datum for neat [MOIm][BF_4] is also shown (filled black circle).

Figure III.2. shows the dependence of γ for the three systems on X_{ML} at 293.0 K. The value of γ for neat [MOIm][BF_4] was consistent with those reported in previous studies[41,53,55,124]

and those for the neat MLs were also similar to the values in the CRC Handbook[52] within the experimental error ranges. Table B3 of the Appendix listed all values of γ for the mixtures. The X_{ML} dependence of γ showed different trends in each system. The values of γ for the [MOIm][BF_4]/MeOH gradually decreased with increasing X_{ML}, and in particular at $X_{ML} \geq 0.6$. The values of γ for the [MOIm][BF_4]/MeCN were almost similar to that for neat [MOIm][BF_4] up to $X_{ML} \approx 0.8$ and decreased in the $X_{ML} \geq 0.9$. The values of γ for the [MOIm][BF_4]/DMSO increased with increasing X_{ML}, especially in $X_{ML} \geq 0.8$.

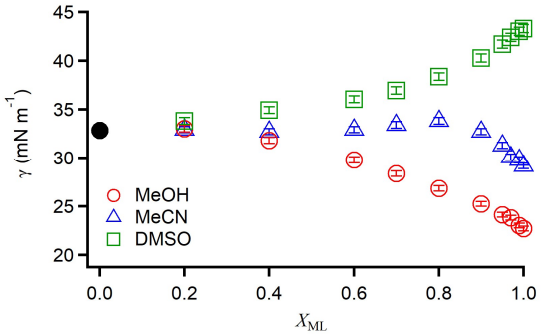

Figure III.2. Plots of γ vs. X_{ML} for [MOIm][BF_4] mixtures with MeOH (red circles), MeCN (blue triangles), and DMSO (green squares). Datum for neat [MOIm][BF_4] is also shown (filled black circle).

The semi-logarithmic plots of η vs. X_{ML} for the [MOIm][BF_4] mixtures with MeOH, MeCN, and DMSO is shown in Figure III.3. The measurement temperature is 293.0 K. The η value of neat [MOIm][BF_4] was almost in accordance with the reported values in previous studies[41,53,55,124] and those of the neat MLs agreed well with the values in CRC handbook[52] within experimental error regions. Table B3 of the Appendix summarized all η values. As shown in Figure III.3, since the η of [MOIm][BF_4] was significantly higher than those of the neat MLs, the η decreased significantly with increasing X_{ML}.

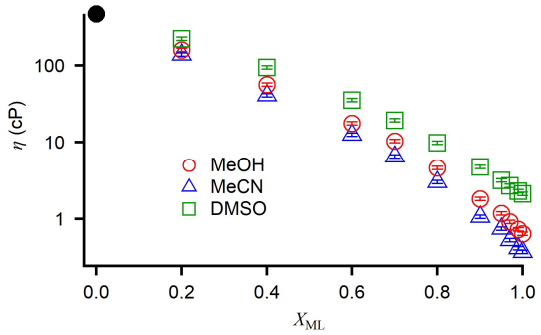

Figure III.3. Plots of η vs. X_{ML} for [MOIm][BF_4] mixtures with MeOH (red circles), MeCN (blue triangles), and DMSO (green squares). Datum for neat [MOIm][BF_4] is also shown (filled black circle).

The semi-logarithmic plots of σ vs. X_{ML} for the [MOIm][BF_4] mixtures with MeOH, MeCN, and DMSO is shown in Figure III.4. The measurement temperature is 293.0 K. The σ value of neat [MOIm][BF_4] almost coincided with the values in previous reports[41,125] and those of the neat MLs were similar to the values in CRC handbook within experimental error regions. Table B3 of the Appendix summarized all σ values. As shown in Figure III.4, all systems had a maximum point of σ to X_{ML} each other. In [MOIm][BF_4]/MeOH and [MOIm][BF_4]/DMSO, the maximum values of σ were at X_{ML} = 0.90. In [MOIm][BF_4]/MeCN, that is found at X_{ML} = 0.95. Such a maximum value of σ has been observed in other IL/ML mixtures.[4,126,127]

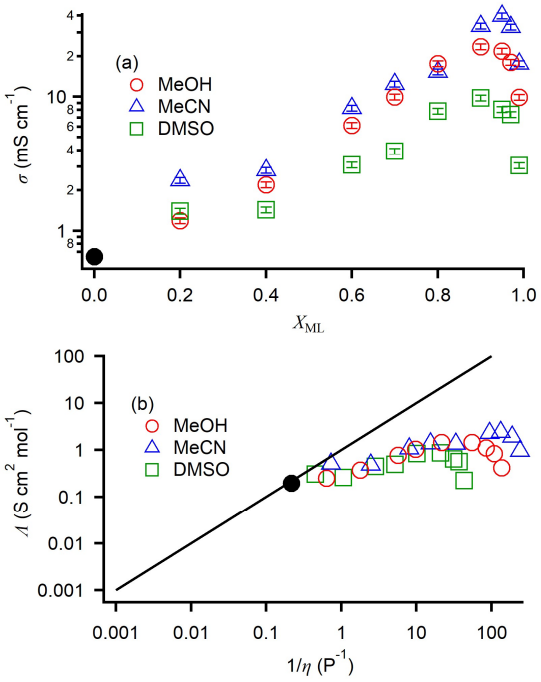

Figure III.4. Plots of (a) σ vs X_{ML} and (b) Λ vs η^{-1} (Walden plot) for [MOIm][BF_4] mixtures with MeOH (red circles), MeCN (blue triangles), and DMSO (green squares). Datum for neat [MOIm][BF_4] is also shown (filled black circle). Ideal Walden line with a unity slope is also given by a black line. Error bars for σ data are also given.

III.3.2. Low-Frequency Kerr Spectra via fs-RIKES

Figure III.5 shows the time-domain transients obtained by fs-RIKES measurements for the [MOIm][BF_4] mixtures with MeOH, MeCN, and DMSO at 293.0 K. The intensity is due to the nuclear response from ~0.03 ps to ~0.3 ps. With increasing X_{ML}, the intensity of nuclear responses for [MOIm][BF_4]/MeCN increased, while that for [MOIm][BF_4]/DMSO decreased. On the other hand, that of [MOIm][BF_4]/MeOH showed a more complicated trend.

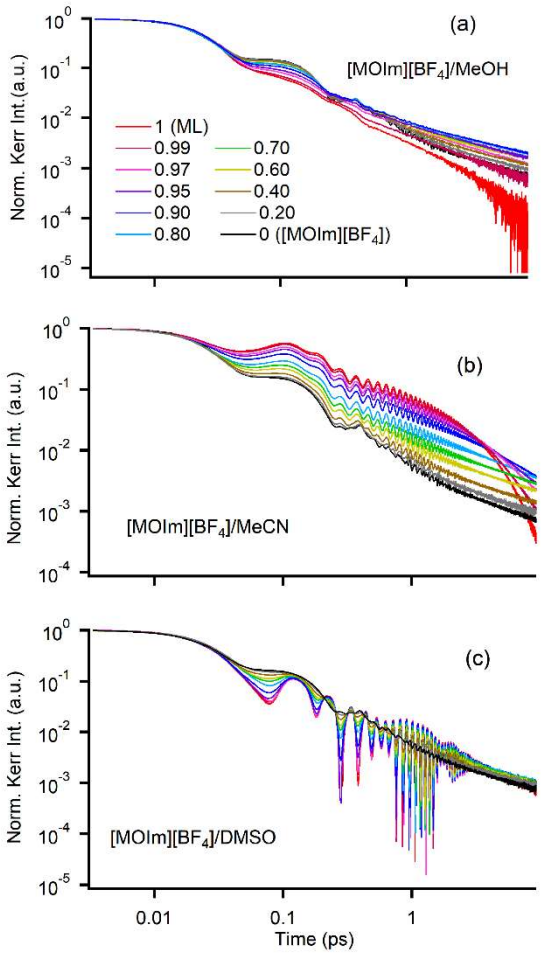

Figure III.5. Kerr transients for (a) [MOIm][BF_4]/MeOH, (b) [MOIm][BF_4]/MeCN, and (c) [MOIm][BF_4]/DMSO as functions of X_{ML}.

Figure III.6 shows the Kerr transients of [MOIm][BF_4]/MeOH at X_{ML} = 0–0.90 and 0.90–1 separately to compare the X_{ML}-dependent features. With increasing X_{ML}, a bump of the Kerr transients at ~0.1 ps gradually decreased, while the Kerr intensity over ~0.5 ps increased in $X_{ML} \leq 0.90$ and decreased in $X_{ML} \geq 0.95$.

These Kerr transients were fitted by a biexponential function ($a_0 + a_1\exp(-t/\tau_1) + a_2\exp(-t/\tau_2)$) to analyze the slow relaxation component over 3 ps. Table B4 of the Appendix summarized the fit parameters for the Kerr transients. Previous results of the fit parameters for the Kerr transients of the neat [MOIm][BF_4] are similar to this study's results (See Table B4 in Appendix). Although fs-RIKES used in this study can measure the range of the delay time up to 300 ps, the slow relaxation component, which is derived from the collective reorientation of ILs, typically exhibits the order of nanoseconds.[128,129] Therefore, I could not obtain the entire reorientation processes of [MOIm][BF_4]. However, I concentrate on the intermolecular vibrational dynamics of condensed phases and the long-time-window data have little effect on the spectral shapes of the intermolecular vibration spectra. Thus, the relaxation components of over tens of picoseconds is unnecessary.[70]

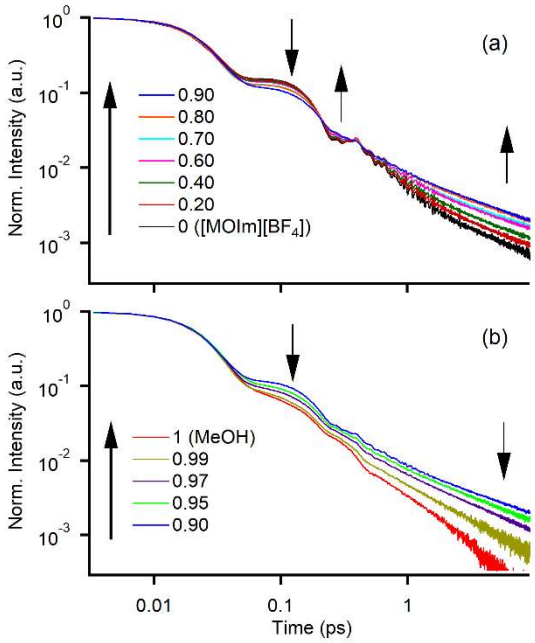

Figure III.6. Normalized Kerr transients of [MOIm][BF_4]/MeOH at X_{ML} = (a) 0–0.90 and (b) 0.90–1.

The low-frequency Kerr spectra were obtained from the Kerr transients by the Fourier transform deconvolution analysis. This Fourier transform procedure was developed by McMorrow and Lotshaw and explained in Chapter II.3.2.4. The Fourier transform Kerr spectra

of the [MOIm][BF_4] mixtures with MeOH, MeCN, and DMSO are shown in Figure III.7. The slow relaxational components ($a_0 + a_2\exp(-t/\tau_2)$) were removed from these spectra to concentrate on the intermolecular vibrational bands. The sharp bands due to the intramolecular vibrational modes appeared in the frequency region over 200 cm^{-1}. In the [MOIm][BF_4]/MeOH, the intramolecular vibrational bands were mainly attributed from $[MOIm]^+$ and $[BF_4]^-$. In the [MOIm][BF_4] mixtures with MeCN and DMSO, the intramolecular vibrational bands are due to both ML and [MOIm][BF_4], but the strong bands are derived from MeCN or DMSO. Additionally, intermolecular vibrational bands appeared in the frequency region below 150 cm^{-1}.

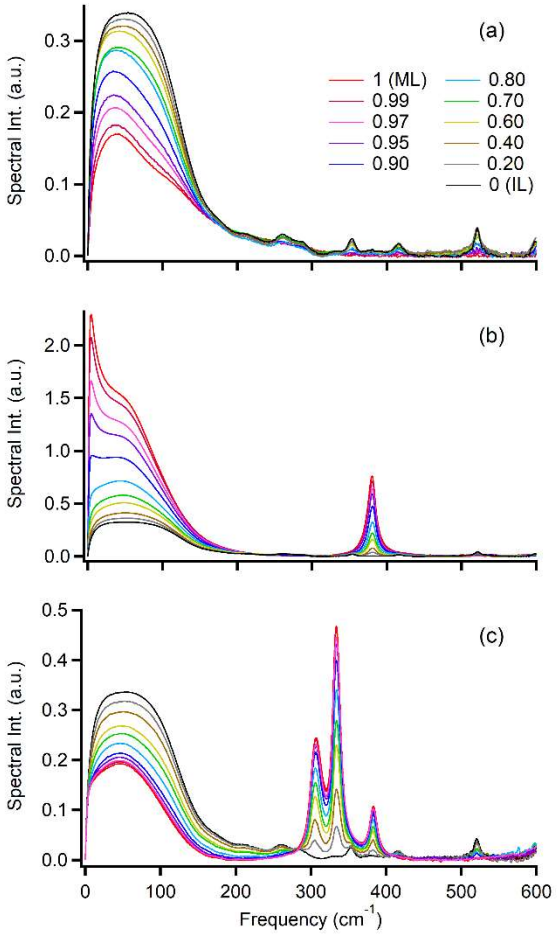

Figure III.7. Kerr spectra at the frequency range of 0–600 cm^{-1} for (a) [MOIm][BF_4]/MeOH, (b) [MOIm][BF_4]/MeCN, and (c) [MOIm][BF_4]/DMSO with a function of X_{ML}.

Figure III.8 exhibits the Kerr spectra in 0–250 cm^{-1}. It can be seen that the results of the low-frequency Kerr spectra of neat [MOIm][BF_4],[41,53,55,130] MeOH,[131,132] MeCN,[132,133] and DMSO[133,134] are very similar to the previous results. Figure III.8 shows that, with increasing X_{ML}, the spectral intensity in the low-frequency region decreases in the [MOIm][BF_4] mixtures with MeOH and DMSO, while that increases in [MOIm][BF_4]/MeCN. There are no reports of

low-frequency Kerr spectra of the imidazolium ILs mixtures with MeOH and DMSO, but low-frequency spectra of 1-methyl-3-pentylimidazolium bis(trifluoromethylsulfonyl)amide ([MPIm][NTf_2])/MeCN mixtures were reported by Quitevis[82] and coworkers and their results are good agreement with the present results.

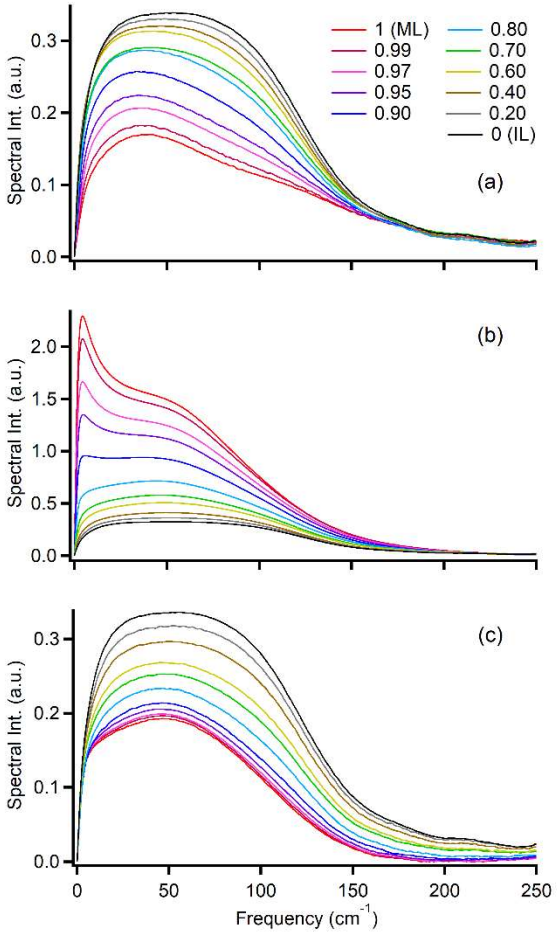

Figure III.8. Low-frequency Kerr spectra at the frequency range of 0–250 cm^{-1} for (a) [MOIm][BF_4]/MeOH, (b) [MOIm][BF_4]/MeCN, and (c) [MOIm][BF_4]/DMSO at various values of X_{ML}.

To analyze the concentration dependence of line shape for the low-frequency spectrum $I(\omega)$, I used the sum of Ohmic and anti-symmetrized Gaussian functions. Ohmic function is a kind of Bucaro-Litovitz function[135] and this function is an empirical function to represent a depolarized Rayleigh scattering of simple molecule at gas and liquid. Bucaro-Litovitz function is written by

$$I_{BL}(\omega) = \sum_{i=1}^{n} a_{\mathrm{BL,i}} \omega^n \exp\left(-\frac{\omega}{\omega_{BL,i}}\right) \qquad \text{(III-1)}$$

where $a_{o,n}$, and $\omega_{o,n}$ are the amplitude and characteristic frequency. When n = 1, Bucaro-Litovitz function call Ohmic function. On the other hand, anti-symmetrized Gaussian function[136] represent the molecular motion in which the spectrum has a non-uniform broadening (such as librational motion). The equation of anti-symmetrized Gaussian function is

$$I_G(\omega) = \sum_{i=1}^{n} a_{\mathrm{G},i} \left\{ \exp\left[\frac{-2\left(\omega - \omega_{\mathrm{G},i}\right)^2}{\Delta\omega_{\mathrm{G},i}^2}\right] - \exp\left[\frac{-2\left(\omega + \omega_{\mathrm{G},i}\right)^2}{\Delta\omega_{\mathrm{G},i}^2}\right] \right\}, \qquad \text{(III-2)}$$

where $a_{G,n}$, $\omega_{G,n}$, and $\Delta\omega_{G,n}$ are the amplitude, characteristic frequency, and width parameters of each function, respectively. Then, to fit a clear intramolecular vibrational band appeared in the low-frequency spectrum, I also used a Lorentzian function $I_L(\omega)$:

$$I_L(\omega) = \frac{a_{\mathrm{L}}}{(\omega - \omega_{\mathrm{L}})^2 + \Delta\omega_{\mathrm{L}}^2}, \qquad \text{(III-3)}$$

where a_{L}, ω_{L}, and $\Delta\omega_{\mathrm{L}}$ are the amplitude, characteristic frequency, and width parameters of the Lorentzian function, respectively.

As an example, Figure III.9 shows the results of the line shape analysis for the low-frequency spectra of [MOIm][BF_4]/DMSO at X_{DMSO} = 0.20 and 0.95. The results for the other low-frequency spectra also showed similar quality fits. Figure B6-B8 and Table B5 of the Appendix summarize the results of the line shape analysis of the low-frequency spectra.

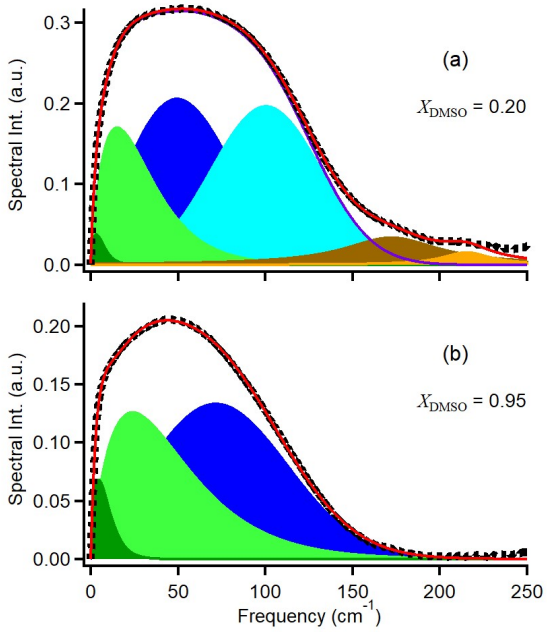

Figure III.9. Line-shape analysis results of low-frequency Kerr spectra of [MOIm][BF_4]/DMSO at (a) X_{DMSO} = 0.20 and (b) X_{DMSO} = 0.95. Dark and light green areas denote Ohmic components, dark and light blue areas denote anti-symmetrized Gaussian components, and dark and light brown ones denote Lorentzian components.

To evaluate the concentration dependence of the low-frequency spectra semi-qualitatively, I estimated the M_1 of the low-frequency spectrum using following eq. (III-4).

$$M_1 = \int \omega I(\omega) d\omega / \int I(\omega) d\omega, \qquad \text{(III-2)}$$

where $I(\omega)$ is the intensity of the spectrum after removing the picosecond overdamped relaxational components and the intramolecular vibrational ones from the entire spectrum. The plots of M_1 vs. X_{ML} for the three systems are shown in Figure III.10. Table B5 of the Appendix summarize the estimated values of M_1 for the samples. The M_1 value for neat [MOIm][BF_4] was the averaged values for the three systems. Figure III.10 shows that M_1 did not change significantly in $X_{ML} \leq 0.6$. In the region of X_{ML} = 0.6–0.9, the values of M_1 gradually increased for [MOIm][BF_4]/MeOH and decreased in the [MOIm][BF_4] mixtures with MeCN and DMSO. In $X_{ML} \geq 0.9$, the degree of change in each system was steeper.

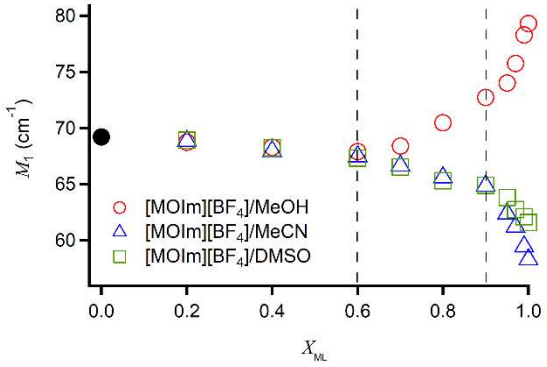

Figure III.10. Plots of M_1 vs. X_{ML} for [MOIm][BF_4]/MeOH (red circles), [MOIm][BF_4]/MeCN (blue triangles), [MOIm][BF_4]/DMSO (green squares), and neat [MOIm][BF_4] (black filled circle).

III.3.3. DOS Spectra via MD Simulations

Figure III.11 shows the snapshots for the [MOIm][BF_4] mixtures with MeOH, MeCN, and DMSO (X_{ML} = 0 (neat [MOIm][BF_4]), 0.6, and 0.9) at 10 ns (the end of production runs) from MD simulations. As shown in Figure III.11, the IL structures of the three mixtures at X_{ML}

= 0.6 are similar to that of neat [MOIm][BF_4]. Voth and coworkers performed MD simulations of [MPIm][NTf_2]/MeCN mixtures at X_{MeCN} = 0.05, 0.10, 0.20, and 0.50.[82] Their results suggest that the MeCN molecules interact with the imidazolium rings of the IL and are dispersed in the IL. In this study, the snapshots of the [MOIm][BF_4] structure at X_{ML} = 0.6 exhibited that not only MeCN but also MeOH and DMSO mainly interact with the ionic region. At X_{ML} = 0.9, in [MOIm][BF_4]/MeOH, the red and green regions deriving from the IL were most separated from the blue region of MeOH among the three ML solutions and this may be due to the hydrogen bonding network of MeOH in the [MOIm][BF_4] mixture. Canongia Lopes and coworkers investigated the microscopic structures of 1-butyl-3-methylimidazolium hexafluorophosphate mixtures with *n*-hexane, MeCN, MeOH, and H_2O by MD simulations.[62] They found that the MeOH mixtures exhibited a similar hydrogen-bonding network to the H_2O mixtures. Despite the different ILs used, the present results are similar to their results. However, the IL structure of the [MOIm][BF_4]/DMSO showed a looser structure at X_{ML} = 0.9. This indicated that the IL constituent ions are relatively well mixed with the DMSO molecules making the ion pairs compared to the other two systems. The results for the [MOIm][BF_4]/MeCN system were an intermediate situation between the [MOIm][BF_4]/MeOH and [MOIm][BF_4]/DMSO systems.

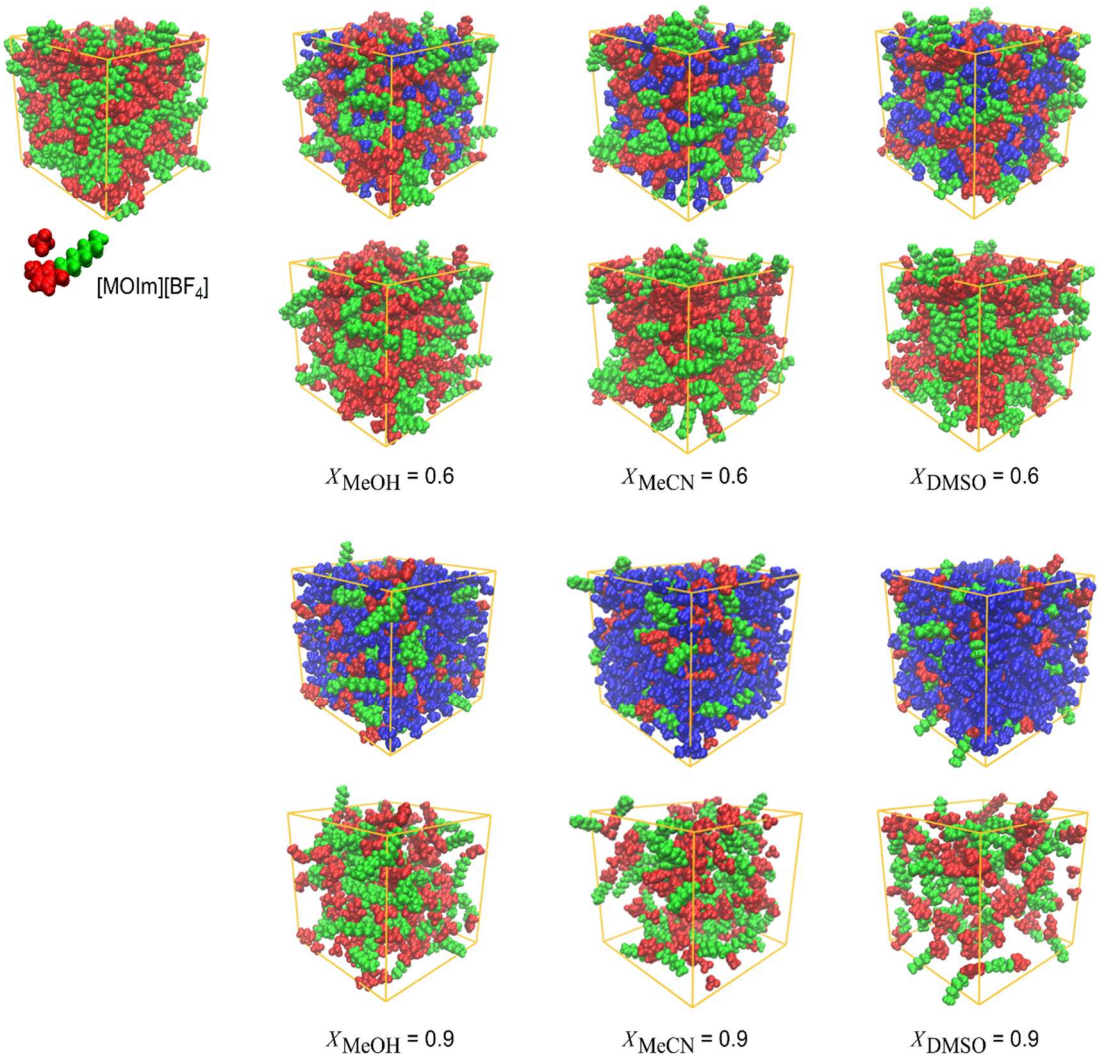

Figure III.11. Snapshots of [MOIm][BF_4] mixtures with MeOH (left column), MeCN (middle column), and DMSO (right column) at X_{ML} = 0 (neat [MOIm][BF_4]), 0.6, and 0.9 at 10 ns. Red parts denote the ionic regions (anion and imidazolium ring with the methyl group and methylene part attached to the imidazolium ring), green parts denote the nonpolar regions (alkyl group except for the methylene part attached to the imidazolium ring), and blue parts denote the ML. The upper snapshots denote the whole mixtures and the lower ones denote the mixtures without the MLs.

Based on the MD simulation runs,[137] the DOS spectra were then obtained from the Fourier transforms of the calculated velocity autocorrelation functions for the centers of masses of the ionic and molecular species. As shown in Figure III.12, the X_{ML} dependence of the total DOS spectra for the mixtures and neat [MOIm][BF_4] and ML from 0 cm^{-1} to 250 cm^{-1}. Each system showed a unique concentration dependent DOS spectrum. With increasing X_{ML}, the total

DOS spectral intensity of the [MOIm][BF_4]/MeOH system decreased, while that of the [MOIm][BF_4]/MeCN system increased. In the [MOIm][BF_4]/DMSO system, the total DOS spectral intensity did not clearly change with increasing X_{ML}.

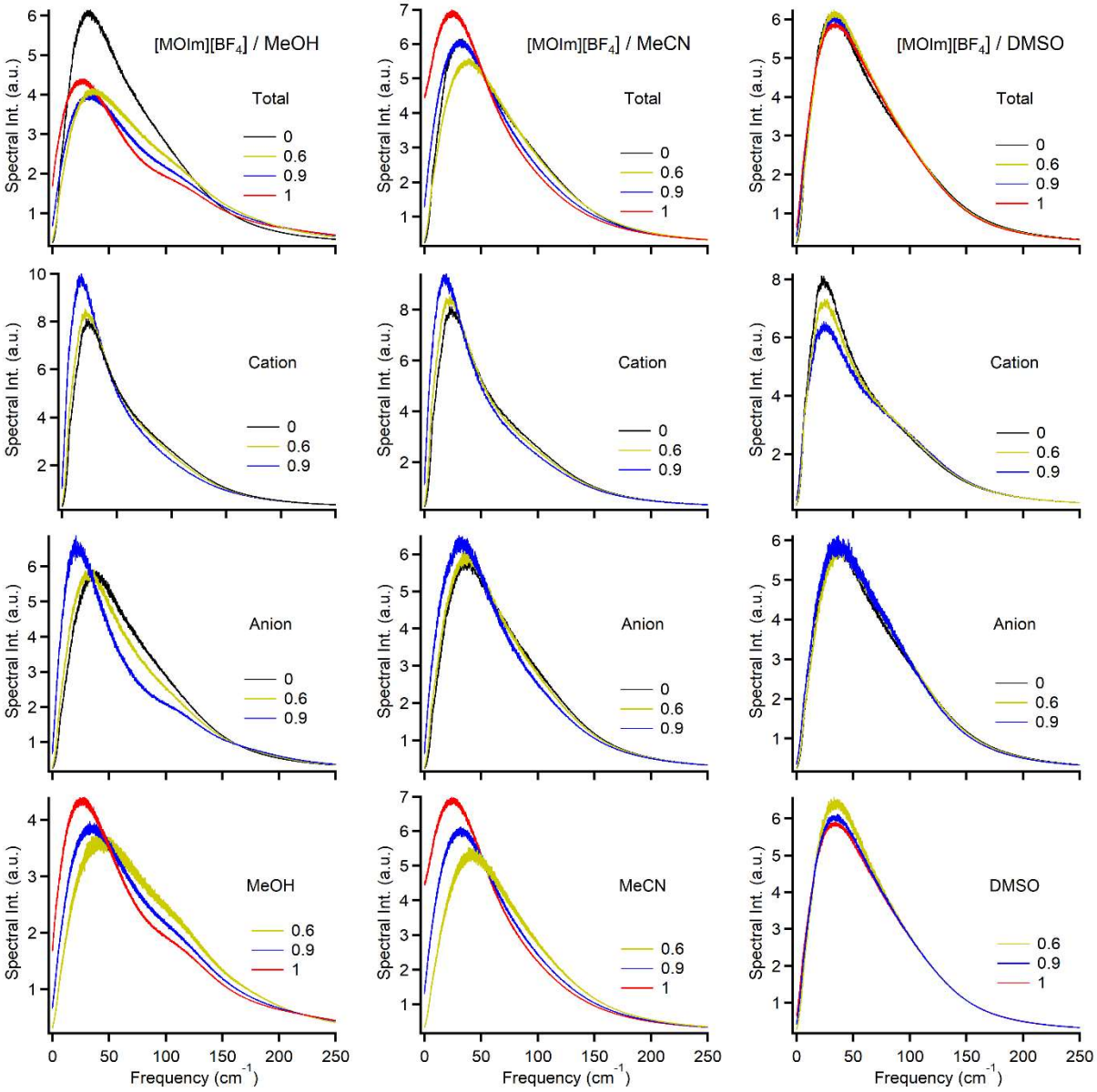

Figure III.12. Calculated DOS spectra of total, $[MOIm]^+$, $[BF_4]^-$, and ML for [MOIm][BF_4] mixture systems with MeOH, MeCN, and DMSO at X_{ML} = 0, 0.6, 0.9, and 1.

To compare the contribution of each component, Figure III.12 shows the DOS spectra for the constituent cations ($[MOIm]^+$), anions ($[BF_4]^-$), and ML. As shown in Figure III.12, the intensity of the DOS spectra for the MeOH component decreased with increasing X_{ML}. This mainly attributed to the decrease in the intensity of the total spectrum in the MeOH system.

Although the intensity of each DOS component from 0 to 50 cm^{-1} increased, that around 100 cm^{-1} decreased with increasing X_{ML}. The low-frequency shift in the total DOS spectra of the [MOIm][BF_4]/MeOH system is due to the change in the DOS spectra of each component with increasing X_{ML}.

The total DOS spectra of the [MOIm][BF_4]/MeCN system are attributed by the increase in the intensity of all components. The intensities of $[MOIm]^+$ and MeCN increased significantly. In addition, the peaks of both components shifted to lower frequency side, and thus the total DOS spectra also shifted to lower frequency side due to $[MOIm]^+$ and MeCN components.

In the [MOIm][BF_4]/DMSO system, the total DOS spectral intensity did not change so much with increasing ML concentration. However, the intensity of the DOS spectrum of the $[MOIm]^+$ component decreased significantly and that of the DMSO component decreased slightly with increasing X_{ML}.

III.3.4. Polarizability Anisotropies via Quantum Chemistry Calculations

The polarizability tensor elements α_{ij} of the optimized structures for $[MOIm]^+$, $[BF_4]^-$, MeOH, MeCN, and DMSO were calculated by quantum chemistry calculations based on the B3LYP/6-311+G(d,p) level of theory. The polarizability tensor elements are listed in Table III.2. Table III.2 are also summarized the mean polarizability α_0 and polarizability anisotropy α_{anis} values. The values of α_0 and α_{anis} were obtained by the following equations.[138]

$$\alpha_0 = \frac{\alpha_{xx} + \alpha_{yy} + \alpha_{zz}}{3} \quad \text{(III-5)}$$

$$\alpha_{anis} = \sqrt{\frac{(\alpha_{xx} - \alpha_{yy})^2 + (\alpha_{yy} - \alpha_{zz})^2 + (\alpha_{zz} - \alpha_{xx})^2 + 6\left(\alpha_{xy}{}^2 + \alpha_{yz}{}^2 + \alpha_{zx}{}^2\right)}{2}} \quad \text{(III-6)}$$

The polarizability anisotropy per volume was also estimated as $\alpha_{anis}N_A/V_m$, where N_A is the Avogadro constant, and V_m is the molar volume obtained from the density and formula weight. In [MOIm][BF_4], $\alpha_{anis}N_A/V_m$ was calculated as the sum of $a_{anis}([MOIm]^+)$ and $a_{anis}([BF_4]^-)$. Table III.2 shows that α_{anis} of $[MOIm]^+$ was much larger than those of the MLs, but the values of $\alpha_{anis}N_A/V_m$ for [MOIm][BF_4] was between those of MeCN and DMSO.

Table III.2. Polarizability Tensor Elements α_{ij}, Mean Polarizability α_0, and Polarizability Anisotropy α_{anis} Estimated by DFT Calculations Based on the B3LYP/6-311+G(d,p) Level of Theory.

	α_{xx} (Å^3)	α_{yy} (Å^3)	α_{zz} (Å^3)	α_{xy} (Å^3)	α_{yz} (Å^3)	α_{zx} (Å^3)	α_0 (Å^3)	α_{anis} (Å^3)	$\alpha_{anis}N_A/V_m$ (–)
$[MOIm]^+$	29.883	19.025	19.013	1.222	−1.034	0.732	22.640	11.284	
$[BF_4]^-$	3.057	3.057	3.057	0	0	0	3.057	0	0.0267
MeOH	3.021	2.682	2.613	0.063	0	0	2.772	0.394	0.0059
MeCN	3.091	3.091	5.774	0	0	0	3.985	2.683	0.0311
DMSO	8.156	8.193	6.305	0	0	0.155	7.551	1.889	0.0160

III.4. DISCUSSION

III.4.1. Dependence of Low-Frequency Kerr Spectrum on X_{ML}

As shown in Figure III.10, the [MOIm][BF_4] mixtures with MeCN, MeOH, and DMSO show similar X_{ML}-dependent M_1, which is the average frequency of the low-frequency broadened band. With increasing ML concentration, M_1 is almost constant in all systems at X_{ML} = 0–0.6. Then, M_1 mildly changes from X_{ML} = 0.6 to X_{ML} = 0.9 and steeply varies in X_{ML} = 0.9–1.

The previous study about the [MOIm][BF_4]/H_2O system reported that the low-frequency spectra of the [MOIm][BF_4]/H_2O system showed little change not only in the M_1 but also in the line shape at X_{ML} = 0–0.6.[53] This suggested that H_2O molecules were localized at the boundary between the ionic and nonpolar regions and had little effect on the interionic interactions. Alternatively, the M_1 of the low-frequency spectra in the [MOIm][BF_4]/benzene[55] and [MOIm][NTf_2]/benzene[130] systems exhibited a linear dependence on X_{ML}. These results suggest that benzene has a more significant effect on the interionic interactions of [MOIm][BF_4] even in the low X_{ML} concentration than H_2O.

The MeCN, MeOH, and DMSO systems in this study show intermediate results between the [MOIm][BF_4]/H_2O and [MOIm][BF_4]/benzene systems. The addition of MeCN, MeOH, or DMSO does not perturb the interionic interaction (or ionic network) in [MOIm][BF_4] in less than X_{ML} = 0.6. As shown in the MD simulation results of Figure III.11, there is almost no structural change in the IL region for the three systems at X_{ML} = 0.6. Quitevis and coworkers also reported a similar structure (segregated ions and alkyl groups together with dispersed MeCN molecules) for the [MPIm][NTf_2]/MeCN mixture by MD simulations.[82] Then, in X_{ML} = 0.6–0.9, the ML molecules began to weaken the interionic interactions or segregate the mixture structure between the IL and ML regions. The MD snapshots at X_{ML} = 0.9 show that the ML region is dominant in the mixtures. Finally, in more than X_{ML} = 0.9, the ML molecules completely disturb the interionic interactions of [MOIm][BF_4] and form a ML network. This characteristic is well-correlated with the relationship between micro and macroscopic features. Later, I will discuss this feature in detail in section III.4.3.

Recently, Takamuku and coworkers investigated the microscopic interactions of 1-ethyl-3-methylimidazolium bis(trifluoromethylsulfonyl)amide ([EMIm][NTf_2]) mixtures with MeOH, MeCN, and DMSO by ^1H and ^{13}C NMR, steady-state Raman, and attenuated total reflectance infrared spectroscopies.[98] They reported that the order of the strengths of the interactions between the imidazolium ring and these three MLs was DMSO >> MeOH > MeCN by probing the H−C(2) of the imidazolium ring. They also pointed out that the electron donicity

of MLs affected the interaction between the imidazolium ring and the ML molecule. However, in the present study, I do not find significant differences in the low-frequency intermolecular vibrations of the [MOIm][BF_4] mixtures with MeOH, MeCN, and DMSO. This discrepancy may come from the differences in the spatial scale of probing or from IL differences ([MOIm][BF_4] has longer alkyl groups and lower hydrophobicity than [EMIm][NTf_2]). Further investigation of the present system by IR and NMR will reveal the origin of the different features. However, probing the different spatial scales via intra- and intermolecular scales does not always bring the same features as reported in the [MOIm][BF_4]/benzene system.[130]

III.4.2. Comparison between Kerr and DOS Spectra

While the low-frequency Kerr spectrum exhibits the depolarized Raman spectrum corrected with the Bose-Einstein thermal occupation function,[139,140] the DOS spectrum corresponds with the density of the vibrational states. In other words, the former includes the depolarized Raman activity and the latter does not. The calculation of a spectrum derived from the collective polarizability anisotropy response is much more complicated and time-absorbing than that of a DOS spectrum. Thus, the number of the calculations of Kerr spectra is not so much.[51,141,142] However, the comparison between the Kerr and DOS spectra provided a detailed understanding of the molecular-level aspects of intermolecular vibrations in the temperature-dependent properties of the IL.[77] Therefore, I think that the comparison between the Kerr and DOS spectra is useful to understand the features of the X_{ML}-dependence of low-frequency spectra in the three [MOIm][BF_4]/ML systems.

As shown in Figure III.8, the intensities of the low-frequency Kerr spectra in [MOIm][BF_4]/MeOH and [MOIm][BF_4]/DMSO systems decreased with increasing X_{ML}, but that in [MOIm][BF_4]/MeCN system increased. On the other hand, as exhibited in Figure III.12, the DOS spectra for [MOIm][BF_4]/MeOH and [MOIm][BF_4]/MeCN show the similar tendencies to the Kerr spectra, but those for neat [MOIm][BF_4] and DMSO are almost the same and little affected by X_{ML}.

The molecular polarizability anisotropy is also a good measure for the intensity of the low-frequency spectrum,[143] though fs-RIKES detects the collective polarizability anisotropy response of the sample. Especially, the intensity of the Kerr spectrum (depolarized Raman spectrum, as well) is associated with the magnitude of the polarizability anisotropy per volume, $\alpha_{anis}N_A/V_m$. Table III.2 exhibits that the order of $\alpha_{anis}N_A/V_m$ is MeCN > [MOIm][BF_4] > DMSO > MeOH, which is qualitatively similar to the intensity of the Kerr spectra for the neat liquids shown in Figure III.8. Therefore, the different X_{ML}-dependence between the Kerr and DOS

spectra of the [MOIm][BF_4]/DMSO system could be mainly derived from the difference in the magnitudes of the polarizability anisotropy, rather than to DOS. Conversely, the X_{ML}-dependence of the [MOIm][BF_4]/MeOH and [MOIm][BF_4]/MeCN systems could likely be due to both DOS and polarizability anisotropy.

In the DOS spectra, the X_{ML}-dependent features of the DOS spectra for [MOIm][BF_4]/DMSO are different from those for the [MOIm][BF_4]/MeOH and [MOIm][BF_4]/MeCN. The peak frequencies of the DOS spectra of $[MOIm]^+$, $[BF_4]^-$, DMSO, and the total mixture, change little with increasing the X_{ML}. However, the DOS spectral peaks of the constituents for [MOIm][BF_4]/MeOH and [MOIm][BF_4]/MeCN shift to lower frequency side with an increase in the X_{ML}. These X_{ML}-dependent differences may originate from the intermolecular interactions in the mixtures.

At X_{ML} = 0 and 0.6, the DOS spectra of $[MOIm]^+$ and $[BF_4]^-$ almost overlap and are different from those at X_{ML} = 0.9 in [MOIm][BF_4]/MeOH and [MOIm][BF_4]/MeCN systems. Especially, the spectrum at X_{ML} = 0.9 is red-shifted compared to those at X_{ML} = 0 and 0.6. This is because the ML solvation may weaken the intermolecular interactions in the IL. Furthermore, this feature supports the X_{ML}-dependent feature in M_1 of the Kerr spectra for [MOIm][BF_4]/MeOH and [MOIm][BF_4]/MeCN. The MD simulations show further red shifts with increasing the X_{ML} from 0.9 to X_{ML} = 1, which are confirmed in the DOS spectra of the two mixture systems.

In the experimental Kerr spectra, the tendency of the X_{ML}-dependence for M_1 in [MOIm][BF_4]/MeCN (Figure III.10) is similar to that for the calculated DOS spectra. However, the M_1 values are different for [MOIm][BF_4]/MeOH and [MOIm][BF_4]/DMSO. The DOS spectra of neat MeOH and [MOIm][BF_4]/MeOH showed weak shoulder peaks at ~120 cm^{-1} and ~220 cm^{-1} (Figure III.12), as well as the Kerr spectra (~120 cm^{-1} and ~250 cm^{-1}) shown in Figure III.8. These vibrational bands in neat MeOH have been reported in other RIKES and steady-state Raman spectroscopic studies.[131,132,144-146] Therefore, the X_{ML}-dependence of M_1 in [MOIm][BF_4]/MeOH is mainly affected by the high-frequency bands of bulk MeOH. The line shape of the low-frequency Kerr spectrum in [MOIm][BF_4]/MeOH system varies from trapezoidal to triangular and exhibits a low peak frequency at ~40 cm^{-1} with increasing X_{ML}. As shown in Figure III.12, the MD simulation results can reproduce this experimental feature well. Additionally, the line shape of the low-frequency Kerr spectrum in [MOIm][BF_4]/DMSO system varies from trapezoidal to monomodal with a peak frequency at ~50 cm^{-1}, which is almost the center frequency of neat DMSO, with increasing X_{ML}. This experimental feature of [MOIm][BF_4]/DMSO is similar to that in the DOS spectra, as shown in Figure III.8 and III.12.

III.4.3. Comparison with Bulk Parameter

Previously, aprotic MLs[133] show a linear relationship between M_1 of the low-frequency band and bulk parameter $(\gamma/\rho)^{1/2}$. Furthermore, recently, a mild linear dependence of M_1 on $(\gamma/\rho)^{1/2}$ has also been observed in aromatic and non-aromatic cation-based ILs.[41] These relationships between M_1 and $(\gamma/\rho)^{1/2}$ are based on the harmonic oscillator; the surface tension corresponds to the force constant and the density is comparable to the reduced mass for the intermolecular vibrations in liquids.

Figure III.13 displays the plots of M_1 vs. $(\gamma/\rho)^{1/2}$ for the [MOIm][BF_4]/ML systems. The relationships between M_1 and $(\gamma/\rho)^{1/2}$ for aprotic MLs[133,147,148] and aromatic cation-based ILs[41] are also shown in Figure III.13. The tendencies of the X_{ML}-dependence of the relationships between M_1 and $(\gamma/\rho)^{1/2}$ for the three [MOIm][BF_4]/ML systems are almost the same. The plots vary with an increase in X_{ML} up to 0.6 along with the relationship of aromatic cation-based ILs. Then, the plots move away from the relationship of aromatic cation-based ILs as X_{ML} increases further. The plots of the [MOIm][BF_4]/MeCN and [MOIm][BF_4]/DMSO systems at X_{ML} = 0.6–0.9 are between the relationships of aromatic cation-based ILs and aprotic MLs. At $X_{ML} \geq 0.9$, the plots of [MOIm][BF_4] mixtures with MeCN and DMSO are around the relationship for aprotic MLs. Although the relationship for hydrogen-bonding liquids is not reported, the plots for [MOIm][BF_4]/MeOH at $X_{ML} \geq 0.9$ are likely around the relationship of the hydrogen-bonding protic ML.

These results show that the X_{ML}-dependent features of the plots of M_1 vs. $(\gamma/\rho)^{1/2}$ for the three [MOIm][BF_4]/ML systems indicate that the three mixtures behave like aromatic cation-based ILs in the region of X_{ML} = 0-0.6, and like MLs in the region of X_{ML} = 0.9-1 with regard to the relationship between micro- and macroscopic quantities, The region with XML = 0.6-0.9 is a transitional region between aromatic cation-based ILs and MLs.

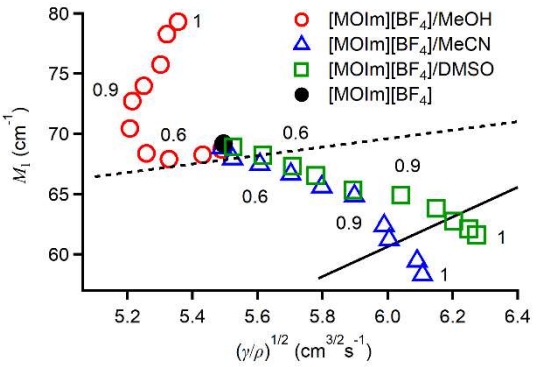

Figure III.13. Plots of M_1 vs. $(\gamma/\rho)^{1/2}$ for [MOIm][BF$_4$]/MeOH (red circles), [MOIm][BF$_4$]/MeCN (blue triangles), [MOIm][BF$_4$]/DMSO (green squares), and neat [MOIm][BF$_4$] (black circle). Relationships between M_1 and $(\gamma/\rho)^{1/2}$ for aprotic MLs[133,147,149] (black solid line) and aromatic cation-based ILs[41] (black dotted line) are also shown.

The snapshots of the [MOIm][BF$_4$]/ML mixtures in Figure III.11 exhibit that, at X_{ML} = 0.6, segregate structures between the alkyl group and ionic regions together with dispersed ML molecules and the network (or region) of ML molecules has not been developed so much. On the other hand, the [MOIm][BF$_4$]/ML mixtures at X_{ML} = 0.9 exhibit the dominant ML regions. Thus, this microscopic aspect of the MD simulations supports the experimental results of the relationship between M_1 and $(\gamma/\rho)^{1/2}$ for the [MOIm][BF$_4$]/ML mixture systems. Additionally, the MD simulations displayed different liquid structures among the three mixture systems at X_{ML} = 0.9: the [MOIm][BF$_4$]/MeOH system shows a more segregated structure, while the [MOIm][BF$_4$]/DMSO system shows a more mixed structure. Then, [MOIm][BF$_4$]/MeCN system shows a middle state between [MOIm][BF$_4$]/MeOH and [MOIm][BF$_4$]/DMSO. These results of MD simulations had mentioned in section 3.3. Fs-RIKES do not clearly capture the trace of the differences in the liquid structure. Probably, the spectral density of the Kerr spectra of [MOIm][BF$_4$]/ML mixtures at $X_{ML} \geq 0.9$ is mainly due to their origin in the bulk ML region.

III.5. CONCLUSIONS

In this chapter, I studied the low-frequency spectra of the [MOIm][BF_4] mixtures with MeCN, MeOH, and DMSO at X_{ML} = 0 (neat [MOIm][BF_4]), 0.20, 0.40, 0.60, 0.70, 0.80, 0.90, 0.95, 0.99, and 1 (neat MLs: MeCN, MeOH, and DMSO) by fs-RIKES and MD simulations. I also measured their density, surface tension, viscosity, and electrical conductivity. The line shape of the low-frequency Kerr spectra of [MOIm][BF_4] mixtures with MeCN, MeOH, and DMSO strongly depended on X_{ML}. For all three mixtures, the X_{ML} dependence of M_1 of the low-frequency spectra showed that M_1 changed little in the X_{ML} range from 0 to 0.6, mildly at X_{ML} = 0.6–0.9, and dramatically at X_{ML} = 0.9–1. The DOS spectra calculated by MD simulations are well-reproduced the X_{ML}-dependence of the line shapes and M_1 of the low-frequency Kerr spectra, which include the quantity of the polarizability anisotropy. The results obtained by fs-RIKES and MD simulations led to the following scenario. When ML is added to the [MOIm][BF_4], ML molecules localize at the interface between the ionic and alkyl group (non-polar) regions. Still, the number of ML molecules is insufficient to make an ML network or bulk region at X_{ML} = 0–0.6. Then, ML molecules begin to form a network or bulk region at X_{ML} = 0.6–0.9 with the further addition of ML. Finally, the [MOIm][BF_4] constituent ion species disperse in ML at X_{ML} = 0.9–1. The results of the relationships between M_1 and $(\gamma/\rho)^{1/2}$ for the three [MOIm][BF_4]/ML systems followed this scenario. The X_{ML}-dependent spectral features of the [MOIm][BF_4]/ML systems were almost quantitatively similar, indicating a very small effect of the hydrogen-bonding donor and acceptor abilities of the MLs.

Chapter IV.

Low-Frequency Spectra of 1-Methyl-3-octylimidazolium Tetrafluoroborate Mixtures with Formamide, *N*-Methylformamide, and *N*,*N*-Dimethylformamide

J. Phys. Chem. B, submitted.

IV.1. INTRODUCTION

Hydrogen bonding is one of the most important interactions between molecules and has a very significant effect on the structure of biomolecule, such as DNA[150] and proteins,[151] especially in vivo. Formamide (FA) is one of the model compounds of peptide and useful for studying the effects of hydrogen bonding.[152,153] Therefore, IL/FA mixtures are good targets for investigating IL applications in peptide chemistry.

In previous chapter, I discussed the low-frequency spectra of the [MOIm][BF_4] mixtures with MeOH, MeCN, and DMSO. The results exhibited that M_1 was a constant with increasing X_{ML} up to $X_{ML} \leq 0.6$. Then the values of M_1 gradually changed in $0.6 \leq X_{ML} \leq 0.9$, and steeply changed in $X_{ML} \geq 0.9$. Previous NMR and IR measurements showed the [MOIm][BF_4] mixtures with benzene possess the stronger interaction of the 2-proton of imidazolium ring than [MOIm] [NTf_2], and the interactions changed drastically in $X_{ML} \geq 0.6$.[130] In the [MOIm][BF_4] mixtures with MeOH, MeCN, and DMSO, the results of NMR and IR also exhibited that the states of the mixtures change in the three ranges of $X_{ML} < \sim 0.6$, $\sim 0.6 < X_{ML} < \sim 0.9$, and $X_{ML} > \sim 0.9$ and are almost coincide with those of fs-RIKES.[154] In addition, small angle neutron scattering and MD simulation results showed that the [MOIm][BF_4]/MeOH mixtures have a highly inhomogeneous structure due to the self-hydrogen-bonding aggregation.[154]

However, since FA is a strongly interacting liquid compared to benzene, methanol, and acetonitrile, the effects of FA on the intermolecular interactions and microscopic structures of IL may be different from previous results. Therefore, in this chapter, I investigated low-frequency spectra of [MOIm][BF_4] mixtures with FA by fs-RIKES. In order to investigate the effects of the hydrogen-bonding abilities, I also measured those of [MOIm][BF_4] mixtures with *N*-methylformamide (NMF), and *N*,*N*-dimethylformamide (DMF). The microscopic pictures of the [MOIm][BF_4]/amide liquid mixtures were studied in more detail by NMR, IR, and MD simulations.

IV.2. EXPERIMENTAL AND COMPUTATIONAL METHODS

IV.2.1. Reagents and Sample Preparation

In this study, I studied the [MOIm][BF_4] mixtures with FA, NMF, and DMF. The reason for choosing [MOIm][BF_4] is the same as in Chapter III, focusing on the microscopic heterogeneous structure of ILs. Alternatively, the reason for choosing the three amides is to examine how the different number of hydrogen bonding sites in MLs affects the intermolecular vibrations of ILs. [MOIm][BF_4] was synthesized by the procedure which was reported in the previous study[99] and checked by ^{1}H-NMR and elemental analysis (see Apendix). The ratios of carbon, hydrogen, and nitrogen in the elemental analysis were good agreement with the calculated ratios within an error of ±0.4%. This error range was following the criterion in the Journal of Organic Chemistry. The [MOIm][BF_4] was dried in a vacuum at 313 K for over 36 h before using. The water content in [MOIm][BF_4] was 73 ppm measured by Karl Fischer titration using a coulometer (Hiranuma, AQ-300). FA (Wako Pure Chemicals, >98.5%), NMF (Sigma-Aldrich, >99%), and DMF (Wako Pure Chemicals, >99.7%) were dried by molecular sieves (3A, Kanto Chemical) before using. For fs-RIKES measurements, I weighed [MOIm][BF_4] and FA, NMF, and DMF at various ML mole fractions X_{ML} (0 (neat [MOIm][BF_4]), 0.2, 0.4, 0.6, 0.7, 0.8, 0.9, 0.95, 0.97, 0.99, 1 (neat ML)) and prepared all samples. For IR measurements, the two H atoms of an amino group for FA were replaced by D atoms by several cycles of mixing with D_2O (Cambridge Isotope Laboratories, D content = 99.9%) and distillation. Deuterated FA (FA-d_2) was checked by density and IR spectroscopic measurements. The mole fraction of ML for the [MOIm][BF_4] mixtures as the samples of IR measurements were 0 (neat [MOIm][BF_4]), 0.1, 0.2, 0.3, 0.4, 0.5, 0.6, 0.7, 0.8, 0.9, 0.95, 0.97, 0.99, 1 (neat ML).

IV.2.2. IR Measurements.

The IR measurements were performed by the Takamuku's Laboratory at Saga University. To measure the attenuated total reflection-infrared IR (ATR-IR) spectral measurements, an FT-IR spectrometer (JASCO, FT/IR-6100) equipped with an attenuated total reflection (ATR) diamond prism (JASCO, PKS-D 470 with ATR PRO450-S) was used. Each spectrum had 64 accumulation times and a wavenumber resolution of 4.0 cm^{-1}. Correction of the depth of transmission of the evanescent wave on the diamond prism was not done on the original absorption spectrum to avoid some facultative effect.

IV.2.3. NMR Measurements.

The NMR measurements were performed by the Takamuku's Laboratory at Saga University. The NMR spectra of the [MOIm][BF_4] mixtures with FA, NMF, and DMF were obtained by a 400 MHz FT-NMR spectrometer (Agilent Technologies, 400 MHz NMR system). The sample temperature was 298.2 ± 0.1 K controlled by a heater and a dry cold air from a sample cooler (FTS Systems, Air-Jet XR401, TC-84). The ^{1}H, ^{13}C, and ^{19}F NMR measurements have the digital resolutions of 4.9×10^{-4}, 7.6×10^{-3}, and 3.6×10^{-3} ppm, respectively. An external double reference tube (Shigemi) was inserted into the sample tube (Shigemi, PS-001-7). The reference substance was hexamethyldisiloxane (HMDS) (Wako Pure Chemicals, the first purity grade) for ^{1}H and ^{13}C chemical shifts. For ^{19}F NMR chemical shifts, the reference substance was trifluoromethylbenzene (Tokyo Chemical Industry, extra grade). The results of the chemical shifts were corrected by the volume magnetic susceptibility of a sample solution according to an external double-reference method.[155,156]

IV.2.4. MD Simulations.

The MD simulations were also performed by the Takamuku's Laboratory at Saga University. The MD program package GROMACS 5.0.7 was used for neat [MOIm][BF_4] (X_{ML} = 0), neat MLs (X_{ML} = 1), and their mixture systems with FA, NMF, and DMF at X_{ML} = 0.6 and 0.9. The simulation systems are summarized in Table C1. The simulation cells were cubic cells in the periodic boundary conditions. The IL force field was selected from that developed by Lopes and Padua,[28,107,108] and the three ML force fields were constructed based on OPLS-AA.[157] Although the IL force fields in this study was developed by Lopes and Padua, the three MLs' force fields were built on the basis of OPLS-AA. Table C2 summarized the parameters of the simulation. The bending, torsion, Lennard-Jones, and Coulomb terms of the intramolecular interactions were taken into account in the simulations. The bond-stretching terms for all atoms were constrained by the LINCS algorithm.[113] The leapfrog method[114] was used for the integration with a time step of 1 fs. The smooth particle mesh Ewald method was also used for calculating electrostatic interactions with a real space cutoff of 13.5 Å.[115,158] Van der Waals interactions were reduced to null in the 12.0-13.5 Å switching range. The conditions of the simulations were at 298.2K and 1 atm controlled by Nose–Hoover thermostat[119,120] with a time constant of 0.5 ps and Parrinello–Rahman methods[116-118] with a time constant of 1 ps, respectively.

IV.2.5. Quantum Chemistry Calculations.

In order to calculate the optimized structures of the ions, amides, and their clusters, Gaussian 16W program suite[121] was used for quantum chemistry calculations based on the B3LYP/6-311++G(d,p) level. The counterpoise method[159,160] was used to calculate the intermolecular interaction energies of the clusters. The chemical shifts of ^{19}F NMR for $[BF_4]^-$ and its clusters with amides and $[MOIm]^+$ were calculated using the gauge-independent atomic orbital (GIAO) method[161-165] from their geometry optimized structures. To confirm the effect of the distance between the anion and cation on the chemical shift, I calculated the chemical shifts of ^{19}F NMR for $[BF_4]^-$-$[MOIm]^+$ cluster based on not only its optimized structure but also the structure with different distances between $[BF_4]^-$ and $[MOIm]^+$ from the optimized structure (−0.5, −0.25, +0.25, +0.5, +0.75, and +1.0 Å). Additionally, to calculate the optimaized structure of the $[MOIm]^+$−$[BF_4]^-$ cluster taking into account the solvent polarity effects, I used the integral equation formalism polarizable continuum model (IEFPCM).[166-168]

IV.3. RESULTS

IV.3.1. Bulk Properties: Density, Viscosity, Surface Tension, and Electrical Conductivity

Figure IV.1 exhibits the X_{ML} dependence of the density ρ, viscosity η, electrical conductivity σ, and surface tension γ for the $[MOIm][BF_4]$ mixtures with FA, NMF, and DMF at 293 K. Table C3 summarizes the values of the liquid properties for the mixtures. The results of neat $[MOIm][BF_4]$, FA, NMF, and DMF are almost similar to those of previous studies.[41,52,53,55,124,133,169-178] As shown in Figure IV.1a, the value of ρ for neat $[MOIm][BF_4]$ is smaller than that for neat FA but larger than those for neat NMF and DMF. Thus, with increasing X_{ML}, the values of ρ for $[MOIm][BF_4]$/FA increases but those for $[MOIm][BF_4]$ mixtures with NMF and DMF decrease. Figure IV.1b shows that the η gradually decrease with increasing X_{ML} in all systems. This is because the neat $[MOIm][BF_4]$ is very much more viscous than the neat amides. In Figure IV.1c, the σs for all systems have maximum peaks at $X_{ML} = 0.9$ and such maximum σ peaks has been observed in previous studies.[4,126,127,169,170] Figure IV.1d exhibits that, with increasing X_{ML}, the γs for the $[MOIm][BF_4]$ mixtures with NMF and DMF gradually increase. Although that for the $[MOIm][BF_4]$/ FA system also gradually increases in $X_{ML} \leq 0.8$, it steeply increases in $X_{ML} \geq 0.9$.

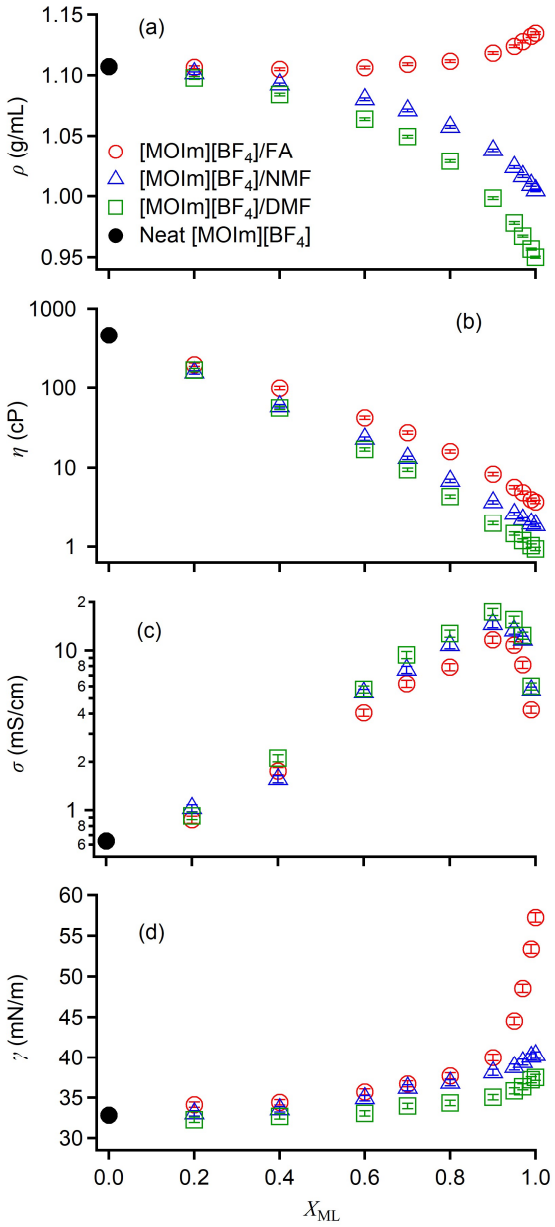

Figure IV.1. Plots of concentration dependences of liquid properties ((a) density: ρ, (b) viscosity: η, (c) electrical conductivity: σ, (d) surface tension: γ) for [MOIm][BF_4] mixtures with FA (red circle), NMF (blue triangle), and DMF (green square). Plots for neat [MOIm][BF_4] are also shown (black filled circle). Error bars are also written.

IV.3.2. Low-Frequency Spectra via fs-RIKES

Figure IV.2 exhibits the Kerr transients of the [MOIm][BF_4] mixtures with FA, NMF, and DMF. The measurement temperature is 293 K. The intensities of the Kerr transients were normalized at the intensity of $t = 0$, which corresponds to the electronic response. The intensity derived from nuclear responses increased with increasing X_{ML} because the formamide liquids

are more polarizable than [MOIm][BF_4]. Large underdumps originating from intermolecular vibrations appeared in all systems after the electronic response. Over 0.5 ps, small beats appeared in all concentrations for [MOIm][BF_4]/NMF and [MOIm][BF_4]/DMF, while the beats became smaller for [MOIm][BF_4]/FA with increasing FA concentration. These little beats are derived from intramolecular vibrations. After a few picoseconds, these transients exhibited overdamping. The overdecay is derived from the collective reorientational motions. The slow reorientational components for over 3 ps were fitted by a triexponential function ($a_0 + \sum_i a_i \exp(-t/\tau_i)$, $i = 3$). Table C4 summarizes the fit parameters of the Kerr transients for all samples.

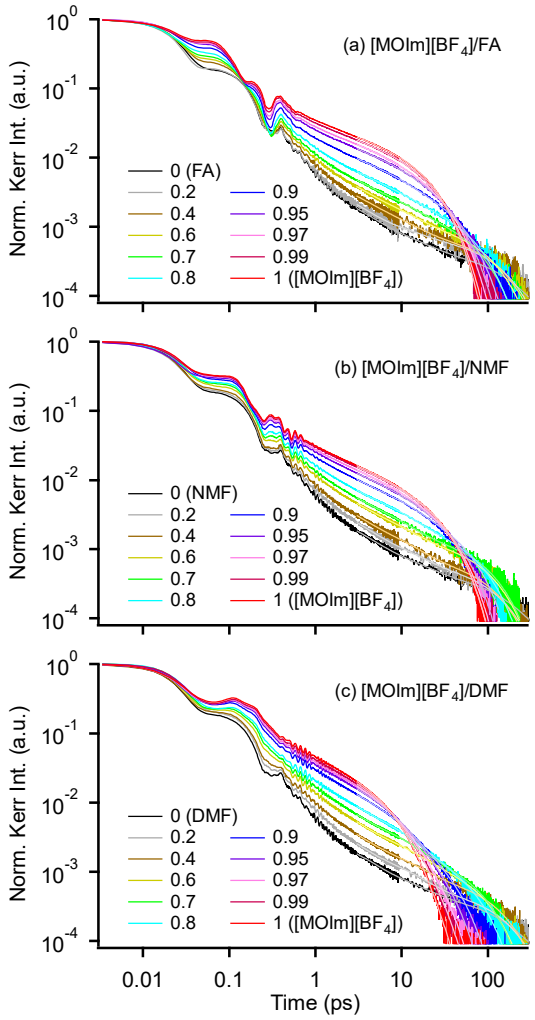

Figure IV.2. Kerr transients for (a) [MOIm][BF_4]/FA, (b) [MOIm][BF_4]/NMF, and (c) [MOIm][BF_4]/DMF with different concentrations. All transients are normalized at $t = 0$ corresponds to the electronic response. Triexponential fits from 3 ps are also shown.

These Kerr transients were converted to spectra by Fourier transform deconvolution analysis procedure which was explained in section II.2.3. Figure IV.3 shows the Fourier transform Kerr spectra for the [MOIm][BF_4] mixtures with FA, NMF, and DMF. In order to concentrate on the intermolecular vibrations, the collective reorientation components ($a_0 + \sum_i a_i \exp(-t/\tau_i)$, ($i$ = 2 or 3)) were removed from the raw entire spectrum. The sharp bands appeared from 300 to 700 cm^{-1} are due to intramolecular vibrations for [MOIm][BF_4] or the formamide liquids and the broadened bands appeared in less than 300 cm^{-1} are mainly due to the intermolecular vibrations. Figure IV.4 exhibits the low-frequency Kerr spectra in 0–300 cm^{-1} to discuss mainly the intermolecular vibrations. The spectral shapes of neat [MOIm][BF_4],[41,53,55,169,170] FA,[140] and DMF[133,140] are good agreement with those in the other literature. On the other hand, although Chan and Castner have reported a Kerr transient of neat NMF,[179] this is the first report about the low-frequency fs-RIKES spectrum of neat NMF.

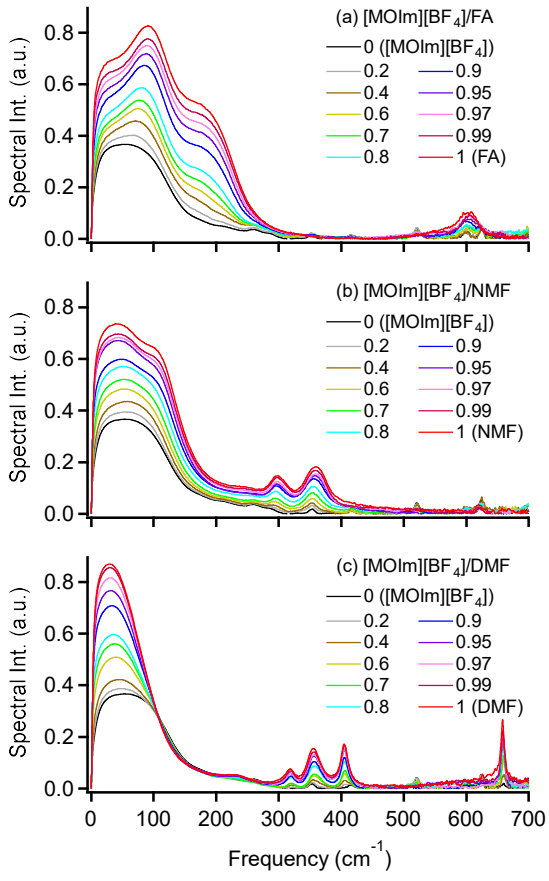

Figure IV.3. Low-frequency Kerr spectra in the frequency range 0–700 cm^{-1} for the [MOIm][BF_4] mixtures with (a) FA, (b) NMF, (c)DMF.

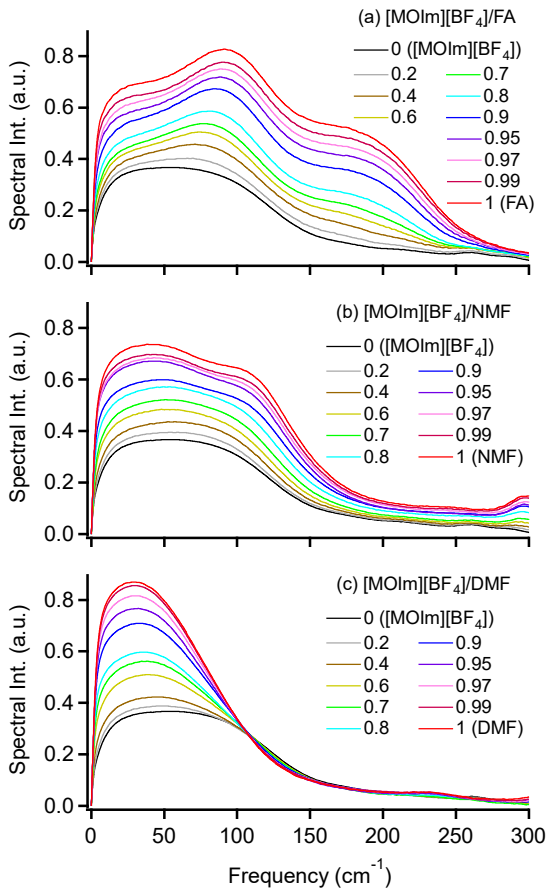

Figure IV.4. Magnifications of Kerr spectra in the frequency range 0–300 cm^{-1} for the [MOIm][BF_4] mixtures with (a) FA, (b) NMF, (c)DMF.

As shown in Figure IV.3 and IV.4, neat [MOIm][BF_4] show lower spectral intensity than the neat amide liquids and the spectral line shapes of the mixtures gradually changed from neat [MOIm][BF_4] with increasing ML concentration. These low-frequency spectra were analyzed by line shape analysis which was introduced in section III.3.2. As an example, Figure IV.5 shows the low-frequency spectra of [MOIm][BF_4]/FA mixtures at X_{ML} = 0, 0.4, and 1 and the results of their fits. I was able to fit the other spectra with the same level of quality. Figure C6-C8 and Table C5 in Appendix summarize the results of the fitted spectra and their fitting parameters.

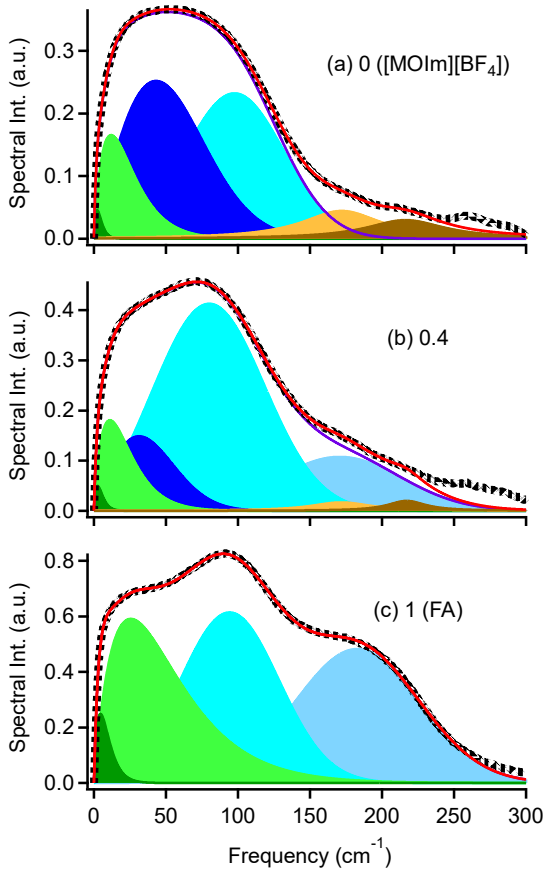

Figure IV.5. Low-frequency spectra for [MOIm][BF_4]/FA system at (a) X_{ML} = 0 (neat [MOIm][BF_4]), (b) X_{ML} = 0.4, and (c) X_{ML} = 1 (neat FA). Their fits are also shown. Black dots described experimental spectra , and solid red lines represented the sum of all fits. Ohmic, antisymmetrized Gaussian, and Lorentz functions are represented by green, blue, and brown areas. Solid purple lines denoted sums of Ohmic and antisymmetrized Gaussian functions.

To discuss the X_{ML} dependence of the low-frequency spectra semiquantitatively, Figure IV.6 exhibits the plots of M_1 against X_{ML} for the [MOIm][BF_4] mixtures with FA, NMF, and DMF. The M_1 of MLs shows higher frequencies for FA, NMF, and DMF, in that order. These results suggest that the intermolecular interaction is strongest for FA and weakest for DMF. With increasing X_{ML}, M_1 of the [MOIm][BF_4]/FA system increased significantly, while that of the [MOIm][BF_4]/DMF system decreased gradually. On the other hand, the [MOIm][BF_4]/NMF system shows that the values of M_1 remains almost unchanged in $X_{ML} \leq$ 0.7 and gradually increased in $X_{ML} \geq$ 0.8. Table C5 list the results of M_1 for all systems.

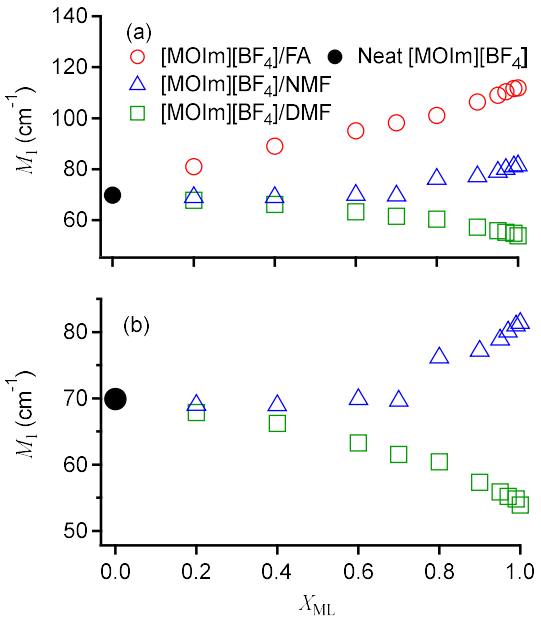

Figure IV.6. (a) Plots of M_1 vs. composition for [MOIm][BF_4] mixtures with FA (red circle), NMF (blue triangle), and DMF (green square) and (b) a magnification of plots of M_1 vs. composition for [MOIm][BF_4] mixtures with NMF and DMF. Plots for neat [MOIm][BF_4] are also shown (black filled circle).

IV.3.3. ATR-IR Spectra

IV.3.3.1. Amide C=O Stretching Mode.

Figure IV.7 exhibits the concentration dependence of the amide C=O band in the samples. The [MOIm][BF_4] mixtures with FA-d_2 were measured for avoiding overlapping the amide C=O band with other bands. The peak frequency of the amide C=O band shifted to the lower frequency side as the X_{ML} increased. This shift indicates that the hydrogen bonding interaction of the C=O group is strengthening. Figure IV.8 plots the peak frequency of the amide C=O band against X_{ML}. The magnitude of the redshift for the [MOIm][BF_4]/DMF system is smaller than those for the [MOIm][BF_4]/FA and [MOIm][BF_4]/NMF systems. The redshifts change gradually in the low X_{ML} region, but they change abruptly in the $X_{ML} > 0.7$. As shown in Figure IV.7 and IV.8, the [MOIm][BF_4] mixtures with FA and FA-d_2 show the similar quantitative trends about the X_{ML} dependence of the amide C=O band.

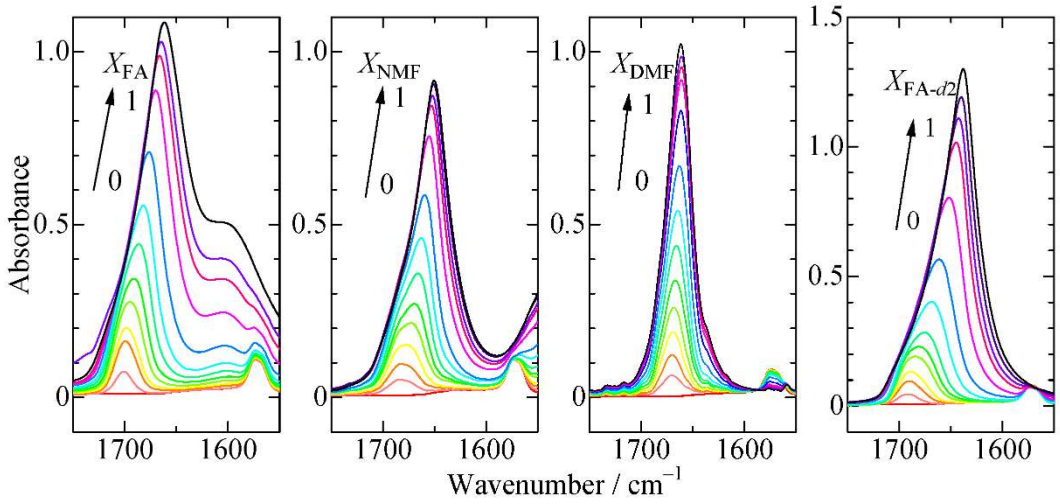

Figure IV.7. X_{ML} dependence of the amide C=O band in the [MOIm][BF_4] mixtures with FA, NMF, DMF, and FA-d_2.

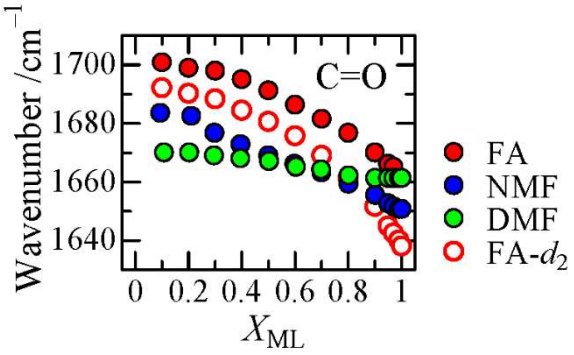

Figure IV.8. Plots of the peak frequency of the the amide C=O band vs. X_{ML} in the [MOIm][BF_4] mixtures with FA, NMF, DMF, FA-d_2.

IV.3.3.2. Imidazolium Ring C–H Stretching Mode.

The concentration dependence of the imidazolium ring C–H stretching bands for the [MOIm][BF_4] mixtures with FA, NMF, and DMF are shown in Figure IV.9. It is noted that the imidazolium ring's protons are acidic and sensitive to hydrogen-bonding acceptor. With increasing X_{ML}, the peak frequency shifts to the lower frequency side due to the strengthening the hydrogen-bond interaction of the C–H group. This trend is good agreement with the trend of the C=O band shown in Figure IV.7. In Figure IV.10, plots for the peak frequency of the imidazolium ring C–H stretching band vs. X_{ML} are shown. The magnitude of the red shift for the [MOIm][BF_4]/FA system is smaller than that for the [MOIm][BF_4] mixtures with NMF and DMF. It can also be seen that the redshift changes gradually in the low X_{ML} region, but abruptly

in the $X_{ML} > 0.7$. This redshift is particularly pronounced for mixtures of [MOIm][BF_4] with NMF and DMF.

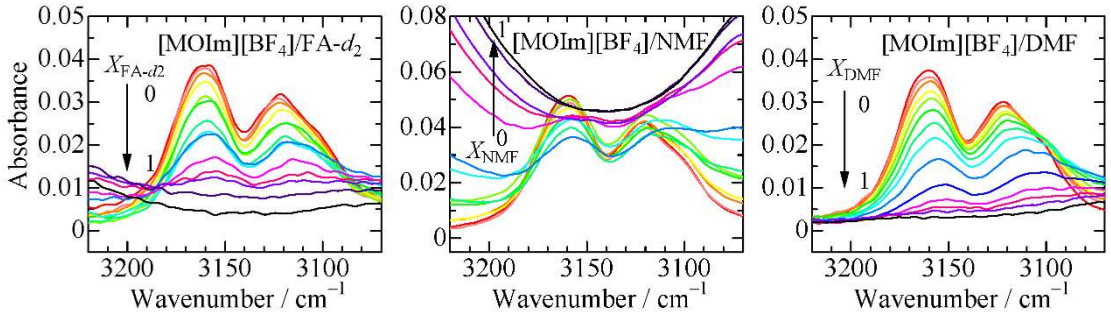

Figure IV.9. X_{ML} dependence of the imidazolium ring C–H stretching band in the [MOIm][BF_4] mixtures with FA-d_2, NMF, and DMF.

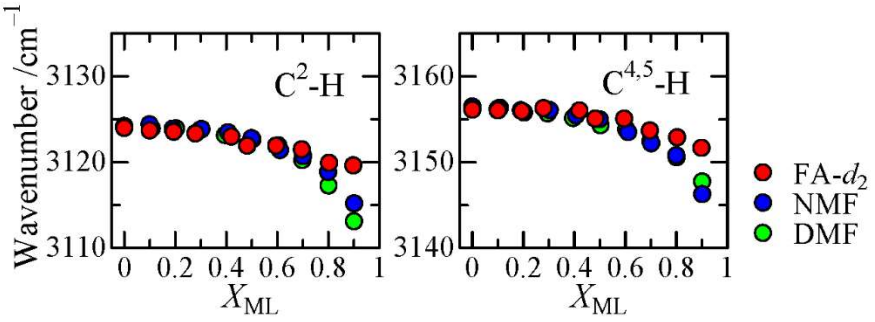

Figure IV.10. Plots of the peak frequency of the imidazolium ring C–H stretching band vs. X_{ML} in the [MOIm][BF_4] mixtures with FA-d_2, NMF, and DMF.

IV.3.4. NMR Spectra

To clarify the specific interactions of each component in the mixtures, Figure IV.11 shows chemical shift data for nuclides that are very sensitive to ML concentration.

Figure IV.11 is plots of the ^{13}C NMR chemical shift of the carbonyl carbon of amides in the [MOIm][BF_4] mixtures with FA, NMF, and DMF against X_{ML}. It is noted that there are two stable isomers of NMF, cis and trans forms. With increasing X_{ML}, the chemical shifts of the [MOIm][BF_4] mixtures with FA and NMF shifted to a lower magnetic field, while that of the [MOIm][BF_4]/DMF mixtures shifted to a higher one.

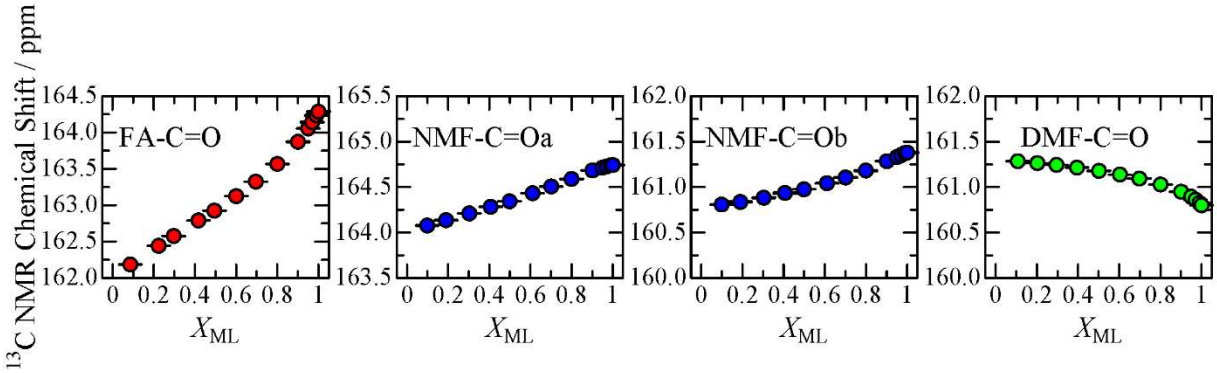

Figure IV.11. Plots of the ^{13}C NMR chemical shifts of the carbonyl carbon of amides vs. X_{ML} in the [MOIm][BF_4] mixtures with FA, NMF (a: transform; b: cis form), and DMF.

Figure IV.12 exhibits the plots of the ^{1}H NMR and ^{13}C NMR chemical shifts for the imidazolium ring against X_{ML} in all systems. As X_{ML} increased, the changes in chemical shift of the imidazolium ring increased for the [MOIm][BF_4] mixtures with NMF and DMF, while was smaller or even opposite for the [MOIm][BF_4] mixture with FA.

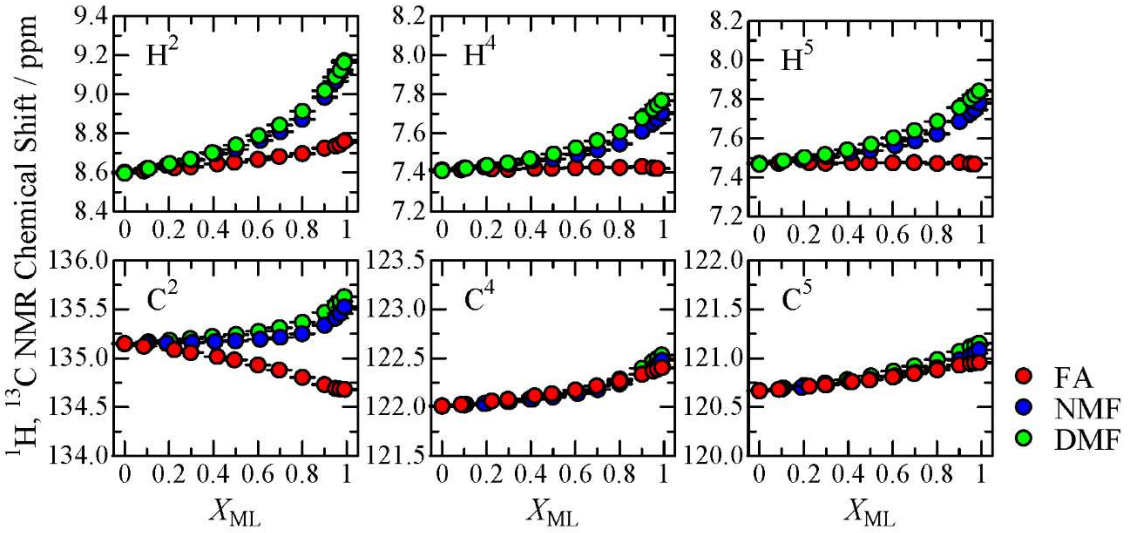

Figure IV.12. Plots of the ^{1}H NMR and ^{13}C NMR chemical shifts of the imidazolium ring of the cation vs. X_{ML} in the [MOIm][BF_4] mixtures with FA, NMF, and DMF.

The ^{19}F NMR chemical shifts of tetrafluoroborate anions in the [MOIm][BF_4] mixtures with FA, NMF, and DMF are plotted against X_{ML} in Figure IV.13. The chemical shifts of [MOIm][BF_4] mixtures with NMF and DMF shifted to a higher magnetic side with increasing

X_{ML}, while those of the FA shifted to a lower magnetic one. The shifts change gradually in the low X_{ML} region, but steeply in the $X_{ML} > 0.7$.

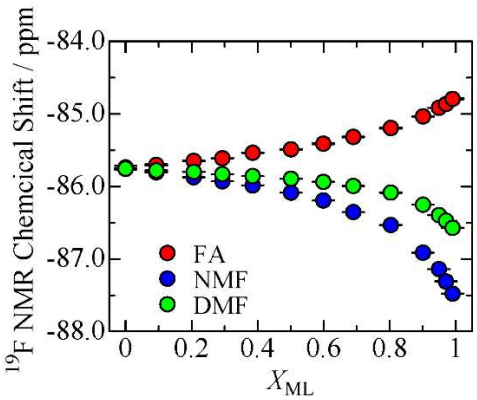

Figure IV.13. Plots of the ^{19}F NMR chemical shift of fluorines in the anion vs. X_{ML} in the [MOIm][BF_4] mixtures with FA, NMF, and DMF.

IV.3.5. MD Simulations

Figure IV.14 is the snapshots of the [MOIm][BF_4] mixtures with FA, NMF, and DMF at X_{ML} = 0 (neat [MOIm][BF_4]), 0.6, and 0.9 based on the MD simulations. The end of the production runs of the MD simulations is at 10 ns. The results show that [MOIm][BF_4]/FA is rather uniformly mixed especially at X_{FA} = 0.6, while [MOIm][BF4]/DMF shows a segregated structure significantly at X_{DMF} = 0.9. [MOIm][BF_4]/NMF exhibits that the structure is in between them.

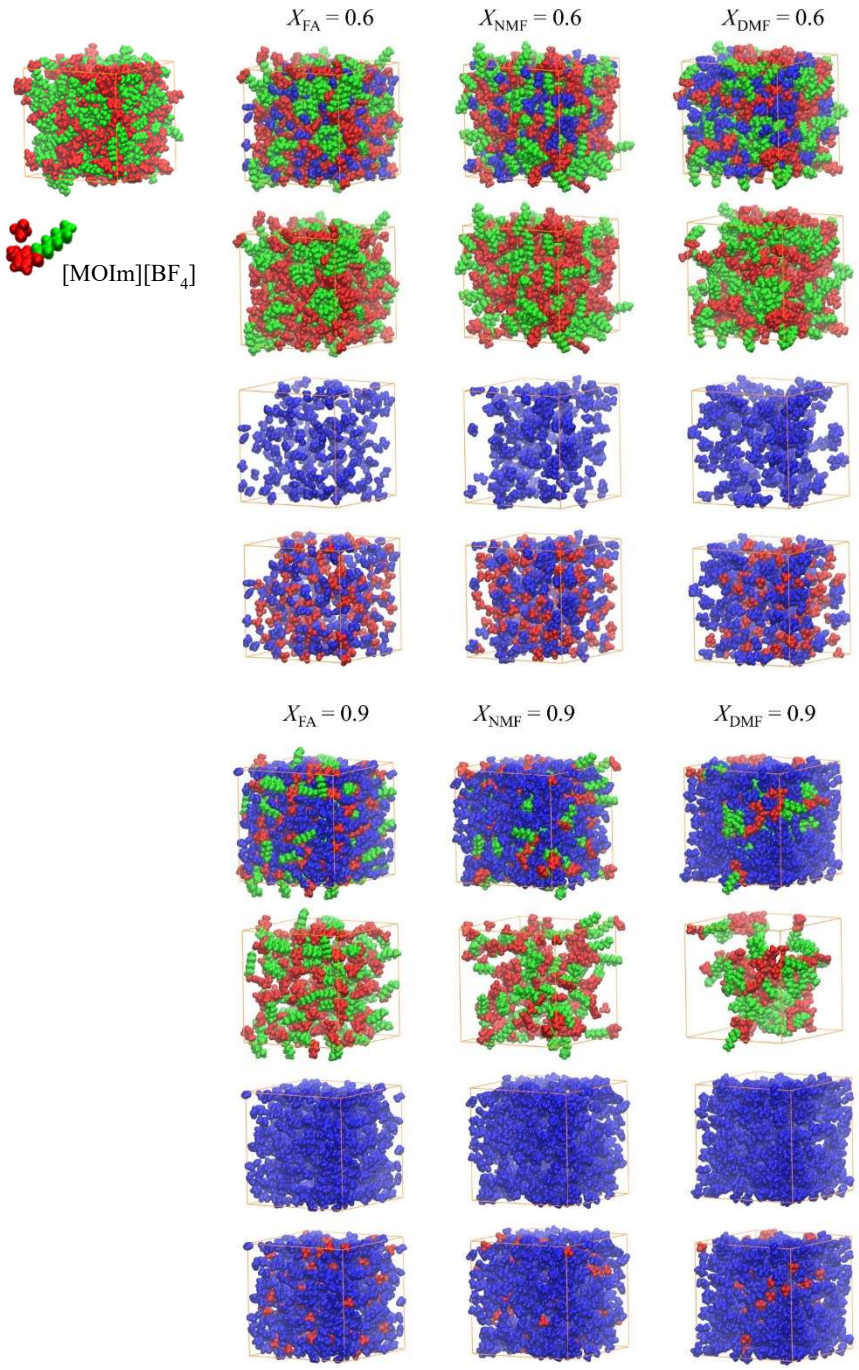

Figure IV.14. Snapshots of neat [MOIm][BF_4] and [MOIm][BF_4] mixtures with FA (left column), NMF (middle column), and DMF (right column) at X_{ML} = 0.6 and 0.9 at 10 ns. Red parts denote the ionic regions (anion and imidazolium ring with the methyl group and methylene part attached to the imidazolium ring), green parts denote the nonpolar regions (alkyl group except for the methylene part attached to the imidazolium ring), and blue parts denote the ML. Upper snapshots denote the whole mixtures, upper middle ones denote the mixtures without the MLs (ILs only), lower middle ones denote the mixtures without [MOIm][BF_4] (MLs only), and lower ones denote the mixtures without cation (MLs and $[BF_4]^-$).

Figure IV.15 exhibits the concentration dependence of the total DOS spectra based on the MD simulations[137] for all systems from 0 to 330 cm^{-1}. Each system shows a unique concentration dependence of DOS spectrum.

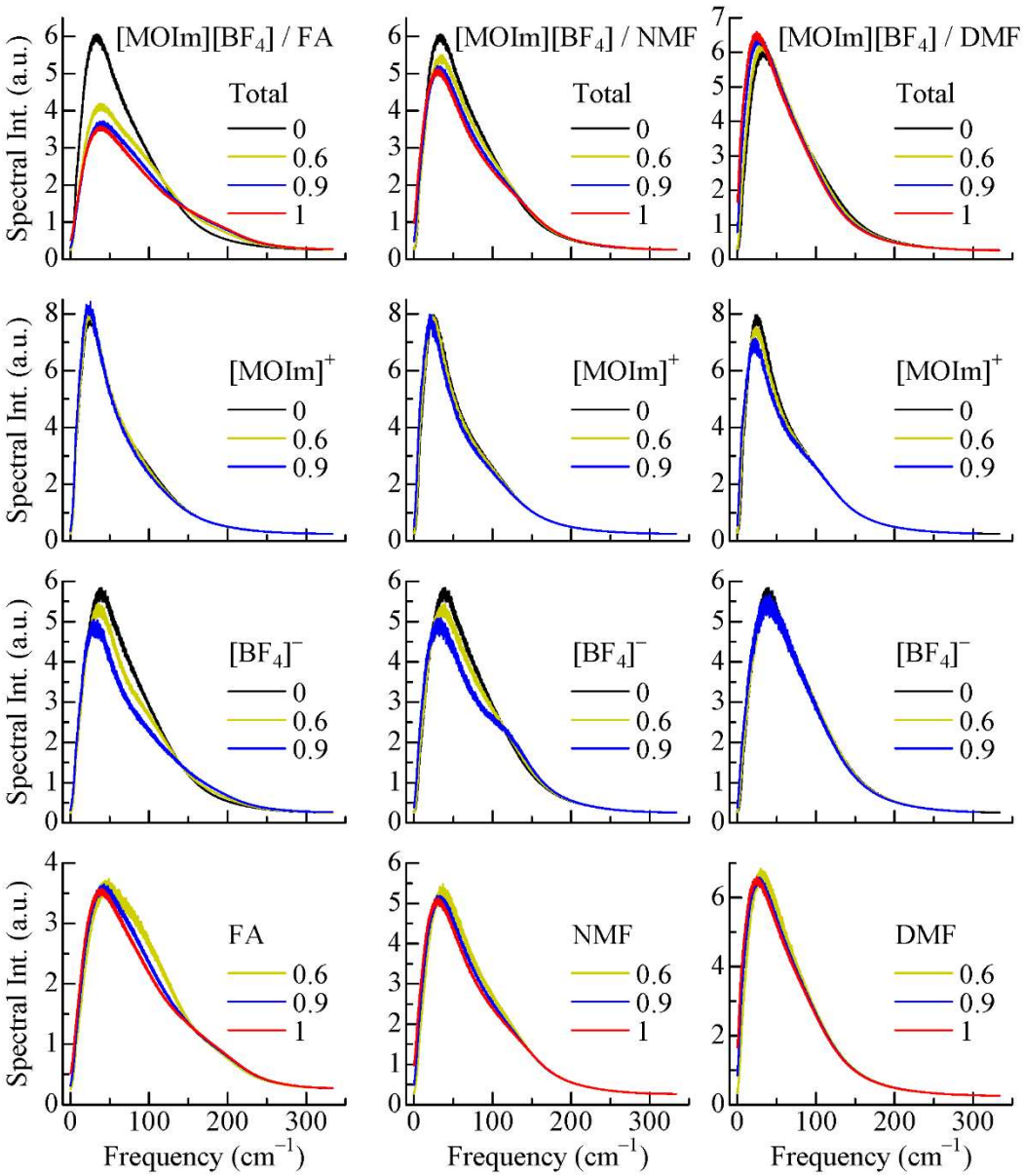

Figure IV.15. Calculated DOS spectra of total, $[MOIm]^+$, $[BF_4]^-$, and ML for [MOIm][BF_4] mixture systems with FA, NMF, and DMF at X_{ML} = 0, 0.6, 0.9, and 1.

As shown in Figure IV.15, in the Total DOS spectrum, [MOIm][BF_4]/FA showed the largest change against X_{ML}. When FA was added to [MOIm][BF_4], the total DOS spectrum was broadened. However, the peak frequency is rather constant with respect to X_{FA}. On the other hand, for the [MOIm][BF_4]/NMF and [MOIm][BF_4]/DMF systems, the Total DOS spectral

peak shifted to the lower frequency side as increasing X_{ML}. As for substituents, the $[BF_4]^-$ anions of the [MOIm][BF_4]/FA and [MOIm][BF_4]/NMF systems were sensitive to ML concentration, while the $[MOIm]^+$ of the [MOIm][BF_4]/DMF system was sensitive to X_{ML}.

IV.3.6 Quantum Chemistry Calculations.

Figure IV.16 displays the optimized structures calculated by quantum chemistry calculations for $[MOIm]^+$, $[BF_4]^-$, FA, NMF, DMF, $[BF_4]^-$–FA, $[BF_4]^-$–NMF, $[BF_4]^-$–DMF, $[MOIm]^+$–FA, $[MOIm]^+$–NMF, $[MOIm]^+$–DMF, $[MOIm]^+$–$[BF_4]^-$, $[MOIm]^+$–$[BF_4]^-$–FA, $[MOIm]^+$–$[BF_4]^-$–NMF, and $[MOIm]^+$–$[BF_4]^-$–DMF. Table IV.1 listed the values of the energies for the optimized ions and amides and their clusters and the interaction energies for the clusters. Table C6 summarized the atom coordinates of the optimized ions, molecules, and clusters. The interaction energies of FA and NMF are more negative (more stabilized) with $[BF_4]^-$ than with $[MOIm]^+$, and the opposite is true for that of DMF. The values of the interaction energies for $[MOIm]^+$–$[BF_4]^-$–FA and $[MOIm]^+$–$[BF_4]^-$–NMF are close but more negative than that for $[MOIm]^+$–$[BF_4]^-$–DMF. When solvent effects were taken into account in the calculations, the interaction energies of $[MOIm]^+$–$[BF_4]^-$ in FA, NMF, and DMF are more stabled than in the gas phase, and the cation-anion distance (the distance between H^2 of the imidazolium ring and the nearest F of the anion) in the solvents was longer than in the gas phase conditions (1.9118 Å), in the order NMF (2.0604 Å) > FA (2.0581 Å) > DMF (2.0440 Å), corresponding to the order of dielectric constants (111.0 for FA, 189.0 for NMF, and 38.25 for DMF at 298 K).[180]

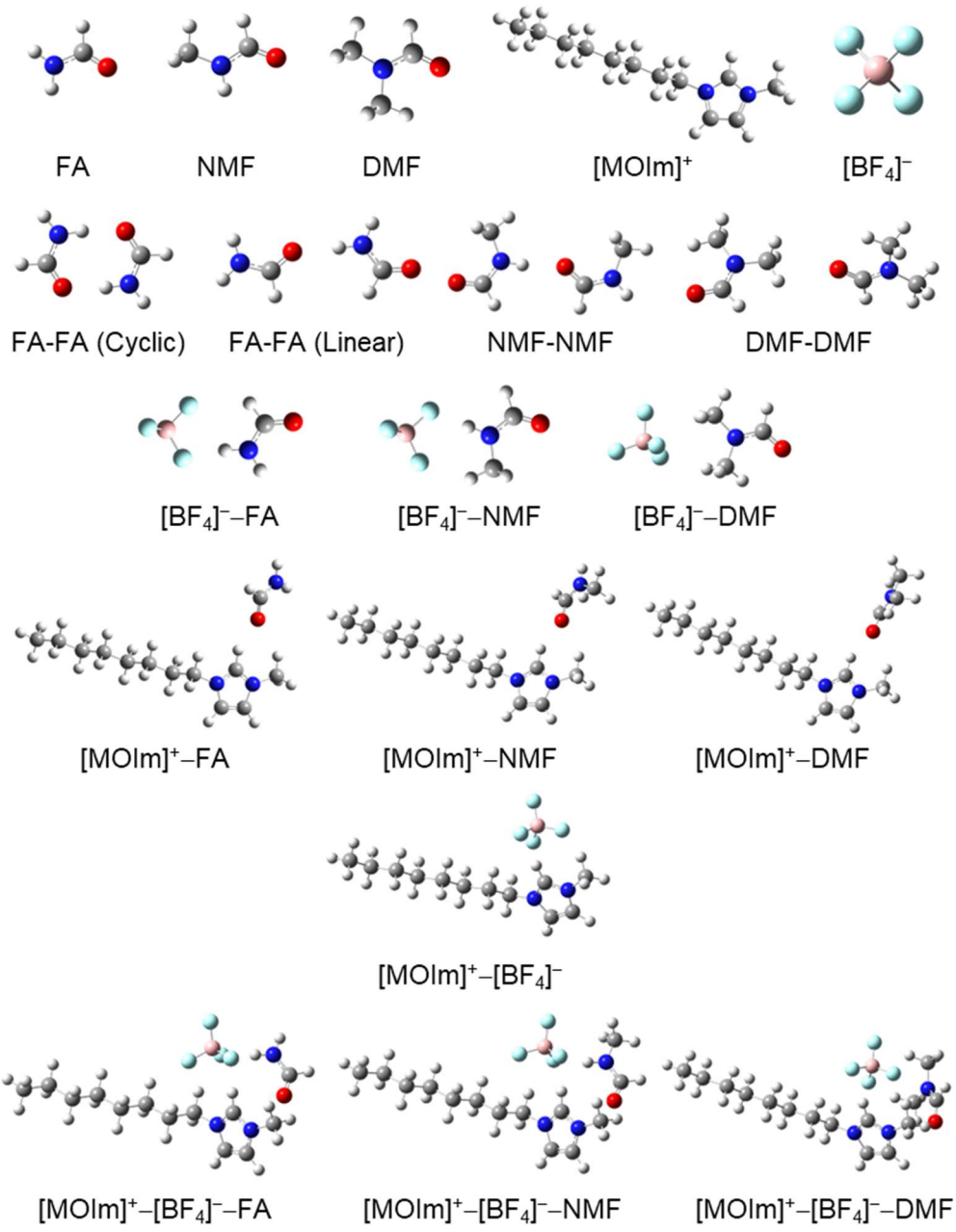

Figure IV.16. Optimized structures of FA, NMF, DMF, $[MOIm]^+$, $[BF_4]^-$, and their clusters based on the B3LYP/6-311++G(d,p) level of theory.

Table IV.1. Energies of the monomers and clusters and interaction energies of the clusters optimized at the B3LYP/6-311++G(d,p) level of theory.

Monomer	Energy (kJ/mol)	Cluster	Energy (kJ/mol)	Interaction Energy (kJ/mol)
$[MOIm]^+$	–1524328.74	FA – FA (Cyclic)	–892486.31	–57.99
$[BF_4]^-$	–1114996.38	FA – FA (Linear)	–892457.80	–25.81
FA	–446216.39	NMF – NMF	–1098915.05	–26.44
NMF	–549445.04	DMF – DMF	–1305355.41	–8.08
DMF	–652673.76	$[BF_4]^-$ – FA	–1561279.06	–69.50
		$[BF_4]^-$ – NMF	–1664509.69	–72.05
		$[BF_4]^-$ – DMF	–1767713.02	–45.73
		$[MOIm]^+$ – FA	–1970607.00	–63.85
		$[MOIm]^+$ – NMF	–2073839.24	–67.99
		$[MOIm]^+$ – DMF	–2177070.95	–71.30
		$[MOIm]^+$ – $[BF_4]^-$	–2639664.14	–349.70
		$[MOIm]^+$ – $[BF_4]^-$ – FA	–3085933.44	–401.00
		$[MOIm]^+$ – $[BF_4]^-$ – NMF	–3189159.18	–402.68
		$[MOIm]^+$ – $[BF_4]^-$ – DMF	–3292375.21	–386.19
		$[MOIm]^+$ – $[BF_4]^-$ (IEFPCM: FA)	–2639637.34	–312.50
		$[MOIm]^+$ – $[BF_4]^-$ (IEFPCM: NMF)	–2639637.12	–312.25
		$[MOIm]^+$ – $[BF_4]^-$ (IEFPCM: DMF)	–2639637.45	–312.63

Figure IV.17 exhibits the chemical shifts of ^{19}F NMR for the isolated $[BF_4]^-$ and the $[BF_4]^-$ in the clusters relative to trifluoromethylbenzene calculated by quantum chemistry calculations. Although $[BF_4]$ shows four NMR signals, the chemical shifts of the two down-field side signals, $[BF_4]^-$–FA and $[BF_4]^-$–NMF, are very close as shown in the numerical data in Table C7. Therefore, they overlap each other in Figure IV.17. In Figure IV.17, the most up-field signals of the F atom of $[BF_4]^-$ is attributed to the site of interaction with the other components; in the cluster of three amides with $[BF_4]^-$, down-field shifts are seen at the F atom close to the amides. In the cluster of three amides with $[BF_4]^-$, the magnitude of the down-field shifts for F atom with neighboring amides is smaller in the order of $[BF_4]^-$–DMF < $[BF_4]^-$–FA ≈ $[BF_4]^-$–NMF. However, among the three clusters, the average chemical shifts of the four F atoms in $[BF_4]^-$ are very similar. The $[MOIm]^+$ and $[BF_4]^-$ cluster show larger downward field shift for the F atoms close to the cation and the average of the four F atoms, compared to clusters containing amides. The average chemical shifts of the four F atoms of $[BF_4]^-$ in $[MOIm]^+$–$[BF_4]^-$–FA and $[MOIm]^+$–$[BF_4]^-$–NMF show down-field shifts compared with that

of $[MOIm]^+$–$[BF_4]^-$ among the three ternary clusters. However, the F atom in $[MOIm]^+$–$[BF_4]^-$–DMF shows a slightly up-field shift to the $[MOIm]^+$–$[BF_4]^-$ cluster.

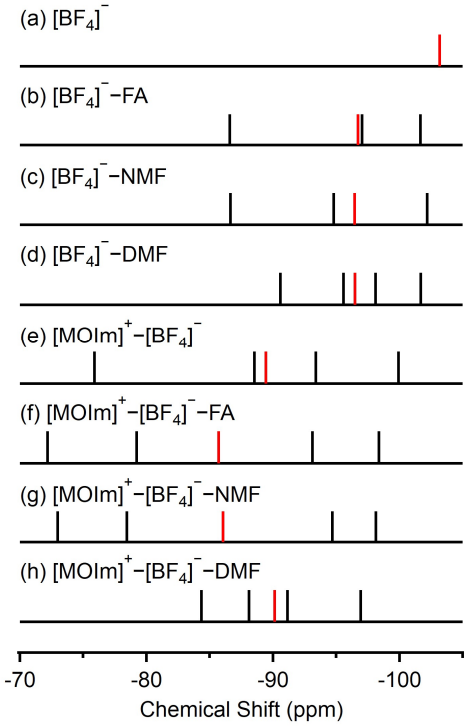

Figure IV.17. Chemical shifts of ^{19}F NMR for $[BF_4]^-$ and its clusters optimized at the B3LYP/6-311++G(d,p) level of theory calculated by the gauge-independent atomic orbital (GIAO) method against the reference substance of trifluoromethylbenzene. Each F atom is shown as black peak, and the average of four F atoms is shown as red peak.

The chemical shift of the nearest F atom of $[BF_4]^-$ to the cation and average chemical shift of F atoms of $[BF_4]^-$ are plotted against the distance between the closest F atom of $[BF_4]^-$ to $[MOIm]^+$ and the 2-positioned proton H^2 of the imidazolium ring of $[MOIm]^+$ in Figure IV.18. Note that the cluster is not optimized because the calculations were based on an optimized structure in which the distances between the cation and anion of $[MOIm]^+$-$[BF_4]^-$ were simply changed to keep the same internal atomic coordinates. Table C8 lists the chemical shift values. As the distance between the anion and cation increased, up-field chemical shifts are observed at the average of the F atom closest to the cation and the four atoms of the anion.

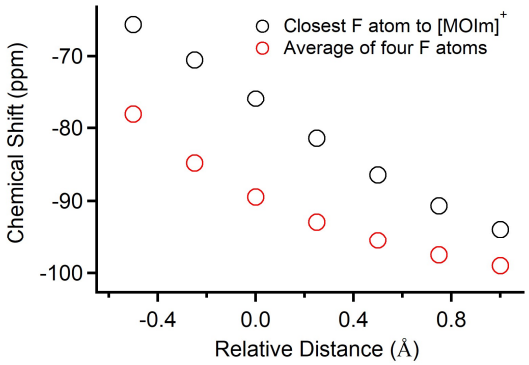

Figure IV.18. Plots of ^{19}F NMR chemical shift of the nearest F atom of $[BF_4]^-$ to $[MOIm]^+$ vs. distance between the F atom and the 2-position H^2 of the cation's imidazolium ring relative to the distance at the optimized structure of $[MOIm]^+$–$[BF_4]^-$. Black circles denote the plot for the F atom close to the cation, and red circles denote the average of the four F atoms.

When the calculations were performed including solvent effects from the IEFPCM model, the ^{19}F NMR results of the $[MOIm]^+$-$[BF_4]^-$ showed that up-field shifts of F atom of the anion compared to the gas phase condition: –96.8384 ppm (FA); –96.8807 ppm (NMF); –96.4790 ppm (DMF); –89.4466 ppm (gas) in average (see Table C9). Since the order of the magnitude of the up-field shift is the same as that of the distances between cation and anion, the dielectric medium due to the solvent affects the cluster structure (distance between the cation and anion, NMF (2.0604 Å) > FA (2.0581 Å) > DMF (2.0440 Å)), which probably led to the up-field shift.

IV.4. DISCUSSION

IV.4.1. Bulk Liquid Properties.

As shown in Figure IV.1a, the ρ values of neat FA were higher than neat [MOIm][BF_4], while those of NMF and DMF were lower. In [MOIm][BF_4]/NMF and [MOIm][BF_4]/DMF, the change in ρ increased with increasing X_{ML}, especially $X_{ML} \geq 0.9$. In [MOIm][BF_4]/FA, the ρ value does not change with increasing X_{FA} in $X_{FA} \leq 0.6$, increased gradually from $X_{FA} = 0.6$ to $X_{FA} = 0.9$, and increased significantly in $X_{FA} \geq 0.9$. The XML dependence of ρ for the [MOIm][BF_4] mixtures with NMF and DMF are similar to that for the [MOIm][BF_4] mixtures with benzene, methanol and acetonitrile.[41,55,169] The X_{ML} dependence of ρ in [MOIm][BF_4]/FA appears to be similar to that of [MOIm][BF_4]/H_2O.[53] Therefore, these results suggest that the type of hydrogen bonding network affects the density of the [MOIm][BF_4] mixture.

The η values of the [MOIm][BF_4] mixtures decrease almost logarithmically with increasing X_{ML}, similar to the results for the [MOIm][BF_4] mixtures with H_2O, benzene, methanol, acetonitrile, DMSO and poly(ethylene glycol).[53,55,169,170] The difference in η between the three amides relative to [MOIm][BF_4] is FA < NMF < DMF, and thus the magnitude of the change is also the smallest for [MOIm][BF_4]/FA and the largest for [MOIm][BF_4]/DMF.

Because of the viscosity and concentration affect the σ values in salt solutions, IL/ML mixtures exhibit a maximum electrical conductivity that depends on the concentration or molar fraction. The [MOIm][BF_4] mixtures with FA, NMF, and DMF also exhibited a maximum σ value at $X_{ML} = 0.9$, as shown in Figure IV.1c. To account for the concentration effects, Walden plot, molar electrical conductivities (Λ) vs. η^{-1}, was made (see Figure C5). The Walden plots for the three mixtures show that the solutions become less electrically conductive with increasing in $X_{ML} = 0.9$. This was also observed for the [MOIm][BF_4] mixtures with MeOH, MeCN, DMSO.[169]

Then, Figure IV.1d exhibits that the values of γs in the [MOIm][BF_4]/FA system increased dramatically, while the [MOIm][BF_4]/NMF and [MOIm][BF_4]/DMF systems did gradually. These results indicate that the intermolecular interaction and/or surface structure of the [MOIm][BF_4]/FA system dramatically change to those of neat FA with increasing FA concentration in $X_{ML} \geq 0.9$ compared to NMF and DMF systems and this may be because of hydrogen bonds. Other well-known molecules that form hydrogen bonds are H_2O and alcohols. Previous studies reported that values of γs for IL/H_2O systems also rapidly increased at water-rich concentrations as well as the FA system.[181-183] In contrast, those for IL/alcohol systems gradually changed from that of neat IL to that of neat alcohol as well as the NMF and DMF

systems.[181-183] Tariq and coworkers reviewed surface tensions of IL mixtures with H_2O and alcohols.[182] They explained that H_2O mainly interacts with polar regions of ILs and it is segregated from surface regions which are conformed by non-polar alkyl chains of ILs in IL-rich concentration. On the other hand, they described that alcohols, which have alkyl chains, can perturb the surface structure even at low alcohol concentrations with their alkyl chains. The current results are similar to the results of IL mixtures with H_2O and alcohols. Therefore, the present results represent the following depictions: FA, which possesses no methyl group, is mainly present in the polar bulk region of [MOIm][BF_4] and has little effect on the surface interactions and structures in $X_{ML} \leq 0.9$ and is rapidly distributed on the surface in $X_{ML} \geq 0.9$. On the other hand, NMF and DMF, which possess methyl groups, can affect the surface properties of [MOIm][BF_4] from low X_{ML} concentration.

IV.4.2. Low-Frequency Spectra.

As Chang and Castner[140] also reported, Figures IV.3 and IV.4 exhibit that the line shapes of the spectra for neat amides differ from each other. Especially, the spectrum of neat FA is more structured. Torii and Tasumi reported quantum chemical calculations of the low-frequency spectra of FA and NMF clusters.[184] Their results suggest that the linear hydrogen-bonded librational bands of FA and NMF appear at about 100 cm^{-1}, and the 2D (antiparallel hexamer) hydrogen-bonding librational bands of FA hexamer appear at about 200 cm^{-1}. They also confirmed that these hydrogen bonding librational bands appear in fs-RIKES spectra by MD simulations.[185] In my results, FA has one peak at ~100 cm^{-1} and one shoulder at ~180 cm^{-1}, while NMF has a shoulder at ~120 cm^{-1}. Thus, the peak at ~100 cm^{-1} in FA and the shoulder at ~120 cm^{-1} in NMF are attributed to linear hydrogen bonds, while the shoulder at ~180 cm^{-1} in FA mainly contributes to the 2D hydrogen bond bands. On the other hand, the spectral shape of DMF is monomodal. This monomodal spectral shape is usually observed in other common aprotic MLs.[133]

The spectrum of neat [MOIm][BF_4] is trapezoidal with a shoulder at about 100 cm^{-1} shown in Figure IV.3 and IV.4. The feature of the [MOIm][BF_4] spectral shape consistent with our previously results[41,53,55,130,169,170] observed by fs-RIKES. This trapezoidal line shape of the low-frequency spectrum is also confirmed in other typical aromatic MLs and ILs.[53,130,186] This trapezoidal shape is discussed later in Section V.4.2, but it is due to the aromatic ring libration of [MOIm][BF_4].

As for X_{ML} dependence of the line shapes of the low-frequency spectra of the mixtures, Figure IV.4 shows that the line shape of each mixture gradually changes from neat [MOIm][BF_4] to neat FA, NMF, and DMF with increasing X_{ML}. When the X_{FA} is 0.2 or 0.4, [MOIm][BF_4]/FA has the bands at about 100 cm^{-1} and 180 cm^{-1}, indicating the presence of FA clusters in [MOIm][BF_4] even at low X_{FA}. The peak frequency of the band at ~100 cm^{-1} in [MOIm][BF4]/FA gradually shifts to higher frequency side with increasing X_{FA}. Thus, the hydrogen bonding network of [MOIm][BF_4]/FA expands with increasing FA concentration. On the other hand, a (shoulder) band at about 100 cm^{-1} appears for [MOIm][BF_4]/NMF in $X_{NMF} \geq 0.9$, suggesting that the hydrogen bonding network develops only in regions of high NMF concentration.

To elucidate the X_{ML} dependent feature of the low-frequency vibrational band in detail, the normalized M_1 in the three mixtures is plotted against X_{ML} in the Figure IV.19. The values of M_1 were normalized by $X_{ML} = 0$ and 1 to reasonably compare the X_{ML} dependence of M_1 among the three IL mixtures. As increasing X_{FA}, the M_1 of [MOIm][BF_4]/FA steeply increases in the range of $X_{FA} < 0.4$, then becomes mild in $0.4 < X_{ML} < 0.7$, and increases dramatically again in $X_{FA} > 0.7$. The 2D hydrogen bonding cluster does not directly network with the cation and anion. Thus, M_1 is calculated again from the low-frequency Kerr spectrum without the antisymmetrized Gaussian band at ca. 180 cm^{-1}, which is exhibited in Figure IV.19. Then, the X_{ML} dependence feature of [MOIm][BF_4]/FA shows the same tendency as [MOIm][BF_4]/NMF, which exhibits that the M_1 is constant in $X_{ML} < 0.7$ and steeply increases in $X_{FA} > 0.7$. This indicates that the effects of the linear hydrogen bonding network on the intermolecular vibrations of cations and anions are not very different for [MOIm][BF_4]/FA and [MOIm][BF_4]/NMF. Conversely, the M_1 of [MOIm][BF_4]/DMF almost constantly increases with increasing X_{ML} and slightly steeply increases in $X_{ML} > \sim 0.7$.

Additionally, I compared these amides' results with the previous results.[53,55,169] The normalized M_1 for the amides and previous MeOH, MeCN, DMSO, H_2O, and Benzene results are shown in Figure C9. Aprotic MLs, MeCN and DMSO, showed similar trends as DMF. On the other hand, for the protic MLs, MeOH and H_2O, the values were almost constant below in $X_{ML} < 0.7$, consistent with the FA without the antisymmetrized Gaussian band and NMF results. These results suggest that aprotic and protic MLs affect the intermolecular vibrations of [MOIm][BF_4] differently. That is, aprotic MLs may perturb the interionic interaction from low ML concentration, while protic MLs may not affect the interionic interaction in low ML concentration. On the other hand, for benzene, the values changed significantly from low X_{ML}

concentrations, similar to the original FA results, and thus benzene may affect the interionic interaction a lot even at low X_{benzen}.

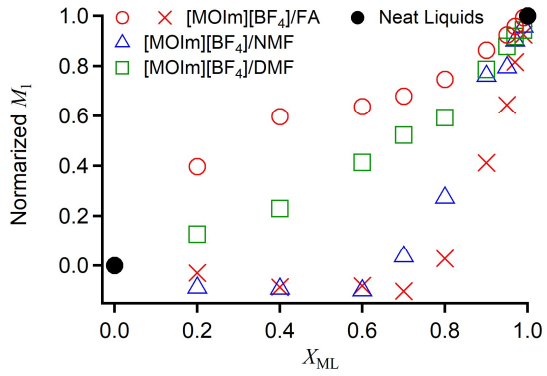

Figure IV.19. Plots of normalized M_1 vs. X_{ML} for [MOIm][BF_4] mixtures with FA (red circles), NMF (blue upper triangles), and DMF (green squares). Plots for neat liquids are also shown (black filled circles). Red crosses denote the plot for [MOIm][BF_4]/FA without the contribution of the third antisymmetrized Gaussian component (2D-HB band).

In order to understand the X_{ML} dependence of M_1 in the low-frequency spectra in detail, snapshots of the mixtures are shown in Figure IV.14. The structure of [MOIm][BF_4]/FA at X_{FA} = 0.9 is well mixed with [MOIm][BF_4] and FA, that of [MOIm][BF_4]/DMF at X_{DMF} = 0.9 is microphase separation, and that of [MOIm][BF_4]/NMF at X_{NMF} = 0.9 is the same as [MOIm][BF_4]/FA. The results of [MOIm][BF_4]/FA and [MOIm][BF_4]/NMF suggest that the structure of [MOIm][BF_4] is loosened by the ML molecules. In the structures of ML solvents at X_{ML} = 0.6, FA molecules are widespread and DMF molecules are localized. Therefore, FA and NMF molecules are distributed in the mixture interacting with the polar regions of [MOIm][BF_4]. In the low X_{ML} region below 0.7, the strength of intermolecular interactions in [MOIm][BF_4] does not change much because the solvent network is not broadened. Then, in high X_{ML} above 0.7 region, the solvent network through hydrogen bonds expands and affect the intermolecular interactions. Therefore, the M_1 for [MOIm][BF_4]/FA and [MOIm][BF_4]/NMF increases with increasing ML concentration in $X_{ML} \geq 0.7$. On the other hand, [MOIm][BF_4]/DMF separates between [MOIm][BF_4] and DMF regions, and thus the X_{ML} dependence of M_1 in [MOIm][BF_4]/DMF is likely due to the X_{ML} weighted sum of the two neat liquids, which likely changes the spectral shape gradually with X_{ML}.

Comparison of the low-frequency Kerr spectra and the DOS spectra can provide deep insight into the IL mixture. The physical quantities observed in the Kerr and DOS spectra are different (polarizability anisotropy response and vibrational density of states, respectively). Nevertheless, the comparison of the Kerr and DOS spectra is very useful for understanding the molecular-level aspects of liquids and solutions. In particular, it can reveal the motion of each component of a mixture. Figure IV.15 shows that neat [MOIm][BF_4], [MOIm][BF_4]/FA, and [MOIm][BF_4]/NMF have shoulders at about 100 cm^{-1} and 180 cm^{-1} at X_{ML} = 0.6, 0.9, and 1. A gradual low-frequency shift was observed with increasing X_{DMF} in the [MOIm][BF_4]/DMF. Thus, the low-frequency Kerr spectral features of the [MOIm][BF_4] mixture are qualitatively well reproduced by DOS.

The DOS spectrum of each component in the mixture suggest that $[BF_4]^-$ is sensitive to X_{ML} in [MOIm][BF_4]/FA and [MOIm][BF_4]/NMF and $[MOIm]^+$ is sensitive to X_{ML} in [MOIm][BF_4]/DMF. Especially, the DOS spectra of $[BF_4]^-$ in the [MOIm][BF_4]/FA at ca. 100 and 180 cm^{-1} and [MOIm][BF_4]/NMF at 100 cm^{-1} show influences of the solvents via hydrogen bonds. In all solvents, the peak of the DOS spectra shifted to the low-frequency side. These shifts indicated that FA and NMF preferentially influence the vibrational motions of $[BF_4]^-$, and DMF mainly affects the motions of $[MOIm]^+$.

Finally, consider the change in hydrogen bonding in the mixtures. Fujii et al. measured low-frequency spectra of the DMF mixtures with FA and NMF by steady Raman spectroscopy.[187,188] They reported the linear hydrogen bonding shifts to high frequency side with increasing concentrations of FA and NMF, but the 2D hydrogen bonding band in FA does not shift. Their results implied that the linear hydrogen bonding network can be perturbed easily by additional molecules, but the 2D hydrogen bonding network is tightly bonded and not easily disturbed. Palombo and Meech reported the low-frequency spectra for FA mixtures with NaI and KI by fs-RIKES.[189] They measured the low-frequency spectra of the mixtures in $X_{FA} \geq 0.85$ due to solubility limitations, but the linear and 2D hydrogen bonding bands shifted to the lower frequency side with increasing salt concentration. Similar to Palombo and Meech's study, the peak of the 2D hydrogen bonding band in the [MOIm][BF_4]/FA system shifted to the lower frequency side with increasing X_{FA}. Therefore, it is considered that ions can disrupt the linear and 2D hydrogen bonding structure.

IV.4.3. IR and NMR Spectra.

While low-frequency Kerr spectra are derived from intermolecular vibrations, IR and NMR can measure intramolecular vibrations and chemical shifts of nuclei, respectively. Thus,

IR and NMR probe smaller length (spatial) scales and are more specific than fs-RIKES. However, many of the groups and nuclei measured by IR and NMR show critical or steep changes at X_{ML} = 0.7 – 0.8, which is consistent with the fs-RIKES results of [MOIm][BF_4]/FA and [MOIm][BF_4]/NMF (see Figure IV.6 and IV.19).

The amide C=O stretching bands shown in Figure IV.7 and IV.8 shift to the low-frequency with increasing X_{ML} in all FA, NMF, and DMF. This indicates strengthening in the hydrogen bonds of the amides with increasing amides. The smaller shift of [MOIm][BF_4]/DMF compared to the other two mixtures suggests that the DMF molecules form weak hydrogen bonds. Figure IV.11 shows that, in the C=O groups, the ^{13}C chemical shifts of NMF and FA show down-field shifts, but that of DMF show an up-field shift. The IR and NMR results for the amide C=O groups indicate that DMF interacts with the hydrogens of the imidazolium ring by hydrogen bonding. On the other hand, FA and NMF self-associate and form strong hydrogen bonds.

Similar to the results for the amide C=O stretching band, the imidazolium ring C–H stretching band also shows a lower frequency shift with increasing X_{ML} in all systems as shown in Figure IV.10. However, the [MOIm][BF_4]/FA system has the smaller magnitude of the shift than the other two mixtures. The NMR results in Figure IV.12 also indicate that the imidazolium ring hydrogens in the [MOIm][BF_4]/NMF and [MOIm][BF_4]/DMF systems forms hydrogen bonds with NMF and DMF molecules, while the [MOIm][BF_4]/FA system appears to have only weak interactions between the imidazolium ring hydrogen (H^2) and FA molecules. Additionally, with increasing X_{ML}, the [MOIm][BF_4]/FA shows an up-field shift of C^2 atom and the [MOIm][BF_4]/NMF and [MOIm][BF_4]/DMF exhibit down-field shifts of C^2 atoms.

Similar to the ^{13}C NMR results for the C^2 atom of the imidazolium cation, the ^{19}F NMR results show that the F atom of the anion in the [MOIm][BF_4]/FA system shifts inversely to X_{ML} relative to that in in the [MOIm][BF_4]/NMF and [MOIm][BF_4]/DMF systems. As shown in Figure IV.13, the ^{19}F chemical shifts of the anions showed an up-field shift in the [MOIm][BF_4]/NMF and [MOIm][BF_4]/DMF systems and a down-field shift in the [MOIm][BF_4]/FA system. The quantum chemical calculations in Figure IV.17 show a down-field in the $[MOIm]^+$–$[BF_4]^-$–FA and $[MOIm]^+$–$[BF_4]^-$–NMF clusters and a slight up-field in the $[MOIm]^+$–$[BF_4]^-$–DMF cluster when compared to the $[MOIm]^+$–$[BF_4]^-$ cluster. Based on the results in Table IV.1, the opposite direction of the chemical shifts for $[MOIm]^+$–$[BF_4]^-$–FA/NMF and $[MOIm]^+$–$[BF_4]^-$–DMF is likely due to different stable pairs for the amide. Therefore, the direction of the chemical shift of the F atoms of $[BF_4]^-$ in the

[MOIm][BF_4]/FA and [MOIm][BF_4]/DMF observed by ^{19}F NMR can be qualitatively reproduced by the quantum chemical calculations.

Figure IV.18 show that the chemical shift of the F atom in $[BF_4]^-$ is an up-field shift as the distance between the cation and anion increases and a down-field shift as the distance between the cation and anion increases. Similar chemical shift was observed for $LiBF_4$ in solutions with different solvent polarities.[190] The distance dependence of the chemical shifts of the F atoms suggests that the addition of amide increases the distance between the cation and anion in the [MOIm][BF_4]/NMF system. As shown in Table IV.1, the interaction strengths between the $[BF_4]^-$–NMF and $[MOIm]^+$–NMF clusters calculated by quantum chemical calculations are very competitive, and this energy competition may have affected the change in the distance between the cation and anion. Furthermore, the relative dielectric constant of NMF is higher than those of FA and DMF (FA: 111.0, NMF: 189.0, DMF: 38.25 at 298 K).[180] Therefore, the up-field shift of the F atom in the [MOIm][BF4]/NMF with increasing X_{NMF} may be due to the longer distance between the cation and anion in the high dielectric constant medium.

The mesoscopic aspects revealed from the MD simulations exhibited in Figure IV.14 show clear segregation in the [MOIm][BF_4]/DMF system relative to the other system. This situation is apparently inconsistent with the self-association of FA and NMF in the [MOIm][BF_4] mixture in the molecular level. At present, I am considering the following scenario. The self-aggregates of FA and NMF have a high affinity with [MOIm][BF_4] and its constituent ions. Therefore, the [MOIm][BF_4] swells in the high-X_{ML} region. On the contrary, DMF and [MOIm][BF_4] have a low affinity, but specific sites of the [MOIm][BF_4] constituent ions interact with the DMF molecule and segregate while maintaining the IL structure. That is, the hydrogen bonding ability of the amino H atoms of FA and NMF to cations and anions is a major contributing factor to the mesoscopic mixing of [MOIm][BF_4] and amides.

IV.5. CONCLUSIONS

In this chapter, I studied the microscopic picture of mixtures of [MOIm][BF_4] with FA, NMF, and DMF by multiple spectroscopic approaches using fs-RIKES, FT-IR, and NMR. To discuss these spectroscopic experimental results in detail, MD simulations and quantum chemistry calculations were also performed. The fs-RIKES results revealed that the first moment of the low-frequency spectral bands of the [MOIm][BF_4]/FA and [MOIm][BF_4]/DMF systems, which are mainly due to intermolecular vibrations, gradually varied with the molecular liquid mole fraction X_{ML}, while that of the [MOIm][BF_4]/NMF system was almost constant up to $X_{NMF} = 0.7$ constant and gradually increases in $X_{NMF} \geq 0.7$. When the contribution of the 2D hydrogen-bonding network of FA to the low-frequency spectra is excluded, both the [MOIm][BF_4]/FA and [MOIm][BF_4]/NMF systems show little change in $X_{ML} < 0.7$ and a sharp increase in $X_{ML} \geq 0.7$ for the normalized first moment in the low frequency band. The FT-IR results showed that the amide C=O bands shifted to lower frequency side in all mixtures as the X_{ML} increased, indicating that this trend was due to hydrogen bonds. The C–H band of the imidazolium ring also showed the same trend as the amide C=O band. The microenvironment of $[BF_4]^-$ in the mixtures was probed by ^{19}F NMR, and it was shown that in the [MOIm][BF_4]/FA system the F atom of the anion shift to a down-field side with increasing X_{FA}, while in [MOIm][BF_4]/NMF and [MOIm][BF_4]/DMF shift to a up-field side. Drastic changes in chemical shifts were observed in the region of $X_{ML} > 0.8$. The chemical shifts in the [MOIm][BF_4]/FA and [MOIm][BF_4]/DMF systems are mainly due to the many-body interactions of the cation, anion, and amides, while that in [MOIm][BF_4]/NMF are likely due to the long distances between the cation and anion resulting from the high dielectric medium.

Chapter V.

Low-Frequency Spectra of 1-Methyl-3-octylimidazolium Tetrafluoroborate Mixtures with Poly(Ethylene Glycol)

J. Phys. Chem. B **2021**, 125, 12006-12019.

V.1. INTRODUCTION

In recent years, a lot of people concern about the depletion of fossil fuels such as coal and petroleum, and many researchers have investigated various studies on solving the energy problems to realize a sustainable society.[191-194] One of the studies is the development of secondary batteries. The first rechargeable battery is the lead-acid battery developed by Gaston Planté in 1859,[195] and this is still widely used as a battery for automobiles today. However, since lead-acid batteries are large and heavy, they are not suitable for carrying around. Therefore, smaller and larger-capacity secondary batteries have been needed. As a result, lithium-ion secondary batteries, which are small and lightweight and have large electric capacities and a long battery life, have been studied,[196] and they are now widely used as batteries for mobile phones and personal computers. Although, flammable organic solvents are used as electrolytes in the lithium-ion batteries, and thus there are risks of ignition or explosion. [24] Thus, the developments of solid electrolytes using a polymer, which are batteries with no liquid leakage and higher stability, have been studied, but most of these polymer solid electrolytes have a problem of low electrical conductivity. Therefore, ionic liquid (IL) and polymer mixtures have attracted attention to solve these problems.

The liquid properties of IL/polymer mixtures are related to the microscopic information, such as structure, intermolecular interactions, and molecular dynamics. Therefore, it is important to understand the microscopic information of IL/polymer mixtures to tone their liquid properties. Several papers have reported on the microscopic information of IL/polymer mixtures including structure, intermolecular interactions, and molecular dynamics.[197-204] For example, Aakriti Kharel and Timothy P. Lodge reported the microscopic structure of [BMIM][BF_4] and polyethylene oxides (PEO) mixtures by small-angle neutron scattering.[205] They clarified that, with increasing the molecular weight of PEO, the infinite dilution radius of gyration for PEO increased. However, low-frequency spectra (~200 cm^{-1}), which reflect intermolecular dynamics of liquids and solutions, of IL/polymer mixtures were not reported, so far. Thus, the intermolecular dynamics of IL/polymer mixtures are not well understood, and it is important to understand them to change the liquid properties of IL/polymer mixtures.

In this chapter, I measured low-frequency spectra of [MOIm][BF_4] mixtures with poly(ethylene glycol) (PEG) which is a molecular weight of 400 (PEG400). PEG is one of the typical polymers used in electrochemical materials and can mix with [MOIm][BF_4] at any concentration. As the neutral analog of $[MOIm]^+$, I also measured low-frequency 1-octhylimidazole (OIm) and PEG400 mixtures to confirm effects of ionic on the intermolecular vibrations. In addition, [MOIm][BF_4] mixtures with ethylene glycol (EG), PEG400, PEG with

a molecular weight of 4000 (PEG4000) were studied to compare the effects of molecular weight on the low-frequency spectra. This is the first report on the low-frequency spectra of IL/polymer mixtures as far as I know.

V.2. EXPERIMENTAL METHODS

V.2.1. Reagents and Sample Preparation

The reasons for choosing [MOIm][BF_4] was explained in the previous chapters. PEG is one of the common polymers and has attracted attention as an all-solid-state polymer electrolyte. This study aims to obtain the fundamental knowledge of the IL/polymer mixtures as novel battery materials by studying their intermolecular dynamics. [MOIm][BF_4] (Iolitec, >99%) and PEG400 (M_n = 400, Wako) were dried in vacuum at 313 K for over 36 h before using. OIm was synthesized following the synthesis procedure summarized in the Appendix. The purity of OIm was confirmed by ^{1}H NMR and ^{13}C NMR. The synthesized OIm was used after drying in vacuum at room temperature for over 36 h. EG (Kanto Chemical, >99.5%) was dried with molecular sieve 3A (Kanto Chemical) before using. PEG4000 (M_n = 4000, TCI) was used as received without other procedures. The water content of [MOIm][BF_4] was 81 ppm estimated by Karl Fischer titration using a coulometer (Hiranuma, AQ-300).

V.3. RESULTS

V.3.1. Liquid Properties: Density, Viscosity, Surface Tension, and Electrical Conductivity

The concentration dependence of ρ for the [MOIm][BF_4]/PEG400 and OIm/PEG400 systems is shown in Figure V.1a, and the molecular weight dependence of ρ for the [MOIm][BF_4] mixtures with EG, PEG400, and PEG4000 is exhibited in Figure V.1b. Table V.1 lists the ρ values of neat [MOIm][BF_4], OIm, PEG400, and EG. These ρ values are similar to the reported values in previous studies.[41,124,125,169,170,176,206,207] Table D1 also lists the ρ data for the mixtures. As shown in Figure V.1a, the values of ρ for [MOIm][BF_4]/PEG400 slightly increase with increasing PEG400 concentration because that for neat PEG400 is closer to that for neat [MOIm][BF_4]. However, the values of ρ for OIm/PEG400 gradually increase with increasing PEG400 concentration. On the other hand, Figure V.1b suggests that the ρ of the [MOIm][BF_4] mixtures are independent on the molecular weight of PEG.

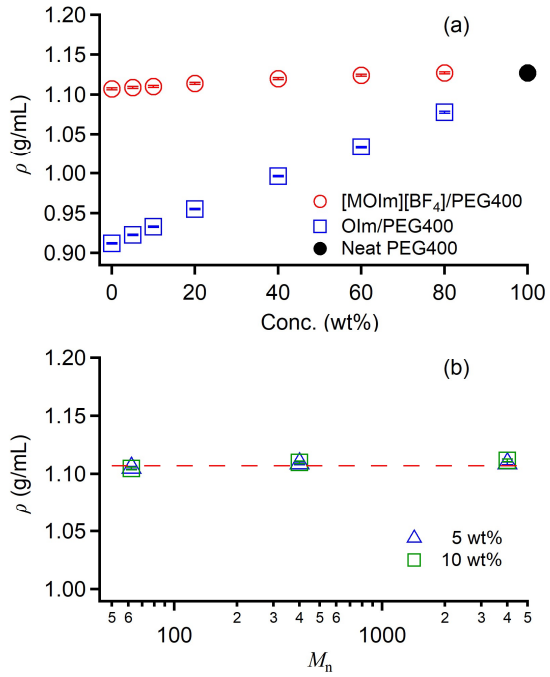

Figure V.1. (a) Concentration dependence of ρ for [MOIm][BF_4]/PEG400 (red circles) and OIm/PEG400 (blue squares) and (b) dependence of ρ on molecular weight (M_n) of PEG for [MOIm][BF_4] mixtures with EG, PEG400, and PEG4000 at 5 wt % (blue triangles) and 10 wt% (green squares). Plot for neat PEG400 in (a) is also shown (black filled circle). Red dashed line in (b) denotes ρ of neat [MOIm][BF_4]. (Error bar is ±0.1 %)

Table V.1. Density ρ, viscosity η, surface tension γ, electrical conductivity σ, and molar electrical conductivity Λ of neat [MOIm][BF_4], OIm, PEG400, and EG at 293 K.

Liquid	FW (M_n)	ρ [a] (g/mL)	η [b] (cP)	γ [c] (mN/m)	σ [b] (mS/cm)	Λ [b] (S cm^2/mol)
[MOIm][BF_4]	282.1	1.107	483.5	32.2	0.794	0.202
OIm	181.3	0.912	8.822	31.1	–	–
PEG400	400	1.127	118.8	44.0	–	–
EG	62.1	1.114	20.53	48.0	–	–

[a] ±0.1 %. [b] ±5 %. [c] ±1 %.

Figure V.2a exhibits the PEG400 concentration dependence of η for [MOIm][BF_4] and OIm systems, and Figure V.2b shows the molecular weight dependence of η for the [MOIm][BF_4] mixtures with EG, PEG400, and PEG4000. Table V.1. summarizes the values of η for neat [MOIm][BF_4], OIm, PEG400, and EG and they are in accordance with the results of other reports.[41,124,125,169,170,176,206-209] Table D1 also lists the values of η for the mixtures. With increasing PEG400 concentration, the values of η for [MOIm][BF_4]/PEG400 gradually decrease, while those for OIm/PEG400 increase as shown in Figure V.2a. Figure V.2b shows that the values of η for the [MOIm][BF_4] mixtures increase as increasing molecular weight of the solute. Additionally, the decrease in η for [MOIm][BF_4]/PEG400 is milder than that for [MOIm][BF_4]/EG, and the η values for [MOIm][BF_4]/PEG4000 increase with increasing PEG4000 concentration.

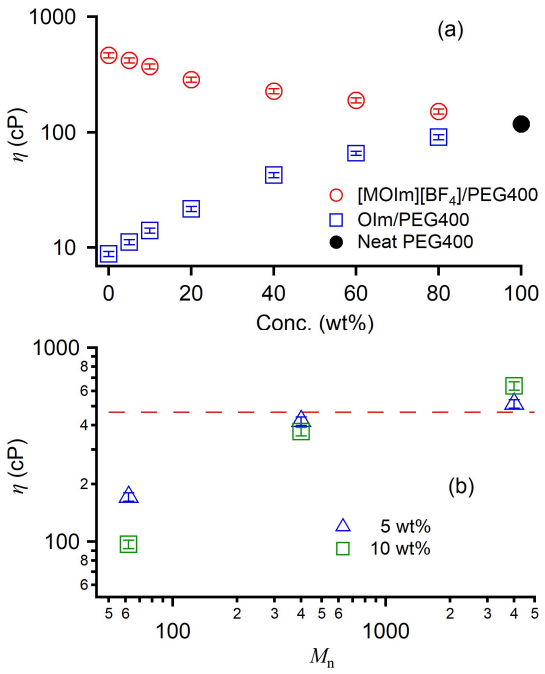

Figure V.2. (a) Concentration dependence of η for [MOIm][BF_4]/PEG400 (red circles) and OIm/PEG400 (blue squares) and (b) dependence of η on molecular weight of PEG for mixtures of [MOIm][BF_4] with EG, PEG400, and PEG4000 at 5 wt% (blue triangles) and 10 wt% (green squares). Data for neat PEG400 in (a) are also shown (filled black circle). Red dashed line in (b) denotes η of neat [MOIm][BF_4]. (Error bar is ±5 %)

The concentration dependence of γ for [MOIm][BF_4]/PEG400 and OIm/PEG400 and the molecular weight dependence of γ for the [MOIm][BF_4] mixtures with EG, PEG400, and PEG4000 are shown in Figure V.3a and Figure V.3b, respectively. Table V.1 lists the values of γ for neat [MOIm][BF_4], OIm, PEG400, and EG. The γ value of neat [MOIm][BF_4] is similar to the results of previous studies.[41,53,55,169,170] Table D1 summarizes the values of γ for the mixtures. The values of γ for both [MOIm][BF_4]/PEG400 and OIm/PEG400 systems gradually increase with increasing PEG400 concentration, and the γ value for [MOIm][BF_4]/PEG400 is slightly higher than that for OIm/PEG400 as shown in Figure V.3a. On the other hand, Figure V.3b suggests that the γ values for the [MOIm][BF_4] mixtures with EG, PEG400, and PEG4000 are slightly higher compared to that for neat [MOIm][BF_4], and γ values for [MOIm][BF_4] mixtures show no independent on the molecular weight of PEG, as well as on the ρ values of [MOIm][BF_4] mixtures.

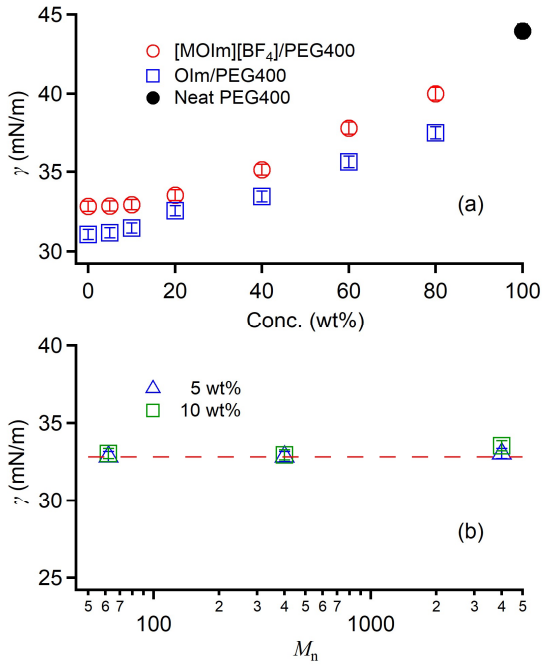

Figure V.3. (a) Concentration dependence of γ for [MOIm][BF_4]/PEG400 (red circles) and OIm/PEG400 (blue squares) and (b) dependence of γ on molecular weight of PEG for mixtures of [MOIm][BF_4] with EG, PEG400, and PEG4000 at 5 wt% (blue triangles) and 10 wt% (green squares). Data for neat PEG400 in (a) are also shown (black filled circle). Red dashed line in (b) denotes the γ of neat [MOIm][BF_4]. (Error bar is ±1 %)

Figure V.4a and Figure V.4b exhibit the concentration dependence of σ for [MOIm][BF_4]/PEG400 and the molecular weight dependence of σ for the [MOIm][BF_4] mixtures with EG, PEG400, and PEG4000, each other. Table V.1 lists the σ value of neat and the value of neat [MOIm][BF_4] is almost similar to the values reported in previous studies.[41,169,170] Table D1 summarizes the σ values for the mixtures. Figure V.4a shows that the [MOIm][BF_4]/PEG400 system has a maximum σ at 40 wt% of a PEG400 concentration. This σ peak was measured for some IL mixtures with a molecular liquid in other literatures.[4,126,127,169,170] As shown in Figure V.4b, σ for [MOIm][BF_4]/EG drastically increases with increasing EG concentration, while that for [MOIm][BF_4]/PEG400 slightly increases and that for [MOIm][BF_4]/PEG4000 gradually decreases with increasing PEG concentration.

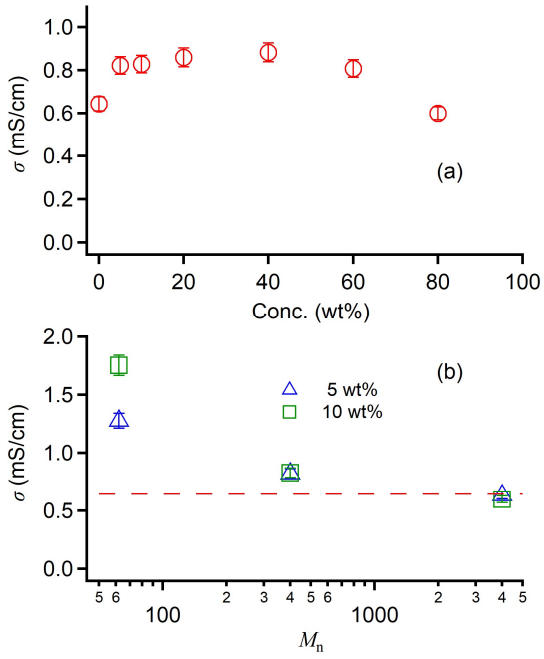

Figure V.4. (a) Concentration dependence of σ for [MOIm][BF_4]/PEG400 (red circles) and (b) dependence of σ on molecular weight of PEG for mixtures of [MOIm][BF_4] with EG, PEG400, and PEG4000 at 5 (blue triangles) and 10 wt% (green squares). Red dashed line in (b) denotes σ of neat [MOIm][BF_4]. (Error bar is ±5 %)

V.3.2. Low-Frequency Kerr Spectra via fs-RIKES

Figure V.5 shows the concentration dependence of the Kerr transients of fs-RIKES measurements for [MOIm][BF_4]/PEG400, OIm/PEG400, [MOIm][BF_4]/EG, and [MOIm][BF_4]/PEG4000 at 293 K. All Kerr transients were normalized at the signal's intensity corresponding to the electronic response (t = 0). As shown in Figure V.5, the intensity of the nuclear response decreases with increasing the solute concentration in all systems. This is because [MOIm][BF_4] and OIm are more polarizable than EG, PEG400, and PEG4000 due to the electron-rich aromatic rings.

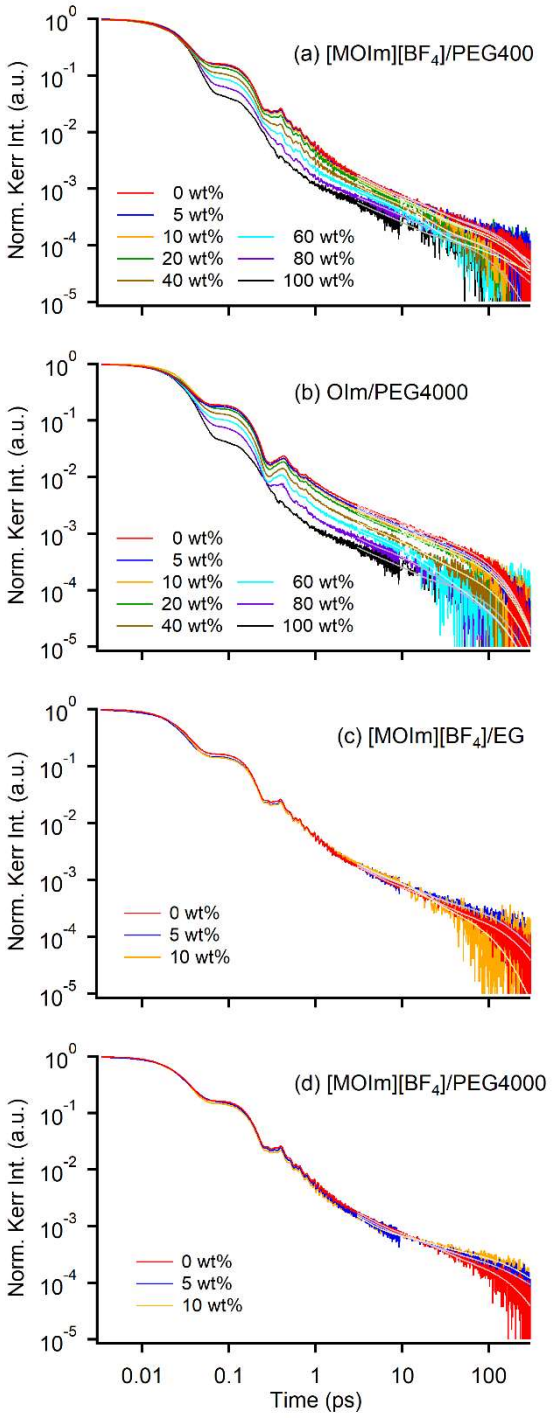

Figure V.5. Normalized Kerr transients for (a) [MOIm][BF_4]/PEG400, (b) OIm/PEG400, (c) [MOIm][BF_4]/EG, and (d) [MOIm][BF_4]/PEG4000 with different concentrations. Multiexponential fits from 3 to 300 ps are also shown.

I used a multiexponential function ($a_0 + \sum_i a_i \exp(-t/\tau_i)$, i = 3 or 4) to fit the slow relaxation component for over 3 ps of each Kerr transient. Table D2 summarize the fit parameters for the Kerr transients in all samples. To convert these Kerr transients to spectra, I

performed Fourier transform deconvolution analysis expounded in section II.3. Figure V.6 displays the spectra for [MOIm][BF_4]/PEG400 and OIm/PEG400 systems. I concentrate on the intermolecular vibrations, and thus the slow relaxation components ($a_0 + \sum_i a_i \exp(-t/\tau_i)$, ($i \geq 2$)) are removed from the entire spectrum in the spectra shown in Figure V.6. As shown in Figures V.6a and 6b, sharp bands appear from 200 to 700 cm^{-1}. They are caused by the constituent cation and anion of [MOIm][BF_4] or OIm. Broadened bands are also located below ~150 cm^{-1}, mainly due to intermolecular vibrations. Magnified Kerr spectra in the frequency range 0–300 cm^{-1} are shown in Figure V.6c and V.6d. The line shape of low-frequency Kerr spectra for neat [MOIm][BF_4] in this study is similar to previous results.[41,53,55,169,170] On the other hand, this is the first report of Kerr spectrum for PEG400. However, the Kerr spectra for PEG with M_n = 600 (PEG600), penta(ethylene glycol) (EG5, FW = 238), and tetra(ethylene glycol) (EG4, FW = 194) were already reported.[210] The spectral shapes of PEG600, EG5, and EG4 are very similar to that of PEG400, although the molecular weights are different. This is also the first report on the Kerr spectrum of neat OIm, but the spectral shapes of 1-methylimidazole (MIm) and 1-buthylimidazole (BIm) were reported previously.[133] The spectral shapes of MIm and BIm are similar to that of OIm.

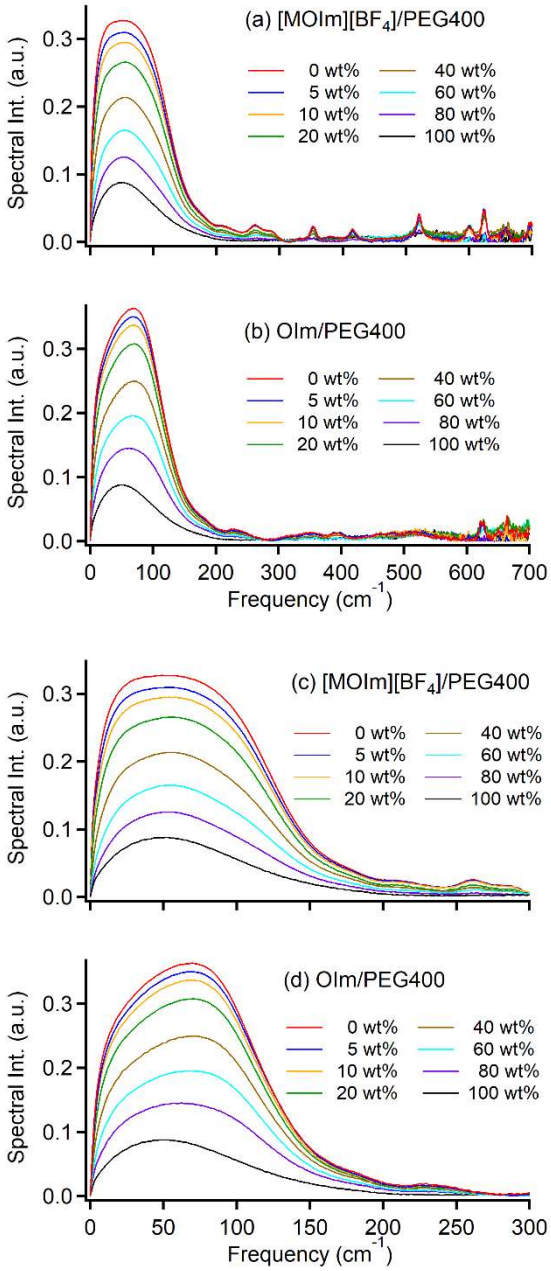

Figure V.6. Fourier transform Kerr spectra in the frequency range 0–700 cm^{-1} for (a) [MOIm][BF_4]/PEG400 mixtures and (b) OIm/PEG400 mixtures with different concentrations. Magnifications of spectra in the frequency range 0–300 cm^{-1} for (c) [MOIm][BF_4]/PEG400 mixtures and (d) OIm/PEG400 mixtures.

Figure V.7 displays the Fourier transform Kerr spectra of the [MOIm][BF_4] mixtures with EG an PEG4000 at 5 and 10 wt% of EG, PEG400 or PEG4000. Similar to the spectra in Figure V.6, those in Figure V.7 do not include slow relaxation components. Figure V.7a and V.7b show that the spectra of the [MOIm][BF_4] mixtures with EG, PEG400, and PEG4000 at

5 and 10 wt% are very similar each other. Figure V.7c and V.7d also display the magnified spectra in the frequency range of 0–300 cm^{-1}.

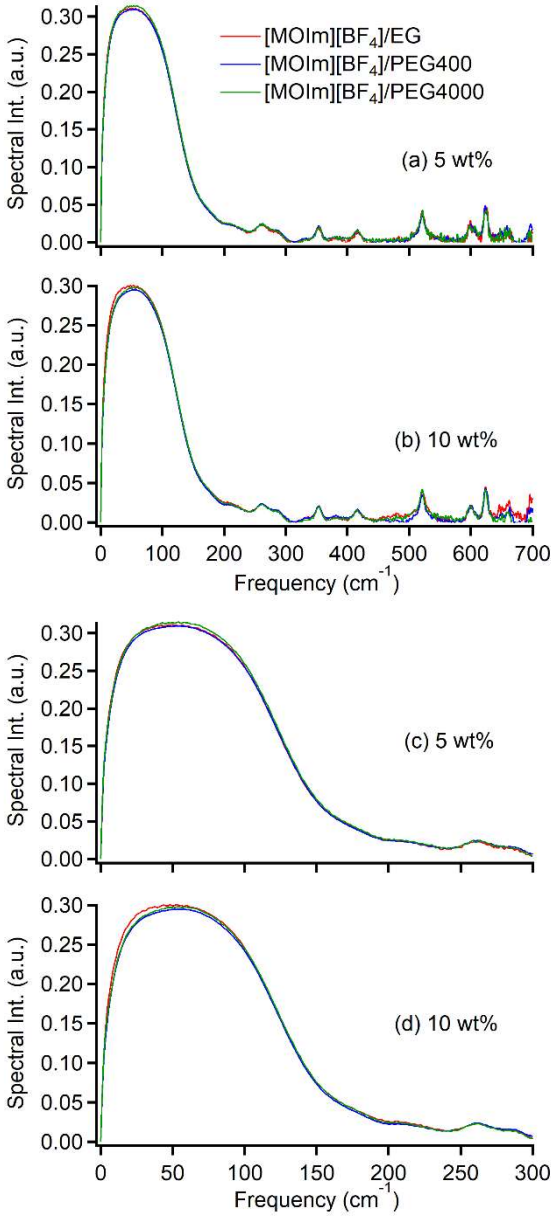

Figure V.7. Kerr spectra in the frequency range 0–700 cm^{-1} for [MOIm][BF_4]/EG, [MOIm][BF_4]/PEG400, and [MOIm][BF_4]/PEG4000 with concentrations of (a) 5 and (b) 10 wt%, as well as Kerr spectra in the frequency range 0–300 cm^{-1} for [MOIm][BF_4]/EG, [MOIm][BF_4]/PEG400, and [MOIm][BF_4]/PEG4000 with the PEG or EG concentrations of (c) 5 and (d) 10 wt%.

As shown in Figure V.6 and V.7, the spectral intensities of the low-frequency spectra decrease with increasing solute concentration. The line shape of the low-frequency spectrum

for neat [MOIm][BF_4] is trapezoidal and gradually changes to monomodal with increasing PEG400 concentration. In contrast, the line shapes of the low-frequency bands for the OIm/PEG400 system, except for neat PEG400, retain a similar spectral shape as increasing PEG400 concentration, although the spectral intensity gradually changes. On the other hand, the spectral shapes of the [MOIm][BF_4] mixtures with EG, PEG400, and PEG4000 are similar at the same concentration.

According to the procedure explained in section III.3.2, I performed line shape analysis for the low-frequency spectra. Figure V.8 exhibits the low-frequency spectra and fits for the [MOIm][BF_4]/PEG400 at 40 wt% of PEG400 and OIm/PEG400 at 80 wt% of PEG400 as examples. The other spectra were able to be fitted with similar quality. Table D4 and D5 list the fit parameters and Figure D3– D6 also show the plots of each parameter vs. concentration.

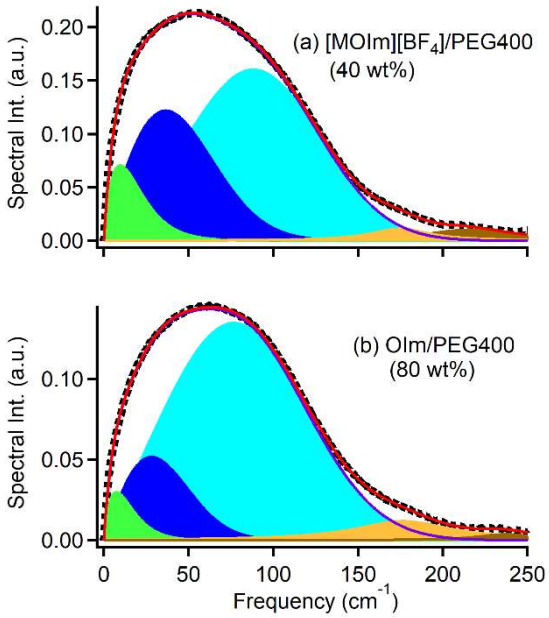

Figure V.8. Low-frequency spectra and their fits for (a) [MOIm][BF_4]/PEG400 at 40 wt% PEG400 and (b) OIm/PEG400 at 80 wt% PEG400. Dots represent experimental spectra, solid red lines represent the full fits, green areas represent the Ohmic functions, blue areas represent antisymmetrized Gaussian functions, and brown areas represent Lorentz functions. Solid purple lines denote the sums of Ohmic and antisymmetrized Gaussian functions.

To evaluate the composition dependence of the low-frequency spectra, Figure V.9 shows the plots of M_1 as a function of composition for [MOIm][BF_4]/PEG400, OIm/PEG400, [MOIm][BF_4]/EG, and [MOIm][BF_4]/PEG4000. Table D4 and D5 summarize the values of M_1 for the samples. As shown in Figure V.9a, M_1 for both [MOIm][BF_4]/PEG400 and OIm/PEG400 systems increases slightly as increasing PEG400 concentration, although the

difference in M_1 between neat PEG400 and [MOIm][BF_4] or OIm is only a few cm^{-1} (74.6 cm^{-1} for PEG400, 71.1 cm^{-1} for [MOIm][BF_4], and 69.1 cm^{-1} for OIm). The values of M_1 for the [MOIm][BF_4]/PEG400, [MOIm][BF_4]/EG, and [MOIm][BF_4]/PEG4000 are almost the same values at the same concentration, as seen in Figure V.9b.

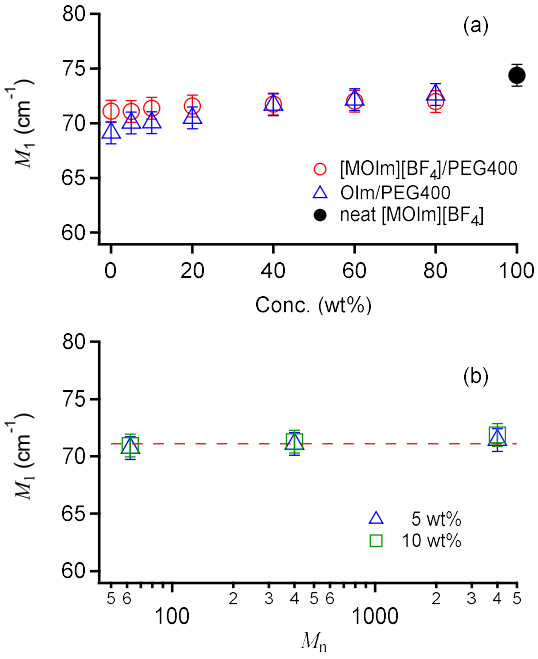

Figure V.9. Plots of (a) M_1 vs. PEG400 concentration for [MOIm][BF_4]/PEG400 (red circles) and OIm/PEG400 (blue triangles) and (b) M_1 vs. molecular weight for [MOIm][BF_4] mixtures with EG, PEG400, and PEG4000 at 5 wt% (blue triangles) and 10 wt% (green squares). Black filled circle in (a) denotes M_1 for neat PEG400 and red dashed line in (b) denotes M_1 for neat [MOIm][BF_4]. (Error bar is ± 1 cm^{-1})

V.4. DISCUSSION

V.4.1. Liquid Properties

As shown in Figure V.1, V.2, and V.3, the density, viscosity, and surface tension for the [MOIm][BF_4]/PEG400 and OIm/PEG400 systems gradually change with increasing the concentration of PEG400. This tendency is common in binary mixture systems, including polymer solutions.[211] In the molecular weight dependence of PEG (including EG) in the [MOIm][BF_4] mixtures, the density and the surface tension are almost constant at each concentration. When the alkyl group of ILs lengthens, the surface tension of ILs decrease. It might be interesting that the surface tension of the [MOIm][BF_4]/PEG system is almost independent of the molecular weight of PEG. However, such molecular weight independent surface tension was observed in another polymer solution system, polystyrene/CCl_4. Thus, in the present study, surface structure and intermolecular force are maybe independent of the molecular weight (or length) of the PEG. On the other hand, the viscosity of the [MOIm][BF_4]/PEG systems depends on the molecular weight of the PEG, which is a typical trend for polymer solutions.[212,213]

I estimated the molar electrical conductivity based on the σ and ρ values and IL concentrations of the sample mixtures. Figure V.10. shows the plots of Λ as a function concentration and molecular weight. Table D1 listed the values of Λ in the sample mixtures. Figure V.10a shows that the change in Λ with respect to the concentration is not so great, but there is a peak at ~40 wt%. Then, Figure V.10b exhibits that [MOIm][BF_4]/PEG4000 possess the lowest Λ among the three systems. Figure V.10c displays the Walden plots for the [MOIm][BF_4]/PEG400, [MOIm][BF_4]/EG, and [MOIm][BF_4]/PEG4000 systems. The plot of neat [MOIm][BF_4] is around the ideal line of KCl solution. While the data for many ILs plot near the ideal Walden plot line, there is a slight tendency for the more viscous ILs to be better ILs than the less viscous ILs. As shown in Figure V.10c, the [MOIm][BF_4]/PEG4000 system exhibits more ideal electrical conductivity than the [MOIm][BF_4]/EG and [MOIm][BF_4]/PEG400 systems, although the [MOIm][BF_4]/PEG4000 system has lower electrical conductivity than the other two systems. This trend is, to some extent, similar to the trend in neat ILs. This PEG4000 trend also differs from the [MOIm][BF_4] mixtures results measured in Chapter III and IV.[169,170] At this time, the origin of this trend in the molar conductivity is not clear. However, this implies that the [MOIm][BF_4]/PEG4000 system has the potential to be a better (solid) electrolyte than the shorter PEG.

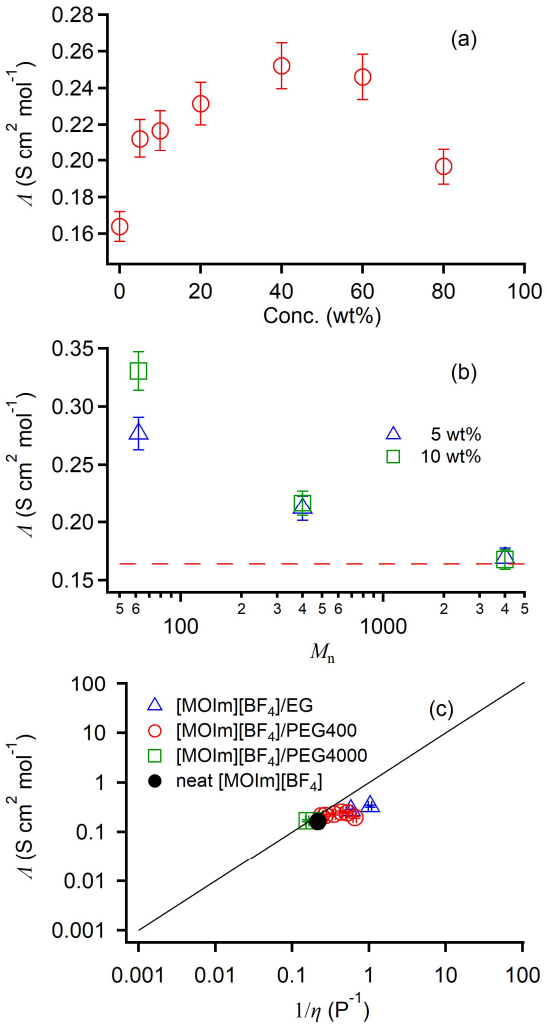

Figure V.10. (a) Molar electrical conductivity, Λ, of [MOIm][BF_4]/PEG400 as a function of concentration. (b) Molar electrical conductivity, Λ, of [MOIm][BF_4]/PEG400, [MOIm][BF_4]/EG, and [MOIm][BF_4]/PEG4000 with concentrations of 5 wt% (blue triangles) and 10 wt% (green squares) as a function of molecular weight of PEG. (c) Walden plots for systems [MOIm][BF_4]/PEG400 (red circles), [MOIm][BF_4]/EG (blue triangles), and [MOIm][BF_4]/PEG4000 (green squares) as well as for neat [MOIm][BF_4] (black filled circle). Black line denotes the ideal Walden line with the unity slope.

V.4.2. Comparison in Low-Frequency Spectra between [MOIm][BF_4]/PEG400 and OIm/PEG400

The line shapes of the low-frequency spectra of neat liquids show different spectral shapes each other as seen in Figure V.6. Neat [MOIm][BF_4] and OIm have strong spectral intensities in the high-frequency region above 50 cm^{-1}, while neat PEG400 does not show such strong spectral intensity in this region. This spectral feature was previously observed in

aromatic molecular liquids[133,186,214,215] and aromatic ILs.[41,53,66] For example, liquid benzene showed a trapezoidal spectral shape in the low-frequency region, although 1,4-cyclohexadiene and cyclohexane show triangular or monomodal line shape peaked at ca. 10–30 cm^{-1}.[143] Detailed comparisons of the spectra of bis(trifluoromethylsulfonyl)amide ($[NTf_2]^-$) ILs with the 1-benzyl-3-methylimidazolium ($[BzMIm]^+$), 1-benzyl-1-methylpyrrolidinium ($[BzMPyrr]^+$), 1-benzylpyridinium ($[BzPy]^+$), 1-cyclohexylmethyl-3-methylimidazolium ($[CHxmMIm]^+$), 1-cyclohexylmethyl-1-methylpyrrolidinium ($[CHxmMPyrr]^+$), and 1-cyclohexylmethylpyridinium ($[CHxmPy]^+$) reveals that the neutral ones appear at lower frequencies than the charged ones.[69,78] Comparison between IL (1-methoxyethylpyridinium dicyanoamide) and an equimolar mixture of neutral analogs (1:1 mixture of methoxyethylbenzene and dicyanomethane) shows that the low-frequency spectrum of IL has a peak at a higher frequency and is broader than that of an equimolar neutral binary mixture.[68] From these reports, the broad (trapezoidal) line shapes of the low-frequency spectra in aromatic liquids are derived from the aromatic ring libration.

Stratt and coworkers calculated the low-frequency Kerr spectra of liquid benzene using MD simulations.[216,217] The results showed that translational motion appears in the low-frequency region at less than 50 cm^{-1}, and rotational motion (such as the libration of aromatic ring) affects the entire spectra. The cross-term of the two motions also appears in the low-frequency region at less than 50 cm^{-1}. Accordingly, the spectral intensity in the high-frequency region at over 50 cm^{-1} for imidazolium-based ILs is mainly due to librational motion.[66,218] In contrast, the spectral intensity in the low-frequency region below 50 cm^{-1} for ILs based on aromatic cations is often attributed to translational motion and/or a cross-term of translational and rotational motion in ion species (some anions such as bis(perfluoroalkylsulfonyl)amides, including bis(trifluoromethylsulfonyl)amide, could also include the vibration).[50,51,219]

Concerning the concentration-dependence of the low-frequency spectra, Figure V.6a and V.6c show that the spectral shapes of the [MOIm][BF_4]/PEG400 and OIm/PEG400 systems gradually changes from neat [MOIm][BF_4] or OIm to PEG400 with increasing PEG400 concentration. However, careful examination of the spectra also shows that the low-frequency spectra of the OIm/PEG400 system were less affected than those of the [MOIm][BF_4]/PEG400 system at low concentrations of PEG400. This suggests that [MOIm][BF_4] is more affected and interacts more with PEG400 than OIm.

To understand the concentration dependence of the low-frequency spectra of the [MOIm][BF_4]/PEG400 system semi-quantitatively, I will discuss the concentration dependence of M_1 (Figure V.9a). As increasing PEG400 concentration, M_1 gradually shifts toward the

higher frequency side, while the magnitude of the shift is not very large. This result suggests that PEG400 make the microscopic intermolecular interaction of the [MOIm][BF_4] mixtures strong. such a gradual concentration dependence of M_1 has been reported in other IL/ML mixture systems (e.g., [MOIm][BF_4]/benzene,[55,130] [MOIm][NTf_2]/benzene,[130] and 1-methyl-3-pentylimidazolium bis(trifluoromethanesulfonyl)amide/CS_2[80]). However, some of IL/ML mixture systems show a constant M_1 in a certain concentration range (e.g., [MOIm][BF_4]/H_2O,[53] [MOIm][BF_4]/MeOH,[169] [MOIm][BF_4]/MeCN,[169] and [MOIm][BF_4]/DMSO[169]). In short, in the former case to which the present [MOIm][BF_4]/PEG400 system belongs, the solvent molecules are dispersed and mixed with ILs at the molecular level. In contrast, in the latter case, the solvent molecules are localized in a certain region, for example, at the interface between polar and nonpolar regions. Therefore, the structure of ILs maintained at a relatively low solvent concentration.[82,220]

As shown in Figure V.8, the low-frequency spectra of the present samples are well fitted by the sum of the Ohmic and two antisymmetrized Gaussian functions. (See Figure D3-D6 for details.) These amplitudes of the Ohmic function (lowest frequency component) and the high-frequency antisymmetrized Gaussian function (highest frequency component) become smaller with increasing PEG concentration for both [MOIm][BF_4]/PEG400 and OIm/PEG400 systems. In addition, the frequencies of the fit functions for the [MOIm][BF_4]/PEG400 system shift to a higher frequency side as the concentration of PEG400 increases, while those for the OIm/PEG400 system show only a little concentration dependence. As explained earlier, the lower frequency side of the low-frequency spectral intensity includes the translational motions and the higher frequency side of the low-frequency spectral intensity is essentially associated with the librational motions of the aromatic ring. Therefore, this result indicates that translational and librational motions in the [MOIm][BF_4]/PEG400 system are more sensitive to PEG400 than in the OIm/PEG400 system.

To elucidate the mixing states of the [MOIm][BF_4]/PEG400 and OIm/PEG400 systems, the low-frequency spectra were analyzed in more detail. The experimental spectrum, $I(\omega)$, consists of the contributions of neat [MOIm][BF_4] or OIm ($I_{[\mathrm{MOIm}][\mathrm{BF4}]}(\omega)$ or $I_{\mathrm{OIm}}(\omega)$), and PEG400 ($I_{\mathrm{PEG400}}(\omega)$). When the components are well mixed, the experimental spectrum is smaller than the sum of the spectra weighted by mole fractions ($x_A I_A(\omega) + x_B I_B(\omega)$). This reduction of the spectrum is defined as the loss spectrum, $I_{loss}(\omega)$. Thus, the experimental spectrum is expressed as,

$$I(\omega) = x_A I_A(\omega) + x_B I_B(\omega) - I_{loss}(\omega) \quad \text{(V-1)}$$

where x_n denotes the mole fraction of component n, and $x_A + x_B = 1$. Previously, Quitevis and coworkers also performed a similar analysis for IL/ML mixtures, but they used the sum spectra of the neat components weighted by volume fraction.[80] In this study, the weighting mole fractions is used instead of volume fractions for a simple consideration of the spectra. Figure V.11 exhibits the experimental spectrum of [MOIm][BF_4]/PEG400 at 60 wt%, the sum spectrum weighted by mole fraction, and the spectra of neat [MOIm][BF_4] and PEG400 in the sum spectrum. Figure V.11 clearly shows that the experimental spectrum of a mixture cannot be represented by a simple additive of the two components and has a lower spectral intensity than the sum spectrum. This spectral feature is also exhibited in the other samples (see Figure D7 and D8). If they were not well mixed, the spectrum should be constructed only by two neat components weighted by the mole fraction. Therefore, the results suggest that PEG400 are well mixed with [MOIm][BF_4] and OIm together at the molecular level.

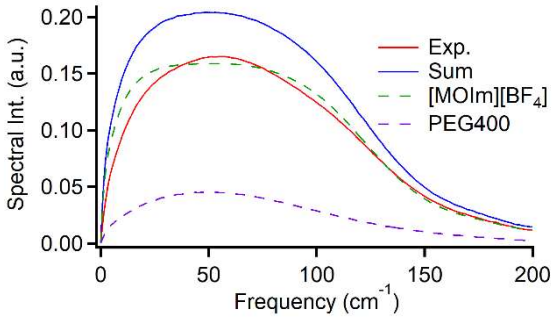

Figure V.11. Comparisons of the experimental low-frequency spectrum of [MOIm][BF_4]/PEG400 (60 wt%) (red solid line) with the sum spectrum (blue solid line) of the mole fraction weighted spectra of neat [MOIm][BF_4] (green broken line) and PEG400 (purple broken line).

Figure V.12 shows the loss spectra calculated by eq. 5 for the [MOIm][BF_4]/PEG400 and OIm/PEG400 systems. The spectral intensities in the loss spectra of the two systems are found to increase with increasing PEG400 concentration from 0 to 60 wt%, but to decrease with further increases in PEG400 concentration. The contribution of the components should be large (the contributions of the neat liquids should be small, on the contrary) under equimolar conditions and the PEG400 concentrations under equimolar conditions for the [MOIm][BF_4]/PEG400 and OIm/PEG400 systems are approximately 59 and 69 wt%,

respectively. Therefore, it is quite reasonable that the spectral intensity of the loss spectra in the two systems is maximized at 60 wt%.

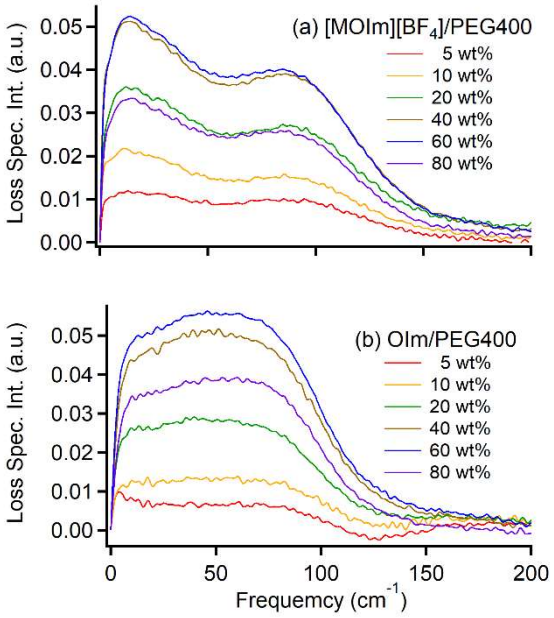

Figure V.12. Loss spectra estimated by eq. 5 for (a) [MOIm][BF_4]/PEG400 and (b) OIm/PEG400 mixtures with different concentrations.

Figure V.12 shows that the line shape of the loss spectrum for the [MOIm][BF_4]/PEG400 system is bimodal, and that for the OIm/PEG400 system is trapezoidal, except for OIm/PEG400 with the concentration of 5 wt%, which may be due to the low intensity of the loss spectrum. I analyzed the loss spectra were analyzed by line shape analysis and estimated the M_1 values (see Table D6 and Figure D9 and D10 in Appendix). Except for the exception of the 5 wt% sample, the M_1 values for the [MOIm][BF_4]/PEG400 and OIm/PEG400 systems were almost independent of PEG400 concentration, showing constant values of ~65 and ~57 cm^{-1} , respectively.

The intensity at ~15 cm^{-1} in the bimodal loss spectra of [MOIm][BF_4]/PEG400 mixtures is greater than at ~85 cm^{-1} as shown in Figure V.12. The translational motions of ion species often occur in the lower frequency side (~50 cm^{-1}) of the low-frequency spectrum, and the libration of the imidazolium ring completely cover the low-frequency spectrum.[50,51,218,221] In addition, the librational motion of charged aromatic rings in IL is faster (higher in frequency) than the librational motion of a comparable neutral aromatic ring.[68,69,78] Therefore, the results of the loss spectra suggest that PEG400 mixes with [MOIm][BF_4] very well and disrupts translational (collision-induced) and librational motions of the IL (and ion species). On the other

hand, in the case of the OIm/PEG400 system, the libration of the OIm is lower in frequency than in the $[OIm]^+$. Thus, the line shape of the loss spectrum for the OIm/PEG400 system is trapezoidal rather than bimodal.

V.4.3. Comparison in Low-Frequency Spectra of [MOIm][BF_4] Mixtures with PEG400, EG, and PEG4000

Concerning the molecular weight dependence of the low-frequency spectra, the spectral shapes of the low-frequency spectra of [MOIm][BF_4] mixtures with EG, PEG400, and PEG4000 are similar to each other as shown in Figure V.6a, V.6c, and V.7. To understand the similarities of the spectral shapes in more detail, Figure V.13 displays the normalized spectra of mixtures of [MOIm][BF_4] with EG, PEG400, and PEG400. In the high-frequency region (>50 cm^{-1}), the three spectra of [MOIm][BF_4] mixtures showed almost the same spectral shapes at each concentration. As discussed in Section V.4.1., the librational motions of the aromatic molecules appeared over the low-frequency spectrum, while the interaction-induced and librational motions appeared in less than 50 cm^{-1}. Therefore, the results in the high-frequency region (>50 cm^{-1}) suggest that the frequency of librational motion in the imidazolium ring does not change even if the molecular weights of EG and PEGs increase.

On the other hand, in the low-frequency region (below 50 cm^{-1}), the spectral intensity of the [MOIm][BF_4]/EG system is slightly higher than those of the [MOIm][BF_4]/PEG400 and [MOIm][BF_4]/PEG4000 systems. The difference is greater at 10 wt% than 5 wt%.

The molecular weight dependence in this study is qualitatively similar to that in aqueous solutions of polyacrylamide,[222,223] polyvinylpyrrolidone,[224] poly(acrylic acid),[223] and carbon tetrachloride solutions of polystyrene.[211,225] Spectral intensity at low frequencies in less than ~50 cm^{-1} for model monomer solutions is larger than that for corresponding polymer solutions. These results suggest that the large mass and moment of inertia of the polymer suppress the interaction-induced (or collision-induced) motion of molecules more than the monomer.

In the previous polymer solutions' system, the polymer or model monomer have larger contributions to the low-frequency spectrum than solvent molecules, because the polymer or model monomer has the greater anisotropy of polarizability than the solvent. Conversely, since the spectral intensity of EG and PEG polymer is much weaker than that of [MOIm][BF_4], the low-frequency spectra of the [MOIm][BF_4]/EG and [MOIm][BF_4]/PEG systems are mainly contributed by the ion species' motions. The translational motions of the ion species are not strongly suppressed, because ion collisions can occur without any restriction on the part of the

polymer. Thus, the molecular weight dependence of the low-frequency spectra between the [MOIm][BF_4]/EG and [MOIm][BF_4]/PEG systems is much smaller than polymer solution systems. The M_1 values for the three systems showed almost identical values, as shown in Figure V.9b, supporting this consideration.

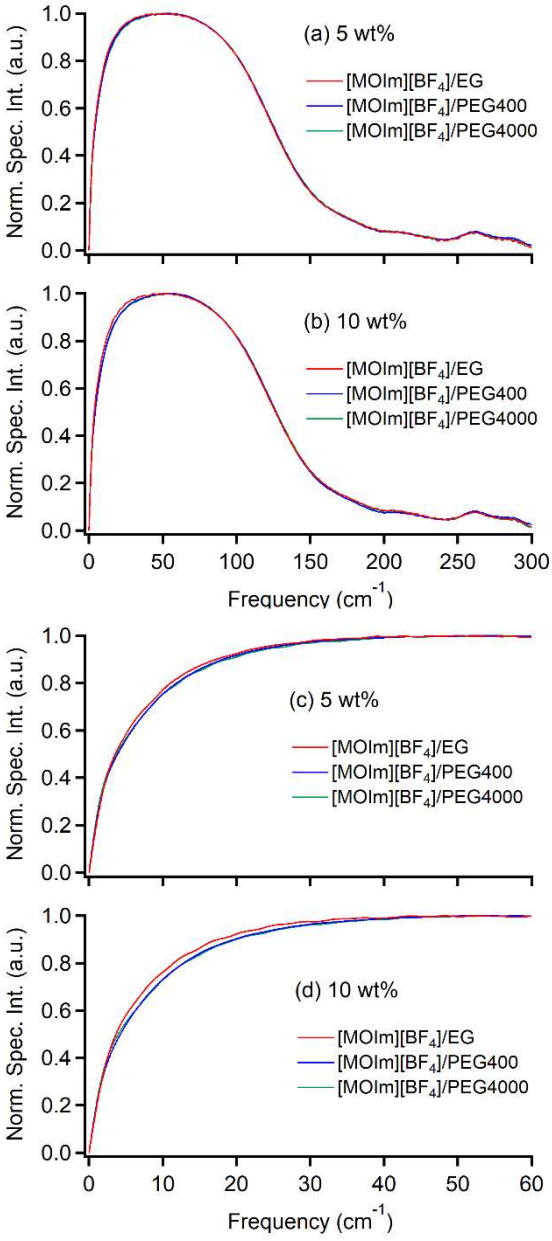

Figure V.13. Normalized spectra for mixtures of [MOIm][BF_4] with EG (red lines), PEG400 (blue lines), and PEG4000 (green lines) at concentrations of EG, PEG 400, or PEG4000 (a) 5 and (b) 10 wt%. Magnifications of the spectra at concentrations of EG, PEG 400, or PEG4000 (c) 5 and (d) 10 wt%.

V.4.4. Comparison between Low-Frequency Spectrum and Bulk Parameter

As discussed in Chapter III.4.3., I will consider the relationship between the intermolecular vibrational band (M_1) and bulk parameter ($\sqrt{\gamma/\rho}$). The plots of M_1 vs. $\sqrt{\gamma/\rho}$ for the [MOIm][BF_4]/PEG400 and OIm/PEG400 systems are shown in Figure V.14. The relations for aprotic MLs,[133] aromatic cation-based ILs,[41] and nonaromatic cation-based ILs[42] are also exhibited. The plots for the [MOIm][BF_4]/PEG400 and OIm/PEG400 mixtures are around the relation of the aromatic ILs. The plot for neat PEG400 is also somewhat closer to the relation of aromatic ILs than aprotic molecular liquids. This may imply that the liquid polymer exhibits a different relation between the intermolecular vibrational band and bulk parameter from aprotic molecular liquids. The [MOIm][BF_4]/PEG400 system shows that the values of M_1 and $\sqrt{\gamma/\rho}$ gradually change from neat [MOIm][BF_4] to neat PEG400. This suggests that the small concentration dependence of M_1 in the [MOIm][BF_4]/PEG400 system is derived from homogeneous mixing even on a microscopic scale in the [MOIm][BF_4]/PEG400 mixtures.

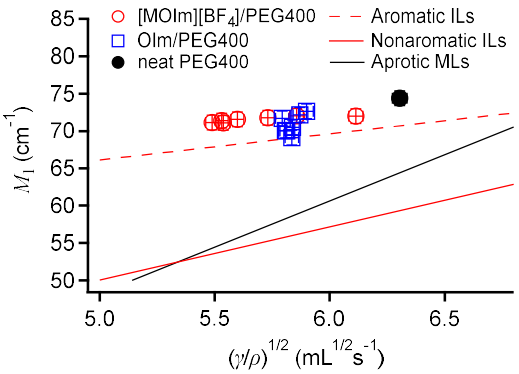

Figure V.14. Plots of M_1 vs. $\sqrt{\gamma/\rho}$ for [MOIm][BF_4]/PEG400 mixtures (red circles), OIm/PEG400 mixtures (blue squares), and neat PEG400 (black filled circle). Relations for aromatic cation-based ILs (red broken line),[41] nonaromatic cation-based ILs (red solid line),[42] and aprotic molecular liquids (black solid line)[133,147,149] are also shown.

The plots of OIm/PEG400 mixtures are located at the same region with respect to that of neat OIm. As displayed in Figure V.1a and V.3a, both ρ and γ in OIm/PEG400 mixtures increase with increasing PEG concentration, and thus the bulk parameter, $\sqrt{\gamma/\rho}$, is almost independent on the PEG concentration. On the other hand, the value of M_1 is slightly dependent on the PEG concentration, as exhibited in Figure V.9. These results suggest that the M_1 value for OIm/PEG400 mixtures is not greatly affected by the bulk properties. Additionally, the plots

of neat OIm differ from the relation of aprotic molecular liquids. Compared to the surface tensions of 1-methylimidazole, 1-butylimidazole, and OIm, the γ value of neat OIm is smallest (1-methylimidazole: 44.9 mN/m, 1-butylimidazole: 34.8 mN/m, OIm: 31.0 mN/m).[133] As with aqueous solutions of surfactants[226,227] and 1-alkyl-3-methylimidazolium ILs,[228-230] alkyl groups tend to align on the liquid surface of OIm, resulting in low surface tension in OIm. This results in a smaller value of $\sqrt{\gamma/\rho}$. I assume that the intermolecular force in bulk liquid for OIm is similar to 1-methylimidazole (mainly comes from imidazole ring) and estimate $\sqrt{\gamma/\rho}$ using the γ value of 1-methylimidazole. Then I get $\sqrt{\gamma/\rho}$ value of 6.98 ($mL^{1/2}\ s^{-1}$). Using this value, the plot for OIm overlaps well with the relation of aprotic molecular liquids. Therefore, the structure of the OIm surface probably affects the bulk parameter.

V.5. CONCLUSIONS

In this chapter, I studied the low-frequency intermolecular vibrational motions of [MOIm][BF_4]/PEG400 mixtures via fs-RIKES. OIm/PEG400 mixtures were also studied as a neutral molecular model. In addition, I investigated the low-frequency spectrum of [MOIm][BF_4] mixtures with EG, PEG400, and PEG4000 to elucidate the effect of the molecular weight of poly(ethylene glycol). As increasing the concentration of PEG400, the spectral intensity decreases, and the first moments of the low-frequency spectra are slightly and gradually blue-shifted for both [MOIm][BF_4]/PEG400 and OIm/PEG400 systems. I calculated the loss spectra, defined as the subtraction of the experimental spectrum from the sum of the molar fraction weighted spectra of neat liquids. The line shape of the loss spectrum in the [MOIm][BF_4]/PEG400 system is bimodal, while that in the OIm/PEG400 is trapezoidal. This result suggests that PEG400 disrupts the translational (collision- or interaction-induced) motions in the ion species and slows down the librational motions of the imidazolium ring. In the molecular weight dependence, the normalized low-frequency spectrum of the [MOIm][BF_4] mixtures with EG, PEG400, and PEG4000 show almost the same line shape each other in the high frequency region (>50 cm^{-1}) at each concentration. However, those of the [MOIm][BF_4] with PEG400 and PEG4000 slightly differs in the low-frequency region below ~40 cm^{-1} from that of the [MOIm][BF_4]/EG system. This suggests that translational motion is suppressed in the [MOIm][BF_4]/PEG system because of its larger (heavier) component compared to EG.

Chapter VI.

Low-Frequency Spectra of Phosphonium Bis(fluorosulfonyl)amide Ionic Liquids with Pentyl, Ethoxyethyl, or 2-(Ethylthio)ethyl Group

J. Phys. Chem. B, **2023**, *127*, 542-556.

VI.1. INTRODUCTION

In the studies of IL/ML mixtures discussed in Chapters III and IV, the values of the viscosity for IL/ML mixtures were greatly lower than that for neat IL. Thus, it is useful to add ML to IL to reduce the viscosity of IL. On the other hand, it has been reported that the introduction of other atom into the alkyl group of IL decreases the viscosity of the ionic liquid. One of the examples is ether functional group and it makes ILs lower viscosity than alkyl group.[47,231-237] In addition, ether functional group affects not only bulk properties but also microscopic properties. For example, the microscopic structure of ILs with an ether functional group shows less segregated structure than those with an analog alkyl group[238,239] and ILs with ether groups show the faster self-diffusion than that of ILs with alkyl groups. [235-237]

So far, limited research has been done on thioether functionalized ILs compared to ether ones.[240-242] According to Dyson and co-workers, alkylthioalkyl functionalized imidazolium-based ILs exhibit lower viscosity than alkoxyalkyl functionalized ILs.[242] These results follow the heavy atom substitution effect on the viscosity of ILs[148] and suggest that ILs with lower viscosity may be synthesized by the introduction of thioethers to the alkyl group.

Therefore, to synthesize ionic liquids with lower viscosity, new alkylthioalkyl group substituted phosphonium-based ILs were synthesized in our laboratory.[243] However, contrary to expectations, the new synthesized ILs exhibited higher viscosity than the phosphonium-based ILs with pentyl groups.[243] These results are in conflict with the heavy atom substitution effects in ILs and thioethers may affect the intermolecular interactions of phosphonium-based ILs differently than other ionic liquids.

Thus, in this chapter, I compared the liquid properties (glass transition temperature, viscosity, density, surface tension, and electrical conductivity) and the low-frequency spectra of three phosphonium-based ILs: triethylpentylphosphonium bis(fluorosulfonyl)amide ($[P_{2225}][NF_2]$), ethoxyethyltriethylphosphonium bis(fluorosulfonyl)amide ($[P_{222(2O2)}][NF_2]$), and triethyl[2-(ethylthio)ethyl]phosphonium bis(fluorosulfonyl)amide ($[P_{222(2S2)}][NF_2]$) (Figure VI.1). The low-frequency spectra were measured by fs-RIKES and terahertz time-domain spectroscopy (THz-TDS) at various temperatures (293, 308, 323, 338, and 353 K). Although the low-frequency spectra of ILs using fs-RIKES and THz-TDS or Raman and IR spectroscopy were reported so far, this study is significant because few studies have focused on collective directional relaxation of ILs. Quantum chemistry calculations and molecular dynamics (MD) simulations were also performed and compared with experimental results to provide more detailed interpretations of the low-frequency spectra.

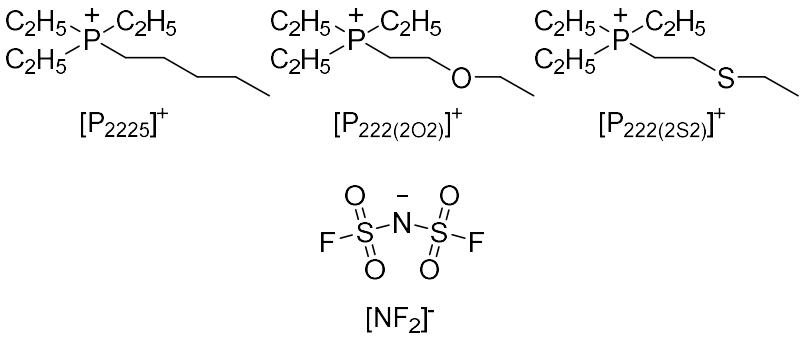

Figure VI.1. Structural formulas of the target ILs.

VI.2 Experimental and Computational Methods

VI.2.1. Preparation Methods and Liquid Property Measurements.

The reason for choosing $[P_{2225}][NF_2]$, $[P_{222(2O2)}][NF_2]$ and $[P_{222(2S2)}][NF_2]$ is to examine how the different atoms introduced into the functional groups affect the intermolecular interactions of the phosphonium based ILs. $[P_{2225}][NF_2]$, $[P_{222(2O2)}][NF_2]$ and $[P_{222(2S2)}][NF_2]$ were synthesized according to the procedures of the preparation process of phosphonium-based ILs in the previous report.[47] I checked the ILs by ^{1}H NMR and elementary analysis (<0.2%). Appendix summarizes the IL synthesis procedures in detail. The water contents of $[P_{2225}][NF_2]$, $[P_{222(2O2)}][NF_2]$, and $[P_{222(2S2)}][NF_2]$ were estimated by Karl Fischer titrations using a coulometer (Hiranuma, AQ-300) and were 26, 67, and 39 ppm, respectively.

VI.2.2. THz-TDS Measurements.

The THz-TDS measurements were performed in the Tominaga's Laboratory at Kobe University. In this study, two different THz-TDS setups were used to measure different frequency regions. One THz-TDS setup[244] was based on a photoconductive antenna using a titanium sapphire laser (Integral Pro200, Femtolasers) which has a center wavelength of 800 nm. A pair of photoconductive antennas was used for the THz emitter and detector (AISPEC) and was switched by the laser light. This photoconductive antenna-based THz-TDS can measure the frequency region of approximately 6–100 cm^{-1}.

The other one was the fs laser-induced plasma and air-biased coherent detection-based THz-TDS using a titanium sapphire regenerative amplifier (Spitfire Pro, Spectra Physics).[245,246] The output laser was divided into the pump pulse and the probe pulse. The pump laser pulse produced the pump THz pulse. The second harmonic light of the THz radiation was generated by a BBO crystal (type I, 0.1 mm thickness). The second harmonic and the residual fundamental

pulses were polarization tuned by a thin dual-wavelength wave plate (~45 μm) and focused into the nitrogen gas to generate the THz pulses. After that, the electric field of the THz pulses was measured with an air-biased coherent detection scheme. To measure the THz-induced second harmonic generation, the THz pulse was mixed with the probe laser pulse. Note that a high-voltage AC bias field of ±1.5 kV was applied at the focal point to generate a local oscillator for heterodyne detection. This THz-TDS can measure the frequency range of 30-200 cm^{-1}.

For the THz-TDS measurement, the cell with an optical path length of about 200 μm with a lead spacer sandwiched between silicon windows was used. The sample temperature was controlled using a laboratory-built temperature control device with a heater using a thermal resistive material. For comparison with the fs-RIKES spectra, the high-frequency THz-TDS spectra were factorized to match the low-frequency THz-TDS spectra, and then the two THz-TDS spectra were patched at 50 cm^{-1}. The details are given in Appendix.

VI.2.3. MD Simulations.

The MD simulations were performed by Dr. Tateki Ishida at the Institute for Molecular Science. The GROMACS 2016.1 was used for the MD simulations of $[P_{2225}][NF_2]$ with the reported force field parameters[247-250] for the cation and anion. For different temperatures (293 K and 353 K), 1024 ion pairs (48128 atoms) of $[P_{2225}][NF_2]$ were placed in a cubic box and the periodic boundary condition were applied.

The Lennard-Jones interactions were calculated with a cutoff of 12 Å. To compute Coulombic interactions, the Particle-mesh Ewald method[251] with an electrostatic cutoff of 12 Å and a Fourier grid spacing of 1.2 Å was used. A time step was 1.0 fs. Initially, each temperature system was equilibrated under NPT conditions at a pressure of 1 atm for 20 ns.

The Nosé-Hoover thermostat[119,252] was used to keep the temperature and the Parrinello-Rahman barostat[253] was used to control the pressure. The time constants for temperature and pressure were set at 1.0 ps. The cubic box size lengths at 293K and 353K are 79.997 and 81.108 Å, respectively, based on the NPT simulation results. After that, NVT simulations were performed for a 20 ns equilibration run and then a 40 ns production run at 293K and 353K. The collection interval of the simulation data during production run was 100 fs.

The polarizability time correlation function was obtained by calculating the gas-phase molecular polarizability tensors for each of the cation and anion using the Gaussian 09 program package.[254] The low-frequency depolarized Raman spectrum (DRS) corresponds to the RIKES spectrum and was calculated based on the dipole-induced-dipole (DID) model approximation.[255,256] Referring to the previously reported computational procedure,[51,141,142] the

low-frequency spectra were also analyzed for the decomposition analysis into the compositions of cation and anion and motions. The calculation of THz spectra (ABS) was based on previous study.[257-259] Similar to the decomposition analysis of the DRS spectrum, the contributions of translational and rotational motions to the THz absorption spectra were investigated.[260,261] Then, to obtain the vibrational density of states (VDOS) spectra, the Fourier transform of the autocorrelation function of the velocity of ionic species was used. Appendix summarizes the computational procedure in detail.

VI.2.4. Quantum Chemistry Calculations.

Density functional theory (DFT) calculations was performed based on the B3LYP/6-311++G(d,p) level of theory for geometry optimizations of the three cations and anion using the Gaussian 16 program.[121] Raman and IR active normal modes and atom charges of the cations were calculated from optimized cation and anion structures.

VI.3. RESULTS

VI.3.1. Liquid Properties: Glass Transition Temperature, Melting Point, Viscosity, Density, Surface Tension, and Electrical Conductivity.

The formula weights, melting points, and glass transition temperatures of the ILs, $[P_{2225}][NF_2]$, $[P_{222(2O2)}][NF_2]$, and $[P_{222(2S2)}][NF_2]$ are given in Table VI.1. The DSC chart of each IL are also shown in Figure E1. The glass transition temperature of the $[P_{222(2S2)}][NF_2]$ measured in this study is similar to that in a previous report.[83] As far as I know, $[P_{222(2O2)}][NF_2]$ have not been reported its liquid properties, such as the melting point, glass transition temperature, viscosity, density, surface tension, and electrical conductivity, whereas $[P_{2225}][NF_2]$ has been reported its liquid properties by other groups.[262,263] The trend of the glass transition temperatures was $[P_{222(2O2)}][NF_2] < [P_{2225}][NF_2] < [P_{222(2S2)}][NF_2]$. The melting point was $[P_{222(2O2)}][NF_2] < [P_{2225}][NF_2]$ (As the previous report, $[P_{222(2S2)}][NF_2]$ did not show the melting point.).

Table VI.1. Values of Formula Weight FW, Melting Point T_m, Glass Transition Temperature T_g, and Vogel-Tammann-Fulcher (VTF) Fit Parameters for Phosphonium-Based ILs.

ILs	FW (g mol^{-1})	T_m (K)	T_g (K)	ln(η_0) (ln(cP))	D	T_0 (K)
$[P_{2225}][NF_2]$	369.4	239.5	169.2	−2.728	8.436	134.5
$[P_{222(2O2)}][NF_2]$	371.4	229.0	164.9	−2.157	6.845	135.9
$[P_{222(2S2)}][NF_2]$	387.5	n.o.	177.2	−2.290	7.153	145.0

n.o.: not observed.

The temperature dependence of the viscosities for the three ILs is shown in Figure VI.2a. The values of viscosities are given in Table E1. $[P_{222(2S2)}][NF_2]$ showed the highest viscosity at each temperature, followed by the $[P_{2225}][NF_2]$ and the $[P_{222(2O2)}][NF_2]$. The previous results[47,48,148,264-267] suggest that the viscosity in ILs decreases by substituting an atom of the constituent ion with a heavier atom in the same group. However, the viscosity of $[P_{222(2S2)}][NF_2]$ obtained in this study at 293 K was about 2.6 times higher than that of $[P_{222(2O2)}][NF_2]$. The Vogel-Tammann-Fulcher (VTF) equation[268-271] was often used to characterize the temperature-dependent viscosity in glass-forming liquids and is given as follows:

$$\eta(T) = \eta_0 \exp\left(\frac{DT_0}{T - T_0}\right) \quad \text{(VI-1)}$$

where T is the temperature, η_0 is a reference viscosity at which the exponential term is zero, D is a parameter inversely proportional to the fragility, and T_0 is the characteristic temperature at which viscosity diverges. In VTF plots, the shear viscosity value, 10^{13} cP, at the glass transition temperature is incorporated to obtain VTF parameters.[196] To correctly manage the deviations over several orders of magnitude in η, the logarithmic form of Equation VI-1 was used to fit the data. The fits are shown in Figure VI.2b and the fit parameters are given in Table VI.1.

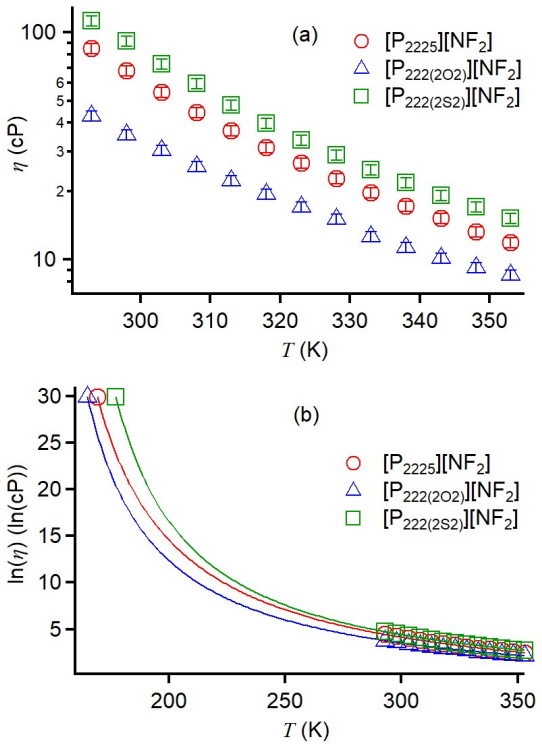

Figure VI.2. (a) Plots of η vs. T and (b) semi-logarithmic plots of η vs. T for $[P_{2225}][NF_2]$ (red circles), $[P_{222(2O2)}][NF_2]$ (blue triangles), and $[P_{222(2S2)}][NF_2]$ (green squares). VTF fits with a η value of 10^{13} cP at T_g are also shown by the respective color solid lines.

The T-dependent density, ρ, of the $[P_{2225}][NF_2]$, $[P_{222(2O2)}][NF_2]$, and $[P_{222(2S2)}][NF_2]$ are shown in Figure VI.3. The values of ρ are summarized in Table E1. Figure VI.3 also exhibits the linear fits, $\rho(T) = c_\rho T + \rho_0$. The linear fit parameters are given in Table E2. Table E2 exhibits that the order of the intercept densities, ρ_0, of the three ILs was $\rho_0([P_{2225}][NF_2]) < \rho_0([P_{222(2O2)}][NF_2]) < \rho_0([P_{222(2S2)}][NF_2])$ and the temperature sensitivities in density, c_ρ, of the three ILs were slightly different: $c_\rho([P_{2225}][NF_2]) < c_\rho([P_{222(2S2)}][NF_2]) < c_\rho([P_{222(2O2)}][NF_2])$.

The molar volume, V_m, estimated from the density values and formula weights of the three ILs at various temperatures. Figure VI.3b plots V_m vs. various temperature and also displays the linear fits, $V_m(T) = c_{Vm}T + V_{m0}$. Table E2 lists the values of V_m and the fit parameters. The trends of V_m and the intercept, V_{m0}, of the three ILs were $V_{m\ or\ m0}([P_{2225}][NF_2]) > V_{m\ or\ m0}([P_{222(2S2)}][NF_2]) > V_{m\ or\ m0}([P_{222(2O2)}][NF_2])$, although the temperature sensitivities in density, c_{Vm}, of the three ILs were slightly different: $c_{Vm}([P_{2225}][NF_2]) > c_{Vm}([P_{222(2O2)}][NF_2]) > c_{Vm}([P_{222(2S2)}][NF_2])$.

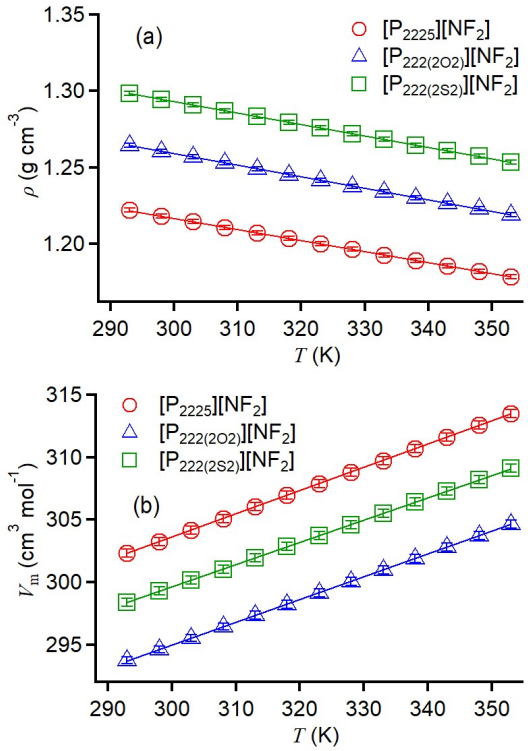

Figure VI.3. Plots of (a) ρ vs. T and (b) V_m vs. T for $[P_{2225}][NF_2]$ (red circles), $[P_{222(2O2)}][NF_2]$ (blue triangles), and $[P_{222(2S2)}][NF_2]$ (green squares). Linear fits are also shown by the solid lines of their respective colors.

The T-dependence of the γ of each IL is shown in Figure VI.4. The γ values are listed in Table E1. Their linear fits, $\gamma(T) = c_\gamma T + \gamma_0$, are also shown in Figure VI.4 and their fit parameters are listed in Table E2. The γ values of the $[P_{2225}][NF_2]$ and $[P_{222(2O2)}][NF_2]$ were similar, but that of the $[P_{222(2S2)}][NF_2]$ was larger than those of the other two ILs. Although the temperature sensitivities of the γ of the three ILs were similar, the $[P_{222(2S2)}][NF_2]$ has a larger surface tension at $T = 0$ K (γ_0) and each temperature than those of the ILs.

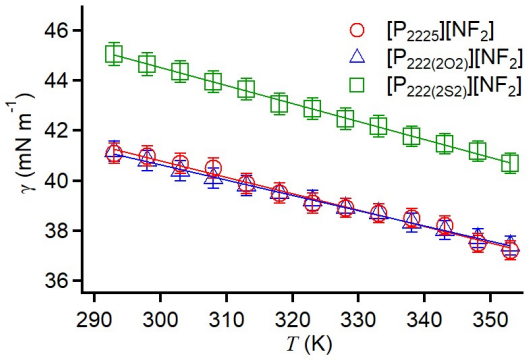

Figure VI.4. Plots of γ vs. T for $[P_{2225}][NF_2]$ (red circles), $[P_{222(2O2)}][NF_2]$ (blue triangles), and $[P_{222(2S2)}][NF_2]$ (green squares). Linear fits are also shown by the solid lines of their respective colors.

The temperature-dependent electrical conductivities, σ, of the $[P_{2225}][NF_2]$, $[P_{222(2O2)}][NF_2]$, and $[P_{222(2S2)}][NF_2]$ are exhibited in Figure VI.5a. The values of σ are summarized in Table E1. Their linear fits, $\sigma(T) = c_\sigma T + \sigma_0$, are also shown in Figure VI.5a. Table E2 lists the fit parameters. As shown in Figure VI.5, the $[P_{222(2O2)}][NF_2]$ had the highest σ, whereas the $[P_{222(2S2)}][NF_2]$ had the lowest σ. Figure VI.5 also demonstrates that the σ of $[P_{222(2O2)}][NF_2]$ was the most temperature-sensitive among the three ILs, and that of $[P_{222(2S2)}][NF_2]$ was the most insensitive.

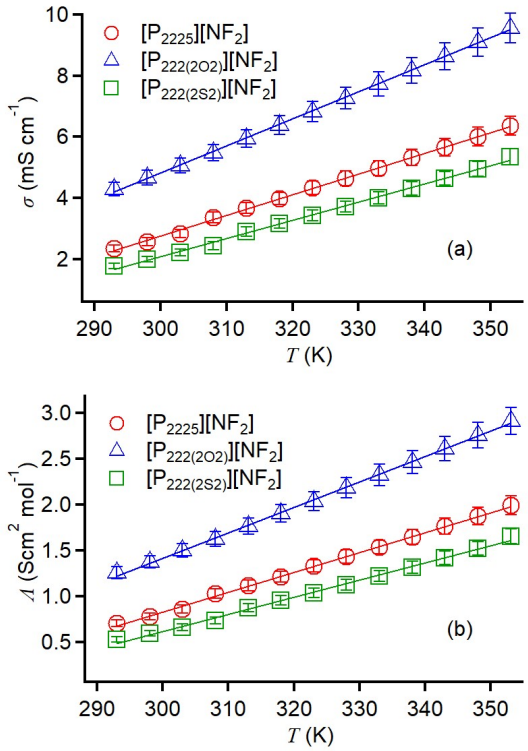

Figure VI.**5.** Plots of (a) σ vs. T and (b) Λ vs. T for $[P_{2225}][NF_2]$ (red circles), $[P_{222(2O2)}][NF_2]$ (blue triangles), and $[P_{222(2S2)}][NF_2]$ (green squares). Linear fits are also shown by the solid lines of their respective colors.

The molar electrical conductivities, Λ, of the $[P_{2225}][NF_2]$, $[P_{222(2O2)}][NF_2]$, and $[P_{222(2S2)}][NF_2]$ at various temperatures are shown in Figure VI.5b, and the values are listed in Table E1. The temperature-dependent Λ is defined as follows:

$$\Lambda(T) = \sigma(T)\mathrm{FW}/\rho(T) \qquad \text{(VI-2)}$$

As shown in Figure VI.5b, the data are fitted by a linear function, $\Lambda(T) = c_\Lambda T + \Lambda_0$. Their parameters are listed in Table E3. As the electrical conductivity, the $[P_{222(2O2)}][NF_2]$ shows the most temperature-sensitive to Λ and $[P_{222(2S2)}][NF_2]$ shows the most temperature-insensitive to Λ.

VI.3.2. Low-Frequency Spectra

VI.3.2.1. fs-RIKES.

Figure VI.6 exhibits the low-frequency RIKES spectra of the $[P_{2225}][NF_2]$, $[P_{222(2O2)}][NF_2]$, and $[P_{222(2S2)}][NF_2]$ at 293 K observed by fs-RIKES. Figure E2 summarizes the normalized Kerr transients before Fourier-transform deconvolution analysis. To concentrate on the intermolecular vibrations, the entire spectra do not include the picosecond relaxation components. The sharp bands observed above 250 cm^{-1} were due to the intramolecular vibrational modes of the ILs and the broad bands below 150 cm^{-1} were essentially attributed by the intermolecular vibrational modes. As shown in Figure VI.6, the line shapes of the three ILs were rectangular triangles with a peak at ~20 cm^{-1}. The rectangular triangle spectral shapes for the ILs were similar to those for nonaromatic cation-based ILs, such as tetraalkylphosphonium-, tetraalkylammonium-, and 1-alkyl-1-methylpyrrolidinium-based ILs, with the anions of $[NF_2]^-$, bis(trifluoromethylsulfonyl)amide, bis(pentafluoroethylsulfonyl)amide, and cyclohexafluoropropane-1,3-bis(sulfonyl)amide.[47,66,71,272-275] A detailed comparison of the spectra for the ILs shows that the $[P_{222(2S2)}][NF_2]$ exhibits slightly higher peak frequency and a broader spectral width than the other two ILs. The $[P_{2225}][NF_2]$ and $[P_{222(2S2)}][NF_2]$ possess the band at ~165 cm^{-1}, while $[P_{222(2O2)}][NF_2]$ has additional bands in the frequency ranging from 110 to 200 cm^{-1}.

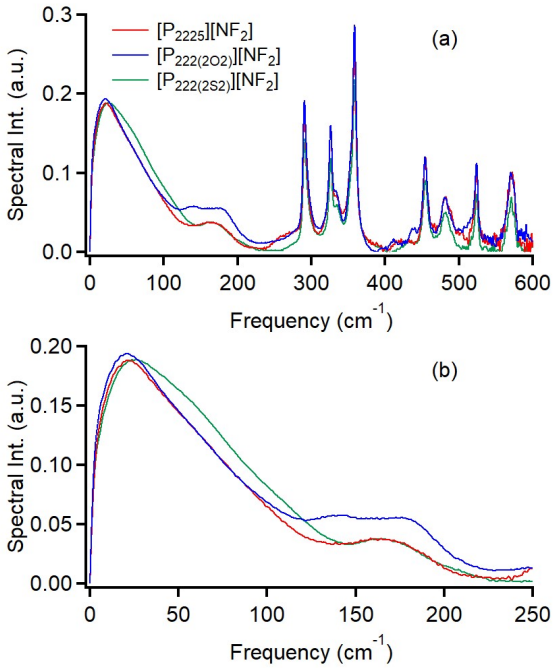

Figure VI.6. Low-frequency RIKES spectra with the frequency ranges of (a) 0–600 cm^{-1} and (b) 0–250 cm^{-1} of $[P_{2225}][NF_2]$, $[P_{222(2O2)}][NF_2]$, and $[P_{222(2S2)}][NF_2]$ at 293 K.

The temperature dependence of the low-frequency RIKES spectra of the $[P_{2225}][NF_2]$, $[P_{222(2O2)}][NF_2]$, and $[P_{222(2S2)}][NF_2]$ are shown in Figure VI.7. With increasing the temperature, the spectral intensity of the three ILs at ~20 cm^{-1} increased and the peak also shifted to the low-frequency side. Such temperature-dependent spectral features were well observed for nonaromatic cation-based ILs, including phosphonium-based ILs.[78,274-276] The temperature dependence of the low-frequency spectra of each liquid/solution containing IL is unique and different from that of the Bose-Einstein thermal occupation factor.[77,275,277]

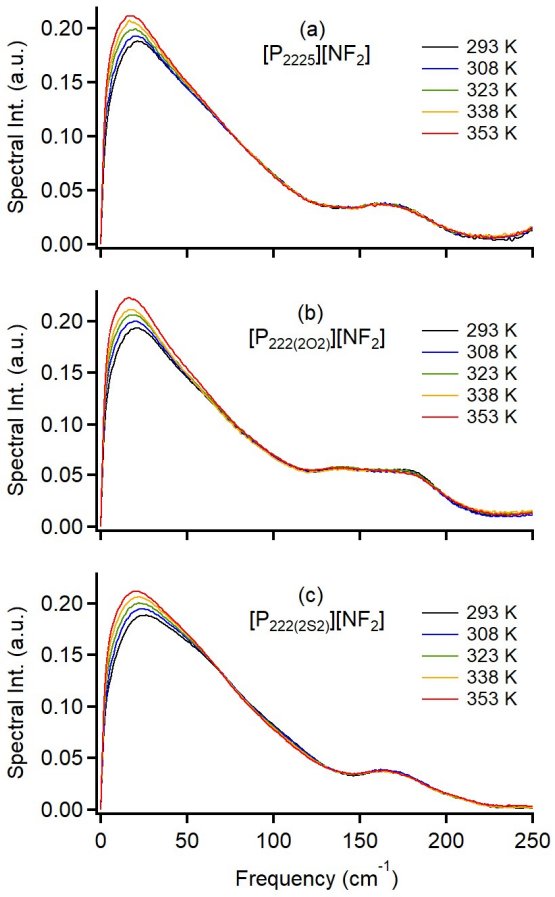

Figure VI.7. Low-frequency RIKES spectra of (a) $[P_{2225}][NF_2]$, (b) $[P_{222(2O2)}][NF_2]$, and (c) $[P_{222(2S2)}][NF_2]$ at 293 K (black lines), 308 K (blue lines), 323 K (green lines), 338 K (orange lines), and 353 K (red lines).

Figure VI.8 shows the plots of the peak frequencies, ν_p, of the spectra for the three ILs as a function of temperature to elucidate the temperature dependence of the low-frequency spectrum semiquantitatively. Figure VI.8 also shows the linear fits and the equations of the

linear fits are shown below: $\nu_p(T) = 43.0 - 0.0723T$ for the $[P_{2225}][NF_2]$; $\nu_p(T) = 42.9 - 0.0745T$ for the $[P_{222(2O2)}][NF_2]$; $\nu_p(T) = 48.8 - 0.0793T$ for the $[P_{222(2S2)}][NF_2]$.

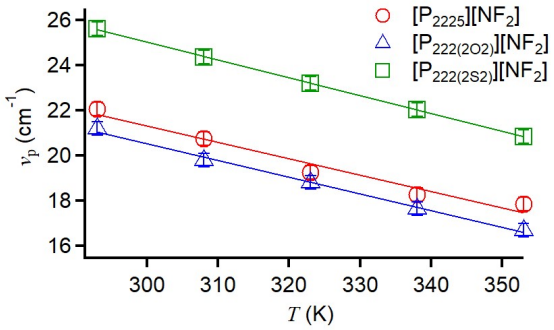

Figure VI.8. Plots of ν_p vs. T for the RIKES spectra of $[P_{2225}][NF_2]$ (red circles), $[P_{222(2O2)}][NF_2]$ (blue triangles), and $[P_{222(2S2)}][NF_2]$ (green squares). Linear fits are also shown by the respective color lines.

VI.3.2.2. THz-TDS.

The low-frequency THz-TDS spectra of the $[P_{2225}][NF_2]$, $[P_{222(2O2)}][NF_2]$, and $[P_{222(2S2)}][NF_2]$ at 293 K are shown in Figure VI.9. This is the first report about the low-frequency absorption spectra of phosphonium-based ILs, while the low-frequency absorption spectra (or THz spectra) of nonaromatic cation-based ILs have been reported so far.[278-283] Notably, the low-frequency absorption spectra of molten salts with the anion of bis(fluorosulfonyl)amide have not been reported, thus far. The peak frequencies of the low-frequency THz-TDS spectra of the $[P_{2225}][NF_2]$, $[P_{222(2O2)}][NF_2]$, and $[P_{222(2S2)}][NF_2]$ were ~70 cm^{-1}. Additionally, the low-frequency THz-TDS spectra of $[P_{222(2O2)}][NF_2]$ possess the broadened band(s) in the frequency range of 110–200 cm^{-1}.

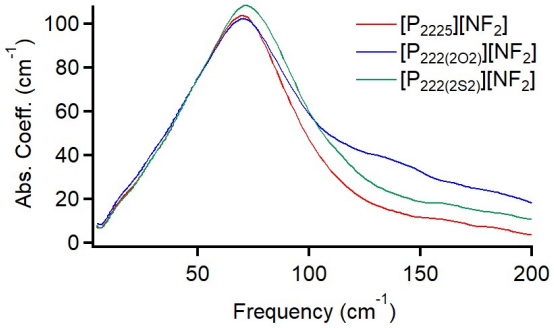

Figure VI.9. Low-frequency THz-TDS spectra of $[P_{2225}][NF_2]$, $[P_{222(2O2)}][NF_2]$, and $[P_{222(2S2)}][NF_2]$ in the frequency ranges of 5–200 cm^{-1} at 293 K.

Figure VI.10 displays the temperature dependence of the low-frequency THz-TDS spectra for $[P_{2225}][NF_2]$, $[P_{222(2O2)}][NF_2]$, and $[P_{222(2S2)}][NF_2]$. The spectral intensity of the three ILs decreased and their peaks shifted to the low-frequency side with increasing temperature.

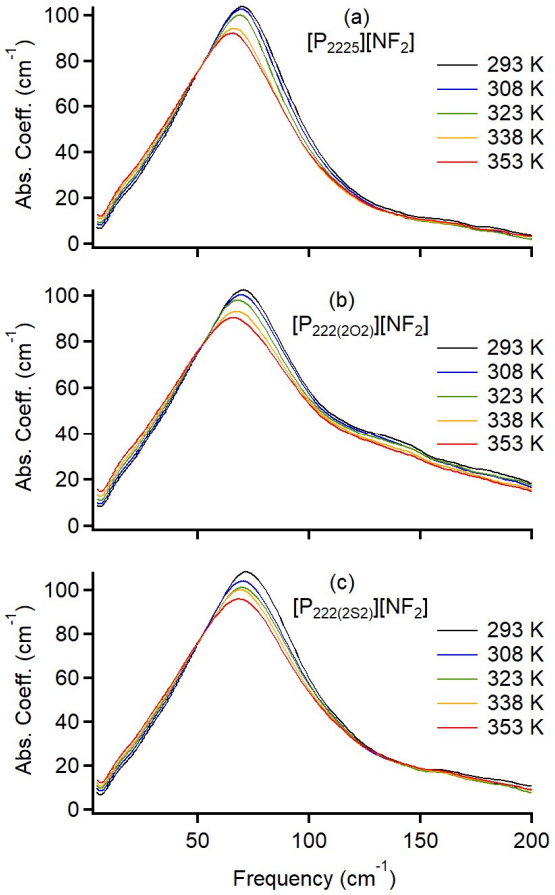

Figure VI.10. Low-frequency THz-TDS spectra of (a) $[P_{2225}][NF_2]$, (b) $[P_{222(2O2)}][NF_2]$, and (c) $[P_{222(2S2)}][NF_2]$ at 293 K (black lines), 308 K (blue lines), 323 K (green lines), 338 K (orange lines), and 353 K (red lines).

Figure VI.11 shows the plots of the peak frequencies, ν_p, for the low-frequency THz-TDS spectra as a function of temperature for the $[P_{2225}][NF_2]$, $[P_{222(2O2)}][NF_2]$, and $[P_{222(2S2)}][NF_2]$. Linear fits also fit these plots as following equations: $\nu_p(T) = 94.4 - 0.0819T$ for the $[P_{2225}][NF_2]$; $\nu_p(T) = 91.8 - 0.0725T$ for the $[P_{222(2O2)}][NF_2]$; $\nu_p(T) = 86.4 - 0.0509T$ for the $[P_{222(2S2)}][NF_2]$.

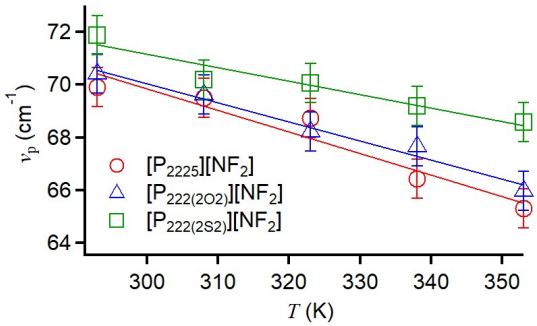

Figure VI.11. Plots of ν_p vs. T for the THz-TDS spectra of $[P_{2225}][NF_2]$ (red circles), $[P_{222(2O2)}][NF_2]$ (blue triangles), and $[P_{222(2S2)}][NF_2]$ (green squares). Linear fits are also shown by their respective color lines.

VI.3.2.3. MD Simulations.

Based on the MD simulations, the low-frequency depolarized Raman spectra (DRS) and absorption spectra (ABS) of $[P_{2225}][NF_2]$ are shown in Figure VI.12. The temperatures of the simulations are at 293 and 353 K. The spectral intensities are normalized with the maximum intensities at 293 K. As shown in Figure VI.12, the line shapes and temperature-dependent features of DRS and ABS are good agreement with those of the low-frequency RIKES and THz-TDS spectra displayed in Figure VI.7 and VI.10.

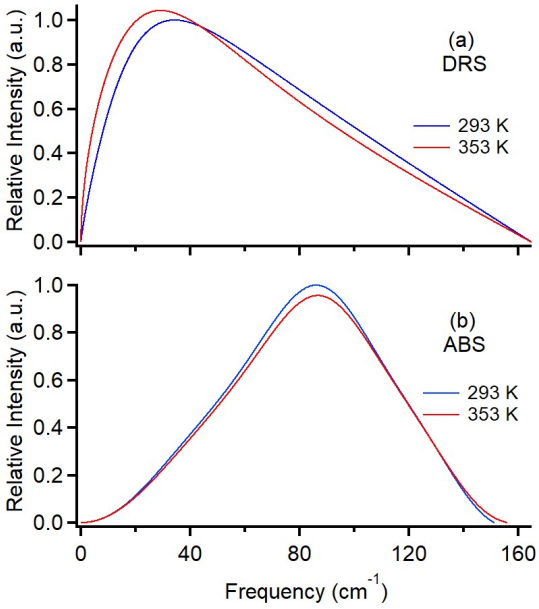

Figure VI.12. Calculated depolarized Raman spectra (DRS) and absorption spectra (ABS) of $[P_{2225}][NF_2]$ at 293 and 353 K based on the MD simulations.

Figure VI.13 exhibits the decomposition analysis results based on the constituent ion species for the low-frequency DRS and ABS of $[P_{2225}][NF_2]$ at 293 K. The analysis result of the calculated DRS shows that the cation, not the anion, mainly contributes to the spectral density. On the other hand, the spectral density of low-frequency ABS is due to both cation and anion equally, and the lineshape of the ABS composition are different from those of the DRS composition. In the DRS at 353K, the cation contribution was smaller and the cross-term one was larger than the DRS at 293K. However, in the ABS at 293K, the contributions of cation, anion, and cross-terms were similar to the ABS at 353K.

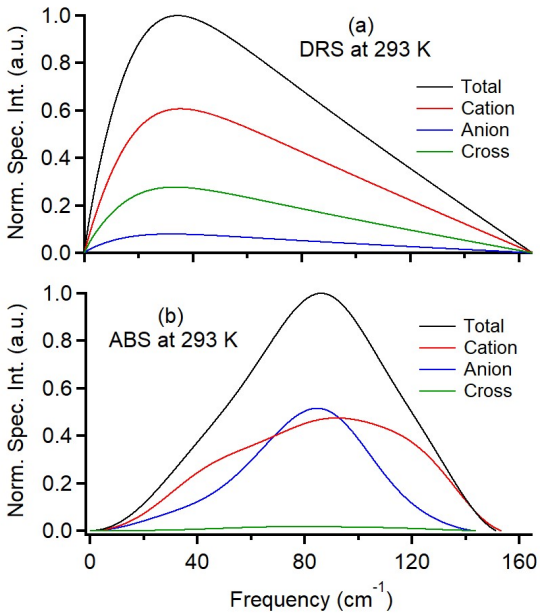

Figure VI.13. Decomposition analysis results of (a) DRS and (b) ABS of $[P_{2225}][NF_2]$ at 293 K. Black lines denote the total spectra, red lines denote the cation spectra, blue lines denote the anion spectra, and green lines denote the cross-term spectra.

Figure VI.14 exhibits the decomposition analysis results based on rotational, translational, and cross-term components for the DRS and ABS of $[P_{2225}][NF_2]$ at 293 K. As shown in Figure VI.14, the DRS lineshape is mainly due to the rotational component, while the ABS lineshape is essentially attributed by the translational component. The DRS and ABS spectra at 353 K also showed similar tendencies (Figure E10).

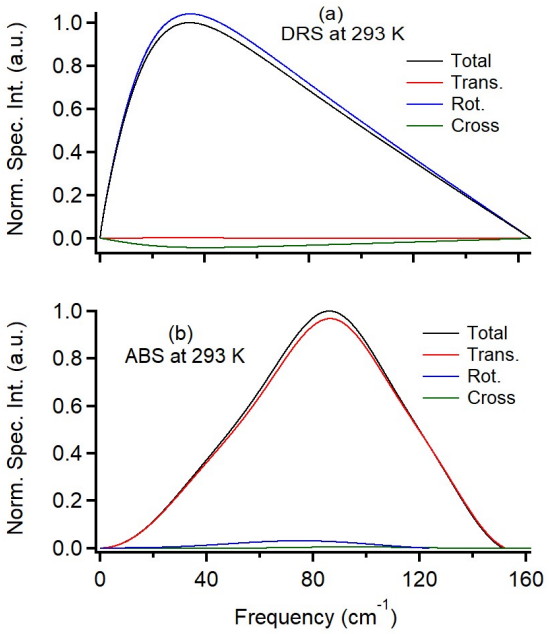

Figure VI.14. Decomposition analysis results of (a) DRS and (b) ABS of $[P_{2225}][NF_2]$ at 293 K. Black lines denote the total spectra; red lines denote the translational component; blue lines denote the rotational component; green lines denote the cross-term component.

VI.3.3. Quantum Chemistry Calculations.

Figure VI.15 shows the quantum chemistry calculations of Raman and IR spectra for $[P_{2225}]^+$, $[P_{222(2O2)}]^+$, $[P_{222(2S2)}]^+$, and $[NF_2]^-$. These calculations are based on the optimized structures calculated by the B3LYP/6-311++G(d,p) level of theory. The atomic coordinates of the stable ions are listed in Table E8. The results of $[NF_2]^-$ showed an intramolecular vibrational band at about 140 cm^{-1}. In the RIKES spectra of all three ILs, these intramolecular vibrational bands were appeared in a band at about 160 cm^{-1}. $[P_{222(2S2)}]^+$ had stronger intramolecular vibrational bands in the calculated Raman- and IR-active normal modes than the other two cations less than 100 cm^{-1}.

Figure E13 exhibited the atom charges of the three cations. In the substitution atoms, the charge magnitude of the O atom is the most negative (−0.077), followed by the S atom (0.000), and the most positive was the C atom (+0.046). And also, the charge magnitude of the P atom in $[P_{222(2S2)}]^+$ is the most positive (−0.321), followed by $[P_{2225}]^+$ (−0.406), and the most negative P atom was in $[P_{222(2O2)}]^+$ (−0.839).

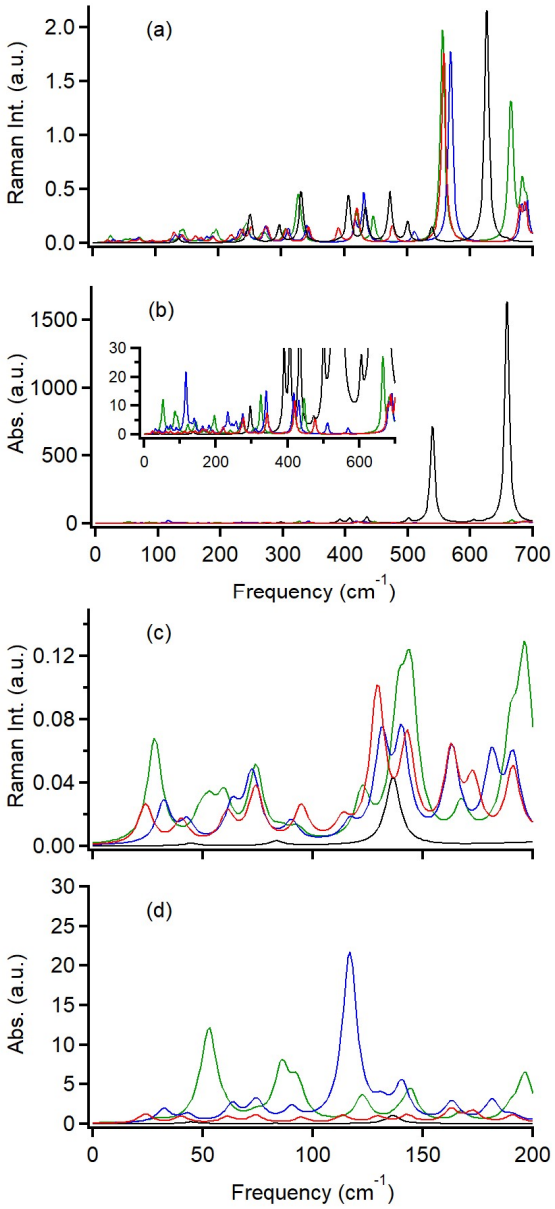

Figure VI.15. Calculated (a) Raman and (b) IR spectra of $[P_{2225}]^+$ (red), $[P_{222(2O2)}]^+$ (blue), $[P_{222(2S2)}]^+$ (green), and $[NF_2]^-$ (black) optimized at B3LYP/6-311++G(d,p) level of theory. Magnifications from 0 to 200 $cm^{-1}$for (c) Raman and (d) IR spectra are also shown.

VI.4. DISCUSSION

VI.4.1. Liquid Properties.

As shown in Table VI.1, the $[P_{222(2O2)}][NF_2]$ had lower melting and glass transition temperatures than the $[P_{2225}][NF_2]$. This is known as the effect of substituting an alkyl group for its equivalent ether group on the transition temperatures of ILs.[47,231,232,237,284,285] The $[P_{222(2S2)}][NF_2]$ had a highest glass transition temperature among the three ILs, while its melting point was not measured in the DSC chart (see Figure E1). Diethyl ether's melting point was higher than diethyl sulfide's (diethyl ether: 157 K, diethyl sulfide: 169 K), although not with the glass transition temperature behavior.[52] This trend was similar to that observed for the glass transition temperatures of $[P_{222(2O2)}][NF_2]$ and $[P_{222(2S2)}][NF_2]$ in this study.

In Figure VI.2, the trend of the viscosities of the three ILs was $[P_{222(2O2)}][NF_2] < [P_{2225}][NF_2] < [P_{222(2S2)}][NF_2]$. Commonly, the viscosity in ILs decreases with the substitution of an alkyl group with a similar ether group.[47,231,232,237,284,285] Therefore, the $[P_{222(2O2)}][NF_2]$ followed this trend. However, the $[P_{222(2S2)}][NF_2]$ showed a highest viscosity among the three ILs. This opposite heavy atom substitution effect is also reported in phosphonium cation-based ILs with a similar anion.[243] When ether groups are substituted with similar thioether groups, the heavy atom substitution effect on IL viscosity is different between aromatic and non-aromatic cationic ILs.[240-243,265,286] For example, the viscosity of 1-ethylthioethyl-3-methylimidazolium bis(trifluoromethylsulfonyl)amide is 40 cP at 284 K, whereas that of 1-ethoxyethyl-3-methylimidazolium bis(trifluoromethylsulfonyl)amide is 48 cP.[242] On the other hand, for nonaromatic cation-based ILs, the viscosity of 1-methylthioethyl-1-methylpyrrolidinium bis(trifluoromethylsulfonyl)amide (222 cP at 296 K)[243] shows higher than that of 1-methoxyethyl-1-methylpyrrolidinium bis(trifluoromethylsulfonyl)amide (63.0 cP at 296 K)[265] and triethylmethylthiomethylphosphonium bis(trifluoromethylsulfonyl)amide is higher viscosity than triethylmethoxymethylphosphonium bis(trifluoromethylsulfonyl)amide.[286] The results of the glass transition temperatures and viscosities of the $[P_{222(2S2)}][NF_2]$ and $[P_{222(2O2)}][NF_2]$ suggest that the $[P_{222(2S2)}][NF_2]$ has less fluidity than the $[P_{222(2O2)}][NF_2]$. Therefore, the high dispersion force of the sulfur influence the IL's fluidity, viscosity, and glass transition temperature more than the oxygen of the side group in the phosphonium cation. As discussed in previous study,[286] the heavy-atom substitution effect on viscosity in phosphonium-based ILs is different from that reported in common imidazolium-based ILs, which is due to the difference in the charged moieties of the cations (quaternary phosphonium versus aromatic imidazolium).

As shown in Table VI.1, the $[P_{222(2O2)}][NF_2]$ had the smallest *D* value and the $[P_{2225}][NF_2]$ had the largest *D* value. The D parameter indicates how far away from Arrhenius behavior the material is; the larger D suggests a more Arrhenius-like behavior, and the material is considered strong. On the other hand, the smaller D suggests a more non-Arrhenius-like behavior, and the substance is considered fragile.[196] Therefore, the $[P_{222(2O2)}][NF_2]$ is the most fragile IL and $[P_{2225}][NF_2]$ is the strongest IL among the three IL. Comparing the VTF parameter D of the ether and alkyl groups in IL cations,[47] the ether-substituted ILs have smaller D values than the comparable alkyl-substituted ILs in the ammonium and phosphonium systems. Furthermore, this study finds that the thioether group in the phosphonium-based IL provides a stronger liquid than the respective ether group but is more fragile than the analog alkyl group.

Density and molar volume orders were similar for the three ILs. However, the surface tension showed characteristic results (see Figure VI.4 and Table E1). First, the values of the surface tensions for the $[P_{2225}][NF_2]$ and $[P_{222(2O2)}][NF_2]$ were almost the same. In the previous report, (2-ethoxyethoxy)ethyltriethylphosphonium bis(trifluoromethylsulfonyl)amide showed higher surface tension (35.0 mN m^{-1}) than triethyloctylphosphonium bis(trifluorometylsulfonyl)amide (32.7 mN m^{-1}).[47] This trend is also confirmed in the respective ammonium-based ILs.[47] The pentyl group (and ethoxyethyl group) in this study is shorter than the octyl group (and (2-ethoxyethoxy)ethyl group), and thus the pentyl group may not be long enough to align the groups at the liquid surface, like surfactants. This short alkyl group might cause the surface tension to decrease. Conversely, the $[P_{222(2S2)}][NF_2]$ had a larger surface tension than the $[P_{2225}][NF_2]$ and $[P_{222(2O2)}][NF_2]$. This implies that the surface structure of $[P_{222(2S2)}][NF_2]$ is different from those of $[P_{2225}][NF_2]$ and $[P_{222(2O2)}][NF_2]$ and/or the intermolecular force of the $[P_{222(2S2)}][NF_2]$ in the surface is higher than those of the $[P_{2225}][NF_2]$ and $[P_{222(2O2)}][NF_2]$.

Figure VI.5 shows that the $[P_{222(2O2)}][NF_2]$ has the highest electrical conductivity among the three ILs. In order to elucidate the effects of the functional groups and temperature on the molar electrical conductivity, Figure VI.16 exhibits the logarithmic plots of Λ vs. η^{-1} for the three ILs. The molar electrical conductivity value increased with increasing temperature, but the plots of the ILs moved away from the ideal condition. Figure VI.16 also shows that the $[P_{222(2O2)}][NF_2]$ was closest to the ideal liquid, while the $[P_{2225}][NF_2]$ was slightly more ideal than the $[P_{222(2S2)}][NF_2]$. Since the molar conductivity takes into account the effect of ionic concentration, $[P_{222(2O2)}][NF_2]$ showed the highest conductivity among the three ILs.

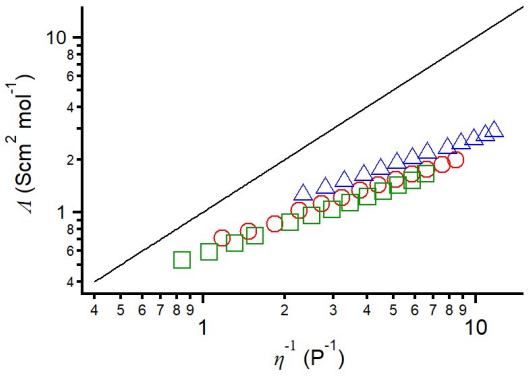

Figure VI.16. Logarithmic plots of Λ vs. η^{-1} for the $[P_{2225}][NF_2]$ (red circles), $[P_{222(2O2)}][NF_2]$ (blue triangles), and $[P_{222(2S2)}][NF_2]$ (green squares). The black line denotes the ideal Walden line with a unity slope.

VI.4.2. Low-Frequency Spectra.

VI.4.2.1. Difference between RIKES and THz-TDS Spectra.

As seen in Figure VI.6 and VI.8, the line shapes of the low-frequency RIKES and THz-TDS spectra of the ILs were significantly different. The low-frequency RIKES spectra showed rectangular triangle shapes, while the THz-TDS spectra exhibited isosceles triangle shapes. The MD simulations, shown in Figure VI.12, reproduced the line shapes of the fs-RIKES and THz-TDS spectra of $[P_{2225}][NF_2]$ very well. Additionally, MD simulation analysis of the low-frequency spectrum of $[P_{2225}][NF_2]$ resolved into cation and anion species indicates that the RIKES spectrum of $[P_{2225}][NF_2]$ is derived from cation and cross-term motions. On the other hand, MD simulation showed that the spectral density of the THz-TDS spectrum includes both cation and anion motions, especially the peaks with isosceles triangle spectral shapes, suggesting that they are basically derived from anion motions. Comparison with the VDOS spectra in Figure E12 shows that the lower frequency (<~60 cm-1) vibrational states are more depolarized Raman active, while the higher frequency (>~60 cm-1) vibrational states are more IR active.

Previously studies have reported a unique rectangular triangle line shape of using fs-RIKES for the low-frequency spectra of most ILs (for both nonaromatic and aromatic cation-based ILs) with the anions of bis(perfluoroalkylsulfonyl)amides and $[NF_2]^-$.[41,77,272,275] Since this rectangular triangle spectral shapes were characteristic of ILs with the anions, the line shape of the low-frequency RIKES spectrum in ILs was thought to be due to anions. However, as shown in Figure VI.13, the MD simulation in our study suggests different interpretation: The rectangular triangle shape of the spectrum is mainly due to the cation and cross-term. This

implies that the cross-term (a type of coupling contribution between cation and anion) is not small in DRS, which means that anions may contribute to the spectral density by coupling with the motion of cations. Furthermore, it may seem surprising that the anions contribute significantly to the low-frequency spectra in the ABS. Since the polarizability anisotropy of the stable structure of $[NF_2]^-$ based on the B3LYP/6-311++G(d,p) level theory is insignificant as shown in Table E9, it is unlikely that the anions contribute only to the spectral density. Figure VI.13 also shows that the contribution of the cross-term is very little.

A similar anion, bis(trifluoromethylsulfonyl)amide, has two stable conformers, transoide and cisoide.[287-290] The transoide of bis(trifluoromethylsulfonyl)amide has a much smaller dipole moment than the cisoide.[288,290] In the Raman spectra, including RIKES spectra, the Raman active bands of each conformer appear in the frequency range of 250-380 cm^{-1}. When $[NF_2]^-$ anion have two stable conformers, such as the bis(trifluoromethylsulfonyl)amide anion, the cisoid form is expected to affect the IR spectrum due to its larger dipole moment than the transoid form. Thus, the characteristic spectral line shape of the THz-TDS spectra of ILs observed in this study is mainly derived from the motions for the cisoid form of the anion.

As shown in Figure VI.14, the MD simulation results indicate that the DRS of $[P_{2225}][NF_2]$ is derived from the rotational and vibrational motions, while the THz-TDS spectrum is due to the translational motion. Therefore, the difference in the line shapes of the low-frequency RIKES and THz-TDS spectra in $[P_{2225}][NF_2]$ is derived from the difference in the type of the molecular motion: fs-RIKES and THz-TDS capture mainly orientational and translational vibration motion, respectively. Since there were no significant differences in the spectral shapes of the three ILs studied in this study, I believe that this spectral assignment is also applicable to the experimental spectra of $[P_{222(2O2)}][NF_2]$ and $[P_{222(2S2)}][NF_2]$.

VI.4.2.2. Comparison between $[P_{2225}][NF_2]$, $[P_{222(2O2)}][NF_2]$, and $[P_{222(2S2)}][NF_2]$.

Figure VI.6b showed that the line shapes of the low-frequency RIKES spectra of the three ILs were rectangular triangles and they were somewhat similar. In three respects, however, the low-frequency RIKES spectral shapes of the three ILs differed. First, the peaks of the low-frequency RIKES spectra of the $[P_{222(2S2)}][NF_2]$ shifted to a higher frequency side than those of the $[P_{2225}][NF_2]$ and $[P_{222(2O2)}][NF_2]$. Second, the low-frequency band less than 150 cm^{-1} of the $[P_{222(2S2)}][NF_2]$ was slightly broader than those of the $[P_{2225}][NF_2]$ and $[P_{222(2O2)}][NF_2]$. Third, the $[P_{222(2O2)}][NF_2]$ had an extra band in the frequency range of 120–200 cm^{-1} unlike the $[P_{2225}][NF_2]$ and $[P_{222(2O2)}][NF_2]$. Even though the entire line shapes of the THz-TDS spectra

were completely different from the RIKES spectra, similar differences were observed in the low-frequency THz-TDS spectra of the three ILs (see Figure VI.8).

If the reduced mass of harmonic oscillator is constant, a higher frequency of harmonic oscillator indicates a stronger force constant. In the same way, the frequency of intermolecular vibrations in the condensed phase should be sensitive to parameters related to microscopic intermolecular force and a mass-related parameter. The center frequency of the broadened low-frequency band in nonprotic molecular liquids is linearly proportional to the square root of the surface tension divided by the density ($\sqrt{\gamma/\rho}$).[133] Aromatic and nonaromatic cation-based ILs also show such relationship.[41,272] Since both the density and formula weight of $[P_{222(2S2)}][NF_2]$ are larger than $[P_{2225}][NF_2]$ and $[P_{222(2O2)}][NF_2]$ (Table VI.1), the higher frequency of the low frequency spectral peak of $[P_{222(2S2)}][NF_2]$ compared to $[P_{2225}][NF_2]$ and $[P_{222(2O2)}][NF_2]$ indicates that $[P_{222(2S2)}][NF_2]$ has stronger intermolecular forces.

There are some possibilities as to why $[P_{222(2S2)}][NF_2]$ shows a broader spectrum than $[P_{2225}][NF_2]$ and $[P_{222(2O2)}][NF_2]$. In many cases, the spectral width is discussed with a focus on the liquid structure. Castner and co-workers investigated the liquid structures of phosphonium-based ILs with the octyl and (2-ethoxyethoxy)ethyl groups by X-ray scattering and MD simulations.[239] They reported that the IL with the octyl group showed a prepeak, which was derived from a microsegregation structure due to amphiphilicity of the cation, between 3 and 4 nm^{-1}, but the IL with the ether group did not show the prepeak. Therefore, their results suggest that the ether group, which has high polarity, homogenized the microscopic structure of the IL. However, the polarity of the ethylthioethyl group is in between the pentyl and ethoxyethyl groups. Thus, the reason why the spectrum of $[P_{222(2S2)}][NF_2]$ is broader than that of the other two ILs does not seem to result from differences in the liquid structure.

Another possibility is homogeneous broadening of the spectrum. In other words, the intermolecular vibrational lifetime of $[P_{222(2S2)}][NF_2]$ could be shorter than those of $[P_{2225}][NF_2]$ or $[P_{222(2O2)}][NF_2]$. Furthermore, another possibility is the influence of intramolecular vibrational bands. Quantum chemical calculations show that there are several Raman and IR-active normal modes in the frequency range of 50-100 cm^{-1} for the structure of $[P_{222(2S2)}]^+$ optimized by the B3LYP/6-311++G(d,p) level theory (see Figure VI.15). Therefore, the intramolecular vibrational bands in the spectrum of $[P_{222(2S2)}][NF_2]$ may broaden its spectral bands.

Additionally, quantum chemical calculations showed that the extra band of $[P_{222(2O2)}][NF_2]$ in the frequency region of 120-200 cm^{-1}, which the other two ILs did not have,

was derived from the intramolecular vibrational bands of the cation (see Figure VI.15). In particular, the ether group, like the alkyl and thioether groups, can take several conformations, indicating the presence of diverse intramolecular vibrational modes in the low-frequency spectrum.[210] Therefore, as in the case of $[P_{222(2O2)}][NF_2]$, the broadened band feature can be attributed to several conformers.

VI.4.2.3. Temperature-Dependent Spectral Features.

The characteristics of the temperature dependence of the low-frequency spectrum differed between fs-RIKES and THz-TDS as shown in Figure VI.7 and VI.9. As increasing temperature, the spectral intensity of the low-frequency spectrum in the RIKES spectrum increased, while that in the THz-TDS spectrum decreased. The MD simulations also reproduced the temperature-dependent trends of the low-frequency spectra using fs-RIKES and THz-TDS as shown in Figure VI.10. The THz-TDS spectra show the vibrational transitions (absorption) from a lower state to a higher one. Thus, as the temperature increases, the spectral intensity of the THz-TDS spectra decreases due to a change in the density of states as the population of the higher states increases. In fs-RIKES, unlike conventional steady-state Raman spectroscopy, both the Stokes and anti-Stokes processes are detected simultaneously. Thus, the cause of the temperature dependence in the RIKES spectra is not the same as those in the THz-TDS spectra. Previously, the temperature dependence of the RIKES spectra was mainly derived from the activation of intermolecular vibrational motions, such as collision-induced motions, by increased temperature.[276] The results of VDOS spectra from MD simulations (Figure E12) confirm this interpretation.

On the other hand, the peak frequencies of the RIKES and THz-TDS low-frequency spectra were both red-shifted with increasing temperature. These shifts could have several causes. The first is a weakening of intermolecular interactions in liquids. The second is an increase in anharmonic properties. The third is a slowing down of the intermolecular vibrational period due to the increase in the magnitude of the intermolecular vibrations caused by the increase in free volume. The other possibility is motional narrowing, but in the present IL, there was almost no change in the spectral width of the low-frequency spectra in fs-RIKES (see Figure VI.7).

The fs-RIKES results showed that the temperature sensitivity of the peak frequency in the low-frequency spectrum was comparable for the three ILs. However, THz-TDS results showed that $[P_{222(2S2)}][NF_2]$ was slightly less temperature sensitive than $[P_{2225}][NF_2]$ and $[P_{222(2O2)}][NF_2]$. Since the temperature sensitivity of the densities and surface tensions of the

three ILs was similar (see Table E2), the smaller temperature sensitivity of the spectrum of $[P_{222(2S2)}][NF_2]$ could be derived from the experimental error or the lower temperature sensitivity of the intramolecular vibrational mode in the $[P_{222(2S2)}]^+$ cation.

VI.5. CONCLUSIONS

In this chapter, I studied the physical properties of $[P_{2225}][NF_2]$, $[P_{222(2O2)}][NF_2]$, and $[P_{222(2S2)}][NF_2]$ ILs, including glass transition temperature, melting point, viscosity, density, surface tension, electrical conductivity, and low-frequency spectra using fs-RIKES and THz-TDS. In order to understand the low-frequency spectra of ILs in detail, MD simulations and quantum chemical calculations were also performed. The liquid properties of the three ILs were found to show the following magnitude relations.

(i) Glass transition temperature, T_g: $[P_{222(2S2)}][NF_2] > [P_{2225}][NF_2] > [P_{222(2O2)}][NF_2]$.

(ii) Viscosity, η: $[P_{222(2S2)}][NF_2] > [P_{2225}][NF_2] > [P_{222(2O2)}][NF_2]$.

(iii) Fragility parameter, D^{-1}: $[P_{222(2O2)}][NF_2] > [P_{222(2S2)}][NF_2] > [P_{2225}][NF_2]$.

(iv) Density, ρ: $[P_{222(2S2)}][NF_2] > [P_{222(2O2)}][NF_2] > [P_{2225}][NF_2]$.

(v) Surface tension, γ: $[P_{222(2S2)}][NF_2] > [P_{2225}][NF_2] \sim [P_{222(2O2)}][NF_2]$.

(vi) Electrical conductivity, σ: $[P_{222(2O2)}][NF_2] > [P_{2225}][NF_2] > [P_{222(2S2)}][NF_2]$.

In the low-frequency spectra of the three ILs, the line shapes of the spectra obtained by fs-RIKES and THz-TDS were very different, with the RIKES spectra being a rectangular triangle with a peak at ~20 cm^{-1} and the THz-TDS spectra being an isosceles triangle with a peak at ~70 cm^{-1}. The MD simulations were able to accurately reproduce these line shapes of the RIKES and THz-TDS spectra for $[P_{2225}][NF_2]$. The rectangular triangle observed in the RIKES spectrum are mainly attributed to the cation and cross-term contributions and the isosceles triangle obtained in the THz-TDS spectrum were mainly due to the anion and cation contributions.

Furthermore, the spectral decomposition analysis based on the motion types indicated that the RIKES spectrum was primarily attributed to the rotational motions, while the THz-TDS spectrum is mainly due to translational motions. These results clearly suggest that the combination of fs-RIKES and THz-TDS is very useful in revealing molecular motions in the low-frequency spectrum of ILs, complementary.

The low-frequency spectra of the three ILs, $[P_{2225}][NF_2]$, $[P_{222(2O2)}][NF_2]$, and $[P_{222(2S2)}][NF_2]$, were similar overall, but there were slight differences in both fs-RIKES and THz-TDS. $[P_{222(2S2)}][NF_2]$ showed that the peak frequencies of the low-frequency RIKES and THz-TDS spectra shifted to a higher frequency side than the other two ILs. This shift indicates that $[P_{222(2S2)}][NF_2]$ exhibits the strongest intermolecular interactions among the three ILs. The spectral width of the $[P_{222(2S2)}][NF_2]$ was also broader than those of the other two ILs. This is derived from the faster dephasing of the intermolecular vibrations or the intramolecular

vibrations of the cation. $[P_{222(2O2)}][NF_2]$ showed extra bands in the frequency range 110-200 cm^{-1}, while $[P_{2225}]$[NF2] and $[P_{222(2S2)}][NF_2]$ showed only a single band at ~165 cm^{-1}. The extra band in $[P_{222(2O2)}][NF_2]$ was due to the intramolecular vibrational bands of the cation.

Chapter VII.

Summary

In this thesis, I investigated the low-frequency spectra of various IL and IL mixtures to understand the intermolecular interactions of ILs, which are not straightforward due to the microscopic heterogeneity of ILs. The four themes discussed in this thesis are listed below: (Chapter III) the effect of the common solvent MLs on the intermolecular vibrations of IL, (Chapter IV) the effect of the hydrogen bonding of MLs on the intermolecular vibrations of IL, (Chapter V) the effect of the polymer on the intermolecular vibrations of IL, and (Chapter VI) the temperature dependence of the low-frequency spectra of phosphonium bis(fluorosulfonyl)amide ILs with pentyl, ethoxyethyl, or 2-(ethylthio)ethyl group. The studies in Chapters III to V are on IL mixtures, and that in Chapter VI is on the heavy atom substitution effects in phosphonium-based ILs. Additionally, in Chapter VI, I discussed the benefits of using fs-RIKES and THz-TDS to discuss multiple approaches in IL study.

In Chapter III, I investigated the low-frequency spectra of the [MOIm][BF_4] mixtures with MeOH, MeCN, and DMSO. With increasing ML concentration, the line shape of the low-frequency spectra gradually changed from neat [MOIm][BF_4] to each ML. However, the M_1 of the low-frequency spectra, which is related to the intermolecular vibrations, is almost constant in all systems less than X_{ML} = 0.6. Then, the M_1 changed mildly in X_{ML} = 0.6–0.9 and dramatically in X_{ML} = 0.9–1. These spectral and M_1 changes are intermediate between the previous H_2O and benzene results. Given the results of MD simulations and quantum chemical calculations, these low-frequency spectral results indicate that the ML molecules localize in the interface between the ionic and alkyl group (non-polar) regions, but the number of ML molecules is not sufficient to make an ML network or bulk region in X_{ML} = 0–0.6. Therefore, the values of M_1 did not change in the low ML concentration. The obtained results also indicate that ML molecules begin to form ML networks or bulk regions in X_{ML} = 0.6–0.9, affecting the intermolecular vibrations, while the constituent ionic species of [MOIm][BF_4] are dispersed in the ML more than X_{ML} = 0.9.

Next, I investigated the intermolecular vibrations of the [MOIm][BF_4] mixtures with FA, NMF, and DMF in Chapter IV. The line shape of the low-frequency spectra of neat FA and NMF are more structured than that of neat DMF due to the hydrogen-bonding network of FA and NMF. The M_1 of the low-frequency spectra of the [MOIm][BF_4]/FA and [MOIm][BF_4]/DMF gradually varied with increasing X_{ML}, while that of the [MOIm][BF_4]/NMF was almost constant in $X_{NMF} \leq 0.7$ and gradually increases in $X_{NMF} \geq 0.7$. When the contribution of the 2D hydrogen-bonding network of FA is removed from the [MOIm][BF_4]/FA mixture spectra, both the [MOIm][BF_4]/FA and [MOIm][BF_4]/NMF systems show almost constant in $X_{ML} < 0.7$ and a drastic increase in $X_{ML} \geq 0.7$ for the normalized M_1. The results of FT-IR

suggested that imidazolium ring C-H of [MOIm][BF_4] mainly interacts with the amide C=O of amides. ^{19}F NMR of $[BF_4]^-$ exhibited that the [MOIm][BF_4]/NMF and [MOIm][BF_4]/DMF showed an up-field shift of the F atoms of the anion with increasing X_{ML}, while the [MOIm][BF_4]/FA exhibited a down-field shift. Considering the results of quantum chemistry calculations, in [MOIm][BF_4]/FA and [MOIm][BF_4]/DMF, the observed chemical shifts were mainly attributed to the many-body interactions of ions and amides, while, in [MOIm][BF_4]/NMF, the high dielectric constant of NMFs increases the distance between cations and anions, which results in an up-field shift.

In addition, I measured the low-frequency spectra of [MOIm][BF_4]/PEG400 mixtures Chapter V. The values of the M_1 for the low-frequency spectra increased slightly with increasing PEG400 concentration, suggesting a slight enhancement of microscopic intermolecular interactions in the mixtures. I also compared the [MOIm][BF_4] mixtures with EG, PEG400, and PEG4000. Although the low-frequency spectra of the samples at the same concentrations were almost similar, normalized low-frequency spectra indicated that the spectral intensity of the [MOIm][BF_4] mixture with PEG400 and PEG4000 was slightly lower than that with EG in the low-frequency region below about 50 cm^{-1}. These results implied that the effect of the polymer is small, but the polymer can suppress the translational motion of [MOIm][BF_4] molecule due to the greater mass of PEG than EG. In addition, the Walden plots evaluating the electrical conductivity showed that the [MOIm][BF_4]/PEG4000 exhibited more ideal electrical conductivity than the [MOIm][BF_4]/PEG400 and [MOIm][BF_4]/EG. The results of the Walden plots suggest that the addition of polymer can potentially enhance the electrical conductivity of ILs.

Finally, in Chapter VI, the temperature dependence of the low-frequency spectra of [P_{2225}][NF_2], [$P_{222(2O2)}$][NF_2], and [$P_{222(2S2)}$][NF_2] were discussed. [$P_{222(2S2)}$][NF_2], which has a higher viscosity than the others, has the highest frequency peak and broadest band among the three ILs. These spectral features suggested that the intermolecular interaction of [$P_{222(2S2)}$][NF_2] is stronger than the other ILs. The MD simulations of the low-frequency spectrum of [P_{2225}][NF_2] reproduced the line shape of the experimental spectrum, and the decomposition analysis of the MD simulations showed that the RIKES spectrum is mainly due to cation and cross-terms and their rotational motion, while the THz-TDS spectrum is mainly due to anion and its translational motion. Therefore, these results clearly showed that the combination of fs-RIKES and THz-TDS is a very useful tool in multicomponent systems such as ILs and IL mixtures.

References

(1) Welton, T. *Chem. Rev.* **1999**, *99* (8), 2071.

(2) Wilkes, J. S. *Green Chemistry* **2002**, *4* (2), 73.

(3) Rogers, R. D. S., K. R. *Science* **2003**, *302* (5646), 792.

(4) Wasserscheid, P.; Welton, T. Ionic Liquids in Synthesis. 2 ed.; Wiley-VCH: Weinheim, 2008.

(5) Hallett, J. P.; Welton, T. *Chem. Rev.* **2011**, *111* (5), 3508.

(6) Wasserscheid, P.; Keim, W. *Angewandte Chemie-International Edition* **2000**, *39* (21), 3773.

(7) Holbrey, J. S., K. *Clean Products and Processes* **1999**, *1*, 223.

(8) Welton, T. *Biophysical Reviews* **2018**, *10*, 691.

(9) Huddleston, J. G.; Willauer, H. D.; Swatloski, R. P.; Visser, A. E.; Rogers, R. D. *Chemical Communications* **1998**, (16), 1765.

(10) Walden, P. *Bull. Acad. Imper. Sci. (St. Petersburg)* **1914**, 405.

(11) Hurley, F. H. W., T. P. *Journal of The Electrochemical Society* **1951**, *98* (5), 203.

(12) Chum, H. L. K., V. R.; Miller, L. L.; Osteryoung R. A. *J. Am. Chem. Soc.* **1975**, *97* (11), 3264.

(13) Ford, W. T. H., R. J.; Hart, D. J. *The Journal of Organic Chemistry* **1973**, *38* (22), 3916.

(14) Robinson, J. O., R. A. *J. Am. Chem. Soc.* **1979**, *101* (2), 323.

(15) Gale, R. J. O., R. A. *Journal of the Electrochemical Society* **1980**, *127* (10), 2167.

(16) Wilkes, J. S. L., J. A.; Wilson, R. A.; Hussey, C. L. *Inorganic Chemistry* **1982**, *21* (3), 1263.

(17) Wilkes, J. S.; Zaworotko, M. J. *Journal of the Chemical Society, Chemical Communications* **1992**, (13), 965.

(18) Seddon, K. R. *Journal of Chemical Technology and Biotechnology* **1997**, *68* (4), 351.

(19) Earle, M. J.; Esperanca, J. M. S. S.; Gilea, M. A.; Lopes, J. N. C.; Rebelo, L. P. N.; Magee, J. W.; Seddon, K. R.; Widegren, J. A. *Nature* **2006**, *439*, 831.

(20) Armstrong, J. P. H., C.; Jones, R. G.; Licence, P.; Lovelock, K. R.; Satterley, C. J.; Villar-Garcia, I. J. *Phys. Chem. Chem. Phys.* **2007**, *9* (8), 982.

(21) Hagiwara, R. L., J. S. *Electrochemistry* **2007**, *75* (1), 23.

(22) Sato, T. M., G.; Takagi, K. *Electrochimica Acta* **2004**, *49* (21), 3603.

(23) Lockett, V. S., R.; Ralston, J.; Horne, M.; Rodopoulos, T. *The Journal of Physical Chemistry C* **2008**, *112* (19), 7486.

(24) Hess, S. W.-M., M.; Wachtler, M. *Journal of The Electrochemical Society* **2015**, *164*, A3084.

(25) Giffin, G. A. *Journal of Materials Chemistry A* **2016**, *4* (35), 13378.

(26) Yang, Q. Z., Z.; Sun, X. G.; Hu, Y. S.; Xing, H.; Dai, S. *Chem. Soc. Rev.* **2018**, *47* (6), 2020.

(27) Sun, H. Z., G.; Xu, X; et al. *Nature Communications* **2019**, *10*, 3302.

(28) Lopes, J. N. A. C.; Padua, A. A. H. *J. Phys. Chem. B* **2006**, *110* (7), 3330.

(29) Triolo, A.; Russina, O.; Bleif, H.-J.; Di Cola, E. *J. Phys. Chem. B* **2007**, *111* (18), 4641.

(30) Anthony, J. L. A., J. L.; Maginn, E. J.; Brennecke, J. F. *J. Phys. Chem. B* **2005**, *109* (13),

6366.
(31) Cadena, C.; Anthony, J. L.; Shah, J. K.; Morrow, T. I.; Brennecke, J. F.; Maginn, E. J. *J. Am. Chem. Soc.* **2004**, *126* (16), 5300.
(32) Lei, Z. D., C.; Chen, B. *Chem. Rev.* **2014**, *114* (2), 1289.
(33) Seddon, K. R.; Stark, A.; Torres, M. J. *Pure and Applied Chemistry* **2000**, *72* (12), 2275.
(34) Marsh, K. N., Boxall, J. A., & Lichtenthaler, R. *Fluid Ph. Equilibria* **2004**, *219* (1), 93.
(35) Abbott, A. P. M., K. J. *Phys. Chem. Chem. Phys.* **2006**, *8* (37), 4265.
(36) Poole, C. F. P., S. K. *Journal of Chromatography A* **2010**, *1217* (16), 2268.
(37) Zhao, H. X., S.; Ma, P. *Journal of Chemical Technology & Biotechnology: International Research in Process, Environmental & Clean Technology* **2005**, *80* (10), 1089.
(38) Zhao, H.; Malhotra, S. V. *Aldrichimica Acta* **2002**, *35* (3), 75.
(39) Sheldon, R. *Chemical Communications* **2001**, *23*, 2399.
(40) Ahosseini, A. S., A. M. *International Journal of Thermophysics* **2008**, *29* (4), 1222.
(41) Shirota, H.; Kakinuma, S.; Takahashi, K.; Tago, A.; Jeong, H.; Fujisawa, T. *Bull. Chem. Soc. Jpn.* **2016**, *89* (9), 1106.
(42) Shirota, H.; Ando, M.; Kakinuma, S.; Takahashi, K. *Bulletin of the Chemical Society of Japan* **2020**, *93* (12), 1520.
(43) Tokuda, H.; Hayamizu, K.; Ishii, K.; Abu Bin Hasan Susan, M.; Watanabe, M. *J. Phys. Chem. B* **2004**, *108* (42), 16593.
(44) Seki, S. K., T.; Kobayashi, Y.; Takei, K.; Miyashiro, H.; Hayamizu, K.; Seiji, T.; Mitsygi, T.; Umebayashi, Y. *J. Mol. Liq.* **2010**, *152* (1-3), 9.
(45) Seddon, K. R.; Stark, A.; Torres, M. J. *ACS Symp. Ser.* **2002**, *819*, 34.
(46) Tokuda, H.; Hayamizu, K.; Ishii, K.; Susan, M.; Watanabe, M. *J. Phys. Chem. B* **2005**, *109* (13), 6103.
(47) Shirota, H.; Fukazawa, H.; Fujisawa, T.; Wishart, J. F. *J. Phys. Chem. B* **2010**, *114* (29), 9400.
(48) Shirota, H.; Castner, E. W., Jr. *J. Phys. Chem. B* **2005**, *109* (46), 21576.
(49) Shirota, H.; Wishart, J. F.; Castner, E. W., Jr. *J. Phys. Chem. B* **2007**, *111* (18), 4819.
(50) Shirota, H.; Nishikawa, K.; Ishida, T. *J. Phys. Chem. B* **2009**, *113* (29), 9831.
(51) Ishida, T.; Nishikawa, K.; Shirota, H. *J. Phys. Chem. B* **2009**, *113* (29), 9840.
(52) Lide, D. R. CRC Handbook of Chemistry and Physics. 89 ed.; CRC Press: Boca Raton, 2008.
(53) Shirota, H.; Biswas, R. *J. Phys. Chem. B* **2012**, *116* (46), 13765.
(54) Canongia Lopes, J. N. C. G., M. F.; Husson, P.; Pádua, A. A.; Rebelo, L. P. N.; Sarraute, S.; Tariq, M. . *J. Phys. Chem. B* **2011**, *115* (19), 6088.
(55) Shirota, H. *J. Phys. Chem. B* **2013**, *117* (26), 7985.
(56) Fendt, S. P., S.; Blanch, H. W.; Prausnitz, J. M. *J. Chem. Eng. Data* **2011**, *56* (1), 31.
(57) Schröder, U., Wadhawan, J. D., Compton, R. G., Marken, F., Suarez, P. A., Consorti, C. S., Souza, R. F. d.; Dupont, J. *New Journal of Chemistry* **2000**, *24* (12), 1009.

(58) Hayes, R. I., S.; Warr, G. G.; Atkin, R. *Angewandte Chemie International Edition* **2012**, *51* (30), 7468.
(59) Jiang, W. W., Y.; Voth, G. A. *J. Phys. Chem. B* **2007**, *111* (18), 4812.
(60) Maia, F. M. R., O.; Macedo, E. A. *The Journal of Chemical Thermodynamics* **2012**, *48* (221-228).
(61) Takekiyo, T. Y., K.; Yamaguchi, E.; Abe, H.; Yoshimura, Y. *J. Phys. Chem. B* **2012**, *116* (36), 11092.
(62) Lopes, J. N. C.; Gomes, M. F. C.; Padua, A. A. H. *J. Phys. Chem. B* **2006**, *110* (34), 16816.
(63) Padua, A. A. H.; Gomes, M. F. C.; Lopes, J. N. C. *Acc. Chem. Res.* **2007**, *40* (11), 1087.
(64) Asaki, M. L. T.; Redondo, A.; Zawodzinski, T. A.; Taylor, A. J. *J. Chem. Phys.* **2002**, *116* (23), 10377.
(65) Chakraborty, A. I., T.; Banno, M.; Mochida, T.; Tominaga, K. *The Journal of Physical Chemistry A* **2011**, *115* (8), 1313.
(66) Giraud, G.; Gordon, C. M.; Dunkin, I. R.; Wynne, K. *J. Chem. Phys.* **2003**, *119* (1), 464.
(67) Shirota, H.; Funston, A. M.; Wishart, J. F.; Castner, E. W., Jr. *J. Chem. Phys.* **2005**, *122* (18), 184512.
(68) Shirota, H.; Castner, E. W., Jr. *J. Phys. Chem. A* **2005**, *109* (42), 9388.
(69) Shirota, H.; Matsuzaki, H.; Ramati, S.; Wishart, J. F. *J. Phys. Chem. B* **2015**, *119* (13), 9173.
(70) Shirota, H.; Kakinuma, S. *J. Phys. Chem. B* **2015**, *119* (30), 9835.
(71) Hyun, B. R.; Dzyuba, S. V.; Bartsch, R. A.; Quitevis, E. L. *J. Phys. Chem. A* **2002**, *106* (33), 7579.
(72) Rajian, J. R.; Li, S. F.; Bartsch, R. A.; Quitevis, E. L. *Chem. Phys. Lett.* **2004**, *393* (4-6), 372.
(73) Xiao, D.; Rajian, J. R.; Cady, A.; Li, S.; Bartsch, R. A.; Quitevis, E. L. *J. Phys. Chem. B* **2007**, *111* (18), 4669.
(74) Xiao, D.; Hines, L. G., Jr.; Li, S.; Bartsch, R. A.; Quitevis, E. L.; Russina, O.; Triolo, A. *J. Phys. Chem. B* **2009**, *113* (18), 6426.
(75) Turton, D. A.; Sonnleitner, T.; Ortner, A.; Walther, M.; Hefter, G.; Seddon, K. R.; Stana, S.; Plechkova, N. V.; Buchner, R.; Wynne, K. *Faraday Discussions* **2012**, *154* (0), 145, 10.1039/C1FD00054C.
(76) Sonnleitner, T.; Turton, D. A.; Hefter, G.; Ortner, A.; Waselikowski, S.; Walther, M.; Wynne, K.; Buchner, R. *J. Phys. Chem. B* **2015**, *119* (29), 8826.
(77) Kakinuma, S.; Ishida, T.; Shirota, H. *J. Phys. Chem. B* **2017**, *121* (1), 250.
(78) Kakinuma, S.; Ramati, S.; Wishart, J. F.; Shirota, H. *J. Chem. Phys.* **2018**, *148* (19), 193805/1.
(79) Kakinuma, S.; Shirota, H. *J. Phys. Chem. B* **2018**, *122* (22), 6033.
(80) Xiao, D.; Hines, L. G., Jr.; Bartsch, R. A.; Quitevis, E. L. *J. Phys. Chem. B* **2009**, *113* (14), 4544.

(81) Xue, L.; Tamas, G.; Gurung, E.; Quitevis, E. L. *J. Chem. Phys.* **2014**, *140* (16), 164512.
(82) Bardak, F.; Xiao, D.; Hines, L. G., Jr.; Son, P.; Bartsch, R. A.; Quitevis, E. L.; Yang, P.; Voth, G. A. *ChemPhysChem* **2012**, *13* (7), 1687.
(83) Shirota, H. T., K.; Ando, M.; Kakinuma, S. *Journal of Chemical & Engineering Data* **2019**, *64.* (11), 4701.
(84) Boyd, R. W. *Nonlinear Optics*; Elsevier, 2008.
(85) Hecht, E. *OPTICS*; Pearson Education, 2016.
(86) Mukamel, S. *Principles of Nonlinear Optics Spectroscopy*; Oxford University Press, 1995.
(87) Levenson, M. D.; Kano, S. S. *Introduction to Nonlinear Laser Spectroscopy*; Academic Press, 1988.
(88) Mukamel, S. *Principles of Nonlinear Optical Spectroscopy*; Oxford University Press, 1995.
(89) Maker, P. D. T., R. W. *Physical Review* **1965**, *137*, A801.
(90) Nibler, J. W. K., G. V. *Raman Sectroscopy of Gases and Liquids*; Springer, 1978.
(91) McMorrow, D.; Lotshaw, W. T.; Kenney-Wallace, G. A. *IEEE J. Quantum Electron.* **1988**, *24* (2), 443.
(92) Lotshaw, W. T.; McMorrow, D.; Thantu, N.; Melinger, J. S.; Kitchenham, R. *J. Raman Spectrosc.* **1995**, *26* (7), 571.
(93) Berne, B. J.; Pecora, R. *Dynamic Light Scattering: With Applications to Chemistry, Biology, and Physics*; Dover Publications, Inc., 2000.
(94) Levenson, M. D.; Eesley, G. L. *Applied Physics* **1978**, *19* (1), 1.
(95) Shirota, H. *J. Chem. Phys.* **2005**, *122* (4), 044514.
(96) Shirota, H.; Ishida, T. *J. Phys. Chem. B* **2011**, *115* (37), 10860.
(97) Kalpouzos, C.; Lotshaw, W. T.; McMorrow, D.; Kenney-Wallace, G. A. *J. Phys. Chem.* **1987**, *91* (8), 2028.
(98) Takamuku, T. H., H.; Idrissi, A.; Marekga, B. A.; Moreau, M.; Honda, Y.; Umecky, T.; Shimomura, T. *Phys. Chem. Chem. Phys.* **2014**, *16* (43), 23627.
(99) Masaki, T.; Nishikawa, K.; Shirota, H. *J. Phys. Chem. B* **2010**, *114* (19), 6323.
(100) Bekker, H.; Berendsen, H. J. C.; Dijkstra, E. J.; Achterop, S.; van Drunen, R.; van der Spoel, D.; Sijbers, A.; Keegstra, H.; Reitsma, B.; Renardus, M. K. R. GROMACS: A Parallel Computer for Molecular Dynamics Simulations. In *Physics Computing 92*, de Groot, R. A., Nadrchal, J. Eds.; World Scientific, 1993; pp 252.
(101) Berendsen, H. J. C.; van der Spoel, D.; van Drunen, R. *Computer Physics Communications* **1995**, *91* (1-3), 43.
(102) Lindahl, E.; Hess, B.; van der Spoel, D. *Journal of Molecular Modeling* **2001**, *7* (8), 306.
(103) van der Spoel, D.; Lindahl, E.; Hess, B.; Groenhof, G.; Mark, A. E.; Berendsen, H. J. C. *Journal of Computational Chemistry* **2005**, *26* (16), 1701.
(104) Hess, B. K., C.; van der Spoel, D.; Lindahl, E. *Journal of Chemical Theory and Computation* **2008**, *4* (3), 435.
(105) Pronk, S.; Pall, S.; Schulz, R.; Larsson, P.; Bjelkmar, P.; Apostolov, R.; Shirts, M. R.;

Smith, J. C.; Kasson, P. M.; van der Spoel, D.; et al. *Bioinformatics* **2013**, *29* (7), 845.
(106) Pall, S.; Abraham, M. J.; Kutzner, C.; Hess, B.; Lindahl, E. Trackling Exascale Software Challenges in Molecular Dynamics Simulations with GROMACS. In *Solving Software Challenges for Exascale*, Markidis, S., Laure, E. Eds.; Vol. 8759; Springer International Publishing, 2015; pp 3.
(107) Lopes, J. N. C.; Deschamps, J.; Padua, A. A. H. *J. Phys. Chem. B* **2004**, *108* (30), 11250.
(108) Lopes, J. N. C. D., J.;Padua, A. A. H. *J. Phys. Chem. B* **2004**, *108*, 11250.
(109) Kaminski, G. J., William L. *J. Phys. Chem.* **1996**, *100* (46), 18010.
(110) Price, M. L. P. O., Dennis; Jorgensen, William L. *Journal of Computational Chemistry* **2001**, *22* (13), 1340.
(111) Zheng, Y.-J. O., Rick L. *J. Am. Chem. Soc.* **1996**, *118* (17), 4175.
(112) Vasudevan, V. M., Samir H. *RSC Advances* **2015**, *5* (27), 20756.
(113) Hess, B. B., Henk; Berendsen, Herman J. C.; Fraaije, Johannes G. E. M. *Journal of Computational Chemistry* **1997**, *18* (12), 1463.
(114) Hockney, R. W. G., S. P.; Eastwood, J. W. *J. Comput. Phys.* **1974**, *14*, 148.
(115) Essmann, U. P., Lalith; Berkowitz, Max L.; Darden, Tom; Lee, Hsing; Pedersen, Lee G. *J. Chem. Phys.* **1995**, *103* (19), 8577.
(116) Parrinello, M. R., A. *Physical Review Letters* **1980**, *45* (14), 1196.
(117) Parrinello, M. R., A. *Journal of Applied Physics* **1981**, *51* (12), 7182.
(118) Nose, S. K., M. L. *Molecular Physics* **1983**, *50* (5), 1055.
(119) Nose, S. *Mol. Phys.* **1984**, *52* (2), 255.
(120) Hoover, W. G. *Physical review. A, General physics* **1985**, *31* (3), 1695.
(121) Frisch, M. J.; Trucks, G. W.; Schlegel, H. B.; Scuseria, G. E.; Robb, M. A.; Cheeseman, J. R.; Scalmani, G.; Barone, V.; Petersson, G. A.; Nakatsuji, H.; et al. *Gaussian 16*; Gaussian, Inc., 2016.
(122) Lee, C.; Yang, W.; Parr, R. G. *Physical Review B: Condensed Matter and Materials Physics* **1988**, *37* (2), 785.
(123) Becke, A. D. *J. Chem. Phys.* **1993**, *98* (7), 5648.
(124) Carrera, G. V. S. M.; Afonso, C. A. M.; Branco, L. C. *Journal of Chemical and Engineering Data* **2010**, *55* (2), 609.
(125) Nakamura, K.; Shikata, T. *ChemPhysChem* **2010**, *11* (1), 285.
(126) Nishida, T.; Tashiro, Y.; Yamamoto, M. *J. Fluor. Chem.* **2003**, *120* (2), 135.
(127) Li, W.; Zhang, Z.; Han, B.; Hu, S.; Xie, Y.; Yang, G. *J. Phys. Chem. B* **2007**, *111* (23), 6452.
(128) Cang, H.; Li, J.; Fayer, M. D. *J. Chem. Phys.* **2003**, *119* (24), 13017.
(129) Turton, D. A.; Hunger, J.; Stoppa, A.; Hefter, G.; Thoman, A.; Walther, M.; Buchner, R.; Wynne, K. *J. Am. Chem. Soc.* **2009**, *131* (31), 11140.
(130) Shirota, H.; Kakinuma, S.; Itoyama, Y.; Umecky, T.; Takamuku, T. *J. Phys. Chem. B* **2016**, *120* (3), 513.

(131) Shirota, H.; Yoshihara, K.; Smith, N. A.; Lin, S. J.; Meech, S. R. *Chem. Phys. Lett.* **1997**, *281* (1-3), 27.
(132) Fecko, C. J.; Eaves, J. D.; Tokmakoff, A. *J. Chem. Phys.* **2002**, *117* (3), 1139.
(133) Shirota, H.; Fujisawa, T.; Fukazawa, H.; Nishikawa, K. *Bull. Chem. Soc. Jpn.* **2009**, *82* (11), 1347.
(134) Wiewior, P. P.; Shirota, H.; Castner, E. W., Jr. *J. Chem. Phys.* **2002**, *116* (11), 4643.
(135) Bucaro, J. A.; Litovitz, T. A. *J. Chem. Phys.* **1971**, *54*, 3846.
(136) Roy, S.; Bagchi, B. *J. Chem. Phys.* **1993**, *99* (2), 1310.
(137) McQuarrie, D. A. *Statistical Mechanics*; University Science Books, 2000.
(138) Long, D. A. *The Raman Effect*; John Wiley & Sons, 2002.
(139) Cho, M.; Du, M.; Scherer, N. F.; Fleming, G. R.; Mukamel, S. *J. Chem. Phys.* **1993**, *99* (4), 2410.
(140) Chang, Y. J.; Castner, E. W., Jr. *J. Phys. Chem.* **1994**, *98* (39), 9712.
(141) Hu, Z.; Huang, X.; Annapureddy, H. V. R.; Margulis, C. J. *J. Phys. Chem. B* **2008**, *112* (26), 7837.
(142) Ishida, T.; Shirota, H. *J. Phys. Chem. B* **2013**, *117* (4), 1136.
(143) Kakinuma, S.; Shirota, H. *J. Phys. Chem. B* **2015**, *119* (13), 4713.
(144) Yoshida, K.; Yamaguchi, T. *Zeitschrift für Naturforschung A* **2000**, *56* (8), 529.
(145) Fukasawa, T. S., T.; Watanabe, J.; Hama, Y.; Kunz, W.; Buchner, R. *Physical review letters* **2005**, *95* (19), 197802.
(146) Polok, K.; Idrissi, A.; Gadomski, W. *Journal of Molecular Liquids* **2012**, *176*, 29.
(147) Shirota, H. *J. Phys. Chem. A* **2011**, *115*, 14262.
(148) Shirota, H.; Fukazawa, H. Atom Substitution Effects in Ionic Liquids: A Microscopic View by Femtosecond Raman-Induced Kerr Effect Spectroscopy. In *Ionic Liquids: Theory, Properties, New Approaches*, Kokorin, A. Ed.; InTech, 2011; pp 201.
(149) Shirota, H.; Kato, T. *J. Phys. Chem. A* **2011**, *115*, 8797.
(150) Fonseca Guerra, C. B., F. M.; Snijders, J. G.; Baerends, E. J. *J. Am. Chem. Soc.* **2000**, *122* (17), 4117.
(151) Klotz, I. M. F., J. S. *J. Am. Chem. Soc.* **1962**, *84* (18), 3461.
(152) Nandi, P. K. R., D. R. *J. Am. Chem. Soc.* **1972**, *94* (4), 1299.
(153) Hinton, J. F. H., R. D. *J. Am. Chem. Soc.* **1977**, *99* (2), 349.
(154) Takamuku, T. Mixing States of Ionic Liquid-Molecular Liquid Mixed Solvents and Their Effects on Metal Complex Formation. In *Molecular Basics of Liquids and Liquid-Based Materials*, Nishiyama, K. Y., T.; Takamuku, T.; Yoshida, N. Ed.; Springer, 2021; pp 233.
(155) Mizuno, K. T., Y.; Mekata, M. *Pure and applied chemistry* **2004**, *76* (1), 105.
(156) Shimomura, T.; Fujii, K.; Takamuku, T. *Phys. Chem. Chem. Phys.* **2010**, *12*, 12316.
(157) Jorgensen, W. L. M., D. S.; Tirado-Rives, J. *J. Am. Chem. Soc.* **1996**, *118* (45), 11225.
(158) Darden, T. Y., Darrin; Pedersen, Lee. *J. Chem. Phys.* **1993**, *98* (12), 10089.
(159) Simon, S., Duran, M.; Dannenberg, J. J. *J. Chem. Phys.* **1996**, *105* (24), 11024.

(160) Boys, S. F. B., F. J. M. P. *Molecular Physics* **1970**, *19* (4), 553.
(161) London, F. *J. Phys. Radium* **1937**, *8*, 397.
(162) McWeeny, R. *Physical Review* **1962**, *126*, 1028.
(163) Ditchfield, R. *Molecular Physics* **1974**, *27* (4), 789.
(164) Wolinski, K. H., J. F.; Pulay, P. *J. Am. Chem. Soc.* **1990**, *112* (23), 8251.
(165) Cheeseman, J. R. T., G. W.; Keith, T. A.; Frisch, M. J. *J. Chem. Phys.* **1996**, *104* (14), 5497.
(166) Miertus, S. T., J. *Chemical physics* **1982**, *65* (2), 239.
(167) Miertuš, S. S., E.; Tomasi, J. *Chemical Physics* **1981**, *55* (1), 117.
(168) Pascual‐ahuir; J. L., S., E.; Tunon, I. *Journal of Computational Chemistry* **1994**, *15* (10), 1127.
(169) Ando, M.; Kawano, M.; Tashiro, A.; Takamuku, T.; Shirota, H. *J. Phys. Chem. B* **2020**, *124* (36), 7857.
(170) Ando, M.; Shirota, H. *J. Phys. Chem. B* **2021**, *125* (43), 12006.
(171) Kinart, C. M. K., W. J.; Kolasiński, A. *Phys. Chem. Liquids* **1998**, *36*, 133.
(172) Campos, V.; Marigliano, A. C. G.; Sólimo, H. N. *J. Chem. Eng. Data* **2008**, *53* (1), 211.
(173) Ozcan, C. Z., P.; Hasirci, V.; Hasirci, N. . *Macromolecular Symposia* **2008**, *269* (1), 128.
(174) Checoni, R. F.; Volpe, P. L. O. *J. Solution Chem.* **2010**, *39*, 259.
(175) Shukla, R. K.; Kumar, A.; Awasthi, N.; Srivastava, U.; Gangwar, V. S. *Exp. Therm. Fluid Sci.* **2012**, *37*, 1.
(176) Sturlaugson, A. L.; Fruchey, K. S.; Fayer, M. D. *J. Phys. Chem. B* **2012**, *116*, 1777.
(177) Vraneš, M. B. D., S.; Djerić, V.; Gadžurić, S. B. *J. Chem. Eng. Data* **2013**, *58* (5), 1092.
(178) Zarei, H. G., A. S.; Behroozi, M. *J. Mol. Liq.* **2013**, *187*, 260.
(179) Chang, Y. J.; Castner, E. W., Jr. *J. Chem. Phys.* **1993**, *99* (1), 113.
(180) Rumble, J. R., Ed. *CRC Handbook of Chemistry and Physics*; CRC Press, 2021.
(181) Rilo, E. P., J.; García-Garabal, S.; Varela, L.M.; Cabeza, O. *Fluid Ph. Equilibria* **2009**, *285* (1-2), 83.
(182) Tariq, M.; Freire, M. G.; Saramago, B.; Coutinho, J. A. P.; Lopes, J. N. C.; Rebelo, L. P. N. *Chem. Soc. Rev.* **2012**, *41* (2), 829.
(183) Jiang, H. Z., Y.; Wang, J; Zhao, F.; Liu, R.; Hu, Y. *The Journal of Chemical Thermodynamics* **2013**, *64*, 1.
(184) Tasumi, H. T. a. M. *Int. J. Quant. Chem.* **1998**, *70* (2), 241.
(185) Torii, H.; Tasumi, M. *J. Phys. Chem. A* **2000**, *104* (18), 4174.
(186) Zhong, Q.; Fourkas, J. T. *J. Phys. Chem. B* **2008**, *112* (49), 15529.
(187) Fujii, K.; Kumai, T.; Takamuku, T.; Umebayashi, Y.; Ishiguro, S. *J. Phys. Chem. A* **2006**, *110* (5), 1798.
(188) Fujii, K.; Yoshitake, M.; Watanabe, H.; Takamuku, T.; Umebayashi, Y. *J. Mol. Liq.* **2017**, *238* (518-522).

(189) Palombo, F.; Meech, S. R. *J. Phys. Chem. B* **2012**, *116* (45), 13481.
(190) Plakhotnyk, V. N. S., R.; Ernst, L.; Kovtun, Y. V.; Plakhotnyk, A. V. *J. Fluor. Chem.* **2002**, *116* (1), 41.
(191) Turner, J. A. *Science* **2004**, *305* (5686), 972.
(192) S.M.Al-Salem; P.LettieriJ.Baeyens. *Waste Management* **2009**, *29* (10), 2625.
(193) S.N.Naik; V.Goud, V.; K.Rout, P.; K.Dalai, A. *Renewable and Sustainable Energy Reviews* **2010**, *14* (2), 578.
(194) Goodenough, J. B. *Energy & Environmental Science* **2014**, *7*, 14.
(195) Scrosati, B. *Journal of Solid State Electrochemistry* **2011**, *15*, 1623.
(196) Xu, W.; Cooper, E. I.; Angell, C. A. *J. Phys. Chem. B* **2003**, *107* (25), 6170.
(197) Schafer, T.; Paolo, R. E. D.; Franco, R.; Crespo, J. G. *Chemical Communications* **2005**, (20), 2594.
(198) Sasmal, D. K.; Mandal, A. K.; Mondal, T.; Bhattacharyya, K. *J. Phys. Chem. B* **2011**, *115* (24), 7781.
(199) Kofu, M.; Someya, T.; Tatsumi, S.; Ueno, K.; Ueki, T.; Watanabe, M.; Matsunaga, T.; Shibayama, M.; Sakai, V. G.; Tyagi, M.; et al. *Soft Matter* **2012**, *8* (30), 7888.
(200) Mandal, A. K.; Mojumdar, S.; Das, S.; Kumar, A.; Bhattacharyya, K. *ChemPhysChem* **2012**, *13* (7), 1942.
(201) Wang, G.; Wu, P. *Soft Matter* **2015**, *11* (26), 5253.
(202) Hoher, K.; Cardoso, P. F.; Lepre, L. F.; Ando, R. A.; Siqueira, L. J. A. *Phys. Chem. Chem. Phys.* **2016**, *18* (41), 28901.
(203) Ma, Y.; Lodge, T. P. *macromolecules* **2016**, *49* (9), 3639.
(204) Smith, C. J.; Gehrke, S.; Holloczki, O.; Wagle, D. V.; Heitz, M. P.; Baker, G. A. *J. Chem. Phys.* **2018**, *148* (19), 193845/1.
(205) Kharel, A.; Lodge, T. P. *Macromolecules* **2017**, *50* (21), 8739.
(206) Shannon, M. S.; Bara, J. E. *Industrial & Engineering Chemistry Research* **2011**, *50* (14), 8665.
(207) Bajić, D. M.; Ivaniš, G. R.; Visak, Z. P.; Živković, E. M.; Šerbanović, S. P.; Kijevčanin, M. L. *The Journal of Chemical Thermodynamics* **2013**, *57*, 510.
(208) Shirota, H.; Segawa, H. *J. Phys. Chem. A* **2003**, *107* (19), 3719.
(209) Shirota, H.; Segawa, H. *Chemical Physics* **2004**, *306* (1-3), 43.
(210) Shirota, H. *J. Phys. Chem. B* **2005**, *109* (15), 7053.
(211) Shirota, H.; Moriyama, K. *J. Phys. Chem. B* **2020**, *124* (10), 2006.
(212) Flory, P. J. *Principles of Polymer Chemistry*; Cornell University Press, 1953.
(213) Doi, M.; Edwards, S. F. *The Theory of Polymer Dynamics*; Oxford University Press, 1986.
(214) Chang, Y. J.; Castner, E. W., Jr. *J. Phys. Chem.* **1996**, *100* (9), 3330.
(215) Smith, N. A.; Meech, S. R. *J. Phys. Chem. A* **2000**, *104* (18), 4223.
(216) Ryu, S.; Stratt, R. M. *J. Phys. Chem. B* **2004**, *108* (21), 6782.
(217) Tao, G.; Stratt, R. M. *J. Phys. Chem. B* **2006**, *110* (2), 976.

(218) Shirota, H. *ChemPhysChem* **2012**, *13* (7), 1638.
(219) Fukazawa, H.; Ishida, T.; Shirota, H. *J. Phys. Chem. B* **2011**, *115*, 4621.
(220) Moreno, M.; Castiglione, F.; Mele, A.; Pasqui, C.; Raos, G. *J. Phys. Chem. B* **2008**, *112* (26), 7826.
(221) Giraud, G.; Karolin, J.; Wynne, K. *Biophysical Journal* **2003**, *85* (3), 1903.
(222) Shirota, H.; Castner, E. W., Jr. *J. Am. Chem. Soc.* **2001**, *123* (51), 12877.
(223) Shirota, H.; Ushiyama, H. *J. Phys. Chem. B* **2008**, *112* (43), 13542.
(224) Shirota, H.; Castner, E. W., Jr. *J. Chem. Phys.* **2006**, *125* (4), 034904.
(225) Hunt, N. T.; Jaye, A. A.; Hellman, A.; Meech, S. R. *J. Phys. Chem. B* **2004**, *108* (1), 100.
(226) Patist, A. Determining Critical Micelle Concentration. In *Handbook of Applied Surface and Colloid Chemistry*, Holmberg, K. Ed.; Vol. 2; Cargill Inc., 2002; pp 239.
(227) Rosen, M. J. K., J. T. *Surfactants and interfacial phenomena*; John Wiley & Sons, 2012.
(228) Iimori, T. I., T.; Kanai, K.; Seki, K.; Sung, J.; Kim, D.; Hamaguchi, O; Ouchi, Y. *J. Phys. Chem. B* **2007**, *111*, 4860.
(229) Baldelli, S. *Acc. Chem. Res.* **2008**, *41* (3), 421.
(230) Santos, C. S.; Baldelli, S. *Journal of Physical Chemistry C* **2008**, *112* (30), 11459.
(231) Cooper, E. I.; Angell, C. A. *Solid State Ionics* **1983**, *9&10*, 617.
(232) Matsumoto, H.; Yanagida, M.; Tanimoto, K.; Nomura, M.; Kitagawa, Y.; Miyazaki, Y. *Chemistry Letters* **2000**, (8), 922.
(233) Funston, A. M.; Wishart, J. F. *ACS Symp. Ser.* **2005**, *901*, 102.
(234) Chen, Z. J.; Xue, T.; Lee, J.-M. *RSC. Adv.* **2012**, *2* (28), 10564.
(235) Harris, K. R.; Makino, T.; Kanakubo, M. *Phys. Chem. Chem. Phys.* **2014**, *16* (19), 9161.
(236) Philippi, F.; Rauber, D.; Zapp, J.; Prasang, C.; Scheschkewitz, D.; Hempelmann, R. *ChemPhysChem* **2019**, *20* (3), 443.
(237) Philippi, F.; Rauber, D.; Kuttich, B.; Kraus, T.; Kay, C. W. M.; Hempelmann, R.; Hunt, P. A.; Welton, T. *Phys. Chem. Chem. Phys.* **2020**, *22* (40), 23038.
(238) Triolo, A.; Russina, O.; Caminiti, R.; Shirota, H.; Lee, H. Y.; Santos, C. S.; Murthyd, N. S.; Castner, E. W., Jr. *Chemical Communications* **2012**, *48*, 4959.
(239) Kashyap, H. K.; Santos, C. S.; Daly, R. P.; Hettige, J. J.; Murthy, N. S.; Shirota, H.; Castner, E. W., Jr.; Margulis, C. J. *J. Phys. Chem. B* **2013**, *117*, 1130.
(240) Visser, A. E.; Swatloski, R. P.; Reichert, W. M.; Mayton, R.; Sheff, S.; Wierzbicki, A.; Jr., J. H. D.; Rogers, R. D. *Environ Sci. Technol.* **2002**, *36* (11), 2523.
(241) Torriero, A. A. J.; Siriwardana, A. I.; Bond, A. M.; Burgar, I. M.; Dunlop, N. F.; Deacon, G. B.; MacFarlane, D. R. *J. Phys. Chem. B* **2009**, *113* (32), 11222.
(242) Fei, Z.; Zhu, D.-R.; Yan, N.; Scopelliti, R.; Katsuba, S. A.; Laurenczy, G.; Chisholm, D. M.; McIndoe, J. S.; Seddon, K. R.; Dyson, P. J. *Chem.-Eur. J.* **2014**, *20* (15), 4273.
(243) Shirota, H.; Takahashi, K.; Ando, M.; Kakinuma, S. *J. Chem. Eng. Data* **2019**, *64* (11), 4701.
(244) Andachi, T. Y., N.; Tamura, A.; Tominaga, K. *Journal of Infrared, Millimeter, and*

Terahertz Waves **2014**, *35* (1), 147.
(245) Ohta, K. H., S.; Tamura, Y.; Yamada, H.; Tominaga, K. *Applied Physics Letters* **2015**, *107* (18), 103.
(246) Ohta, K. T., S.; Takahashi, K.; Tamura, Y.; Yamada, H.; Tominaga, K. *J. Phys. Chem. B* **2017**, *121* (43), 10157.
(247) Canongia Lopes, J. N.; Deschamps, J.; Padua, A. A. H. *J. Phys. Chem. B* **2004**, *108* (6), 2038.
(248) Canongia Lopes, J. N.; Deschamps, J.; Padua, A. A. H. *J. Phys. Chem. B* **2004**, *108* (30), 11250.
(249) Wang, Y.-L.; Shah, F. U.; Glavatskih, S.; Antzutkin, O. N.; Laaksonen, A. *J. Phys. Chem. B* **2014**, *118* (29), 8711.
(250) Gouveia, A. S. L.; Bernardes, C. E. S.; Tome, L. C.; Lozinskaya, E. I.; Vygodskii, Y. S.; Shaplov, A. S.; Lopes, J. N. C.; Marrucho, I. M. *Phys. Chem. Chem. Phys.* **2017**, *19* (43), 29617.
(251) Darden, T.; York, D.; Pedersen, L. *J. Chem. Phys.* **1993**, *98* (12), 10089.
(252) Hoover, W. G. *Phys. Rev. A* **1985**, *31* (3), 1695.
(253) Parrinello, M.; Rahman, A. *J. Appl. Phys.* **1981**, *52* (12), 7182.
(254) Frisch, M. J.; Trucks, G. W.; Schlegel, H. B.; Scuseria, G. E.; Robb, M. A.; Cheeseman, J. R.; Scalmani, G.; Barone, V.; Mennucci, B.; Petersson, G. A.; et al. *Gaussian 09*; Gaussian, Inc., 2009.
(255) Frenkel, D.; McTague, J. P. *J. Chem. Phys.* **1980**, *72* (4), 2801.
(256) Geiger, L. C.; Ladanyi, B. M. *J. Chem. Phys.* **1987**, *87* (1), 191.
(257) Praprotnik, M.; Janezic, D.; Mavri, J. *J. Phys. Chem. A* **2004**, *108* (50), 11056.
(258) Berens, P. H.; Wilson, K. R. *J. Chem. Phys.* **1981**, *74* (9), 4872.
(259) Bornhauser, P.; Bougeard, D. *J. Phys. Chem. B* **2001**, *105* (1), 36.
(260) Goldstein, H.; Poole, C.; Safko, J. *Classical Mechanics*; Addison Wesley, 2002.
(261) Hansen, F. Y.; Taub, H. *Commun. Comput. Phys.* **2009**, *6* (2), 231.
(262) Tsunashima, K.; Kawabata, A.; Matsumiya, M.; Kodama, S.; Enomoto, R.; Sugiya, M.; Kunugi, Y. *Electrochem. Commun.* **2011**, *13* (2), 178.
(263) Sanchez-Ramírez, N.; Assresahegn, B. D.; Belanger, D.; Torresi, R. M. *J. Chem. Eng. Data* **2017**, *62* (10), 3437.
(264) Shirota, H.; Nishikawa, K.; Ishida, T. *J. Phys. Chem. B* **2009**, *113* (29), 9831.
(265) Tsunashima, K.; Sugiya, M. *Electrochemistry Communications* **2007**, *9* (9), 2353.
(266) Fraser, K. J.; MacFarlane, D. R. *Australian Journal of Chemistry* **2009**, *62* (4), 309.
(267) Seki, S.; Hayamizu, K.; Tsuzuki, S.; Fujii, K.; Umebayashi, Y.; Mitsugi, T.; Kobayashi, T.; Ohno, Y.; Kobayashi, Y.; Mita, Y.; et al. *Phys. Chem. Chem. Phys.* **2009**, *11* (18), 3509.
(268) Vogel, H. *Physik. Z.* **1921**, *22*, 645.
(269) Tammann, G.; Hesse, W. *Z. Anorg. Allg. Chem.* **1926**, *156*, 245.
(270) Fulcher, G. S. *Journal of the American Ceramic Society* **1925**, *8*, 789.
(271) Scherer, G. W. *Journal of the American Ceramic Society* **1992**, *75* (5), 1060.

(272) Shirota, H.; Ando, M.; Takahashi, K.; Kakinuma, S. *Bull. Chem. Soc. Jpn.* **2020**, *93* (11), 1520.
(273) Shirota, H.; Funston, A. M.; Wishart, J. F.; Castner, E. W., Jr. *J. Chem. Phys.* **2005**, *122* (18), 184512/1.
(274) Kakinuma, S.; Shirota, H. *J. Phys. Chem. B* **2018**, *122* (22), 6033.
(275) Kakinuma, S.; Shirota, H. *J. Phys. Chem. B* **2019**, *123* (6), 1307.
(276) Shirota, H.; Kakinuma, S. Temperature-Dependent Features in Low-Frequency Spectra of Ionic Liquids. In *Theoretical and Computational Approaches to Predicting Ionic Liquid Properties*, Joseph, A., Mathew, S. Eds.; Elsevier, 2021; pp 159.
(277) Shimizu, M.; Shirota, H. *J. Phys. Chem. B* **2022**.
(278) Fumino, K.; Reimann, S.; Ludwig, R. *Phys. Chem. Chem. Phys.* **2014**, *16* (40), 21903.
(279) Sonnleitner, T.; Turton, D. A.; Hefter, G.; Ortner, A.; Waselikowski, S.; Walther, M.; Wynne, K.; Buchner, R. *J. Phys. Chem. B* **2015**, *119*, 8826.
(280) Fumino, K.; Wulf, A.; Ludwig, R. *Angewandte Chemie, International Edition* **2009**, *48*, 3184.
(281) Fumino, K.; Fossog, V.; Stange, P.; Wittler, K.; Polet, W.; Hempelmann, R.; Ludwig, R. *ChemPhysChem* **2014**, *15* (12), 2604.
(282) Sonnleitner, T.; Turton, D. A.; Waselikowski, S.; Hunger, J.; Stoppa, A.; Walther, M.; Wynne, K.; Buchner, R. *Journal of Molecular Liquids* **2014**, *192*, 19.
(283) Reichenbach, J.; Ruddell, S. A.; Gonzalez-Jimenez, M.; Lemes, J.; Turton, D. A.; France, D. J.; Wynne, K. *J. Am. Chem. Soc.* **2017**, *139* (21), 7160.
(284) Neale, A. R.; Murphy, S.; Goodrich, P.; Schütter, C.; Hardacre, C.; Passerini, S.; Balducci, A.; Jacquemin, J. *J. Power Sources* **2016**, *326*, 549.
(285) Tang, S.; Baker, G. A.; Zhao, H. *Chem. Soc. Rev.* **2021**, *41* (10), 4030.
(286) Fischer, P. J.; Do, M. P.; Reich, R. M.; Nagasubramanian, A.; Srinivasan, M.; Kuhn, F. E. *Phys. Chem. Chem. Phys.* **2018**, *20* (46), 29412.
(287) Herstedt, M.; Smirnov, M.; Johansson, P.; Chami, M.; Grondin, J.; Servant, L.; Lassegues, J. C. *J. Raman Spectrosc.* **2005**, *36* (8), 762.
(288) Fujii, K.; Fujimori, T.; Takamuku, T.; Kanzaki, R.; Umebayashi, Y.; Ishiguro, S.-I. *J. Phys. Chem. B* **2006**, *110* (5), 8179.
(289) Lassegues, J. C.; Grondin, J.; Holomb, R.; Johansson, P. *J. Raman Spectrosc.* **2007**, *38* (5), 551.
(290) Fujisawa, T.; Nishikawa, K.; Shirota, H. *J. Chem. Phys.* **2009**, *131* (24), 244519.
(291) Bursulaya, B. D.; Kim, H. J. *J. Chem. Phys.* **1998**, *109* (12), 4911.
(292) Dunning, T. H., Jr. *J. Chem. Phys.* **1989**, *90* (2), 1007.
(293) Woon, D. E.; Dunning, T. H., Jr. *J. Chem. Phys.* **1993**, *98* (2), 1358.
(294) Kiyohara, K.; Kamada, K.; Ohta, K. *J. Chem. Phys.* **2000**, *112* (14), 6338.
(295) Thole, B. T. *Chem. Phys.* **1981**, *59* (3), 341.
(296) Sonoda, M. T.; Vechi, S. M.; Skaf, M. S. *Phys. Chem. Chem. Phys.* **2005**, *7* (6), 1176.

(297) Bartolini, P.; Taschin, A.; Eramo, R.; Torre, R. Optical Kerr Effect Experiments on Complex Liquids. In *Time-Resolved Spectroscopy in Complex Liquids*, Torre, R. Ed.; Springer, 2008; pp 73.

Appendix

A. Synthesis Procedures of Samples

A. 1. Chapter III and VI

A. 1. 1. *1-Methyl-3-octylimidazolium Tetrafluoroborate, [MOIm][BF_4]*

1-Methylimidazole was distilled before use. 1-Chlorooctane (24.02 g, 161 mmol) was added to an acetonitrile solution of 1-methylimidazole (11.08 g, 135 mmol) at nitrogen atmosphere in a flask equipped with a reflux condenser and magnetic stirrer, and the solution was stirred for 3 days at 363 K. The solution was then condensed by evaporation, and was washed with diethyl ether for several times. The ionic liquid was then dried in vacuo at 313 K for more than 1 day. The obtained 1-methyl-3-octhylimidazolium chloride was successively used for the preparation of 1-methyl-3-octhylimidazolium tetrafluoroborate. The 1-methyl-3-octhylimidazolium chloride was dissolved in acetonitrile and acetonitrile solution of sodium tetrafluoroborate (16.17 g, 147 mmol) was added. After the mixture was stirred at room temperature for one day, the solution was filtered. The filtrate was evaporated. The liquid was dissolved in chloroform and washed with water several times. Magnesium sulfate was added in the solution. After the mixture was stirred at room temperature for one day, the solution was filtered and the chloroform was evaporated. The residual liquid and activated carbon were added in acetonitrile, and stirred at room temperature over night. The solution was then filtered and evaporated. The colorless ionic liquid was then obtained and dried in vacuo at 313 K for more than 2 days. The yield was 46.5 %. 1H-NMR (400 MHz DMSO-d6): δ = 0.86 (t, 3H, $NC_7H_{14}CH_3$), 1.26 (m, 10H, $NCH_2CH_2C_5H_{10}CH_3$), 1.77 (quin, 2H, $NCH_2CH_2C_5H_{10}CH_3$), 3.84 (s, 3H, NCH_3), 4.14 (t, 2H, $NCH_2C_7H_{15}$), 7.69 (t, 1H, $CH_3NCHCHN$), 7.76 (t, 1H, $CH_3NCHCHN$), 9.10 (s, 1H, CH_3NCHN). Elemental analysis: $C_{12}H_{23}N_2BF_4$: Calcd. C 51.08, H 8.21, N 9.93. Found: C 50.68, H 8.20, N 9.54.

A. 2. Chapter V

A. 2. 1. *1-Octylimidazole, OIm*

Imidazole (9.70 g, 140 mmol) and 1-octylbromide (14.28 g, 70 mmol) were added to toluene (ca. 100 mL) at nitrogen atmosphere in a flask equipped with a reflux condenser and magnetic stirrer. The solution was stirred, and then heated to ca. 120 °C in an oil bath for 4 hours while stirring. After that, the flask was allowed to cool to room temperature. The toluene solution was filtered to remove white precipitate. The filtrate was liberated by aqueous solution with NaOH (2.84 g, 70 mmol). The liberated solution was evaporated. The residual liquid was dissolved in dichloromethane, and the solution was washed with water several times. Na_2SO_4

was then added in the dichloromethane solution, and the mixture was stirred by magnetic stirrer for overnight. After Na_2SO_4 was filtered, the residual liquid was evaporated to eliminate dichloromethane. The obtained liquid was distilled under vacuum at 170 °C. The yield was 64% (8.10 g). ^{1}H-NMR (400 MHz, $CDCl_3$): δ = 0.86 (t, J = 6.9 Hz, $NCH_2(CH_2)_5CH_2CH_3$, 3H), δ = 1.26 (m, $NCH_2(CH_2)_5CH_2CH_3$, 10H), δ = 1.77 (m, $(CH_2)_5CH_2CH_3$, 2H). δ = 3.93 (t, J = 7.1 Hz, $NCH_2(CH_2)_5$, 2H), δ = 6.90 (s, CH, 1H), δ = 7.06 (s, CH, 1H), and δ = 7.56 (s, CH, 1H) . ^{14}C-NMR (100 MHz, $CDCl_3$): δ = 14.0, 22.5, 26.5, 29.0, 29.0, 31.0, 31.6, 47.1, 118.8, 128.7, and 136.9.

A. 3. Chapter VI

A. 3. 1. *Triethylpentylphosphonium bis(fluorosulfonyl)amide, [P_{2225}][NF_2].*

1-Bromopentane (5.2 mL, 42 mmol) was added to triethylphosphine toluene solution (20 %, 27 mL,38 mmol) at nitrogen atmosphere in a flask equipped with a reflux condenser and magnetic stirrer. The solution was stirred and then heated to ca. 90 °C in an oil bath for two days while stirring. After that, the flask was allowed to cool to room temperature. The toluene layer was removed, and the residual solid was washed with toluene five times. The solid was then dissolved by acetonitrile, and the solution was evaporated. The solid was dried in vacuo at 40 °C for approximately 3 hours. The residual solid was washed with ethyl acetate five times. Then, the solid was dried in vacuo at 40 °C for approximately 3 hours. The obtained solid ([P_{2225}]Cl, 9.7 g, 36 mmol) was then successively dissolved in water, and an aqueous solution of lithium bis(fluorosulfonyl)amide (7.8 g, 39 mmol) was added. After the mixture was stirred at room temperature for 1.5 hours, it was settled. The ionic liquid phase was washed with water five times and then hexane five times. The resultant ionic liquid and activated carbon were added to acetonitrile and stirred at room temperature overnight. After the filtration, the solution was evaporated. The obtained ionic liquid was then dried in vacuo at 40 °C for more than 2 days. The yield was 93 % (13.0 g). ^{1}H-NMR (400 MHz, $CDCl_3$): δ = 0.89 (t, J = 7.4 Hz, -$(CH_2)_2CH_2CH_3$, 3H), δ = 1.26 (tt, J = 7.6 and 18.2 Hz, -PCH_2CH_3, 9H), δ = 1.36 (quin, J = 7.6 Hz, -$(CH_2)_2CH_2CH_3$, 2H), δ = 1.49 (m, -$(CH_2)_2CH_2CH_3$, 4H), δ = 2.08 (m, -$PCH_2(CH_2)_2$-, 2H), δ = 2.17 (qq, J = 7.6 and 12.7 Hz, PCH_2CH_3, 6H). Elemental analysis: $C_{11}H_{26}F_2NO_4PS_2$: Calcd. C 35.76, H 7.09, N 3.79. Found C 35.70, H 7.06, N 3.84.

A. 3. 2. *Ethoxyethyltriethylphosphonium bis(fluorosulfonyl)amide, [$P_{222(2O2)}$][NF_2].*

2-Chloroethyl ethyl ether (4.8 mL, 43 mmol) was added to triethylphosphine toluene solution (20 %, 25 mL, 35 mmol) at nitrogen atmosphere in a flask equipped with a reflux

condenser and magnetic stirrer. The solution was stirred and then heated to ca. 90 °C in an oil bath for two days while stirring. After that, the flask was allowed to cool to room temperature. The toluene layer was removed, and the residual solid was washed with diethyl ether several times. The solid was then dissolved by acetonitrile, and the solution was evaporated. The solid was dried in vacuo at 40 °C for approximately 2 hours. The obtained solid ([$P_{222(2O2)}$]Cl, 4.1 g, 18 mmol) was then successively dissolved in water, and an aqueous solution of lithium bis(fluorosulfonyl)amide (4.2 g, 22 mmol) was added. After the mixture was stirred at room temperature for 1.5 hours, it was settled. The ionic liquid phase was washed with water five times and then hexane five times. The resultant ionic liquid and activated carbon were added to acetonitrile and stirred at room temperature overnight. After the filtration, the solution was evaporated. The obtained ionic liquid was then dried in vacuo at 40 °C for 1 day. The yield was 36 % (4.7 g). ^{1}H-NMR (400 MHz, $CDCl_3$): δ = 1.19 (t, J = 7.2 Hz, -OCH_2CH_3, 3H), δ = 1.29 (tt, J = 7.9 and 18.4 Hz, -PCH_2CH_3, 9H), δ =2.23 (qq, J = 7.6 and 12.9 Hz , -PCH_2CH_3, 6H), δ = 2.47 (quin, J = 5.8 Hz, -OCH_2CH_3, 2H), δ = 3.52 (q, -PCH_2CH_2O-, 2H), δ = 3.79 (tt, J = 6.1 and 19.8 Hz, PCH_2CH_2O, 2H). Elemental analysis: $C_{10}H_{24}F_2NO_5PS_2$: Calcd. C 32.34, H 6.51, N 3.77. Found C 32.53, H 6.50, N 3.87.

A. 3. 3. *Triethyl[(ethylthio)ethyl]phosphonium bis(fluorosulfonyl)amide, [$P_{222(2S2)}$][NF_2].*

2-Chloroethyl ethyl sulfide (5.0 mL, 43 mmol) was added to triethylphosphine toluene solution (20 %, 25 mL,35 mmol) at nitrogen atmosphere in a flask equipped with a reflux condenser and magnetic stirrer. The solution was stirred and then heated to ca. 120 °C in an oil bath for 22 hours while stirring. After that, the flask was allowed to cool to room temperature. The toluene layer was removed, and the residual solid was washed with toluene several times. The solid was then dissolved by acetonitrile, and the solution was evaporated. The solid was dried in vacuo at ambient temperature for approximately 2 hours. The obtained solid ([$P_{222(2S2)}$]Cl, 7.1 g, 29 mmol) was then successively dissolved in water, and an aqueous solution of lithium bis(fluorosulfonyl)amide (6.6 g, 35 mmol) was added. After the mixture was stirred at room temperature for 1.5 hours, it was settled. The ionic liquid phase was washed with water five times and then hexane five times. The resultant ionic liquid and activated carbon were added to acetonitrile and stirred at room temperature overnight. After the filtration, the solution was evaporated. The obtained ionic liquid was then dried in vacuo at 40 °C for more than 2 days. The yield was 65 % (8.8 g). ^{1}H-NMR (400 MHz, $CDCl_3$): δ = 1.30 (tt, J = 7.6 and 18.4 Hz, PCH_2CH_3, 9H, and t, J = 7.4 Hz SCH_2CH_3, 3H), δ = 2.28 (qq, J = 7.6 and 12.7 Hz, PCH_2CH_3, 6H), δ = 2.49 (tt, J = 7.4 and 12.1 Hz, PCH_2CH_2S, 2H), δ = 2.64 (q, J = 7.4 Hz, SCH_2CH_3, 2H),

δ = 2.83 (tt, J = 7.4 and 14.4 Hz, PCH_2CH_2S, 2H). Elemental analysis: $C_{10}H_{24}F_2NO_4PS_3$: Calcd. C 31.00, H 6.24, N 3.62. Found C 31.13, H 6.18, N 3.77.

B. Appendix to Chapter III

B. 1. Molecular Dynamics Simulation

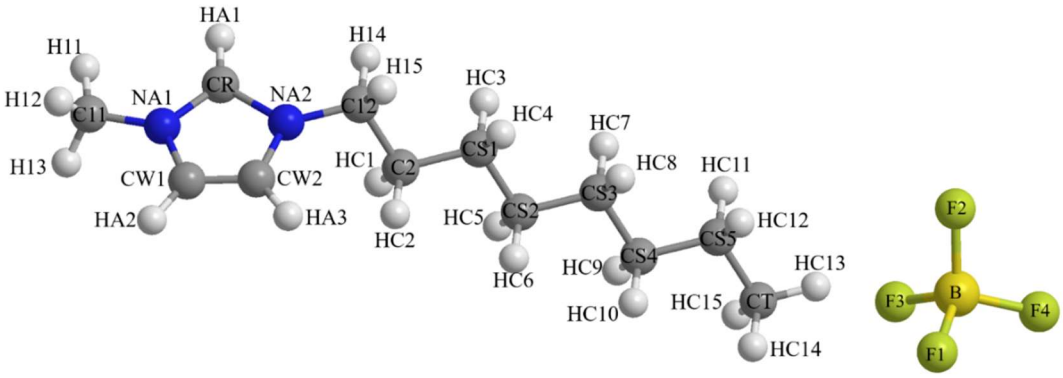

Figure B1. Structure of [MOIm][BF_4].

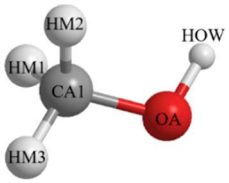

Figure B2. Structure of MeOH.

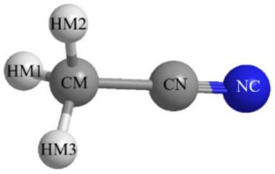

Figure B3. Structure of MeCN.

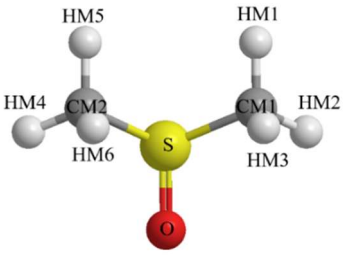

Figure B4. Structure of DMSO.

Table B1. Force Field Parameters Used for $[MOIm]^+$,[B1] $[BF_4]^-$,[B2] MeOH,[B3] MeCN,[B4] and DMSO.[B5,B6] The Notation of the Atoms within the Molecules is Depicted in Figures B1–B4.

Point Charges and van der Waals Parameters.

	Atom	Charge (e)	σ (Å)	ε (kcal mol^{-1})
$[MOIm]^+$	NA1	0.150	3.250	0.170
	NA2	0.150	3.550	0.170
	CR	-0.110	3.550	0.070
	HA1	0.210	2.420	0.030
	CW1	-0.130	3.550	0.070
	HA2	0.210	2.500	0.030
	CW2	-0.130	3.550	0.066
	HA3	0.210	2.420	0.030
	C11	-0.170	3.500	0.066
	H11	0.130	2.500	0.030
	H12	0.130	2.500	0.030
	H13	0.130	2.500	0.030
	C12	-0.170	3.500	0.066
	H14	0.130	2.500	0.030
	H15	0.130	2.500	0.030
	C2	0.010	3.500	0.066
	HC1	0.060	2.500	0.030
	HC2	0.060	2.500	0.030
	CS1	-0.120	3.500	0.066
	HC3	0.060	2.500	0.030
	HC4	0.060	2.500	0.030
	CS2	-0.120	3.500	0.066
	HC5	0.060	2.500	0.030
	HC6	0.060	2.500	0.030
	CS3	-0.120	3.500	0.066
	HC7	0.060	2.500	0.030
	HC8	0.060	2.500	0.030
	CS4	-0.120	3.500	0.066
	HC9	0.060	2.500	0.030
	HC10	0.060	2.500	0.030
	CS5	-0.120	3.500	0.066
	HC11	0.060	2.500	0.030
	HC12	0.060	2.500	0.030
	CT	-0.180	3.500	0.066
	HC13	0.060	2.500	0.030
	HC14	0.060	2.500	0.030
	HC15	0.060	2.500	0.030

	Atom	Charge (e)	σ (Å)	ε (kcal mol^{-1})
$[BF_4]^-$	F1	-0.490	3.120	0.061
	B	0.960	3.580	0.095
	F2	-0.490	3.120	0.061
	F3	-0.490	3.120	0.061
	F4	-0.490	3.120	0.061
MeOH	CA1	0.145	3.500	0.066
	HM1	0.040	2.500	0.030
	HM2	0.040	2.500	0.030
	HM3	0.040	2.500	0.030
	OA	-0.683	3.120	0.170
	HOW	0.418	0.000	0.000
MeCN	NC	-0.560	3.200	0.170
	CN	0.460	3.300	0.066
	CM	-0.080	3.300	0.066
	HM1	0.060	2.500	0.015
	HM2	0.060	2.500	0.015
	HM3	0.060	2.500	0.015
DMSO	CM1	-0.020	3.500	0.066
	HM1	0.060	2.500	0.030
	HM2	0.060	2.500	0.030
	HM3	0.060	2.500	0.030
	S	0.139	3.560	0.395
	CM2	-0.020	3.500	0.066
	HM4	0.060	2.500	0.030
	HM5	0.060	2.500	0.030
	HM6	0.060	2.500	0.030
	O	-0.459	2.930	0.280

Intramolecular Atom-Atom Bond Lengths.

	Bond	*r* (Å)		Bond	*r* (Å)
$[MOIm]^+$	CR-NA1	1.315	$[BF_4]^-$	B-F1	1.394
	CR-NA2	1.315		B-F2	1.394
	C11-H11	1.090		B-F3	1.394
	C11-H12	1.090		B-F4	1.394
	C11-H13	1.090			
	NA2-C11	1.466	MeOH	CA1-OA	1.410
	CR-HA1	1.080		CA1-HM1	1.090
	CW2-NA2	1.378		CA1-HM2	1.090
	CW1-NA1	1.378		CA1-HM3	1.090
	CW2-CW1	1.341		OA-HOW	0.945
	CW2-HA3	1.080			
	CW1-HA2	1.080	MeCN	CN-NC	1.157
	NA1-C12	1.466		CT-CN	1.470
	C12-H14	1.090		CT-HM1	1.090
	C12-H15	1.090		CT-HM2	1.090
	C12-C2	1.529		CT-HM3	1.090
	C2-HC1	1.090			
	C2-HC2	1.090	DMSO	CM1-S	1.810
	C2-CS1	1.529		CM2-S	1.810
	CS1-HC3	1.090		S-O	1.530
	CS1-HC4	1.090		CM2-HM4	1.090
	CS1-CS2	1.529		CM2-HM5	1.090
	CS2-HC5	1.090		CM2-HM6	1.090
	CS2-HC6	1.090		CM1-HM1	1.090
	CS2-CS3	1.529		CM1-HM2	1.090
	CS3-HC7	1.090		CM1-HM3	1.090
	CS3-HC8	1.090			
	CS3-CS4	1.529			
	CS4-HC9	1.090			
	CS4-HC10	1.090			
	CS4-CS5	1.529			
	CS5-HC11	1.090			
	CS5-HC12	1.090			
	CS5-CT	1.529			
	CT-HC13	1.090			
	CT-HC14	1.090			
	CT-HC15	1.090			

Bond Angle Potentials.

	Angle	K (kcal mol^{-1} rad^{-2})	θ (degree)
[MOIm]$^+$	H11-C11-H12	33.00	107.8
	H11-C11-H13	33.00	107.8
	H12-C11-H13	33.00	107.8
	NA2-C11-H11	37.50	110.7
	NA2-C11-H12	37.50	110.7
	NA2-C11-H13	37.50	110.7
	CR-NA2-C11	70.00	126.4
	CW2-NA2-C11	70.00	125.6
	NA2-CR-HA1	35.00	125.1
	NA1-CR-HA1	35.00	125.1
	NA2-CR-NA1	70.00	109.8
	CR-NA2-CW2	70.00	108.0
	CR-NA1-CW1	70.00	108.0
	NA2-CW2-CW1	70.00	107.1
	NA1-CW1-CW2	70.00	107.1
	NA1-CW2-HA3	35.00	122.0
	NA1-CW1-HA2	35.00	122.0
	CW2-CW1-HA2	35.00	130.9
	CW1-CW2-HA3	35.00	130.9
	CW2-NA1-C12	70.00	125.6
	CR-NA1-C12	70.00	126.4
	NA1-C12-H14	37.50	110.7
	NA1-C12-H15	37.50	110.7
	NA1-C12-C2	58.30	112.7
	C2-C12-H14	37.50	110.7
	C2-C12-H15	37.50	110.7
	H14-C12-H15	33.00	107.8
	C12-C2-HC1	37.50	110.7
	C12-C2-HC2	37.50	110.7
	C12-C2-CS1	58.30	112.7
	CT-CS5-HC11	37.50	110.7
	CT-CS5-HC12	37.50	110.7
	CS1-C2-HC1	37.50	110.7
	CS1-C2-HC2	37.50	110.7
	C2-CS1-HC3	37.50	110.7
	C2-CS1-HC4	37.50	110.7
	CS2-CS1-HC3	37.50	110.7
	CS2-CS1-HC4	37.50	110.7
	CS3-CS2-HC5	37.50	110.7
	CS3-CS2-HC6	37.50	110.7
	CS3-CS2-HC5	37.50	110.7
	CS3-CS2-HC6	37.50	110.7
	CS2-CS3-HC7	37.50	110.7
	CS2-CS3-HC8	37.50	110.7
	CS4-CS3-HC7	37.50	110.7
	CS4-CS3-HC8	37.50	110.7

	CS3-CS4-HC9	37.50	110.7
	CS3-CS4-HC10	37.50	110.7
	CS5-CS4-HC9	37.50	110.7
	CS5-CS4-HC10	37.50	110.7
	CS4-CS5-HC11	37.50	110.7
	CS4-CS5-HC12	37.50	110.7
	HC1-C2-HC2	33.00	107.8
	HC3-CS1-HC4	33.00	107.8
	HC5-CS2-HC6	33.00	107.8
	HC7-CS3-HC8	33.00	107.8
	HC9-CS4-HC10	33.00	107.8
	HC11-CS5-HC12	33.00	107.8
	CS4-CS5-CT	58.30	112.7
	C2-CS1-CS2	58.30	112.7
	CS1-CS2-CS3	58.30	112.7
	CS2-CS3-CS4	58.30	112.7
	CS3-CS4-CS5	58.30	112.7
	CS5-CT-HC13	37.50	110.7
	CS5-CT-HC14	37.50	110.7
	CS5-CT-HC15	37.50	110.7
	HC13-CT-HC14	33.00	107.8
	HC13-CT-HC15	33.00	107.8
	HC14-CT-HC15	33.00	107.8
$[BF_4]^-$	F2-B-F1	80.01	109.5
	F3-B-F1	80.01	109.5
	F4-B-F1	80.01	109.5
	F3-B-F2	80.01	109.5
	F4-B-F2	80.01	109.5
	F4-B-F3	80.01	109.5
MeOH	HM1-CA1-OA	35.00	109.5
	HM2-CA1-OA	35.00	109.5
	HM3-CA1-OA	35.00	109.5
	CA1-OA-HOW	55.00	108.5
	HM2-CA1-HM1	33.00	107.8
	HM3-CA1-HM1	33.00	107.8
	HM3-CA1-HM2	33.00	107.8
MeCN	CM-CN-NC	150.00	180.0
	HM1-CM-CN	35.00	108.5
	HM2-CM-CN	35.00	108.5
	HM3-CM-CN	35.00	108.5
	HM2-CM-HM1	33.00	107.8
	HM3-CM-HM1	33.00	107.8
	HM3-CM-HM2	33.00	107.8
DMSO	HM1-CM1-S	35.00	108.5
	HM2-CM1-S	35.00	108.5

HM3-CM1-S	35.00	108.5
CM1-S-CM2	62.00	98.9
CM1-S-O	47.80	107.0
O-S-CM2	47.80	107.0
S-CM2-HM4	35.00	109.5
S-CM2-HM5	35.00	109.5
S-CM2-HM6	35.00	109.5
HM4-CM2-HM5	33.00	107.8
HM6-CM2-HM4	33.00	107.8
HM6-CM2-HM5	33.00	107.8
HM1-CM1-HM2	33.00	107.8
HM3-CM1-HM1	33.00	107.8
HM3-CM1-HM2	33.00	107.8

Torsion Potentials

	Dihedral	V_1 (kcal mol^{-1})	V_2 (kcal mol^{-1})	V_3 (kcal mol^{-1})	V_4 (kcal mol^{-1})
[MOIm]$^+$	CR-NA2-C11-H11	0.000	0.000	0.000	0.000
	CR-NA2-C11-H12	0.000	0.000	0.000	0.000
	CR-NA2-C11-H13	0.000	0.000	0.000	0.000
	CW2-NA2-C11-H11	0.000	0.000	0.124	0.000
	CW2-NA2-C11-H12	0.000	0.000	0.124	0.000
	CW2-NA2-C11-H13	0.000	0.000	0.124	0.000
	C11-NA2-CR-HA1	0.000	4.650	0.000	0.000
	NA1-CR-NA2-C11	0.000	4.650	0.000	0.000
	CW1-CW2-NA-C11	0.000	3.000	0.000	0.000
	C11-NA2-CW2-HA3	0.000	3.000	0.000	0.000
	NA1-CR-NA2-C11	0.000	4.650	0.000	0.000
	NA2-CW2-CW1-HA2	0.000	10.750	0.000	0.000
	NA1-CW1-CW2-HA3	0.000	10.750	0.000	0.000
	NA2-CW2-CW1-NA1	0.000	10.750	0.000	0.000
	CW2-NA2-CR-HA1	0.000	4.650	0.000	0.000
	CW1-NA1-CR-HA1	0.000	4.650	0.000	0.000
	CR-NA2-CW2-HA3	0.000	3.000	0.000	0.000
	CR-NA1-CW1-HA2	0.000	3.000	0.000	0.000
	CR-NA1-CW1-CW2	0.000	3.000	0.000	0.000
	CR-NA2-CW2-CW1	0.000	3.000	0.000	0.000
	C12-NA1-CR-HA1	0.000	4.650	0.000	0.000
	C12-NA1-CW1-HA2	0.000	3.000	0.000	0.000
	C12-NA1-CW1-CW2	0.000	3.000	0.000	0.000
	CR-NA1-C12-H14	0.000	0.000	0.000	0.000

CR-NA1-C12-H15	0.000	0.000	0.000	0.000
C12-C2-CS1-HC3	0.000	0.000	0.366	0.000
C12-C2-CS1-HC4	0.000	0.000	0.366	0.000
HC1-C2-CS1-HC3	0.000	0.000	0.318	0.000
HC1-C2-CS1-HC4	0.000	0.000	0.318	0.000
HC2-C2-CS1-HC3	0.000	0.000	0.318	0.000
HC2-C2-CS1-HC4	0.000	0.000	0.318	0.000
HC3-CS1-CS2-HC5	0.000	0.000	0.318	0.000
HC3-CS1-CS2-HC6	0.000	0.000	0.318	0.000
HC4-CS1-CS2-HC5	0.000	0.000	0.318	0.000
HC4-CS1-CS2-HC6	0.000	0.000	0.318	0.000
HC5-CS2-CS3-HC7	0.000	0.000	0.318	0.000
HC5-CS2-CS3-HC8	0.000	0.000	0.318	0.000
HC6-CS2-CS3-HC7	0.000	0.000	0.318	0.000
HC6-CS2-CS3-HC8	0.000	0.000	0.318	0.000
HC7-CS3-CS4-HC9	0.000	0.000	0.318	0.000
HC7-CS3-CS4-HC10	0.000	0.000	0.318	0.000
HC8-CS3-CS4-HC9	0.000	0.000	0.318	0.000
HC8-CS3-CS4-HC10	0.000	0.000	0.318	0.000
HC9-CS4-CS5-HC11	0.000	0.000	0.318	0.000
HC9-CS4-CS5-HC12	0.000	0.000	0.318	0.000
HC10-CS4-CS5-HC11	0.000	0.000	0.318	0.000
HC10-CS4-CS5-HC12	0.000	0.000	0.318	0.000
HC11-CS5-CT-HC13	0.000	0.000	0.318	0.000
HC11-CS5-CT-HC14	0.000	0.000	0.318	0.000
HC11-CS5-CT-HC15	0.000	0.000	0.318	0.000
HC12-CS5-CT-HC13	0.000	0.000	0.318	0.000
HC12-CS5-CT-HC14	0.000	0.000	0.318	0.000
HC12-CS5-CT-HC15	0.000	0.000	0.318	0.000
HC9-CS4-CS5-CT	0.000	0.000	0.366	0.000
HC10-CS4-CS5-CT	0.000	0.000	0.366	0.000
C12-C2-CS1-CS2	1.739	-0.157	0.279	0.000
C2-CS1-CS2-CS3	1.739	-0.157	0.279	0.000
CS1-CS2-CS3-CS4	1.739	-0.157	0.279	0.000
CS2-CS3-CS4-CS5	1.739	-0.157	0.279	0.000
CS3-CS4-CS5-CT	1.739	-0.157	0.279	0.000
CS3-CS4-CS5-HC11	0.000	0.000	0.366	0.000
CS3-CS4-CS5-HC12	0.000	0.000	0.366	0.000

	CS2-CS3-CS4-HC9	0.000	0.000	0.366	0.000
	CS2-CS3-CS4-HC10	0.000	0.000	0.366	0.000
	CS1-CS2-CS3-HC7	0.000	0.000	0.366	0.000
	CS1-CS2-CS3-HC8	0.000	0.000	0.366	0.000
	C2-CS1-CS2-HC5	0.000	0.000	0.366	0.000
	C2-CS1-CS2-HC6	0.000	0.000	0.366	0.000
	CS2-CS1-C2-HC1	0.000	0.000	0.366	0.000
	CS2-CS1-C2-HC2	0.000	0.000	0.366	0.000
	CS3-CS2-CS1-HC3	0.000	0.000	0.366	0.000
	CS3-CS2-CS1-HC4	0.000	0.000	0.366	0.000
	CS4-CS3-CS2-HC5	0.000	0.000	0.366	0.000
	CS4-CS3-CS2-HC6	0.000	0.000	0.366	0.000
	CS5-CS4-CS3-HC7	0.000	0.000	0.366	0.000
	CS5-CS4-CS3-HC8	0.000	0.000	0.366	0.000
	CS4-CS5-CT-HC13	0.000	0.000	0.366	0.000
	CS4-CS5-CT-HC14	0.000	0.000	0.366	0.000
	CS4-CS5-CT-HC15	0.000	0.000	0.366	0.000
	HA3-CW2-CW1-HA2	0.000	10.750	0.000	0.000
	CW1-NA1-C12-H14	0.000	0.000	0.124	0.000
	CW1-NA1-C12-H15	0.000	0.000	0.124	0.000
	CW1-NA1-C12-C2	-1.709	1.459	0.190	0.000
	CR-NA1-C12-C2	-1.259	0.000	0.000	0.000
	NA1-C12-C2-CS1	-1.787	0.756	-0.287	0.000
	H14-C12-C2-HC1	0.000	0.000	0.318	0.000
	H14-C12-C2-HC2	0.000	0.000	0.318	0.000
	H15-C12-C2-HC1	0.000	0.000	0.318	0.000
	H15-C12-C2-HC2	0.000	0.000	0.318	0.000
	NA1-C12-C2-HC1	0.000	0.000	0.088	0.000
	NA1-C12-C2-HC2	0.000	0.000	0.088	0.000
	CS1-C2-C12-HC14	0.000	0.000	0.366	0.000
	CS1-C2-C12-HC15	0.000	0.000	0.366	0.000
	NA1-CR-NA2-CW2	0.000	4.650	0.000	0.000
	NA2-CR-NA1-CW1	0.000	4.650	0.000	0.000
MeOH	HM1-CA1-OA-HOW	0.000	0.000	0.450	0.000
	HM2-CA1-OA-HOW	0.000	0.000	0.450	0.000
	HM3-CA1-OA-HOW	0.000	0.000	0.450	0.000
MeCN	HM1-CM-CN-NC	0.000	0.000	0.000	0.000
	HM2-CM-CN-NC	0.000	0.000	0.000	0.000
	HM3-CM-CN-NC	0.000	0.000	0.000	0.000
DMSO	HM1-CM1-S-CM2	0.000	0.000	0.647	0.000
	HM1-CM1-S-O	0.000	0.000	0.647	0.000
	HM2-CM1-S-CM2	0.000	0.000	0.647	0.000
	HM2-CM1-S-O	0.000	0.000	0.647	0.000

HM3-CM1-S-CM2	0.000	0.000	0.647	0.000
HM3-CM1-S-O	0.000	0.000	0.647	0.000
CM1-S-CM2-HM4	0.000	0.000	0.647	0.000
CM1-S-CM2-HM5	0.000	0.000	0.647	0.000
CM1-S-CM2-HM6	0.000	0.000	0.647	0.000
O-S-CM2-HM4	0.000	0.000	0.647	0.000
O-S-CM2-HM5	0.000	0.000	0.647	0.000
O-S-CM2-HM6	0.000	0.000	0.647	0.000

(B1) Lopes, J. N. C.; Deschamps, J.; Pádua, A. A. H. Modeling Ionic Liquids Using a Systematic All-Atom Force Field. *J. Phys. Chem. B*, **2004,** *108*, 2038–2047.

(B2) Lopes, J. N C.; Pádua, A. A. H. Molecular Force Field for Ionic Liquids III: Imidazolium, Pyridinium, and Phosphonium Cations; Chloride, Bromide, and Dicyanamide Anions. *J. Phys. Chem. B* **2006,** *110*, 19586–19592.

(B3) Kaminski, G.; Jorgensen, W. L. Performance of the AMBER94, MMFF94, and OPLS-AA Force Fields for Modeling Organic Liquids. *J. Phys. Chem.* **1996,** *100*, 18010–18013.

(B4) Price, M. L. P.; Ostrovsky, D.; Jorgensen, W. L. Gas-Phase and Liquid-State Properties of Esters, Nitriles, and Nitro Compounds with the OPLS-AA Force Field. *J. Comput. Chem.* **2001,** *22*, 1340–1352.

(B5) Zheng, Y.-J.; Ornstein, R. L. A Molecular Dynamics and Quantum Mechanics Analysis of the Effect of DMSO on Enzyme Structure and Dynamics: Subtilisin. *J. Am. Chem. Soc.* **1996,** *118*, 4175–4180.

(B6) Vasudevan, V.; Mushrif, S. H. Insights into the Solvation of Glucose in Water, Dimethyl Sulfoxide (DMSO), Tetrahydrofuran (THF) and *N,N*-Dimethylformamide (DMF) and Its Possible Implications on the Conversion of Glucose to Platform Chemicals. *RSC Adv.* **2015,** *5*, 20756–20763.

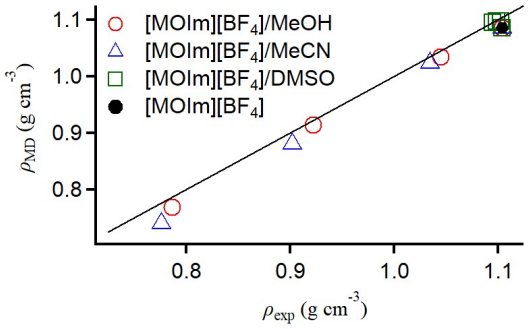

Figure B5. Plots of MD Simulation Densities ρ_{MD} vs. Experimental Densities ρ_{exp} of neat [MOIm][BF_4] and [MOIm][BF_4] mixtures with MeOH, MeCN, and DMSO with X_{ML} = 0.6 and 0.9 at 298.2 K.

B. 2. Quantum Chemistry Calculation

Table B2. Atom coordination parameters of the optimized $[MOIm]^+$, $[BF_4]^-$, MeOH, MeCN, and DMSO Calculated by the B3LYP/6-311++G(d,p) Level of Theory.

$[MOIm]^+$.

Center Number	Atomic Number	Atomic Type	Coordinates (Angstroms) X	Y	Z
1	6	0	3.411096	-1.178369	-0.714072
2	6	0	4.617674	-0.624064	-1.013559
3	6	0	3.709623	0.551722	0.616044
4	7	0	2.859182	-0.431414	0.308456
5	1	0	2.909485	-2.033214	-1.134459
6	1	0	5.360702	-0.906971	-1.739816
7	1	0	3.554832	1.297525	1.378033
8	6	0	1.526098	-0.648845	0.922523
9	1	0	1.449867	-1.715286	1.142780
10	1	0	1.528323	-0.116034	1.874884
11	7	0	4.787085	0.458302	-0.171440
12	6	0	5.958610	1.346605	-0.140111
13	1	0	6.082242	1.818089	-1.114505
14	1	0	5.800556	2.113757	0.615155
15	1	0	6.847158	0.768236	0.111273
16	6	0	0.380367	-0.177558	0.024712
17	1	0	0.423306	-0.709041	-0.932251
18	1	0	0.511134	0.887267	-0.197685
19	6	0	-0.985245	-0.410821	0.684985
20	1	0	-1.101473	-1.476737	0.915938
21	1	0	-1.021643	0.118680	1.644965
22	6	0	-2.155932	0.049227	-0.192915
23	1	0	-2.118330	-0.480389	-1.152989
24	1	0	-2.037431	1.114889	-0.425309
25	6	0	-3.524637	-0.178833	0.459086
26	1	0	-3.641698	-1.244719	0.692151
27	1	0	-3.560669	0.349641	1.420148
28	6	0	-4.697504	0.279912	-0.414820
29	1	0	-4.661824	-0.248066	-1.376467
30	1	0	-4.580856	1.346056	-0.648430
31	6	0	-6.068040	0.053243	0.233886
32	1	0	-6.103891	0.580735	1.194689
33	1	0	-6.184892	-1.011970	0.466894
34	6	0	-7.234032	0.514138	-0.644913
35	1	0	-8.194495	0.338573	-0.154011
36	1	0	-7.165592	1.583797	-0.865836
37	1	0	-7.247135	-0.021164	-1.599330
Rotational constants (GHz):			2.8861246	0.1410664	0.1404856

$[BF_4]^-$.

Center Number	Atomic Number	Atomic Type	Coordinates (Angstroms) X	Y	Z
1	9	0	0.818148	0.818148	0.818148
2	9	0	-0.818148	-0.818148	0.818148
3	9	0	0.818148	-0.818148	-0.818148
4	9	0	-0.818148	0.818148	-0.818148
5	5	0	0.000000	0.000000	0.000000
Rotational constants (GHz):			4.9675917	4.9675917	4.9675917

MeOH.

Center Number	Atomic Number	Atomic Type	Coordinates (Angstroms) X	Y	Z
1	6	0	0.667672	-0.020306	0.000000
2	1	0	1.083940	0.987432	-0.000001
3	1	0	1.028567	-0.544973	-0.893244
4	1	0	1.028567	-0.544971	0.893245
5	8	0	-0.749784	0.122117	0.000000
6	1	0	-1.148834	-0.752592	0.000000
Rotational constants (GHz):			128.0433562	24.6414553	23.794049

MeCN.

Center Number	Atomic Number	Atomic Type	Coordinates (Angstroms) X	Y	Z
1	6	0	0.000000	0.000000	-1.176150
2	1	0	0.000000	1.024910	-1.552841
3	1	0	-0.887598	-0.512455	-1.552841
4	1	0	0.887598	-0.512455	-1.552841
5	6	0	0.000000	0.000000	0.280499
6	7	0	0.000000	0.000000	1.433204
Rotational constants (GHz):			159.1253204	9.2451372	9.2451372

DMSO.

Center Number	Atomic Number	Atomic Type	Coordinates (Angstroms) X	Y	Z
1	16	0	0.000001	0.234317	-0.444120
2	8	0	0.000017	1.500306	0.386766
3	6	0	-1.369676	-0.813548	0.184843
4	1	0	-2.295689	-0.294642	-0.060786
5	1	0	-1.343964	-1.786577	-0.309424
6	1	0	-1.274322	-0.913131	1.267048
7	6	0	1.369661	-0.813573	0.184842
8	1	0	1.274307	-0.913140	1.267048
9	1	0	1.343927	-1.786607	-0.309414
10	1	0	2.295683 -	0.294688	-0.060796
Rotational constants (GHz):			6.7929108	6.6990013	4.0730769

B. 3. Liquid Property

Table B3. Liquid Properties, Density ρ, Surface Tension γ, Viscosity η, and Electrical Conductivity σ, of [MOIm][BF_4] mixtures with MeOH, MeCN, and DMSO at 293 K.

ML Mole Fraction, X_{ML}	ρ [a] (g/mL)	γ [b] (mN/m)	η [c] (cP)	σ [c] (mS/cm)
	[MOIm][BF_4]/MeOH			
0 ([MOIm][BF_4])	1.108	33.4	459	0.771
0.2	1.096	33.0	158	1.19
0.4	1.078	31.8	56.1	2.20
0.6	1.049	29.8	17.6	6.13
0.7	1.026	28.4	10.3	9.94
0.8	0.990	26.8	4.62	17.6
0.9	0.928	25.2	1.82	23.5
0.95	0.875	24.1	1.18	21.9
0.97	0.847	23.8	0.918	18.0
0.99	0.812	23.0	0.734	9.90
1 (MeOH)	0.792	22.7	0.645	–
	[MOIm][BF_4]/MeCN			
0.2	1.092	32.9	137	2.38
0.4	1.072	32.7	40.7	2.82
0.6	1.047	32.9	12.5	8.21
0.7	1.027	33.4	6.47	12.5
0.8	1.006	33.8	3.00	15.3
0.9	0.940	32.7	1.07	33.4
0.95	0.873	31.3	0.753	39.7
0.97	0.834	30.1	0.533	32.9
0.99	0.803	29.8	0.419	17.6
1 (MeCN)	0.782	29.2	0.374	–
	[MOIm][BF_4]/DMSO			
0.2	1.108	33.8	221	1.40
0.4	1.107	34.9	93.3	1.44
0.6	1.106	36.0	35.2	3.09
0.7	1.106	36.9	19.2	3.93
0.8	1.104	38.4	9.82	7.82
0.9	1.104	40.3	4.76	9.79
0.95	1.103	41.7	3.17	8.07
0.97	1.102	42.4	2.70	7.39
0.99	1.101	43.0	2.30	3.07
1 (DMSO)	1.101	43.3	2.13	–

[a] ±0.1%. [b] ±1%. [c] ±5%.

B. 4. Analysis of Low-frequency Spectra

Table B4. Biexponential Fit Parameters for Kerr Transients of [MOIm][BF_4]/MeOH, [MOIm][BF_4]/MeCN, and [MOIm][BF_4]/DMSO at 293 K.

Mole Fraction X	a_0	a_1	τ_1 (ps)	a_2	τ_2 (ps)
		[MOIm][BF_4]/MeOH			
0 ([MOIm][BF_4])	0.00018	0.00375	1.45	0.00133	9.79
0.20	0.00034	0.00455	1.42	0.00154	9.70
0.40	0.00050	0.00523	1.39	0.00182	9.13
0.60	0.00102	0.00588	1.27	0.00238	6.30
0.70	0.00118	0.00782	1.04	0.00286	5.40
0.80	0.00152	0.00941	0.78	0.00412	4.26
0.90	0.00153	0.02018	0.65	0.00473	4.01
0.95	0.00121	0.03140	0.55	0.00469	3.68
0.97	0.00093	0.03285	0.47	0.00430	3.34
0.99	0.00045	0.06082	0.46	0.00311	2.96
1 (MeOH)	0 (Fixed)	0.09552	0.40	0.00247	2.55
		[MOIm][BF_4]/MeCN			
0.20	0.00035	0.00522	1.45	0.00155	9.77
0.40	0.00055	0.00610	1.51	0.00218	9.51
0.60	0.00082	0.00924	1.53	0.00357	9.42
0.70	0.00096	0.01110	1.65	0.00514	8.98
0.80	0.00071	0.01751	1.67	0.00775	8.94
0.90	0.00055	0.03321	1.78	0.01084	7.21
0.95	0.00037	0.05466	1.64	0.01240	5.46
0.97	0.00029	0.06927	1.63	0.01076	5.01
0.99	0 (Fixed)	0.09429	1.54	0.00840	4.04
1 (MeCN)	0 (Fixed)	0.10434	1.53	0.00829	2.31
		[MOIm][BF_4]/DMSO			
0.20	0.00029	0.00509	1.36	0.00149	9.41
0.40	0.00029	0.00547	1.35	0.00159	8.50
0.60	0.00036	0.00629	1.26	0.00180	7.79
0.70	0.00047	0.00627	1.23	0.00187	7.42
0.80	0.00041	0.00763	1.16	0.00221	7.00
0.90	0.00037	0.00845	1.13	0.00238	6.59
0.95	0.00018	0.00848	1.07	0.00276	6.37
0.97	0.00014	0.00958	1.04	0.00278	6.36
0.99	0.00002	0.00986	1.04	0.00309	6.20
1 (DMSO)	0 (Fixed)	0.01072	1.01	0.00315	6.04

Table B5. Fit Parameters for Fourier Transform Kerr Spectra of [MOIm][BF_4]/MeOH, [MOIm][BF_4]/MeCN, and [MOIm][BF_4]/DMSO. Intermolecular (mainly).

ML Mole Fraction, X_{ML}	M_1 (cm^{-1})	$a_{O,1}$	$\omega_{O,1}$ (cm^{-1})	$a_{O,2}$	$\omega_{O,2}$ (cm^{-1})	$a_{G,1}$	$\omega_{G,1}$ (cm^{-1})	$\Delta\omega_{G,1}$ (cm^{-1})	$a_{G,2}$	$\omega_{G,2}$ (cm^{-1})	$\Delta\omega_{G,2}$ (cm^{-1})	$a_{G,3}$	$\omega_{G,3}$ (cm^{-1})	$\Delta\omega_{G,3}$ (cm^{-1})
[MOIm][BF_4]/MeOH														
0 ([MOIm][BF_4])	69.2	0.028	3.3	0.033	14.3	0.219	44.6	65.2	0.221	98.4	65.1	-	-	-
0.20	68.7	0.035	3.3	0.033	14.0	0.211	43.2	64.8	0.216	97.1	66.2	-	-	-
0.40	68.3	0.039	3.3	0.034	14.0	0.170	41.2	57.8	0.230	92.3	69.6	-	-	-
0.60	67.9	0.037	3.7	0.032	13.9	0.178	40.0	61.7	0.211	93.1	70.4	-	-	-
0.70	68.4	0.029	4.2	0.028	14.0	0.157	36.3	63.4	0.198	90.9	74.5	-	-	-
0.80	70.5	0.040	8.6	-	-	0.153	17.5	53.1	0.245	72.3	96.2	0.012	175	34.4
0.90	72.7	0.035	8.5	-	-	0.088	23.2	44.4	0.332	38.8	127	0.019	216	85.1
0.95	74.0	0.029	8.9	-	-	0.088	23.8	48.9	0.249	44.3	129	0.019	219	95.4
0.97	75.8	0.024	9.8	-	-	0.074	29.3	48.2	0.216	46.8	132	0.018	221	93.3
0.99	78.3	0.021	9.1	-	-	0.089	26.9	53.1	0.153	60.3	132	0.017	226	92.7
1 (MeOH)	79.3	0.017	9.6	-	-	0.084	30.9	52.5	0.122	75.3	124	0.020	229	98.7
[MOIm][BF_4]/MeCN														
0.20	68.8	0.039	3.0	0.037	12.4	0.282	39.2	72.7	0.215	98.7	65.9	-	-	-
0.40	67.9	0.052	3.1	0.042	11.8	0.300	38.0	67.0	0.259	94.9	68.0	-	-	-
0.60	67.5	0.088	3.0	0.054	11.7	0.370	41.0	63.2	0.301	95.6	67.0	0.012	155	33.8
0.70	66.6	0.126	2.9	0.066	11.1	0.443	40.6	64.4	0.317	95.7	66.7	0.017	161	41.4
0.80	65.6	0.256	2.4	0.105	9.4	0.559	29.8	67.1	0.420	87.8	74.8	0.019	174	51.0
0.90	64.9	0.484	2.6	0.157	9.6	0.785	36.2	72.9	0.179	82.0	132	0.217	96.2	59.2
0.95	62.4	0.691	2.8	0.204	10.0	0.956	40.5	74.1	0.189	90.8	124	0.179	100	57.2

0.97	61.2	0.883	2.8	0.241	10.0	1.073	41.4	74.3	0.195	94.6	124	0.175	101	56.5
0.99	59.5	1.084	3.1	0.259	10.9	1.591	29.5	93.7	0.263	84.6	123	-	-	-
1 (MeCN)	58.3	1.200	3.1	0.291	10.7	1.693	29.5	92.3	0.267	85.3	121	-	-	-
[MOIm][BF_4]/DMSO														
0.20	68.9	0.031	3.3	0.030	15.2	0.207	48.8	62.9	0.166	103	59.7	-	-	-
0.40	68.2	0.035	3.4	0.028	15.4	0.207	51.2	64.2	0.137	104	59.0	-	-	-
0.60	67.3	0.034	3.6	0.025	15.1	0.197	51.1	65.0	0.117	105	58.5	-	-	-
0.70	66.5	0.035	3.6	0.023	14.7	0.195	51.1	66.8	0.057	110	52.8	-	-	-
0.80	65.3	0.028	4.4	0.019	15.5	0.199	54.9	79.9	0.012	112	36.8	-	-	-
0.90	64.9	0.034	4.4	0.016	17.0	0.186	58.5	92.6	-	-	-	-	-	-
0.95	63.8	0.040	4.6	0.014	24.0	0.133	71.4	82.2	-	-	-	-	-	-
0.97	62.7	0.040	4.6	0.014	22.7	0.136	69.0	82.0	-	-	-	-	-	-
0.99	62.1	0.041	4.6	0.014	21.9	0.140	67.2	81.9	-	-	-	-	-	-

Intramolecular.

ML Mole Fraction, X_{ML}	$a_{L,1}$	$\omega_{L,1}$ (cm^{-1})	$\Delta\omega_{L,1}$ (cm^{-1})	$a_{L,2}$	$\omega_{L,2}$ (cm^{-1})	$\Delta\omega_{L,2}$ (cm^{-1})
[MOIm][BF_4]/MeOH						
0 ([MOIm][BF_4])	29.2	172	30.4	14.1	217	27.4
0.20	27.9	171	30.6	9.02	217	24.4
0.40	32.1	171	32.6	8.88	217	24.3
0.60	29.9	171	32.2	12.7	217	28.3
0.70	27.6	171	32.0	19.7	217	31.4
0.80	-	-	-	17.3	216	30.2
0.90	-	-	-	-	-	-
0.95	-	-	-	-	-	-
0.97	-	-	-	-	-	-
0.99	-	-	-	-	-	-
1 (MeOH)	-	-	-	-	-	-
[MOIm][BF_4]/MeCN						
0.20	24.9	171	29.0	10.4	216	25.5
0.40	27.5	172	30.1	5.96	215	22.6
0.60	15.0	175	23.8	21.8	214	32.3
0.70	24.5	177	32.8	12.2	215	27.0
0.80	24.2	171	35.3	10.5	219	25.2
0.90	-	-	-	-	-	-
0.95	-	-	-	-	-	-
0.97	-	-	-	-	-	-
0.99	-	-	-	-	-	-
1 (MeCN)	-	-	-	-	-	-
[MOIm][BF_4]/DMSO						
0.20	37.8	172	33.5	4.47	215	17.1
0.40	36.7	171	34.8	2.83	216	15.2
0.60	24.3	171*	32.5	2.42	216*	13.6
0.70	24.8	171*	34.8	1.59	216*	14.6
0.80	13.5	171*	33.0	-	-	-
0.90	4.32	171*	39.1	-	-	-
0.95	-	-	-	-	-	-
0.97	-	-	-	-	-	-
0.99	-	-	-	-	-	-
1 (DMSO)	-	-	-	-	-	-

* Fixed

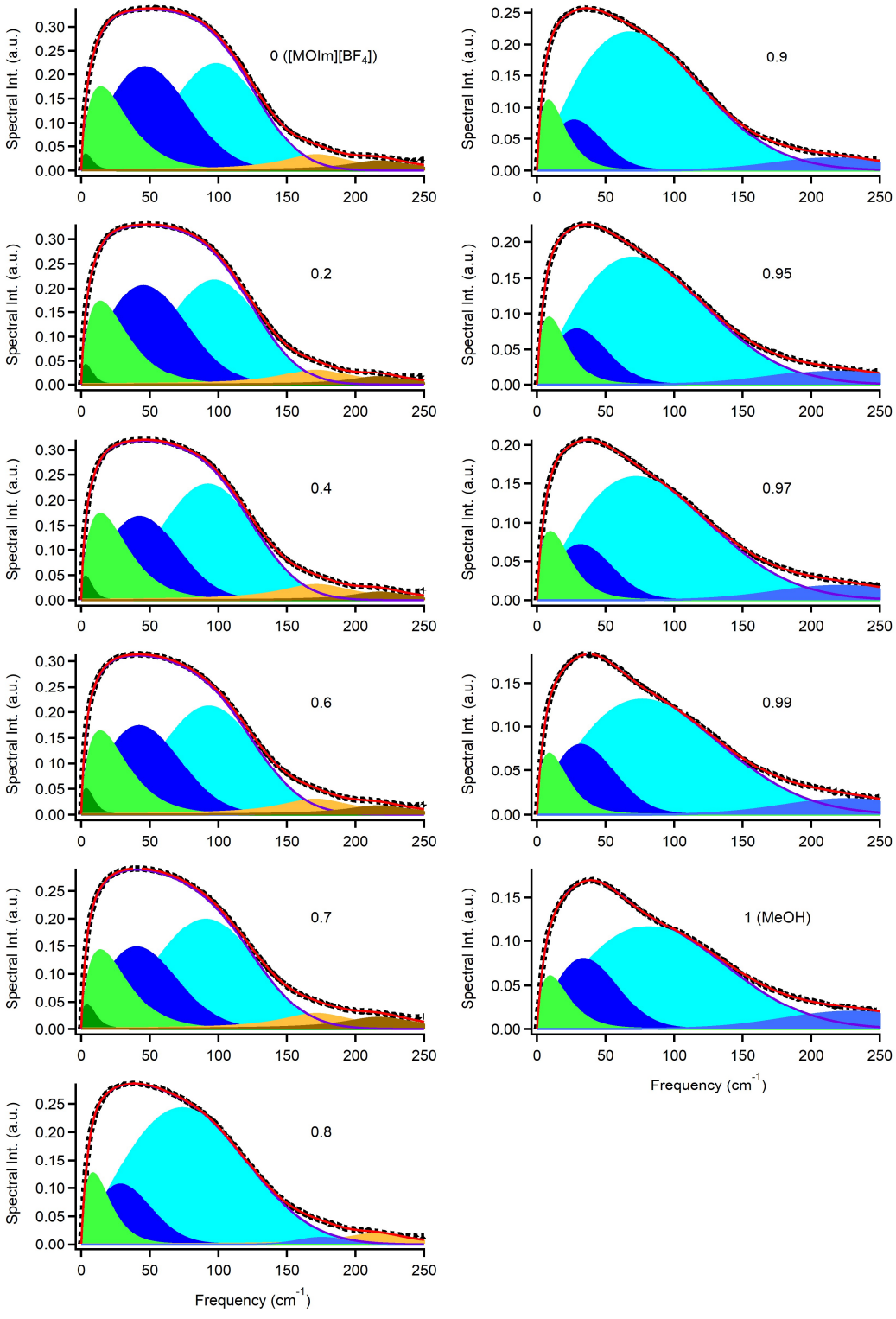

Figure B6. Line-Shape Analysis Results for Low-Frequency Spectra of [MOIm][BF_4] Mixtures with MeOH.

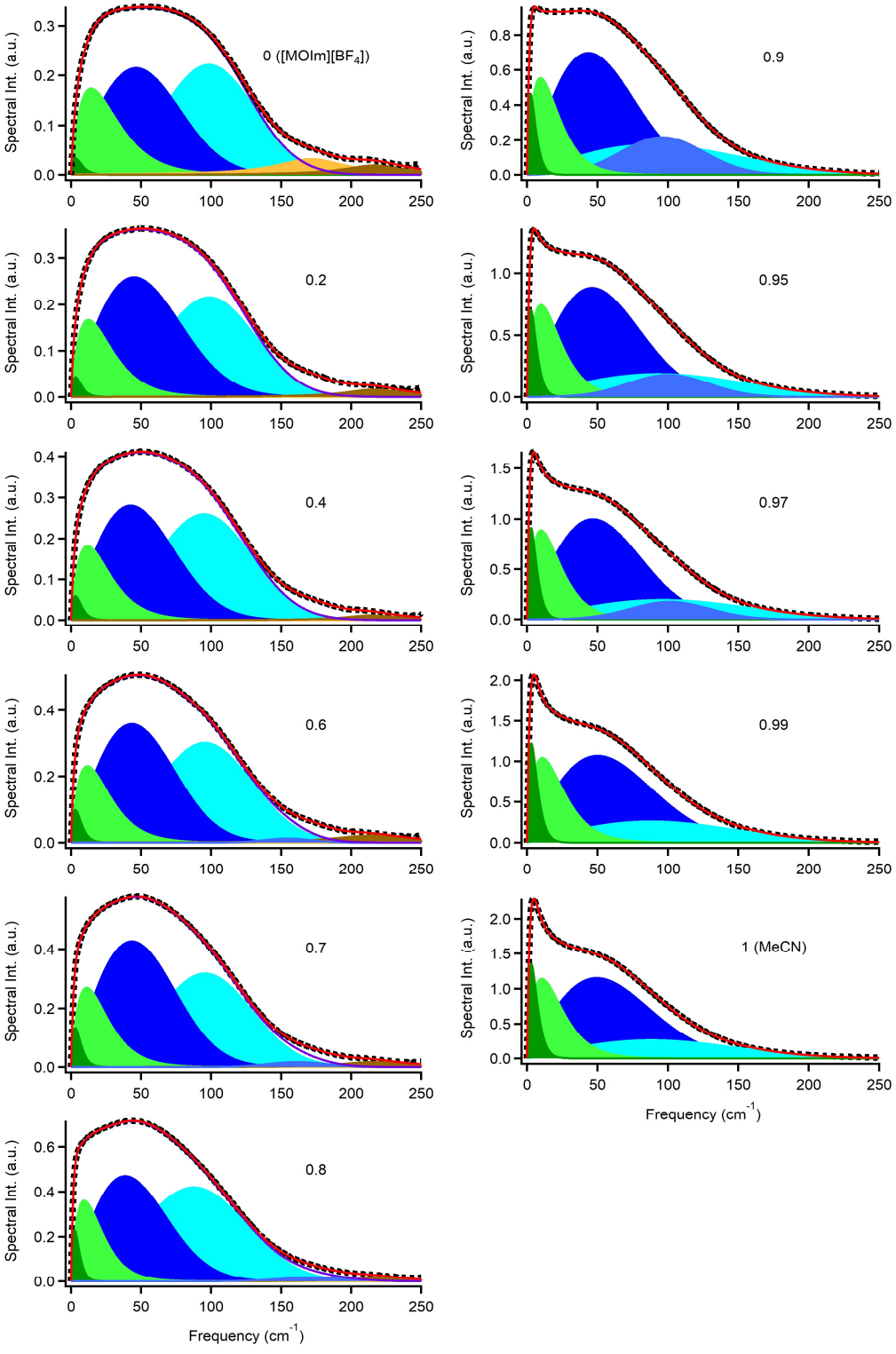

Figure B7. Line-Shape Analysis Results for Low-Frequency Spectra of [MOIm][BF_4] Mixtures with MeCN.

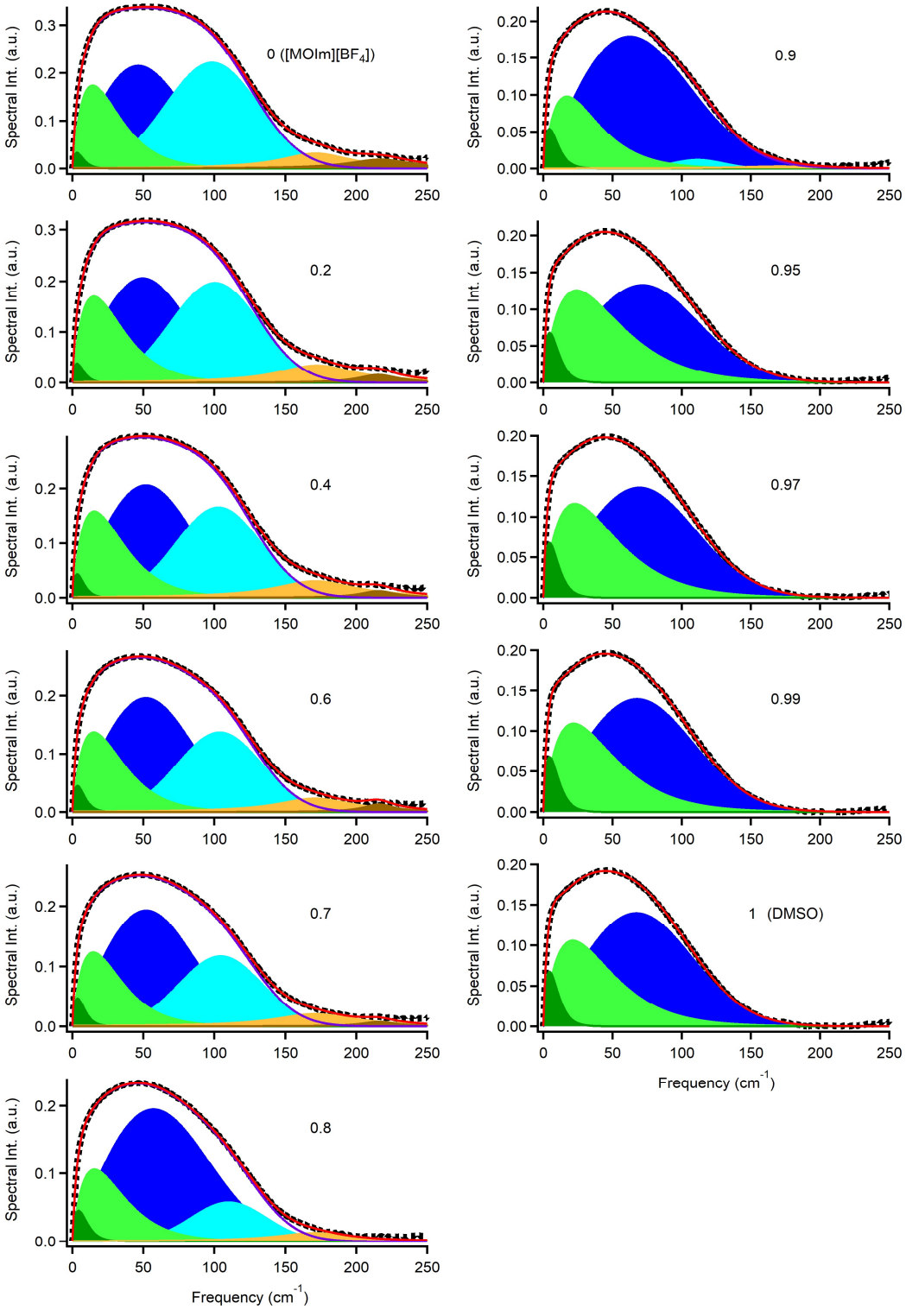

Figure B8. Line-Shape Analysis Results for Low-Frequency Spectra of [MOIm][BF_4] Mixtures with DMSO.

C. Appendix to Chapter IV

C. 1. Molecular Dynamics Simulation

Table C1. Numbers of Molecules in MD Cell of [MOIm][BF_4]/FA, [MOIm][BF_4]/NMF, and [MOIm][BF_4]/DMF Systems.

	Nos. of ion pairs and molecules in an MD cell				
X_{FA}	$N_{[MOIm][BF4]}$	N_{FA}	ρ_{MD}[a] (g cm^{-3})	ρ_{exp}[a] (g cm^{-3})	cell size, l (Å)
0	195		1.093	1.104	43.72
0.6	161	241	1.105	1.104	43.89
0.9	85	769	1.115	1.114	44.37
1		1367	1.115	1.129	45.09
	Nos. of ion pairs and molecules in an MD cell				
X_{NMF}	$N_{[MOIm][BF4]}$	N_{NMF}	ρ_{MD} (g cm^{-3})	ρ_{exp} (g cm^{-3})	cell size, l (Å)
0.6	148	222	1.069	1.076	44.00
0.9	67	600	1.019	1.034	44.58
1		911	0.9749	0.9993	45.09
	Nos. of ion pairs and molecules in an MD cell				
X_{DMF}	$N_{[MOIm][BF4]}$	N_{DMF}	ρ_{MD} (g cm^{-3})	ρ_{exp} (g cm^{-3})	cell size, l (Å)
0.6	137	205	1.042	1.060	44.05
0.9	55	492	0.9660	0.9940	44.56
1		683	0.9148	0.9442	44.92

[a] Densities derived from MD simulations, ρ_{MD}, and experimentally determined, ρ_{exp}, at 298.2 K. MD cell size l represents the length of one side of the cube.

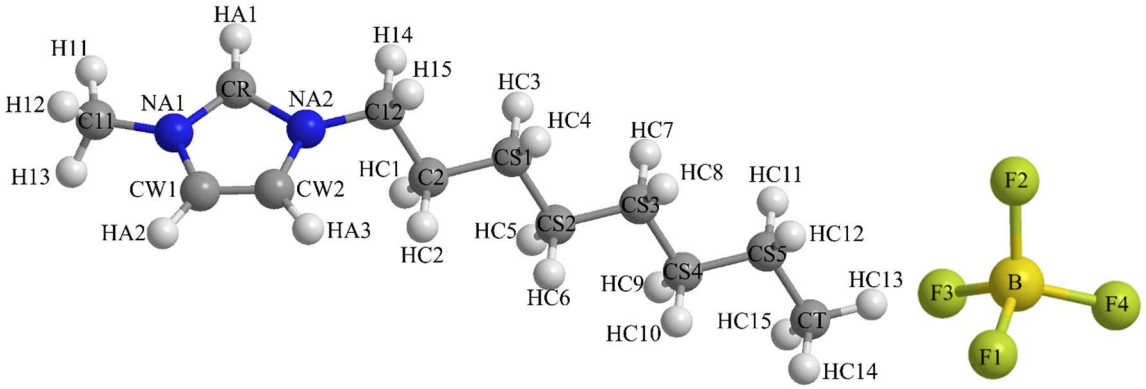

Figure C1. Structures of $[MOIm]^+$ and $[BF_4]^-$.

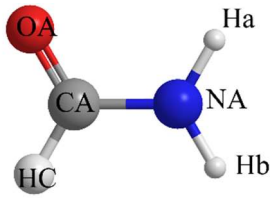

Figure C2. Structure of FA.

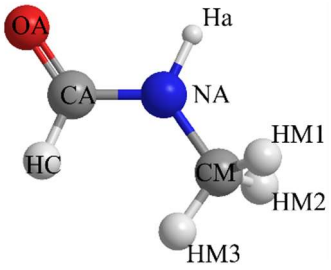

Figure C3. Structure of NMF.

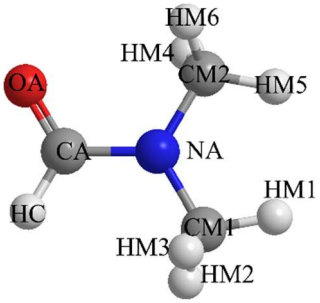

Figure C4. Structure of DMF.

Table C2. Force Filed Parameters Used for $[MOIm]^+$,[C1,C2] $[BF_4]^-$,[C3] FA,[C4] NMF,[C4] and DMF.[C4] Notation of Atoms within Molecules is Depicted in Figures C1–C4.

Point Charge and van der Walls Parameters.

	Atom	Charge (e)	σ (Å)	ε (kcal mol^{-1})
$[MOIm]^+$	NA*	0.150	3.250	0.170
	CR	-0.110	3.550	0.070
	HA*	0.210	2.420	0.030
	CW*	-0.130	3.550	0.070
	C1*	-0.170	3.500	0.066
	H1*	0.130	2.500	0.030
	C2	0.010	3.500	0.066
	HC*	0.060	2.500	0.030
	CS*	-0.120	3.500	0.066
	CT	-0.180	3.500	0.066
$[BF_4]^-$	B	0.960	3.580	0.095
	F*	-0.490	3.120	0.061
FA	CA	0.500	3.750	0.105
	OA	-0.500	2.960	0.210
	NA	-0.760	3.250	0.170
	Ha	0.380	0.000	0.000
	Hb	0.380	0.000	0.000
	HC	0.000	2.420	0.015
NMF	CA	0.500	3.750	0.105
	OA	-0.500	2.960	0.210
	NA	-0.500	3.250	0.170
	Ha	0.300	0.000	0.000
	HC	0.000	2.420	0.015
	CM	0.020	3.500	0.066
	HM*	0.060	2.500	0.030
DMF	CA	0.500	3.750	0.105
	OA	-0.500	2.960	0.210
	NA	-0.140	3.250	0.170
	HC	0.000	2.420	0.015
	CM*	-0.110	3.500	0.066
	HM*	0.060	2.500	0.030

X* means chemically equivalent X atoms in $[MOIm]^+$,$[BF_4]^-$, NMF, and DMF as depicted in Figures C1–C4.

Intramolecular Atom-Atom Bond Lengths.

	Bond	*r* (Å)
$[MOIm]^+$	CR-NA*	1.315
	C1*-H1*	1.090
	NA*-C1*	1.466
	CR-HA*	1.080
	CW*-NA*	1.378
	CW*-CW*	1.341
	CW1-HA*	1.080
	C1*-C2	1.529
	C2-HC*	1.090
	C2-CS*	1.529
	CS1-HC*	1.090
	CS*-CS*	1.529
	CS*-CT	1.529
	CT-HC*	1.090
$[BF_4]^-$	B-F*	1.394
FA	N-Ha	1.010
	N-Hb	1.010
	CA-NA	1.335
	CA-OA	1.229
	CA-HC	1.090
NMA	N-Ha	1.010
	CA-NA	1.335
	CA-OA	1.229
	CA-HC	1.090
	CM-NA	1.149
	CM-HM*	1.090
DMA	CA-NA	1.335
	CA-OA	1.229
	CA-HC	1.090
	CM*-NA	1.149
	CM*-HM*	1.090

X* means chemically equivalent X atoms in $[MOIm]^+$ and $[BF_4]^-$, NMF, and DMF as depicted in Figures C1–C4.

Bond Angle Potentials.

	Angle	K (kcal mol^{-1} degree^{-2})	θ (degree)
$[MOIm]^+$	H1*-C1*-H1*	33.00	107.8
	H1*-C1*-NA*	37.50	110.7
	C1*-NA*-CR	70.00	126.4
	C1*-NA*-CW*	70.00	125.6
	NA*-CR-HA*	35.00	125.1
	NA*-CR-NA*	70.00	109.8
	CR-NA*-CW*	70.00	108.0
	NA*-CW*-CW*	70.00	107.1
	NA*-CW*-HA*	35.00	122.0
	HA*-CW*-CW*	35.00	130.9
	NA*-C1*-C2	58.30	112.7
	H1*-C1*-C2	37.50	110.7
	C1*-C2-HC*	37.50	110.7
	C1*-C2-CS*	58.30	112.7
	HC*-C2-CS*	37.50	110.7
	HC*-CS*-C2	37.50	110.7
	HC*-CS*-CS*	37.50	110.7
	HC*-CS*-CT	37.50	110.7
	HC*-CT-CS*	37.50	110.7
	HC*-CT-HC*	33.00	107.8
	HC*-C2-HC*	33.00	107.8
	HC*-CS*-HC*	33.00	107.8
	C2-CS*-CS*	58.30	112.7
	CS*-CS*-CS*	58.30	112.7
	CS*-CS*-CT	58.30	112.7
$[BF_4]^-$	F*-B-F*	80.01	109.5
FA	HC-CA-NA	40.00	114.0
	HC-CA-OA	35.00	123.0
	OA-CA-NA	80.00	122.9
	CA-NA-Ha	35.00	119.8
	CA-NA-Hb	35.00	119.8
	Ha-NA-Hb	35.00	120.0
NMF	HC-CA-NA	40.00	114.0
	HC-CA-OA	35.00	123.0
	OA-CA-NA	80.00	122.9
	CA-NA-Ha	35.00	119.8
	CM-NA-Ha	38.00	118.4
	CM-NA-CA	50.00	121.9
	NA-CM-HM*	35.00	109.5
	HM*-CM-HM*	33.00	107.8
DMF	HC-CA-NA	40.00	114.0
	HC-CA-OA	35.00	123.0
	OA-CA-NA	80.00	122.9

CM*-NA-CM*	50.00	118.0
CA-NA-CM*	50.00	121.9
NA-CM-HM*	35.00	109.5
HM*-CM-HM*	33.00	107.8

X* means chemically equivalent X atoms in $[MOIm]^+$ and $[BF_4]^-$, NMF, and DMF as depicted in Figures C1–C4.

Torsion Potentials

	Dihedral	V_1 (kcal mol^{-1})	V_2 (kcal mol^{-1})	V_3 (kcal mol^{-1})	V_4 (kcal mol^{-1})
$[MOIm]^+$	CR-NA*-C1*-H1*	0.000	0.000	0.000	0.000
	CW*-NA*-C1*-H1*	0.000	0.000	0.124	0.000
	C1*-NA*-CR-HA*	0.000	4.650	0.000	0.000
	NA*-CR-NA*-C1*	0.000	4.650	0.000	0.000
	CW*-CW*-NA-C1*	0.000	3.000	0.000	0.000
	C1*-NA*-CW*-HA*	0.000	3.000	0.000	0.000
	NA*-CW*-CW*-HA*	0.000	10.750	0.000	0.000
	NA*-CW*-CW*-NA*	0.000	10.750	0.000	0.000
	CW*-NA*-CR-HA*	0.000	4.650	0.000	0.000
	CR-NA*-CW*-HA*	0.000	3.000	0.000	0.000
	CR-NA*-CW*-CW*	0.000	3.000	0.000	0.000
	C1*-C2-CS*-HC*	0.000	0.000	0.366	0.000
	HC*-C2-CS*-HC*	0.000	0.000	0.318	0.000
	HC*-CS*-CS*-HC*	0.000	0.000	0.318	0.000
	HC*-CS*-CT-HC*	0.000	0.000	0.318	0.000
	HC*-CS*-CS*-CT	0.000	0.000	0.366	0.000
	C1*-C2-CS*-CS*	1.739	-0.157	0.279	0.000
	C2-CS*-CS*-CS*	1.739	-0.157	0.279	0.000
	CS*-CS*-CS*-CS*	1.739	-0.157	0.279	0.000
	CS*-CS*-CS*-CT	1.739	-0.157	0.279	0.000
	CS*-CS*-CS*-HC*	0.000	0.000	0.366	0.000
	C2-CS*-CS*-HC*	0.000	0.000	0.366	0.000
	CS*-CS*-C2-HC*	0.000	0.000	0.366	0.000
	CS*-CS*-CT-HC*	0.000	0.000	0.366	0.000
	HA*-CW*-CW*-HA*	0.000	10.750	0.000	0.000
	CW*-NA*-C1*-C2	-1.709	1.459	0.190	0.000
	CR-NA*-C1*-C2	-1.259	0.000	0.000	0.000
	NA*-C1*-C2-CS*	-1.787	0.756	-0.287	0.000
	H1*-C1*-C2-HC*	0.000	0.000	0.318	0.000
	NA*-C1*-C2-HC*	0.000	0.000	0.088	0.000
	CS*-C2-C1*-H1*	0.000	0.000	0.366	0.000
	NA*-CR-NA*-CW*	0.000	4.650	0.000	0.000
FA	OA-CA-NA-Ha	0.000	4.900	0.000	0.000
	OA-CA-NA-Hb	0.000	4.900	0.000	0.000
	HC-CA-NA-Ha	0.000	4.900	0.000	0.000
	HC-CA-NA-Hb	0.000	4.900	0.000	0.000

NMF	OA-CA-NA-Ha	0.000	4.900	0.000	0.000
	HC-CA-NA-Ha	0.000	4.900	0.000	0.000
	HM*-CM-NA-Ha	0.000	0.000	0.000	0.000
	CM-NA-CA-OA	0.000	6.089	0.000	0.000
	CM-NA-CA-HC	2.300	6.089	0.000	0.000
	CA-NA-CM-HM*	0.000	0.000	-0.139	0.000
DMF	CM*-NA-CM*-HM*	0.000	0.000	0.000	0.000
	CM*-NA-CA-OA	0.000	6.089	0.000	0.000
	CM*-NA-CA-HC	2.300	6.089	0.000	0.000
	CA-NA-CM*-HM*	0.000	0.000	-0.139	0.000

X* means chemically equivalent X atoms in $[MOIm]^+$ and $[BF_4]^-$, NMF, and DMF as depicted in Figures C1–C4.

(C1) Canongia Lopes, J. N.; Deschamps, J.; Padua, A. A. H. Modeling Ionic Liquids Using a Systematic All-Atom Force Field. *J. Phys. Chem. B* **2004**, *108*, 2038–2047.
(C2) Canongia Lopes, J. N.; Deschamps, J.; Padua, A. A. H. Modeling Ionic Liquids Using a Systematic All-Atom Force Field (Corrections). *J. Phys. Chem. B* **2004**, *108*, 11250–11250.
(C3) Canongia Lopes, J. N.; Padua, A. A. H. Molecular Force Field for Ionic Liquids III: Imidazolium, Pyridinium, and Phosphonium Cations; Chloride, Bromide, and Dicyanamide Anions. *J. Phys. Chem. B* **2006**, *110*, 19586–19592.
(C4) Jorgensen, W. L.; Maxwell, D. S.; Tirado-Rives, J. Development and Testing of the OPLS All-Atom Force Field on Conformational Energetics and Properties of Organic Liquids. *J. Am. Chem. Soc.* **1996**, *118*, 11225–11236.

C. 2. Liquid Property

Table C3. Liquid Properties, Density ρ, Molar Volume V_m, Viscosity η, Electrical Conductivity σ, and Molar Electrical Conductivity Λ, Surface Tension γ, of [MOIm][BF_4] mixtures with FA, NMF, and DMF at 293 K.

X_{ML}	ρ [a] (g cm^{-3})	V_m (cm^3 mol^{-1})	η [b] (cP)	σ [b] (mS cm^{-1})	Λ (S cm^2 mol^{-1})	γ [c] (mN m^{-1})
			[MOIm][BF_4]/FA			
0 ([MOIm][BF_4])	1.107	255	454	0.366	0.0933	32.9
0.2	1.107	212	195	0.873	0.185	34.1
0.4	1.105	169	99.0	1.76	0.298	34.4
0.6	1.106	126	42.0	4.07	0.514	35.7
0.7	1.109	105	27.4	6.24	0.653	36.7
0.8	1.112	83.2	16.0	7.90	0.657	37.7
0.9	1.118	61.5	8.31	11.7	0.720	40.0
0.95	1.124	50.6	5.66	10.8	0.548	44.6
0.97	1.128	46.2	4.84	8.17	0.378	48.5
0.99	1.132	41.9	3.94	4.25	0.178	53.4
1 (FA)	1.135	39.7	3.68	–	–	57.3
			[MOIm][BF_4]/NMF			
0.2	1.102	216	156	1.03	0.222	33.0
0.4	1.093	177	58.9	1.56	0.276	33.5
0.6	1.080	137	23.1	5.46	0.749	34.9
0.7	1.071	118	13.2	7.58	0.891	36.2
0.8	1.058	98.0	6.82	10.8	1.06	36.8
0.9	1.038	78.4	3.68	14.6	1.14	38.1
0.95	1.024	68.6	2.59	13.3	0.914	38.8
0.97	1.017	64.7	2.21	11.7	0.756	39.4
0.99	1.009	60.7	1.97	5.65	0.343	40.1
1 (NMF)	1.005	58.8	1.87	–	–	40.3
			[MOIm][BF_4]/DMF			
0.2	1.098	219	167	0.923	0.202	32.3
0.4	1.084	183	55.7	2.11	0.386	32.7
0.6	1.064	147	16.8	5.72	0.843	33.0
0.7	1.049	129	9.42	9.40	1.22	33.9
0.8	1.029	112	4.30	12.8	1.43	34.3
0.9	0.998	94.1	1.99	17.4	1.64	35.0
0.95	0.978	85.4	1.47	15.5	1.33	35.8
0.97	0.967	82.1	1.19	12.4	1.01	36.3
0.99	0.957	78.6	1.03	5.98	0.470	37.2
1 (DMF)	0.950	76.9	0.937	–	–	37.5

[a] ±0.5%. [b] ±5%. [c] ±1%.

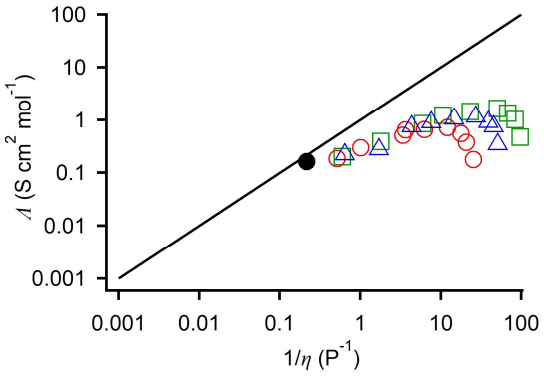

Figure C5. Walden plots for the [MOIm][BF_4] mixtures with FA (red circles), NMF (blue triangles), and DMF (green squares) and neat [MOIm][BF_4] (black filled circle). Black line denotes the ideal Walden line as a unity slope.

C. 3. Analysis of Low-frequency Spectra

Table C4. Triexponential Fit Parameters for Kerr Transients of the [MOIm][BF_4] Mixtures with FA, NMF, and DMF at 293 K.

X_{ML}	a_0	a_1	τ_1 (ps)	a_2	τ_2 (ps)	a_3	τ_3 (ps)
[MOIm][BF_4]/FA							
0 ([MOIm][BF_4])	0.000042	0.00300	2.22	0.00078	11.3	0.00042	145
0.20	0.000003	0.00389	1.90	0.00080	9.37	0.00073	127
0.40	–	0.00414	1.83	0.00171	8.23	0.00081	116
0.60	–	0.00663	1.63	0.00237	7.93	0.00116	86.4
0.70	–	0.00767	1.55	0.00304	7.59	0.00169	56.9
0.80	–	0.00806	1.55	0.00439	6.85	0.00240	50.3
0.90	–	0.00921	1.52	0.00715	6.01	0.00442	33.6
0.95	–	0.01517	1.30	0.00910	5.87	0.00723	25.0
0.97	–	0.01534	1.29	0.01078	5.12	0.00923	20.9
0.99	–	0.02070	1.16	0.00936	4.57	0.01382	16.5
1 (FA)	–	0.02291	1.12	0.01010	4.17	0.01627	15.6
[MOIm][BF_4]/NMF							
0.20	–	0.00430	1.93	0.00123	9.54	0.00063	117
0.40	–	0.00600	1.56	0.00202	8.41	0.00079	100
0.60	–	0.00781	1.52	0.00321	7.25	0.00143	85.3
0.70	–	0.00943	1.43	0.00427	7.05	0.00164	83.4
0.80	–	0.01144	1.42	0.00514	6.75	0.00262	51.5
0.90	–	0.01440	1.42	0.00649	6.48	0.00489	28.8
0.95	–	0.01837	1.31	0.00893	6.20	0.00591	27.5
0.97	–	0.01815	1.30	0.00993	5.51	0.00731	23.3
0.99	–	0.01978	1.23	0.01040	5.19	0.00914	20.4
1 (NMF)	–	0.02250	1.11	0.01200	4.71	0.00980	20.0
[MOIm][BF_4]/DMF							
0.20	–	0.00524	1.67	0.00151	10.4	0.00057	143
0.40	–	0.00702	1.63	0.00206	9.39	0.00090	113
0.60	–	0.01203	1.50	0.00314	8.94	0.00153	67.4
0.70	–	0.01455	1.42	0.00459	8.67	0.00183	61.6
0.80	–	0.01740	1.39	0.00694	7.76	0.00227	45.1
0.90	–	0.02282	1.25	0.01298	5.79	0.00387	22.6
0.95	–	0.02590	1.18	0.01803	5.04	0.00474	16.6
0.97	–	0.03024	1.10	0.02129	4.68	0.00510	13.0
0.99	–	0.03420	1.04	0.02569	4.46	0.00479	11.4
1 (DMF)	–	0.03788	1.01	0.03110	4.27	0.00407	9.36

Table C5. Fit Parameters for Fourier Transform Kerr Spectra of [MOIm][BF_4] Mixtures with FA, NMF, and DMF. Intermolecular (mainly).

X_{ML}	M_1 (cm^{-1})	$a_{O,1}$	$\omega_{O,1}$ (cm^{-1})	$a_{O,2}$	$\omega_{O,2}$ (cm^{-1})	$a_{G,1}$	$\omega_{G,1}$ (cm^{-1})	$\Delta\omega_{G,1}$ (cm^{-1})	$a_{G,2}$	$\omega_{G,2}$ (cm^{-1})	$\Delta\omega_{G,2}$ (cm^{-1})	$a_{G,3}$	$\omega_{G,3}$ (cm^{-1})	$\Delta\omega_{G,3}$ (cm^{-1})
[MOIm][BF_4]/FA														
0 ([MOIm][BF_4])	69.9	0.052	2.33	0.037	12.4	0.299	37.7	38.7	0.210	100	32.8	–	–	–
0.20	81.0	0.061	2.21	0.041	11.4	0.228	25.1	31.8	0.332	85.3	37.7	0.038	168	43.2[a]
0.40	89.0	0.053	2.53	0.044	11.1	0.205	20.1	28.7	0.413	80.0	38.2	0.108	171	43.2[a]
0.60	95.1	0.076	3.44	0.043	19.4	0.433	81.4	37.2	–	–	–	0.165	175	43.2[a]
0.70	98.2	0.079	3.82	0.043	21.2	0.442	83.5	35.5	–	–	–	0.203	176	43.2[a]
0.80	101	0.089	4.24	0.045	24.0	0.449	87.0	33.6	–	–	–	0.247	177	43.2[a]
0.90	106	0.110	4.29	0.050	25.3	0.501	90.0	32.8	–	–	–	0.333	179	43.2[a]
0.95	109	0.130	4.38	0.054	25.3	0.538	91.8	33.2	–	–	–	0.386	181	43.2[a]
0.97	110	0.129	4.48	0.056	26.0	0.551	93.2	33.1	–	–	–	0.418	182	43.2[a]
0.99	112	0.145	4.42	0.060	25.4	0.580	94.0	33.7	–	–	–	0.449	183	43.2[a]
1 (FA)	112	0.149	4.52	0.063	25.6	0.614	94.2	34.0	–	–	–	0.482	183	43.2
[MOIm][BF_4]/NMF														
0.20	69.0	0.060	2.45	0.041	11.7	0.327	31.4	37.4	0.253	96.0	33.6	–	–	–
0.40	68.9	0.054	2.92	0.044	12.1	0.476	34.2	46.9	0.175	104	29.8	–	–	–
0.60	68.8	0.069	3.15	0.050	12.0	0.520	35.7	46.3	0.192	106	29.5	–	–	–
0.70	70.2	0.075	3.41	0.050	13.0	0.606	39.2	54.0	0.116	110	24.3	–	–	–
0.80	72.6	0.101	3.57	0.053	13.9	0.804	32.7	60.3	0.096	113	21.8	–	–	–
0.90	77.6	0.122	3.87	0.051	16.0	0.975	29.7	68.3	0.075	115	18.7	–	–	–
0.95	77.9	0.142	4.09	0.056	17.3	0.994	32.2	69.2	0.087	116	18.4	–	–	–
0.97	79.0	0.138	4.16	0.056	17.5	1.005	32.5	70.2	0.093	116	18.3	–	–	–
0.99	79.6	0.137	4.42	0.055	18.3	1.026	31.6	71.2	0.105	117	18.8	–	–	–
1 (NMF)	80.0	0.130	4.70	0.056	19.0	1.039	32.1	71.8	0.118	117	19.5	–	–	–

[a] Fixed.

[MOIm][BF_4]/DMF														
0.20	67.9	0.049	2.76	0.041	11.7	0.474	25.7	43.8	0.186	101	32.4	–	–	–
0.40	66.2	0.067	2.84	0.046	11.3	0.492	26.5	41.9	0.194	99.8	32.7	–	–	–
0.60	63.3	0.099	2.90	0.058	10.9	0.535	27.7	38.8	0.216	96.8	33.9	–	–	–
0.70	61.5	0.109	3.14	0.064	10.7	0.553	26.7	36.8	0.242	91.8	35.5	–	–	–
0.80	60.4	0.128	3.23	0.069	10.8	0.514	22.4	35.0	0.298	80.6	39.6	–	–	–
0.90	57.3	0.142	3.95	0.069	12.8	0.592	27.2	37.0	0.252	83.6	37.9	–	–	–
0.95	55.9	0.151	4.26	0.070	14.3	0.589	26.5	38.5	0.253	77.7	40.0	–	–	–
0.97	55.2	0.158	4.59	0.068	16.2	0.577	25.7	40.6	0.247	72.8	42.4	–	–	–
0.99	54.8	0.158	4.81	0.069	17.6	0.567	25.9	43.7	0.235	62.9	47.0	–	–	–
1 (DMF)	53.9	0.161	4.99	0.068	19.1	0.550	25.7	47.0	0.226	56.0	45.3	–	–	–

Intramolecular.

X_{ML}	$a_{L,1}$	$\omega_{L,1}$ (cm^{-1})	$\Delta\omega_{L,1}$ (cm^{-1})	$a_{L,2}$	$\omega_{L,2}$ (cm^{-1})	$\Delta\omega_{L,2}$ (cm^{-1})
			[MOIm][BF_4]/FA			
0 ([MOIm][BF_4])	54.3	172	34.6	25.9	217	31.2
0.20	33.9	172	30.3	16.2	216	24.9
0.40	10.5	172	25.0	5.00	217	15.9
0.60	–	–	–	–	–	–
0.70	–	–	–	–	–	–
0.80	–	–	–	–	–	–
0.90	–	–	–	–	–	–
0.95	–	–	–	–	–	–
0.97	–	–	–	–	–	–
0.99	–	–	–	–	–	–
1 (FA)	–	–	–	–	–	–
			[MOIm][BF_4]/NMF			
0.20	75.1	170	38.5	22.9	217	30.2
0.40	84.0	167	38.7	38.5	219	37.2
0.60	89.0	167	38.9	54.9	219	41.5
0.70	92.6	164	41.4	52.6	221	42.4
0.80	58.7	164	39.6	76.7	225	48.1
0.90	–	–	–	185	243	68.4
0.95	–	–	–	118	244	55.8
0.97	–	–	–	117	245	51.2
0.99	–	–	–	95.0	247	46.7
1 (NMF)	–	–	–	93.0	246	44.4
			[MOIm][BF_4]/DMF			
0.20	55.6	171	35.5	24.9	220	31.7
0.40	64.8	171	37.1	23.3	221	31.2
0.60	60.0	170	37.3	38.7	224	38.4
0.70	57.3	169	37.7	45.6	226	41.6
0.80	59.4	171	38.6	52.2	232	42.1
0.90	102	169	45.5	38.6	231	34.8
0.95	90.3	166	45.0	37.8	231	34.2
0.97	106	166	46.8	39.5	232	33.5
0.99	98.2	166	46.9	53.5	230	38.3
1 (DMF)	95.0	162	44.2	51.2	232	36.9

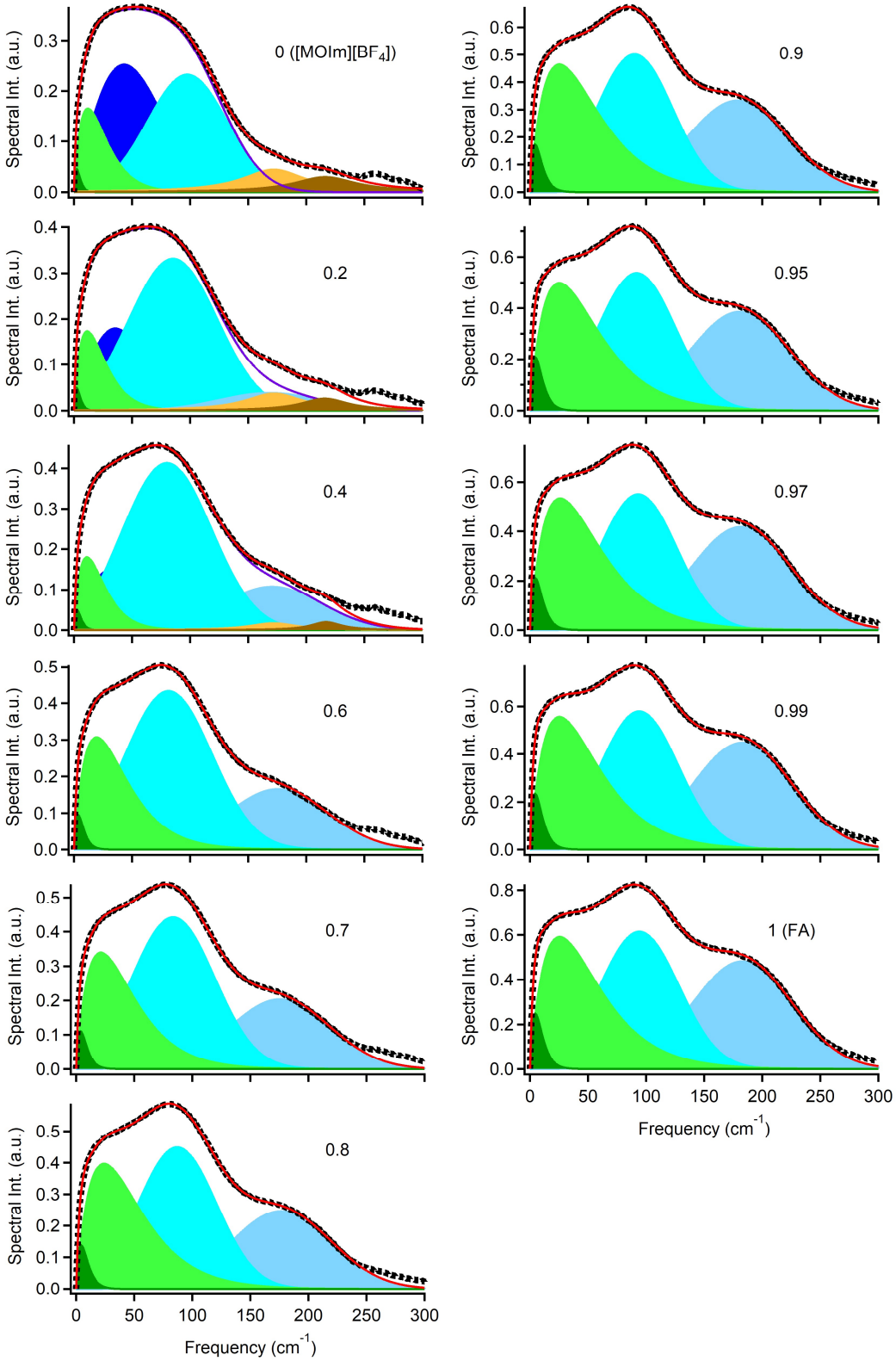

Figure C6. Line-shape analysis results of low-frequency spectra of [MOIm][BF_4] mixtures with FA.

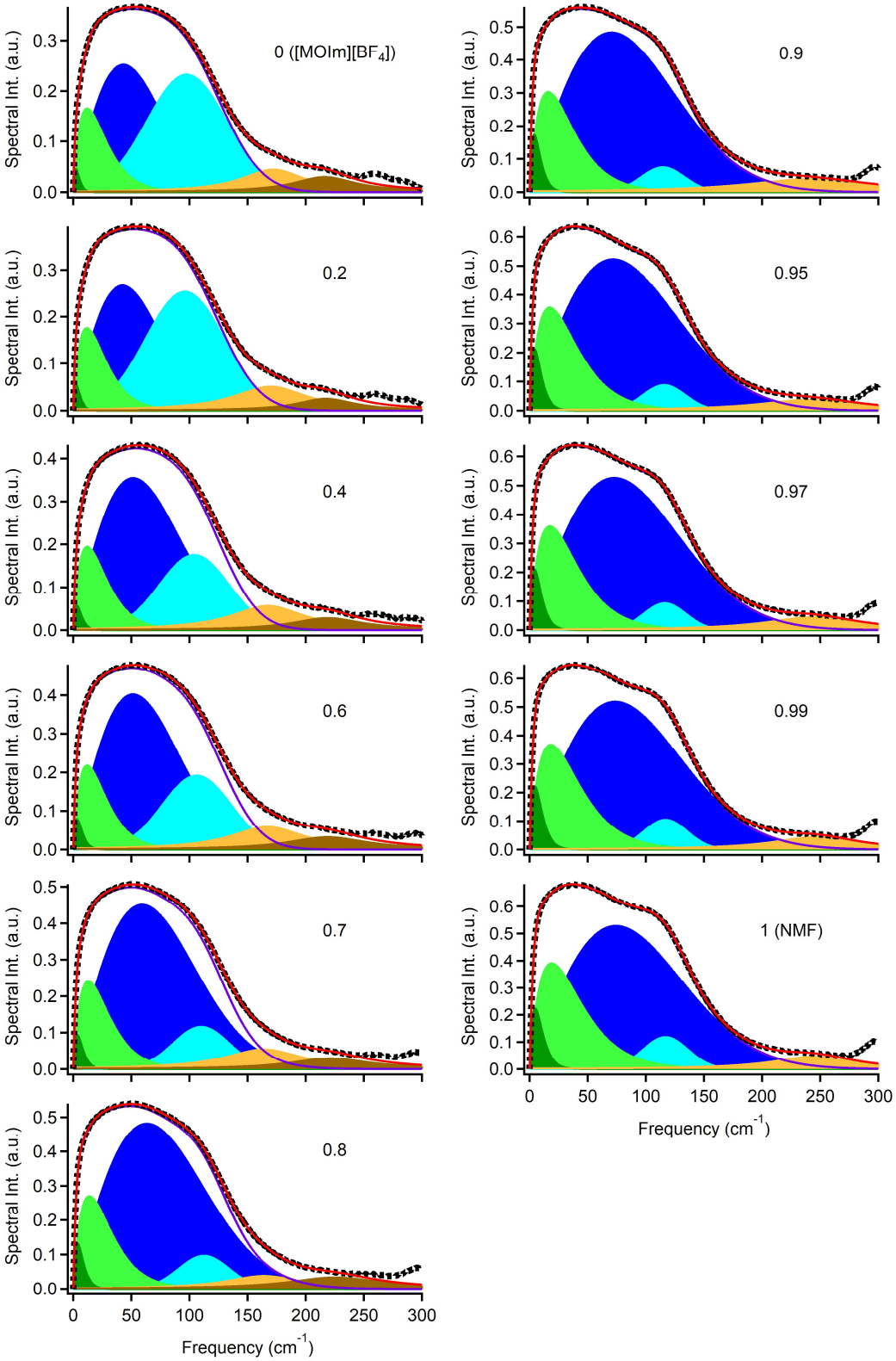

Figure C7. Line-shape analysis results of low-frequency spectra of [MOIm][BF_4] mixtures with NMF.

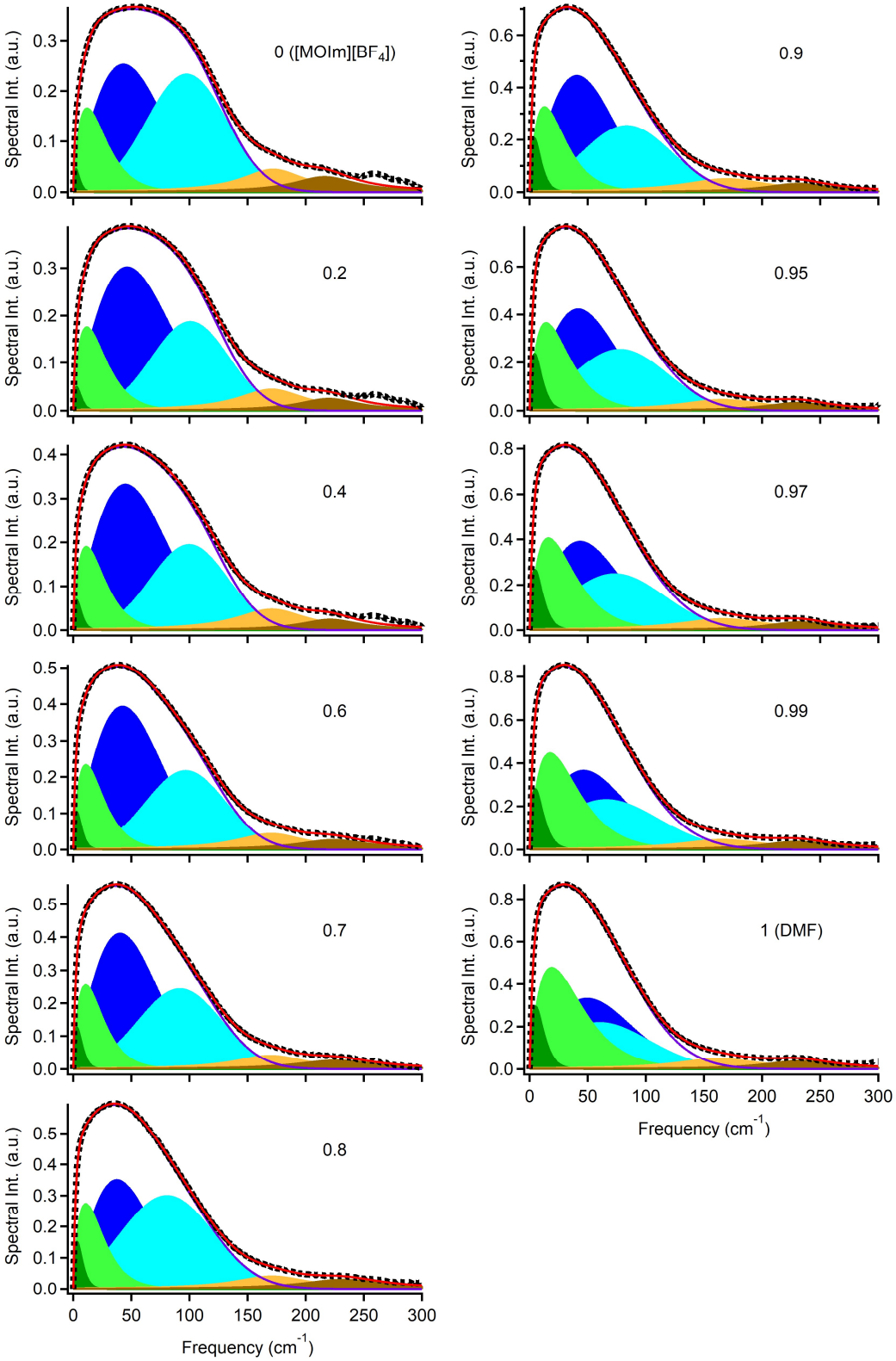

Figure C8. Line-shape analysis results of low-frequency spectra of [MOIm][BF_4] mixtures with DMF.

C. 4. Quantum Chemistry Calculation

Table C6. Atom Coordination Parameters of the Optimized $[BF_4]^-$, $[BF_4]^-$–FA, $[BF_4]^-$–NMF, $[BF_4]^-$–DMF, $[MOIm]^+$–$[BF_4]^-$, $[MOIm]^+$–$[BF_4]^-$ with Different Interionic Distances (–0.5, –0.25, +0.25, +0.5, +0.75, and +1.0 Å), $[MOIm]^+$–$[BF_4]^-$–FA, $[MOIm]^+$–$[BF_4]^-$–NMF, and $[MOIm]^+$–$[BF_4]^-$–DMF. Calculated by the B3LYP/6-311++G(d,p) Level of Theory.

$[BF_4]^-$

Center Number	Atomic Number	Atomic Type	Coordinates (Angstroms) X	Y	Z
1	9	0	0.818148	0.818148	0.818148
2	9	0	-0.818148	-0.818148	0.818148
3	9	0	0.818148	-0.818148	-0.818148
4	9	0	-0.818148	0.818148	-0.818148
5	5	0	0.000000	0.000000	0.000000
Rotational constants (GHz):			4.9675971	4.9675971	4.9675971

$[BF_4]^-$–FA

Center Number	Atomic Number	Atomic Type	Coordinates (Angstroms) X	Y	Z
1	6	0	-2.642871	-0.315825	-0.000381
2	1	0	-1.988862	-1.202385	-0.001332
3	7	0	-1.938005	0.831560	-0.000207
4	1	0	-2.440005	1.706392	0.001176
5	1	0	-0.918057	0.841641	-0.000328
6	8	0	-3.867369	-0.396519	0.000363
7	5	0	1.625036	-0.065099	0.000045
8	9	0	2.417199	-0.144340	-1.154499
9	9	0	0.913820	1.187623	-0.000653
10	9	0	2.416378	-0.143682	1.155211
11	9	0	0.650820	-1.096709	0.000063
Rotational constants (GHz):			4.2245093	0.7110705	0.6932419

$[BF_4]^-$–NMF

Center Number	Atomic Number	Atomic Type	Coordinates (Angstroms) X	Y	Z
1	6	0	2.770740	-0.817153	-0.000200
2	1	0	2.451495	-1.875780	-0.000858
3	7	0	1.727716	0.026100	-0.000796
4	1	0	0.781274	-0.356191	-0.000914
5	8	0	3.957625	-0.498314	0.000724
6	5	0	-1.993564	-0.076745	0.000015
7	9	0	-2.766373	-0.245277	1.157856
8	9	0	-1.392456	1.208856	-0.004123
9	9	0	-2.773519	-0.249482	-1.152358
10	9	0	-0.930318	-1.049314	-0.001445
11	6	0	1.889466	1.470354	0.000279
12	1	0	2.442044	1.800973	0.885416
13	1	0	2.445104	1.801819	-0.882596
14	1	0	0.895645	1.914465	-0.001191
Rotational constants (GHz):			3.2592084	0.5708822	0.5400654

$[BF_4]^-$–DMF

Center Number	Atomic Number	Atomic Type	Coordinates (Angstroms) X	Y	Z
1	6	0	3.359396	0.429262	-0.069414
2	1	0	3.547211	1.519207	-0.117979
3	7	0	2.045297	0.151207	0.033719
4	8	0	4.281371	-0.379820	-0.115184
5	6	0	1.571792	-1.227959	0.116710
6	1	0	0.677465	-1.341589	-0.497689
7	1	0	2.369131	-1.889732	-0.218091
8	1	0	1.300691	-1.477455	1.148148
9	6	0	1.037237	1.205485	0.118448
10	1	0	0.331520	1.137056	-0.710834
11	1	0	0.456990	1.108007	1.038568
12	1	0	1.532820	2.178622	0.098869
13	5	0	-2.320116	-0.042158	-0.023953
14	9	0	-2.287902	1.336393	-0.347982
15	9	0	-1.561005	-0.758645	-0.992255
16	9	0	-1.727206	-0.233319	1.251693
17	9	0	-3.645425	-0.509311	-0.014817
Rotational constants (GHz):			3.0984860	0.4517153	0.4309809

$[MOIm]^{+}$–$[BF_4]^{-}$

Center Number	Atomic Number	Atomic Type	Coordinates (Angstroms) X	Y	Z
1	6	0	4.046785	-2.306003	0.037248
2	6	0	2.912745	-2.583769	-0.661679
3	1	0	2.101548	0.169829	0.865719
4	1	0	4.989345	-2.822672	0.085408
5	1	0	2.686647	-3.384019	-1.344361
6	6	0	2.561455	-0.734111	0.488471
7	7	0	3.806203	-1.144244	0.747023
8	7	0	1.996155	-1.593290	-0.363207
9	6	0	0.676541	-1.397443	-1.008929
10	1	0	0.793777	-0.572212	-1.713602
11	1	0	0.470829	-2.316779	-1.560738
12	6	0	-0.436515	-1.094870	-0.007428
13	1	0	-0.196848	-0.171072	0.526560
14	1	0	-0.496327	-1.903433	0.730804
15	6	0	-1.787721	-0.927023	-0.713366
16	1	0	-2.035370	-1.844669	-1.263210
17	1	0	-1.704245	-0.129149	-1.460433
18	6	0	-2.926945	-0.593097	0.256451
19	1	0	-2.674022	0.323700	0.802149
20	1	0	-3.007657	-1.387266	1.010141
21	6	0	-4.281849	-0.413728	-0.437240
22	1	0	-4.534257	-1.331184	-0.985136
23	1	0	-4.19792	0.378532	-1.191792
24	6	0	-5.421895	-0.072200	0.528523
25	1	0	-5.169474	0.845288	1.075391
26	1	0	-5.506075	-0.863285	1.285393
27	6	0	-6.778358	0.110101	-0.161860
28	1	0	-7.030971	-0.806492	-0.709095
29	1	0	-6.694492	0.901121	-0.916836
30	6	0	-7.911078	0.451843	0.810494
31	1	0	-7.703830	1.382970	1.347191
32	1	0	-8.863344	0.575660	0.287320
33	1	0	-8.042947	-0.337238	1.557769
34	6	0	4.754089	-0.425990	1.608102
35	1	0	4.503198	0.633174	1.572216
36	1	0	4.700126	-0.808666	2.628226
37	1	0	5.758426	-0.568803	1.212284
38	5	0	2.165852	2.314714	-0.286759
39	9	0	1.942929	1.452778	-1.396898
40	9	0	1.271339	1.888671	0.758720
41	9	0	1.958904	3.634149	-0.611086
42	9	0	3.489561	2.084799	0.190708
Rotational constants (GHz):			0.5164892	0.1236451	0.1071349

$[MOIm]^+$–$[BF_4]^-$–FA

Center Number	Atomic Number	Atomic Type	Coordinates (Angstroms) X	Y	Z
1	6	0	2.888349	-3.127972	0.301069
2	6	0	1.781837	-2.956744	-0.471082
3	1	0	2.151152	-0.010655	0.868613
4	1	0	3.521967	-3.985684	0.444253
5	1	0	1.260972	-3.642869	-1.115779
6	6	0	2.202935	-1.042155	0.542256
7	7	0	3.126145	-1.923691	0.934120
8	7	0	1.368891	-1.647261	-0.307701
9	6	0	0.178643	-1.023603	-0.927021
10	1	0	0.386974	0.042530	-1.006180
11	1	0	0.100655	-1.437364	-1.935166
12	6	0	-1.095612	-1.269646	-0.118420
13	1	0	-0.950350	-0.865143	0.887172
14	1	0	-1.275169	-2.347791	-0.022425
15	6	0	-2.306380	-0.588466	-0.765695
16	1	0	-2.443482	-0.968851	-1.786858
17	1	0	-2.099907	0.483478	-0.851802
18	6	0	-3.600616	-0.793134	0.029558
19	1	0	-3.457791	-0.409758	1.047075
20	1	0	-3.803114	-1.867788	0.130360
21	6	0	-4.815978	-0.106312	-0.603244
22	1	0	-4.957957	-0.486789	-1.623410
23	1	0	-4.609742	0.966460	-0.703963
24	6	0	-6.111359	-0.299859	0.192640
25	1	0	-5.969251	0.080989	1.212264
26	1	0	-6.318024	-1.373506	0.295621
27	6	0	-7.328097	0.388536	-0.436288
28	1	0	-7.470624	0.008921	-1.455592
29	1	0	-7.122012	1.460833	-0.537881
30	6	0	-8.617546	0.191146	0.366069
31	1	0	-8.518008	0.593198	1.379282
32	1	0	-9.464886	0.694124	-0.108296
33	1	0	-8.869491	-0.870483	0.455837
34	6	0	4.285387	-1.596724	1.768374
35	1	0	4.050791	-0.710307	2.354728
36	1	0	4.490379	-2.433030	2.436199
37	1	0	5.136298	-1.386498	1.121652
38	5	0	1.119611	2.306470	0.687314
39	9	0	-0.104566	1.643652	0.886234
40	9	0	2.082719	1.768675	1.592352
41	9	0	1.016380	3.672354	0.810588
42	9	0	1.582904	1.956079	-0.643549
43	6	0	5.101871	0.914251	-1.464206
44	1	0	6.094488	1.086477	-1.919557
45	7	0	4.275011	1.964734	-1.589745
46	1	0	4.602397	2.809937	-2.028931
47	8	0	4.829301	-0.147565	-0.916481
48	1	0	3.333430	1.958511	-1.193341
Rotational constants (GHz):			0.3809779	0.0985155	0.0860378

$[MOIm]^{+}$–$[BF_4]^{-}$–NMF

Center Number	Atomic Number	Atomic Type	Coordinates (Angstroms) X	Y	Z
1	6	0	-2.508500	3.472232	0.014244
2	6	0	-1.444011	3.154415	-0.770763
3	1	0	-1.840323	0.435333	0.978491
4	1	0	-3.107993	4.364395	0.061516
5	1	0	-0.931457	3.724551	-1.525708
6	6	0	-1.880088	1.415011	0.516002
7	7	0	-2.755668	2.377001	0.818175
8	7	0	-1.066286	1.865655	-0.443421
9	6	0	0.078059	1.119295	-1.012309
10	1	0	-0.199465	0.065863	-1.011451
11	1	0	0.177479	1.450170	-2.048559
12	6	0	1.370376	1.343995	-0.226024
13	1	0	1.210035	1.021058	0.806700
14	1	0	1.613574	2.413698	-0.206594
15	6	0	2.533742	0.547200	-0.826482
16	1	0	2.687537	0.847899	-1.871619
17	1	0	2.261936	-0.513309	-0.836501
18	6	0	3.842370	0.727701	-0.049164
19	1	0	3.683005	0.421555	0.991754
20	1	0	4.108641	1.792799	-0.020654
21	6	0	5.011204	-0.070580	-0.637197
22	1	0	5.169869	0.232806	-1.680515
23	1	0	4.740878	-1.133362	-0.666321
24	6	0	6.320228	0.097380	0.141988
25	1	0	6.161782	-0.207678	1.184427
26	1	0	6.590184	1.161395	0.174645
27	6	0	7.490850	-0.700799	-0.443196
28	1	0	7.649769	-0.396801	-1.485191
29	1	0	7.221474	-1.763366	-0.474801
30	6	0	8.794156	-0.528574	0.342406
31	1	0	8.676841	-0.858058	1.379632
32	1	0	9.607878	-1.110071	-0.100022
33	1	0	9.108457	0.519946	0.363047
34	6	0	-3.882680	2.218602	1.741793
35	1	0	-3.639841	1.430933	2.452620
36	1	0	-4.037497	3.156055	2.275271
37	1	0	-4.765262	1.931128	1.171783
38	5	0	-0.931659	-2.007504	0.910842
39	9	0	0.404515	-1.584110	0.924593
40	9	0	-1.671869	-1.245751	1.865569
41	9	0	-1.072835	-3.360054	1.133430
42	9	0	-1.483938	-1.661531	-0.387491
43	6	0	-5.073841	-0.696021	-0.935458
44	1	0	-6.121037	-0.910882	-1.219723
45	7	0	-4.284024	-1.777999	-0.985313
46	8	0	-4.719742	0.437109	-0.615767
47	1	0	-3.302064	-1.669281	-0.726211
48	6	0	-4.742984	-3.112488	-1.333828
49	1	0	-5.811506	-3.084237	-1.556580
50	1	0	-4.214655	-3.488674	-2.213729
51	1	0	-4.576308	-3.806996	-0.506857

Rotational constants (GHz): 0.3359778 0.0926167 0.0795479

$[MOIm]^{+}$–$[BF_4]^{-}$–DMF

Center Number	Atomic Number	Atomic Type	Coordinates (Angstroms) X	Y	Z
1	6	0	-2.451960	2.923005	-0.106508
2	6	0	-1.402961	2.756365	-0.956333
3	1	0	-0.686547	0.658196	1.413306
4	1	0	-3.341346	3.521793	-0.189024
5	1	0	-1.196875	3.200518	-1.914214
6	6	0	-1.085869	1.432965	0.778269
7	7	0	-2.230181	2.091470	0.972335
8	7	0	-0.557488	1.822718	-0.385105
9	6	0	0.627857	1.211880	-1.025991
10	1	0	0.341126	0.199005	-1.314631
11	1	0	0.818161	1.796929	-1.927922
12	6	0	1.856482	1.194215	-0.118208
13	1	0	1.634980	0.599058	0.772096
14	1	0	2.085482	2.214955	0.209979
15	6	0	3.069227	0.587714	-0.834464
16	1	0	3.292231	1.168858	-1.738950
17	1	0	2.817131	-0.425051	-1.169834
18	6	0	4.318736	0.530353	0.051622
19	1	0	4.092241	-0.052601	0.952530
20	1	0	4.567690	1.542830	0.395287
21	6	0	5.535830	-0.078574	-0.653498
22	1	0	5.760843	0.503346	-1.556936
23	1	0	5.284163	-1.089767	-0.997413
24	6	0	6.786231	-0.142492	0.230492
25	1	0	6.561387	-0.724547	1.133501
26	1	0	7.038683	0.868665	0.576202
27	6	0	8.004508	-0.753119	-0.471558
28	1	0	8.229270	-0.172266	-1.374565
29	1	0	7.752731	-1.763618	-0.815472
30	6	0	9.249075	-0.813242	0.418794
31	1	0	9.066525	-1.417129	1.313254
32	1	0	10.098507	-1.253587	-0.110731
33	1	0	9.546982	0.186444	0.750892
34	6	0	-3.126369	1.908636	2.119890
35	1	0	-2.883818	0.956721	2.587667
36	1	0	-2.997569	2.731412	2.824949
37	1	0	-4.146371	1.868048	1.740618
38	5	0	-1.289210	-1.760575	0.762478
39	9	0	-0.062573	-1.312923	1.335614
40	9	0	-2.351691	-1.167250	1.502871
41	9	0	-1.386849	-3.140288	0.773509
42	9	0	-1.348693	-1.263271	-0.573263
43	6	0	-5.086358	-0.310919	-0.019378
44	1	0	-5.396546	-0.763105	0.936588
45	7	0	-4.761082	-1.238896	-0.939869
46	8	0	-5.065542	0.908351	-0.179941
47	6	0	-4.682440	-2.652154	-0.592888
48	1	0	-5.073557	-2.803128	0.413441
49	1	0	-5.275700	-3.245950	-1.295513
50	1	0	-3.645783	-2.997151	-0.610594

51	6	0	-4.248314	-0.845941	-2.244502
52	1	0	-4.431885	0.217646	-2.384751
53	1	0	-3.173999	-1.045086	-2.298055
54	1	0	-4.760288	-1.410987	-3.029105
Rotational constants (GHz):			0.3826689	0.0802867	0.0734057

$[MOIm]^{+}$–$[BF_4]^{-}$ (–0.5 Å)

Center Number	Atomic Number	Atomic Type	Coordinates (Angstroms) X	Y	Z
1	6	0	4.058551	-2.197186	0.168047
2	6	0	2.914920	-2.582283	-0.460847
3	1	0	2.103892	0.358884	0.663901
4	1	0	5.006953	-2.694416	0.272848
5	1	0	2.684561	-3.475275	-1.014991
6	6	0	2.565942	-0.587090	0.413742
7	7	0	3.819198	-0.946006	0.705267
8	7	0	1.993995	-1.565525	-0.292409
9	6	0	0.661048	-1.475678	-0.934183
10	1	0	0.757279	-0.761375	-1.753834
11	1	0	0.454625	-2.467215	-1.341901
12	6	0	-0.436726	-1.038189	0.033775
13	1	0	-0.196723	-0.044593	0.422558
14	1	0	-0.475108	-1.730685	0.883078
15	6	0	-1.802065	-0.985065	-0.662864
16	1	0	-2.050398	-1.974949	-1.068075
17	1	0	-1.740078	-0.304263	-1.519805
18	6	0	-2.926888	-0.521378	0.269687
19	1	0	-2.673350	0.467099	0.670818
20	1	0	-2.986030	-1.197529	1.132584
21	6	0	-4.295819	-0.455095	-0.416449
22	1	0	-4.548875	-1.444541	-0.819668
23	1	0	-4.233458	0.219065	-1.279982
24	6	0	-5.421612	0.015515	0.510999
25	1	0	-5.168562	1.004842	0.913197
26	1	0	-5.484194	-0.657146	1.376659
27	6	0	-6.792071	0.085170	-0.172262
28	1	0	-7.045329	-0.903326	-0.574948
29	1	0	-6.729767	0.758042	-1.036031
30	6	0	-7.910424	0.557008	0.761534
31	1	0	-7.702856	1.558013	1.152554
32	1	0	-8.873168	0.596166	0.244386
33	1	0	-8.020878	-0.115418	1.618331
34	6	0	4.775231	-0.102828	1.433885
35	1	0	4.513141	0.937888	1.248727
36	1	0	4.743521	-0.332803	2.499771
37	1	0	5.773641	-0.294610	1.043811
38	5	0	2.166637	2.132979	-0.325432
39	9	0	1.932356	1.116560	-1.293442
40	9	0	1.295448	1.857695	0.788094
41	9	0	1.940670	3.389363	-0.834709
42	9	0	3.500983	1.984888	0.154809
Rotational constants (GHz):			0.5738449	0.1238299	0.1087390

$[MOIm]^{+}$–$[BF_4]^{-}$ (–0.25 Å)

Center Number	Atomic Number	Atomic Type	Coordinates (Angstroms) X	Y	Z
1	6	0	4.053887	-2.249947	0.103355
2	6	0	2.915017	-2.582333	-0.563125
3	1	0	2.103519	0.270324	0.769956
4	1	0	4.999487	-2.757590	0.179678
5	1	0	2.686873	-3.430612	-1.184372
6	6	0	2.564636	-0.656338	0.454354
7	7	0	3.813762	-1.041239	0.730022
8	7	0	1.996085	-1.577066	-0.328025
9	6	0	0.669698	-1.434073	-0.973740
10	1	0	0.776317	-0.661142	-1.736973
11	1	0	0.463733	-2.391625	-1.456091
12	6	0	-0.435800	-1.065243	0.013826
13	1	0	-0.196067	-0.104369	0.477763
14	1	0	-0.484781	-1.818880	0.808792
15	6	0	-1.794177	-0.954650	-0.689637
16	1	0	-2.042067	-1.910563	-1.169756
17	1	0	-1.721559	-0.212205	-1.492869
18	6	0	-2.926290	-0.556943	0.264321
19	1	0	-2.673159	0.397848	0.740315
20	1	0	-2.996103	-1.295206	1.073866
21	6	0	-4.288313	-0.433995	-0.427722
22	1	0	-4.540944	-1.389600	-0.905866
23	1	0	-4.215281	0.302315	-1.238020
24	6	0	-5.421322	-0.029001	0.521654
25	1	0	-5.168687	0.926562	0.998771
26	1	0	-5.494590	-0.763974	1.334182
27	6	0	-6.784890	0.097103	-0.167285
28	1	0	-7.037725	-0.857595	-0.644830
29	1	0	-6.711918	0.832146	-0.977916
30	6	0	-7.910516	0.502816	0.788580
31	1	0	-7.703213	1.471049	1.254997
32	1	0	-8.868096	0.584424	0.266821
33	1	0	-8.031567	-0.231061	1.591842
34	6	0	4.765689	-0.258682	1.528315
35	1	0	4.509044	0.794026	1.418752
36	1	0	4.722917	-0.567238	2.573767
37	1	0	5.767129	-0.425095	1.134377
38	5	0	2.164190	2.219955	-0.309054
39	9	0	1.935674	1.279422	-1.352230
40	9	0	1.281365	1.866205	0.772692
41	9	0	1.947541	3.511709	-0.725419
42	9	0	3.493325	2.030901	0.171259
Rotational constants (GHz):			0.5455705	0.1237401	0.1080273

$[MOIm]^{+}$–$[BF_4]^{-}$ (+0.25 Å)

Center Number	Atomic Number	Atomic Type	Coordinates (Angstroms) X	Y	Z
1	6	0	4.037095	-2.365272	-0.027907
2	6	0	2.907979	-2.587877	-0.754023
3	1	0	2.097896	0.060059	0.950526
4	1	0	4.976350	-2.889720	-0.006882
5	1	0	2.683761	-3.338345	-1.491654
6	6	0	2.556293	-0.818830	0.516519
7	7	0	3.796381	-1.253164	0.757343
8	7	0	1.994114	-1.614516	-0.396687
9	6	0	0.681528	-1.367121	-1.039035
10	1	0	0.809677	-0.496498	-1.684721
11	1	0	0.475853	-2.245440	-1.654049
12	6	0	-0.438950	-1.126787	-0.028977
13	1	0	-0.199135	-0.243006	0.568858
14	1	0	-0.509894	-1.983416	0.651826
15	6	0	-1.782728	-0.903030	-0.733584
16	1	0	-2.030347	-1.779545	-1.346888
17	1	0	-1.688100	-0.056607	-1.423724
18	6	0	-2.928914	-0.629099	0.246776
19	1	0	-2.675989	0.246818	0.855932
20	1	0	-3.020819	-1.472295	0.943800
21	6	0	-4.276439	-0.394660	-0.444860
22	1	0	-4.528832	-1.271089	-1.056248
23	1	0	-4.181321	0.446670	-1.142846
24	6	0	-5.423367	-0.112864	0.531967
25	1	0	-5.170952	0.763667	1.142333
26	1	0	-5.518752	-0.953179	1.232344
27	6	0	-6.772466	0.124284	-0.156182
28	1	0	-7.025066	-0.751327	-0.766854
29	1	0	-6.677412	0.964407	-0.854675
30	6	0	-7.912128	0.405801	0.827299
31	1	0	-7.704715	1.296905	1.428054
32	1	0	-8.858895	0.570757	0.305501
33	1	0	-8.055101	-0.431571	1.517824
34	6	0	4.740273	-0.601030	1.673652
35	1	0	4.495491	0.459617	1.707916
36	1	0	4.674927	-1.052021	2.664784
37	1	0	5.747385	-0.722607	1.277793
38	5	0	2.171818	2.415772	-0.260633
39	9	0	1.954337	1.632881	-1.428889
40	9	0	1.265502	1.924876	0.745501
41	9	0	1.975025	3.755475	-0.495988
42	9	0	3.489846	2.145833	0.211570
Rotational constants (GHz):			0.4872787	0.1235476	0.1060685

$[MOIm]^{+}$–$[BF_4]^{-}$ (+0.5 Å)

Center Number	Atomic Number	Atomic Type	Coordinates (Angstroms) X	Y	Z
1	6	0	4.024618	-2.427962	-0.090154
2	6	0	2.900556	-2.596027	-0.838445
3	1	0	2.092449	-0.056383	1.024473
4	1	0	4.960267	-2.959214	-0.094689
5	1	0	2.678053	-3.296441	-1.624249
6	6	0	2.549016	-0.909036	0.539222
7	7	0	3.784115	-1.366443	0.762302
8	7	0	1.989832	-1.641045	-0.427517
9	6	0	0.684587	-1.344128	-1.063811
10	1	0	0.824017	-0.435085	-1.651617
11	1	0	0.478722	-2.180065	-1.735241
12	6	0	-0.443206	-1.160777	-0.049949
13	1	0	-0.203017	-0.318534	0.604973
14	1	0	-0.525655	-2.058489	0.574273
15	6	0	-1.779244	-0.883270	-0.750142
16	1	0	-2.027053	-1.717223	-1.420104
17	1	0	-1.673095	0.004686	-1.384134
18	6	0	-2.932265	-0.664322	0.236007
19	1	0	-2.679117	0.169262	0.901835
20	1	0	-3.035731	-1.549515	0.877097
21	6	0	-4.272096	-0.376954	-0.450592
22	1	0	-4.524695	-1.210910	-1.118677
23	1	0	-4.165420	0.506416	-1.092734
24	6	0	-5.425777	-0.149926	0.532526
25	1	0	-5.173146	0.684196	1.199597
26	1	0	-5.532734	-1.032433	1.177116
27	6	0	-6.767195	0.139934	-0.150434
28	1	0	-7.020002	-0.693249	-0.817753
29	1	0	-6.660587	1.022133	-0.793160
30	6	0	-7.913672	0.366209	0.839368
31	1	0	-7.705862	1.215800	1.497398
32	1	0	-8.854714	0.570634	0.321198
33	1	0	-8.068107	-0.512403	1.473914
34	6	0	4.724040	-0.780548	1.726201
35	1	0	4.485774	0.277446	1.825911
36	1	0	4.647049	-1.293247	2.686002
37	1	0	5.733810	-0.883692	1.331882
38	5	0	2.182336	2.521821	-0.232672
39	9	0	1.970166	1.816414	-1.450220
40	9	0	1.264036	1.974201	0.732487
41	9	0	1.996228	3.875126	-0.383842
42	9	0	3.494382	2.213199	0.232438
Rotational constants (GHz):			0.4584908	0.1234474	0.1048381

$[MOIm]^{+}$–$[BF_4]^{-}$ (+0.75 Å)

Center Number	Atomic Number	Atomic Type	Coordinates (Angstroms) X	Y	Z
1	6	0	4.009108	-2.494471	-0.148138
2	6	0	2.890268	-2.609460	-0.914085
3	1	0	2.085067	-0.177255	1.088244
4	1	0	4.940809	-3.031896	-0.176308
5	1	0	2.669316	-3.260767	-1.741464
6	6	0	2.539449	-1.003526	0.557440
7	7	0	3.769183	-1.482957	0.763247
8	7	0	1.983150	-1.673098	-0.455137
9	6	0	0.685618	-1.329069	-1.083428
10	1	0	0.836779	-0.388217	-1.615654
11	1	0	0.479324	-2.122505	-1.804463
12	6	0	-0.449409	-1.196664	-0.069706
13	1	0	-0.208606	-0.396235	0.635498
14	1	0	-0.543821	-2.128792	0.499999
15	6	0	-1.777330	-0.868017	-0.763174
16	1	0	-2.025563	-1.659228	-1.482966
17	1	0	-1.659208	0.054758	-1.343013
18	6	0	-2.937083	-0.698252	0.224772
19	1	0	-2.683479	0.092792	0.940459
20	1	0	-3.052562	-1.618707	0.811880
21	6	0	-4.268839	-0.360529	-0.454578
22	1	0	-4.521879	-1.151816	-1.172535
23	1	0	-4.150155	0.558142	-1.042817
24	6	0	-5.429168	-0.182516	0.530812
25	1	0	-5.176086	0.608996	1.247767
26	1	0	-5.548147	-1.100467	1.121544
27	6	0	-6.762523	0.157494	-0.144771
28	1	0	-7.015771	-0.633065	-0.861921
29	1	0	-6.643911	1.075030	-0.733663
30	6	0	-7.915710	0.334306	0.847305
31	1	0	-7.707256	1.142143	1.555781
32	1	0	-8.850755	0.576203	0.334442
33	1	0	-8.082051	-0.578793	1.427855
34	6	0	4.705143	-0.962075	1.767485
35	1	0	4.473860	0.090086	1.927260
36	1	0	4.616168	-1.529605	2.694846
37	1	0	5.717455	-1.049850	1.375973
38	5	0	2.197717	2.631759	-0.204527
39	9	0	1.990748	2.000729	-1.463099
40	9	0	1.267183	2.035683	0.719321
41	9	0	2.022914	3.993028	-0.277414
42	9	0	3.503425	2.286039	0.252250
Rotational constants (GHz):			0.4305488	0.1233420	0.1034567

$[MOIm]^{+}$–$[BF_4]^{-}$ (+1.0 Å)

Center Number	Atomic Number	Atomic Type	Coordinates (Angstroms) X	Y	Z
1	6	0	3.990262	-2.565250	-0.201094
2	6	0	2.876859	-2.629143	-0.980806
3	1	0	2.075574	-0.300788	1.142870
4	1	0	4.917626	-3.108583	-0.250813
5	1	0	2.657292	-3.233180	-1.843652
6	6	0	2.527379	-1.101384	0.572032
7	7	0	3.751310	-1.601979	0.761381
8	7	0	1.973864	-1.710776	-0.479335
9	6	0	0.684492	-1.322133	-1.098344
10	1	0	0.847923	-0.355468	-1.578100
11	1	0	0.477513	-2.073921	-1.862519
12	6	0	-0.457714	-1.234271	-0.087852
13	1	0	-0.216039	-0.474955	0.661160
14	1	0	-0.564636	-2.194734	0.430239
15	6	0	-1.777064	-0.857226	-0.773004
16	1	0	-2.025970	-1.606489	-1.536146
17	1	0	-1.646429	0.094233	-1.301531
18	6	0	-2.943469	-0.730458	0.213563
19	1	0	-2.689159	0.018810	0.972639
20	1	0	-3.071501	-1.680013	0.749494
21	6	0	-4.266694	-0.345074	-0.457034
22	1	0	-4.520423	-1.094468	-1.218386
23	1	0	-4.135462	0.602732	-0.994166
24	6	0	-5.433584	-0.209928	0.527418
25	1	0	-5.179803	0.539745	1.287781
26	1	0	-5.565126	-1.157147	1.067075
27	6	0	-6.758421	0.177552	-0.139308
28	1	0	-7.012358	-0.571158	-0.899815
29	1	0	-6.627264	1.124260	-0.677152
30	6	0	-7.918235	0.311076	0.851812
31	1	0	-7.708871	1.077899	1.604238
32	1	0	-8.846954	0.588354	0.345404
33	1	0	-8.097010	-0.630334	1.381193
34	6	0	4.683282	-1.143958	1.799397
35	1	0	4.459516	-0.099878	2.013618
36	1	0	4.581901	-1.759585	2.694232
37	1	0	5.698020	-1.219534	1.411638
38	5	0	2.218338	2.744611	-0.177401
39	9	0	2.016483	2.183815	-1.469609
40	9	0	1.275246	2.108086	0.705835
41	9	0	2.055559	4.109318	-0.178466
42	9	0	3.517287	2.363404	0.270318
Rotational constants (GHz):			0.4037671	0.1232271	0.1019391

$[MOIm]^{+}$–$[BF_4]^{-}$ (IEFPCM: FA)

Center Number	Atomic Number	Atomic Type	Coordinates (Angstroms) X	Y	Z
1	6	0	-2.636099	-3.378458	-0.404282
2	6	0	-1.415393	-3.260153	0.183730
3	1	0	-2.487443	-0.187670	0.217975
4	1	0	-3.152974	-4.240954	-0.787356
5	1	0	-0.669063	-4.002317	0.407096
6	6	0	-2.331071	-1.251578	0.106518
7	7	0	-3.191121	-2.113483	-0.443217
8	7	0	-1.243929	-1.924628	0.497704
9	6	0	-0.044375	-1.326579	1.115886
10	1	0	-0.347274	-0.362675	1.525305
11	1	0	0.240372	-1.969332	1.950280
12	6	0	1.106596	-1.166458	0.120900
13	1	0	0.774156	-0.537337	-0.711418
14	1	0	1.362338	-2.145203	-0.298434
15	6	0	2.343119	-0.548261	0.783130
16	1	0	2.654511	-1.174828	1.627880
17	1	0	2.079482	0.430031	1.203290
18	6	0	3.519405	-0.383628	-0.185983
19	1	0	3.205646	0.240456	-1.032204
20	1	0	3.780574	-1.363126	-0.606061
21	6	0	4.761059	0.234643	0.466345
22	1	0	5.070627	-0.387999	1.315678
23	1	0	4.498971	1.215029	0.884614
24	6	0	5.941849	0.396246	-0.497373
25	1	0	5.632807	1.018334	-1.347592
26	1	0	6.204434	-0.584298	-0.915681
27	6	0	7.185101	1.014595	0.152223
28	1	0	7.493615	0.393720	1.002229
29	1	0	6.923601	1.994866	0.569142
30	6	0	8.360446	1.170621	-0.817452
31	1	0	8.092810	1.814638	-1.661397
32	1	0	9.229909	1.613884	-0.323564
33	1	0	8.667123	0.201738	-1.224719
34	6	0	-4.511845	-1.770723	-0.985008
35	1	0	-4.656045	-0.696426	-0.894217
36	1	0	-4.555390	-2.063572	-2.033177
37	1	0	-5.279730	-2.298768	-0.420960
38	5	0	-3.843529	2.519211	0.022069
39	9	0	-4.534238	3.041173	1.133015
40	9	0	-2.673024	1.846439	0.470015
41	9	0	-3.477069	3.561490	-0.851094
42	9	0	-4.668204	1.593225	-0.659744
Rotational constants (GHz):			0.3859104	0.1011731	0.0838010

$[MOIm]^{+}$–$[BF_4]^{-}$ (IEFPCM: NMF)

Center Number	Atomic Number	Atomic Type	Coordinates (Angstroms) X	Y	Z
1	6	0	-2.631560	-3.380343	-0.403283
2	6	0	-1.410996	-3.260190	0.184651
3	1	0	-2.486932	-0.189092	0.217158
4	1	0	-3.147317	-4.243719	-0.785869
5	1	0	-0.663729	-4.001284	0.408449
6	6	0	-2.329135	-1.252813	0.106336
7	7	0	-3.188141	-2.116079	-0.442901
8	7	0	-1.241169	-1.924291	0.497892
9	6	0	-0.042278	-1.324675	1.115799
10	1	0	-0.346063	-0.360724	1.524461
11	1	0	0.242931	-1.966579	1.950680
12	6	0	1.108700	-1.164423	0.120837
13	1	0	0.776036	-0.535883	-0.711832
14	1	0	1.364932	-2.143269	-0.297950
15	6	0	2.344902	-0.545417	0.782896
16	1	0	2.656243	-1.171341	1.628136
17	1	0	2.080956	0.433115	1.202321
18	6	0	3.521381	-0.381264	-0.186065
19	1	0	3.207797	0.242337	-1.032715
20	1	0	3.782636	-1.361005	-0.605511
21	6	0	4.762915	0.237342	0.466172
22	1	0	5.072183	-0.384782	1.315991
23	1	0	4.500832	1.218045	0.883715
24	6	0	5.943993	0.398142	-0.497329
25	1	0	5.635315	1.019795	-1.348004
26	1	0	6.206473	-0.582714	-0.914965
27	6	0	7.187215	1.016593	0.152226
28	1	0	7.495331	0.396159	1.002697
29	1	0	6.925853	1.997198	0.568455
30	6	0	8.362879	1.171702	-0.817215
31	1	0	8.095651	1.815261	-1.661642
32	1	0	9.232326	1.615034	-0.323356
33	1	0	8.669397	0.202472	-1.223777
34	6	0	-4.509274	-1.775243	-0.984835
35	1	0	-4.655004	-0.701141	-0.894176
36	1	0	-4.552371	-2.068317	-2.032956
37	1	0	-5.276453	-2.304288	-0.420775
38	5	0	-3.850142	2.517555	0.021691
39	9	0	-4.539222	3.039189	1.134008
40	9	0	-2.677654	1.847119	0.467334
41	9	0	-3.487351	3.560317	-0.852696
42	9	0	-4.675060	1.590384	-0.657877
Rotational constants (GHz):			0.3859472	0.1010695	0.0837308

$[MOIm]^{+}$–$[BF_4]^{-}$ (IEFPCM: DMF)

Center Number	Atomic Number	Atomic Type	Coordinates (Angstroms) X	Y	Z
1	6	0	2.523230	-3.377836	0.311319
2	6	0	1.315702	-3.199577	-0.288585
3	1	0	2.430259	-0.148267	-0.078917
4	1	0	3.022060	-4.273288	0.638769
5	1	0	0.564782	-3.912405	-0.581380
6	6	0	2.255111	-1.214982	-0.047448
7	7	0	3.093506	-2.127051	0.452753
8	7	0	1.167033	-1.842280	-0.506397
9	6	0	-0.013208	-1.186254	-1.102862
10	1	0	0.304954	-0.194988	-1.426429
11	1	0	-0.281572	-1.757844	-1.992736
12	6	0	-1.187390	-1.098376	-0.126069
13	1	0	-0.874430	-0.535070	0.759235
14	1	0	-1.453825	-2.105461	0.211717
15	6	0	-2.407504	-0.429064	-0.768691
16	1	0	-2.698353	-0.988821	-1.666070
17	1	0	-2.134026	0.577945	-1.106525
18	6	0	-3.606930	-0.337165	0.181541
19	1	0	-3.314601	0.221688	1.079424
20	1	0	-3.876508	-1.345340	0.520740
21	6	0	-4.833644	0.328220	-0.452403
22	1	0	-5.121155	-0.228743	-1.353530
23	1	0	-4.563635	1.337383	-0.789182
24	6	0	-6.037860	0.416243	0.491658
25	1	0	-5.751302	0.973425	1.393200
26	1	0	-6.307692	-0.593057	0.829190
27	6	0	-7.266751	1.080001	-0.140191
28	1	0	-7.552692	0.523983	-1.041450
29	1	0	-6.998087	2.088921	-0.476349
30	6	0	-8.465762	1.161916	0.809371
31	1	0	-8.220645	1.741398	1.705323
32	1	0	-9.324218	1.639895	0.328815
33	1	0	-8.779494	0.165019	1.135589
34	6	0	4.403900	-1.842924	1.050725
35	1	0	4.597720	-0.775202	0.974507
36	1	0	4.394866	-2.145802	2.097112
37	1	0	5.170546	-2.397630	0.511427
38	5	0	4.076476	2.400526	-0.020619
39	9	0	4.624103	2.576268	-1.306159
40	9	0	2.761858	1.867717	-0.140053
41	9	0	4.019356	3.634789	0.653295
42	9	0	4.871075	1.489420	0.714687
Rotational constants (GHz):			0.4051059	0.0972556	0.0819252

Table C7. ^{19}F NMR Chemical Shifts of the F Atoms of $[BF_4]^-$ in the Optimized $[BF_4]^-$, $[BF_4]^-$–FA, $[BF_4]^-$–NMF, $[BF_4]^-$–DMF, $[MOIm]^+$–$[BF_4]^-$, $[MOIm]^+$–$[BF_4]^-$–FA, $[MOIm]^+$–$[BF_4]^-$–NMF, and $[MOIm]^+$–$[BF_4]^-$–DMF Relative to F atoms of Trifluoromethylbenzene Calculated by the Gauge-Independent Atomic Orbital (GIAO) Method at the B3LYP/6-311++G(d,p) Level of Theory.

	1-F (ppm)	2-F (ppm)	3-F (ppm)	4-F (ppm)	Average Chemical Shift (ppm)
$[BF_4]^-$	–103.181	–103.181	–103.181	–103.181	–103.181
$[BF_4]^-$ –FA	–86.6065	–97.0533	–101.660	–101.661	–96.7452
$[BF_4]^-$–NMF	–86.6344	–94.8155	–102.188	–102.211	–96.4622
$[BF_4]^-$–DMF	–90.5985	–95.5902	–98.1197	–101.686	–96.4986
$[MOIm]^+$–$[BF_4]^-$	–75.9056	–88.5397	–93.4065	–99.9345	–89.4466
$[MOIm]^+$–$[BF_4]^-$–FA	–72.1820	–79.2265	–93.1165	–98.3775	–85.7256
$[MOIm]^+$–$[BF_4]^-$–NMF	–72.9973	–78.4587	–94.6913	–98.1394	–86.0717
$[MOIm]^+$–$[BF_4]^-$–DMF	–84.3427	–88.1186	–91.1436	–96.9505	–90.1389

Table C8. ^{19}F NMR Chemical Shifts of the F Atoms of $[BF_4]^-$ in the Optimized $[MOIm]^+$–$[BF_4]^-$ with Different Interionic Distances (–0.5, –0.25, +0.25, +0.5, +0.75, and +1.0 Å) Relative to F atoms of Trifluoromethylbenzene Calculated by the Gauge-Independent Atomic Orbital (GIAO) Method Based on the B3LYP/6-311++G(d,p) Level of Theory.

	1-F (ppm)	2-F (ppm)	3-F (ppm)	4-F (ppm)	Average Chemical Shift (ppm)
$[MOIm]^+$–$[BF_4]^-$	–75.9056	–88.5397	–93.4065	–99.9345	–89.4466
$[MOIm]^+$–$[BF_4]^-$ (–0.5 Å)	–65.6247	–70.1455	–79.4659	–97.1627	–78.0997
$[MOIm]^+$–$[BF_4]^-$ (–0.25 Å)	–70.4765	–80.9944	–89.1091	–98.5229	–84.7757
$[MOIm]^+$–$[BF_4]^-$ (+0.25 Å)	–81.3979	–93.4227	–95.4016	–101.313	–92.8838
$[MOIm]^+$–$[BF_4]^-$ (+0.5 Å)	–86.4155	–96.3808	–96.5509	–102.557	–95.4761
$[MOIm]^+$–$[BF_4]^-$ (+0.75 Å)	–90.6484	–97.4695	–98.2438	–103.593	–97.4887
$[MOIm]^+$–$[BF_4]^-$ (+1.0 Å)	–93.9306	–98.3236	–99.4076	–104.391	–99.0132

Table C9. ^{19}F NMR Chemical Shifts of the F Atoms of $[BF_4]^-$ in the Optimized $[MOIm]^+$–$[BF_4]^-$ with Different Solvent Effects (Gas Phase, FA, NMF, and DMF) Relative to F atoms of Trifluoromethylbenzene Calculated by the Gauge-Independent Atomic Orbital (GIAO) Method Based on the B3LYP/6-311++G(d,p) Level of Theory.

	1-F (ppm)	2-F (ppm)	3-F (ppm)	4-F (ppm)	Average Chemical Shift (ppm)
$[MOIm]^+$–$[BF_4]^-$ (Gas)	–75.9056	–88.5397	–93.4065	–99.9345	–89.4466
$[MOIm]^+$–$[BF_4]^-$ (FA)	–88.5778	–93.7849	–102.452	–102.539	–96.8384
$[MOIm]^+$–$[BF_4]^-$ (NMF)	–88.6709	–93.8437	–102.462	–102.546	–96.8807
$[MOIm]^+$–$[BF_4]^-$ (DMF)	–87.9030	–93.3748	–102.149	–102.489	–96.4790

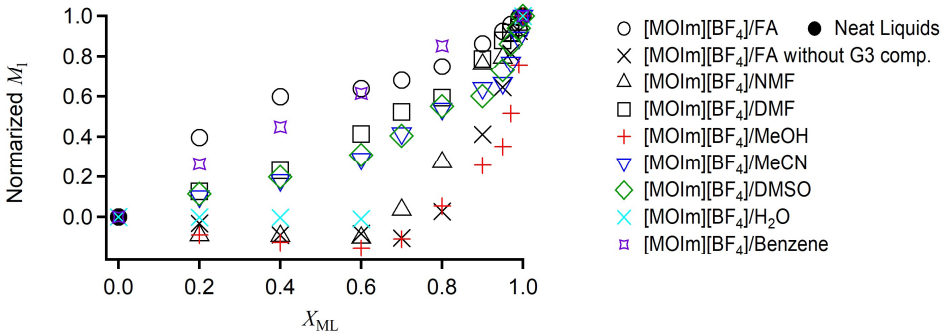

Figure C9. Plots of normalized M_1 vs. X_{ML} for $[MOIm][BF_4]$ mixtures with FA (black circles), NMF (black upper triangles), DMF (black squares), MeOH (red cross), MeCN (blue lower triangles), DMSO (green squares), H_2O (light blue cross), and benzene (purple stars). Plots for neat liquids are also shown (black filled circles). Black crosses denote the plot for $[MOIm][BF_4]$/FA without the contribution of the third antisymmetrized Gaussian component (2D-HB band).

D. Appendix to Chapter V

D. 1. Liquid Property

Table D1. Density ρ, viscosity η, surface tension γ, electrical conductivity σ, and molar electrical conductivity Λ of [MOIm][BF_4]/PEG400, OIm/PEG400, [MOIm][BF_4]/EG, and [MOIm][BF_4]/PEG4000 mixtures at 293 K.

Concentration (wt%)	ρ[a] (g/mL)	η[b] (cP)	γ[c] (mN/m)	σ[b] (mS/cm)	Λ (S cm^2/mol)
[MOIm][BF_4]/PEG400					
0 ([MOIm][BF_4])	1.107	483.5	32.2	0.794	0.202
5	1.109	419.7	32.8	0.822	0.212
10	1.110	371.4	32.9	0.827	0.217
20	1.114	286.4	33.5	0.860	0.231
40	1.120	228.0	35.1	0.883	0.252
60	1.124	190.4	37.8	0.807	0.246
80	1.127	152.2	40.0	0.601	0.197
100 (PEG400)	1.127	118.8	44.0	–	–
OIm/PEG400					
0 (OIm)	0.912	8.822	31.1	–	–
5	0.922	11.13	31.2	–	–
10	0.933	14.00	31.5	–	–
20	0.955	21.59	32.6	–	–
40	0.996	42.05	33.4	–	–
60	1.034	65.51	35.6	–	–
80	1.078	91.41	37.5	–	–
[MOIm][BF_4]/EG					
5	1.105	171.6	32.8	1.277	0.277
10	1.105	96.86	33.0	1.753	0.331
100 (EG)	1.114	20.53	48.0	–	–
[MOIm][BF_4]/PEG4000					
5	1.109	514.8	33.0	0.634	0.168
10	1.112	636.7	33.5	0.599	0.202

[a] ±0.5%. [b] ±5%. [c] ±1%.

D. 2. Analysis of Low-frequency Spectra

Table D2. Multiexponential fit parameters for Kerr transients of [MOIm][BF_4]/PEG400 and OIm/PEG400 mixtures at 293 K.

Concentration (wt%)	a_0	a_1	τ_1 (ps)	a_2	τ_2 (ps)	a_3	τ_3 (ps)	a_4	τ_4 (ps)
[MOIm][BF_4]/PEG400									
0 ([MOIm][BF_4])	0.000002	0.00332	2.03	0.0008	13.8	0.00034	136	–	–
5	0.000004	0.00314	1.96	0.0009	11.4	0.00037	135	–	–
10	0.000032	0.00283	1.88	0.0009	10.8	0.00027	116	–	–
20	0.000019	0.00292	1.74	0.0008	10.7	0.00028	113	–	–
40	0.000019	0.00269	1.32	0.0009	9.77	0.00018	109	–	–
60	0.000030	0.00194	1.26	0.0008	9.32	0.00012	99.2	–	–
80	0.000014	0.00121	1.22	0.0006	6.37	0.00020	93.6	–	–
100 (PEG400)	–	0.00136	1.13	0.0005	5.86	0.00018	82.1	–	–
OIm/PEG400									
0 (OIm)	–	0.00719	1.10	0.0016	3.96	0.00131	9.70	0.00105	75.9
5	–	0.00584	1.07	0.0019	3.75	0.00103	11.8	0.00083	81.4
10	–	0.00644	1.05	0.0019	4.66	0.00067	11.9	0.00078	79.5
20	–	0.00535	1.07	0.0017	4.71	0.00049	13.2	0.00069	79.7
40	–	0.00565	1.02	0.0011	5.23	0.00052	13.6	0.00034	82.8
60	–	0.00273	1.06	0.0009	5.26	0.00049	15.4	0.00015	76.8
80	–	0.00291	1.06	0.0004	5.80	0.00035	15.8	0.00013	80.7

Table D3. Triexponential fit parameters for Kerr transients of [MOIm][BF_4]/EG, and [MOIm][BF_4]/PEG4000 mixtures at 293 K.

Concentration (wt%)	a_0	a_1	τ_1 (ps)	a_2	τ_2 (ps)	a_3	τ_3 (ps)
[MOIm][BF_4]/EG							
5	0.000025	0.00480	1.49	0.0011	9.46	0.00046	126
10	0.000002	0.00516	1.34	0.0014	9.36	0.00044	68.7
[MOIm][BF_4]/PEG4000							
5	0.000055	0.00331	2.02	0.0006	14.2	0.00032	141
10	0.000040	0.00430	1.64	0.0005	14.5	0.00038	191

Table D4. Fit parameters for Fourier transform Kerr spectra of [MOIm][BF_4]/PEG400 and OIm/PEG mixtures at 293 K.

Intermolecular (mainly)

Concentration (wt%)	M_1 (cm^{-1})	a_{O1}	ω_{O1} (cm^{-1})	a_{G1}	ω_{G1} (cm^{-1})	$\Delta\omega_{G1}$ (cm^{-1})	a_{G2}	ω_{G2} (cm^{-1})	$\Delta\omega_{G2}$ (cm^{-1})
[MOIm][BF_4]/PEG400									
0 ([MOIm][BF_4])	71.1	0.0507	6.76	0.2567	13.7	24.9	0.3064	78.0	42.9
5	71.1	0.0443	7.28	0.1968	17.8	25.2	0.2848	78.8	42.5
10	71.3	0.0389	7.72	0.1793	19.3	26.0	0.2678	79.7	42.1
20	71.6	0.0318	8.12	0.1530	20.4	26.9	0.2367	79.8	42.3
40	71.9	0.0199	9.53	0.2205	15.9	34.3	0.1641	86.7	40.1
60	72.8	0.0123	9.94	0.1709	15.2	35.4	0.1225	85.1	42.3
80	73.0	0.0078	10.5	0.1871	12.0	38.4	0.0817	85.6	43.6
100 (PEG400)	74.6	0.0054	11.5	0.1979	10.2	46.9	0.0426	68.2	63.2
OIm/PEG400									
0 (OIm)	69.1	0.0417	7.22	0.1398	22.2	21.8	0.3512	74.8	38.5
5	70.0	0.0369	7.69	0.1222	22.9	21.6	0.3397	74.8	39.6
10	70.1	0.0362	7.35	0.1338	20.3	22.6	0.3264	75.1	39.4
20	70.5	0.0306	7.57	0.1513	17.4	24.8	0.2952	76.8	38.7
40	71.7	0.0224	7.77	0.1278	16.8	25.5	0.2388	77.9	39.3
60	72.2	0.0147	8.67	0.1192	18.4	28.5	0.1795	81.5	38.1
80	73.0	0.0108	7.51	0.1585	7.67	27.8	0.1348	76.5	42.6

Intramolecular

Concentration (wt%)	a_{L1}	ω_{L1} (cm^{-1})	$\Delta\omega_{L1}$ (cm^{-1})	a_{L2}	ω_{L2} (cm^{-1})	$\Delta\omega_{L2}$ (cm^{-1})
		[MOIm][BF_4]/PEG400				
0 ([MOIm][BF_4])	2.90	176	15.0	19.3	213	31.3
5	3.13	175	16.0	21.3	213	33.5
10	3.45	175	16.5	17.5	215	31.5
20	3.63	176	17.7	9.54	215	27.0
40	4.36	175	20.3	11.2	215	32.7
60	2.87	176	20.7	8.38	218	33.9
80	1.92	176	20.7	5.12	218	33.9
		(Fixed)	(Fixed)		(Fixed)	(Fixed)
100 (PEG400)	–	–	–	–	–	–
		OIm/PEG400				
0 (OIm)	42.6	170	38.0	3.32	235	17.6
5	32.3	172	36.0	3.03	235	17.7
10	31.0	173	36.1	2.29	235	15.8
20	29.1	172	35.4	2.27	236	16.7
40	25.0	175	35.2	2.60	236	19.4
60	22.8	174	37.0	1.17	235	15.8
80	14.7	177	35.2	1.50	237	20.0

Table D5. Fit parameters for Fourier transform Kerr spectra of [MOIm][BF_4]/EG and [MOIm][BF_4]/PEG4000 mixtures at 293 K.

Intermolecular (mainly)

Concentration (wt%)	M_1 (cm^{-1})	a_{O1}	ω_{O1} (cm^{-1})	a_{G1}	ω_{G1} (cm^{-1})	$\Delta\omega_{G1}$ (cm^{-1})	a_{G2}	ω_{G2} (cm^{-1})	$\Delta\omega_{G2}$ (cm^{-1})
[MOIm][BF_4]/EG									
5	70.7	0.0469	7.21	0.196	18.3	25.0	0.286	78.8	42.2
10	70.9	0.0439	7.25	0.183	17.7	24.7	0.277	77.7	43.1
[MOIm][BF_4]/PEG4000									
5	71.4	0.0480	6.70	0.193	17.1	24.1	0.294	77.1	43.7
10	71.9	0.0423	6.89	0.176	17.2	24.3	0.279	76.7	44.2

Intramolecular

Concentration (wt%)	a_{L1}	ω_{L1} (cm^{-1})	$\Delta\omega_{L1}$ (cm^{-1})	a_{L2}	ω_{L2} (cm^{-1})	$\Delta\omega_{L2}$ (cm^{-1})
[MOIm][BF_4]/EG						
5	4.12	175	16.9	18.5	212	31.2
10	5.05	176	19.0	17.5	214	30.4
[MOIm][BF_4]/PEG4000						
5	2.73	176	14.9	22.7	214	33.8
10	2.67	176	14.9	18.2	214	31.2

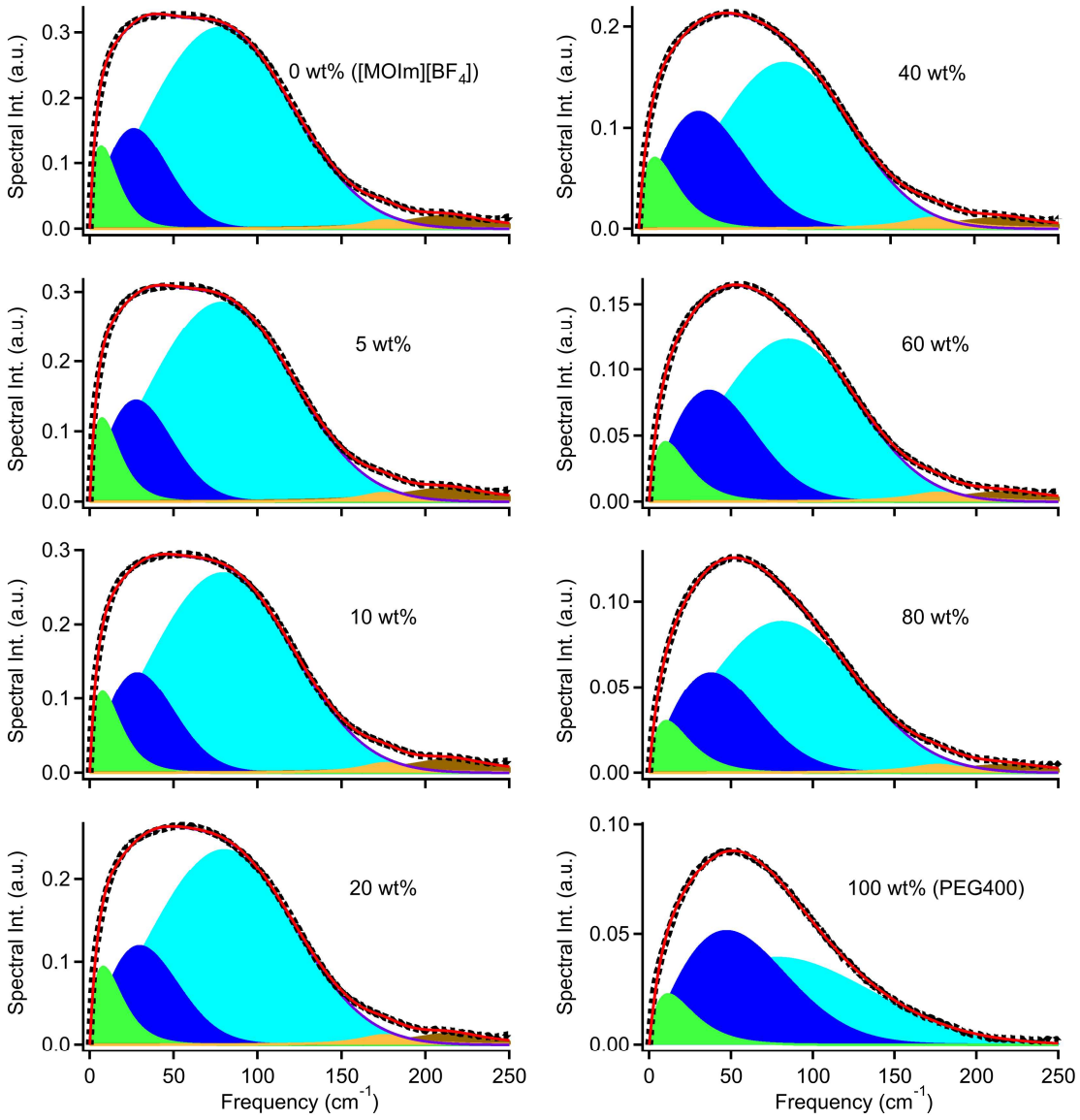

Figure D3. Low-frequency spectra and their fits for [MOIm][BF_4]/PEG400. The dots represent the experimental spectra, solid red lines represent the entire fits, green areas represent the Ohmic functions, blue areas represent the antisymmetrized Gaussian functions, and brown areas represent the Lorentz function. The solid purple lines denote the sums of Ohmic and antisymmetrized Gaussian functions.

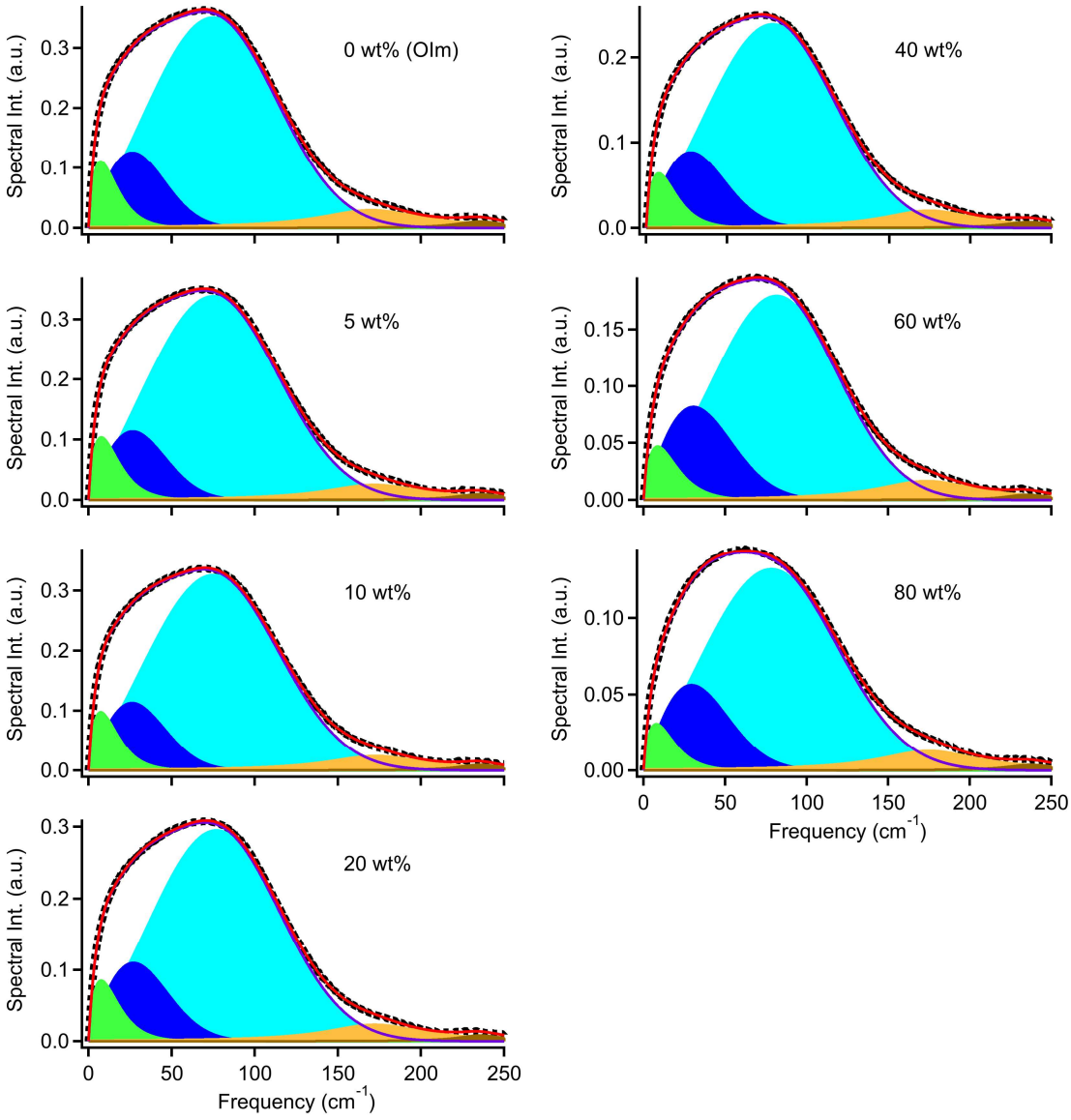

Figure D4. Low-frequency spectra and their fits for OIm/PEG400.

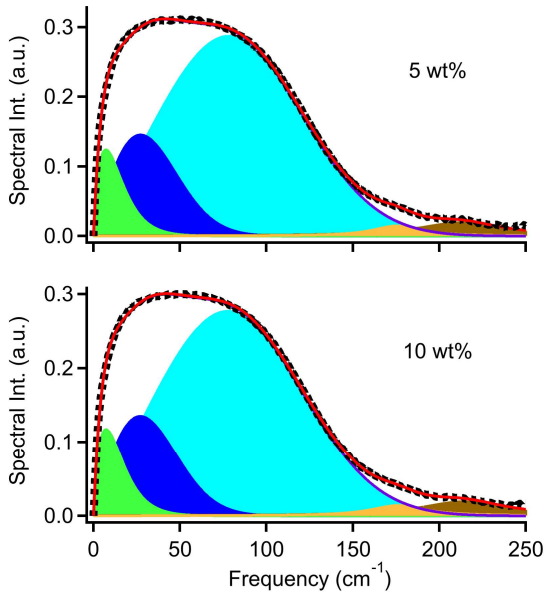

Figure D5. Low-frequency spectra and their fits for [MOIm][BF_4]/EG.

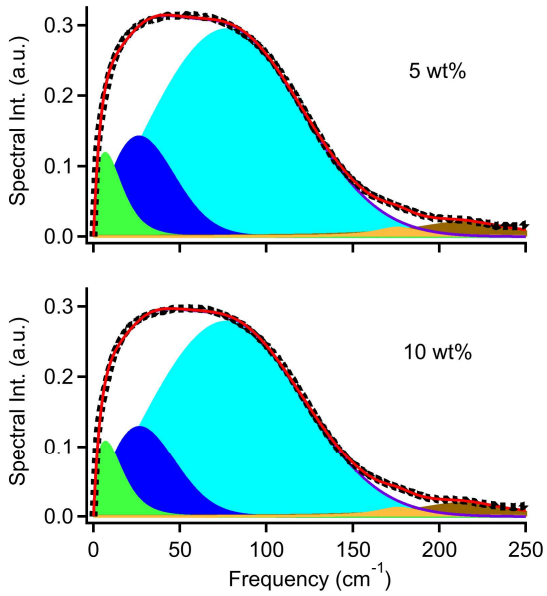

Figure D6. Low-frequency spectra and their fits for [MOIm][BF_4]/PEG4000.

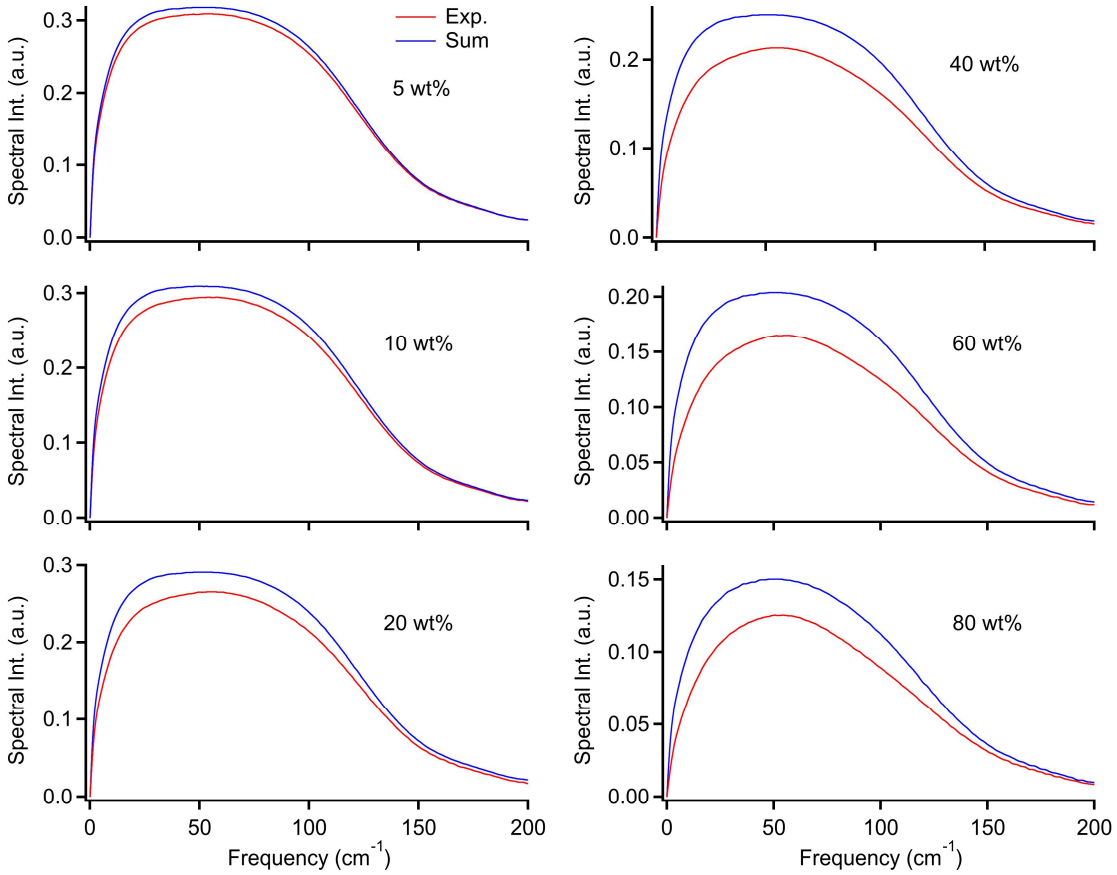

Figure D7. Comparisons of experimental low-frequency spectra of [MOIm][BF_4]/PEG400 (red solid line) with the sum spectra (blue solid line) of the mole fraction weighted spectra of neat [MOIm][BF_4] and PEG400.

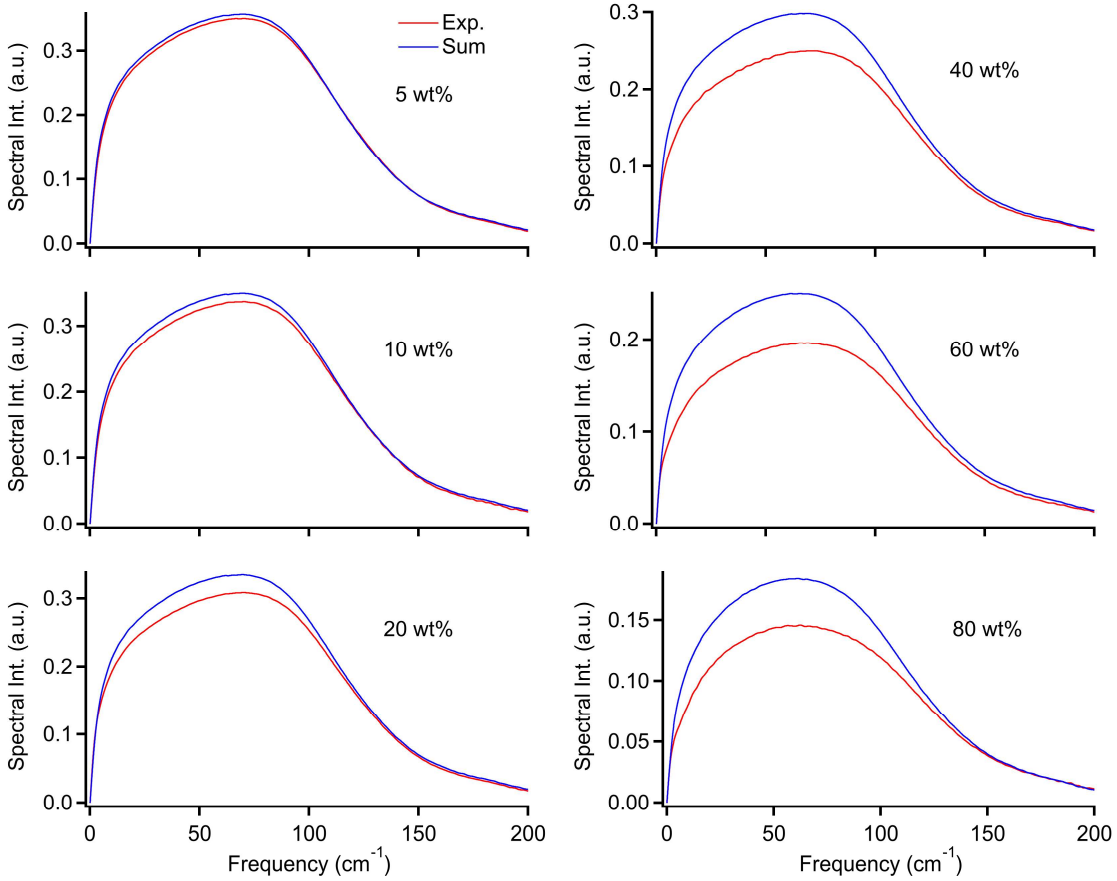

Figure D8. Comparisons of experimental low-frequency spectra of OIm/PEG400 (red solid line) with the sum spectra (blue solid line) of the mole fraction weighted spectra of neat OIm and PEG400.

Table D6. Fit parameters for loss spectra of [MOIm][BF_4]/PEG400 and OIm/PEG mixtures at 293 K.

Concentration (wt%)	M_1 (cm^{-1})	a_{O1}	ω_{O1} (cm^{-1})	a_{G1}	ω_{G1} (cm^{-1})	$\Delta\omega_{G1}$ (cm^{-1})	a_{G2}	ω_{G2} (cm^{-1})	$\Delta\omega_{G2}$ (cm^{-1})
[MOIm][BF_4]/PEG400									
5	66.5	0.0054	4.04	0.0104	16.8	19.5	0.0100	83.7	36.7
10	64.0	0.0101	4.05	0.0187	16.0	19.2	0.0153	81.8	38.2
20	65.7	0.0129	4.83	0.0321	15.9	20.6	0.0267	84.1	38.1
40	64.6	0.0190	4.69	0.0498	14.5	20.8	0.0391	83.3	36.4
60	64.2	0.0173	5.03	0.0504	14.2	21.1	0.0401	81.9	36.6
80	63.9	0.0111	5.11	0.0329	14.1	21.5	0.0258	82.6	35.4
OIm/PEG400									
5	48.8	0.0057	3.88	0.0075	21.3	24.2	0.0059	74.5	19.9
10	55.7	0.0045	5.14	0.0090	22.8	20.1	0.0124	70.6	28.3
20	56.9	0.0081	5.97	0.0091	25.0	14.4	0.0279	61.3	35.0
40	58.1	0.0115	6.99	0.0149	27.6	14.4	0.0495	63.3	34.7
60	58.5	0.0133	6.21	0.0174	23.7	15.1	0.0553	62.3	35.6
80	56.7	0.0083	8.05	0.0149	30.4	15.4	0.0377	68.3	29.5

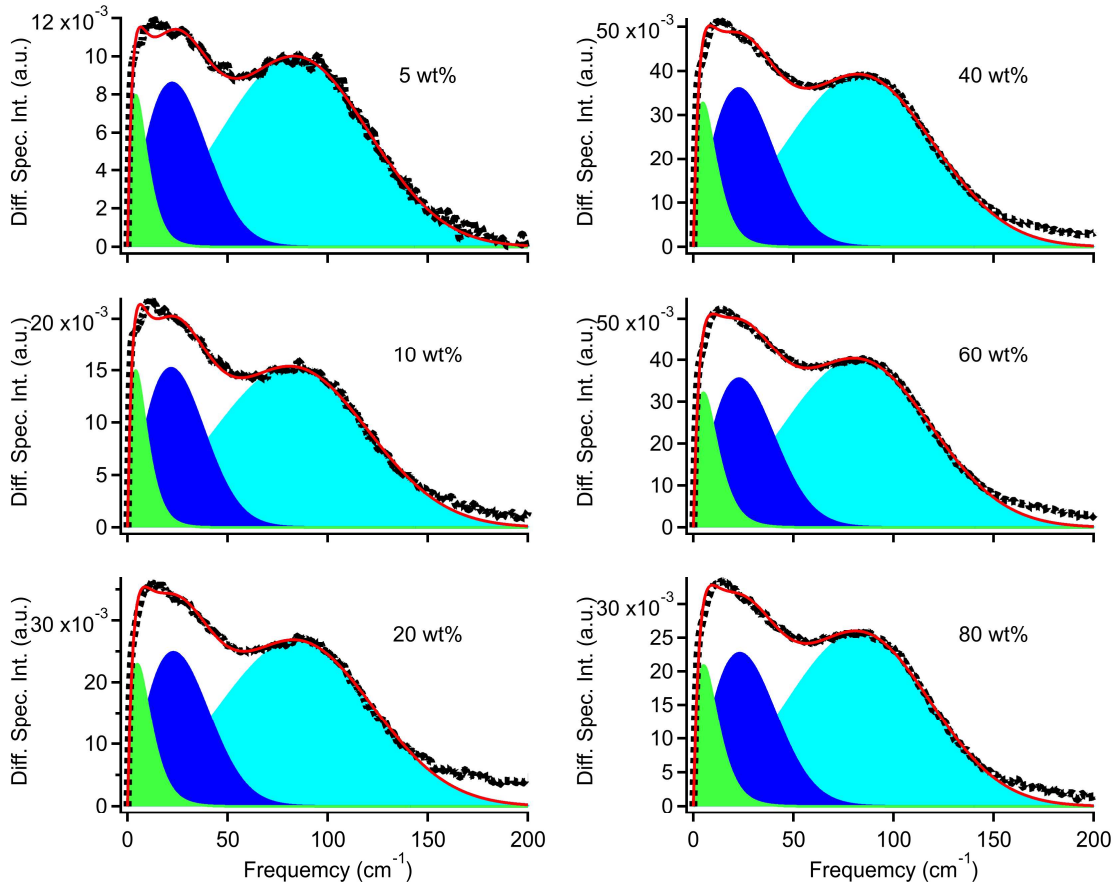

Figure D9. Loss spectra and their fits for [MOIm][BF_4]/PEG400. The dots represent the experimental spectra, solid red lines represent the entire fits, green areas represent the Ohmic functions, blue areas represent the antisymmetrized Gaussian functions.

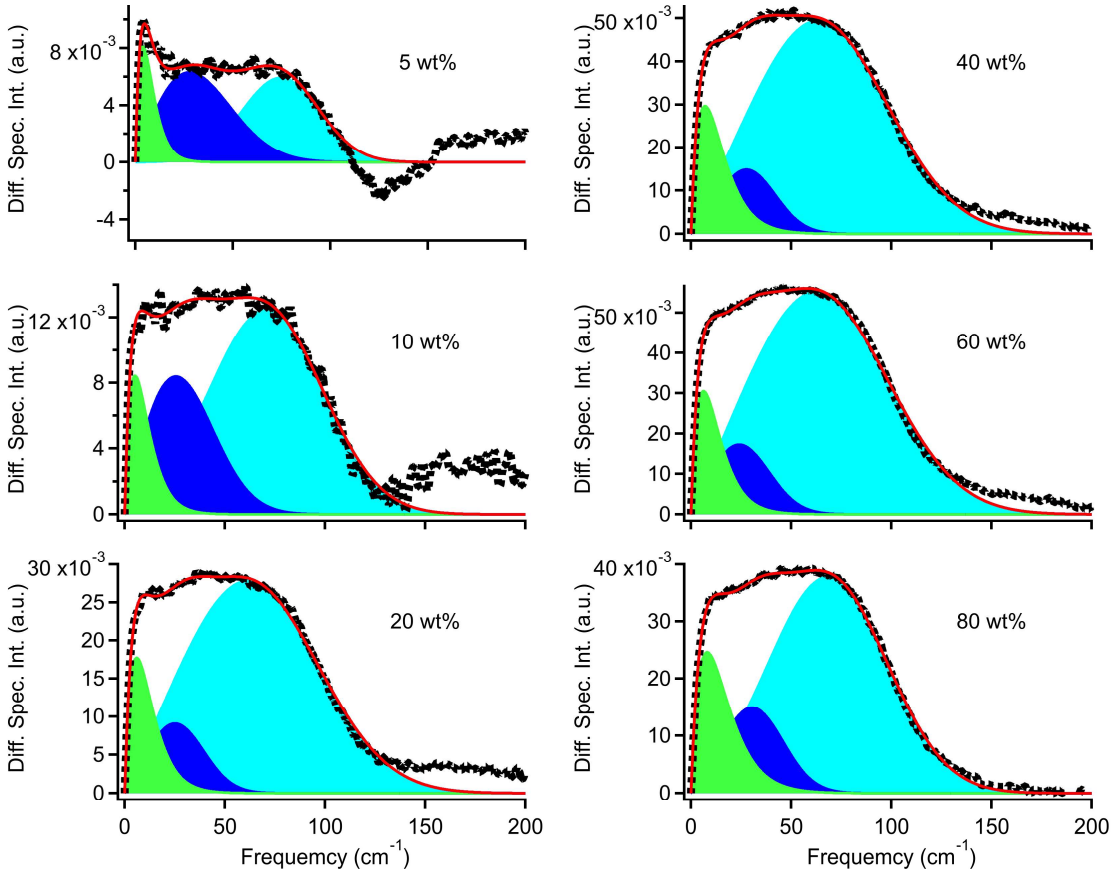

Figure D10. Loss spectra and their fits for OIm/PEG400.

E. Appendix to Chapter VI

E. 1. Liquid Property

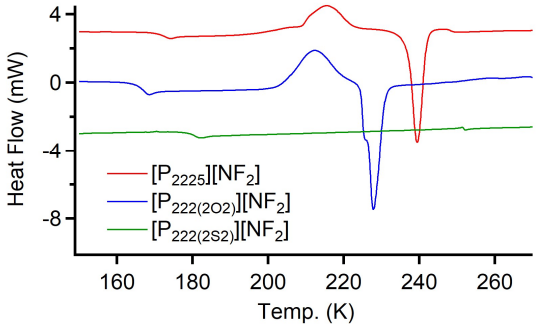

Figure E1. DSC heat flow vs. temperature for $[P_{2225}][NF_2]$ (red line), $[P_{222(2O2)}][NF_2]$ (blue line), and $[P_{222(2S2)}][NF_2]$ (green line). For clarity, offsets are given.

Table E1. Viscosity η, Density ρ, molar volume V_m, surface tension γ, electrical conductivity σ, and molar electrical conductivity Λ of $[P_{2225}][NF_2]$, $[P_{222(2O2)}][NF_2]$, and $[P_{222(2S2)}][NF_2]$.

Temp. (K)	η[a] (cP)	ρ[b] (g cm^{-3})	V_m (cm^3 mol^{-1})	γ[c] (mN m^{-1})	σ[a] (mS cm^{-1})	Λ (Scm^2 mol^{-1})
$[P_{2225}][NF_2]$						
293	83.2	1.220	302.8	40.9	2.31	0.699
298	67.2	1.217	303.7	40.8	2.53	0.768
303	54.3	1.213	304.6	40.4	2.90	0.884
308	44.2	1.209	305.5	40.2	3.33	1.02
313	36.4	1.205	306.5	39.6	3.66	1.12
318	30.8	1.202	307.4	39.2	3.96	1.22
323	26.3	1.198	308.3	38.8	4.30	1.33
328	22.6	1.195	309.2	38.6	4.62	1.43
333	19.5	1.191	310.2	38.4	4.94	1.53
338	16.8	1.187	311.1	38.2	5.27	1.64
343	14.8	1.184	312.0	37.9	5.62	1.75
348	13.1	1.180	313.0	37.5	5.95	1.86
353	11.7	1.177	313.9	37.2	6.29	1.97

[a] ±5%, [b] ±0.1%, [c] ±1%.

Continued.

Temp. (K)	η[a] (cP)	ρ[b] (g cm^{-3})	V_m (cm^3 mol^{-1})	γ[c] (mN m^{-1})	σ[a] (mS cm^{-1})	Λ (Scm^2 mol^{-1})
			$[P_{222(2O2)}][NF_2]$			
293	43.9	1.265	293.7	41.0	4.31	1.26
298	35.9	1.261	294.6	40.6	4.67	1.38
303	30.3	1.257	295.5	40.3	5.05	1.49
308	25.7	1.253	296.4	40.1	5.43	1.61
313	22.3	1.249	297.3	39.7	5.81	1.73
318	19.4	1.245	298.2	39.5	6.18	1.84
323	17.0	1.242	299.1	39.1	6.59	1.97
328	15.0	1.238	300.0	38.9	7.03	2.11
333	12.9	1.234	301.0	38.7	7.44	2.24
338	11.5	1.230	301.9	38.2	7.86	2.37
343	10.4	1.227	302.8	37.9	8.26	2.50
348	9.48	1.223	303.7	37.6	8.68	2.64
353	8.69	1.219	304.6	37.2	9.19	2.80
			$[P_{222(2S2)}][NF_2]$			
293	120	1.298	298.5	45.0	1.78	0.531
298	94.6	1.294	299.4	44.7	1.96	0.588
303	76.5	1.290	300.3	44.4	2.17	0.652
308	64.8	1.286	301.2	43.9	2.48	0.747
313	48.2	1.283	302.1	43.6	2.83	0.854
318	40.2	1.279	303.0	43.1	3.08	0.934
323	33.9	1.275	303.9	42.8	3.33	1.01
328	29.1	1.271	304.8	42.5	3.61	1.10
333	25.3	1.268	305. 7	42.2	3.89	1.19
338	22.1	1.264	306.5	41.9	4.18	1.28
343	19.4	1.260	307.4	41.6	4.48	1.38
348	17.1	1.257	308.3	41.3	4.78	1.47
353	15.3	1.253	309.3	40.8	5.13	1.59

[a] ±5%, [b] ±0.1%, [c] ±1%.

Table E2. Fit Parameters for Temperature Dependent Densities $\rho(T)$, $V_m(T)$, and $\gamma(T)$ for Phosphonium-Based ILs.

IL	$\rho(T)$		$V_m(T)$		$\gamma(T)$	
	c_ρ (g cm^{-3} K^{-1})	ρ_0 (g cm^{-3})	c_{Vm} (cm^3 mol^{-1} K^{-1})	V_{m0} (cm^3 mol^{-1})	c_γ (mN m^{-1} K^{-1})	γ_0 (mN m^{-1})
[P_{2225}][NF_2]	–7.240×10^{-4}	1.432	0.1863	248.2	–0.06346	59.51
[$P_{222(2O2)}$][NF_2]	–7.564×10^{-4}	1.486	0.1822	240.3	–0.06187	59.10
[$P_{222(2S2)}$][NF_2]	–7.487×10^{-4}	1.517	0.1784	246.3	–0.06879	65.10

Table E3. Fit Parameters for Temperature Dependent Densities $\sigma(T)$ and $\Lambda(T)$ for Phosphonium-Based ILs.

IL	$\sigma(T)$		$\Lambda(T)$	
	c_σ (mS cm^{-1} K^{-1})	σ_0 (mS cm^{-1})	c_Λ (S cm^2 mol^{-1} K^{-1})	Λ_0 (S cm^2 mol^{-1})
[P_{2225}][NF_2]	0.06695	-17.34	0.02144	-5.600
[$P_{222(2O2)}$][NF_2]	0.08084	-19.46	0.02540	-6.210
[$P_{222(2S2)}$][NF_2]	0.05622	-14.80	0.01769	-4.689

E. 2. Analysis of Low-Frequency Spectra

Table S4. Temperature Dependence of Low-frequency Spectral Peaks for Phosphonium-Based ILs.

	fs-RIKES	THz-TDS
Temp. (K)	Peaks (cm^{-1})	Peaks (cm^{-1})
	$[P_{2225}][NF_2]$	
293	22.1	69.9
308	20.7	69.5
323	19.3	68.7
338	18.3	66.4
353	17.9	65.3
	$[P_{222(2O2)}][NF_2]$	
293	21.2	70.4
308	19.8	69.6
323	18.8	68.2
338	17.6	67.6
353	16.7	66.0
	$[P_{222(2S2)}][NF_2]$	
293	25.6	71.9
308	24.3	70.2
323	23.2	70.1
338	22.0	69.2
353	20.8	68.6

E. 2. 1. Femtosecond-RIKES

Table E5. Diexponential fit parameters for Kerr transients of $[P_{2225}][NF_2]$, $[P_{222(2O2)}][NF_2]$, and $[P_{222(2S2)}][NF_2]$.

Temperature (K)	a_0	a_1	τ_1 (ps)	a_2	τ_2 (ps)
			$[P_{2225}][NF_2]$		
293	0.000361	0.0053	1.37	0.0021	8.08
308	0.000398	0.0073	1.35	0.0022	7.46
323	0.000571	0.0078	1.34	0.0025	6.97
338	0.000425	0.0079	1.33	0.0030	6.66
353	0.000422	0.0086	1.30	0.0033	6.54
			$[P_{222(2O2)}][NF_2]$		
293	0.000374	0.0065	1.26	0.0028	6.97
308	0.000457	0.0098	1.18	0.0032	6.95
323	0.000506	0.0099	1.17	0.0036	6.32
338	0.000472	0.0112	1.14	0.0040	6.28
353	0.000424	0.0119	1.13	0.0044	5.84
			$[P_{222(2S2)}][NF_2]$		
293	0.000438	0.0046	1.54	0.0017	7.51
308	0.000442	0.0047	1.48	0.0022	7.48
323	0.000426	0.0060	1.43	0.0026	7.29
338	0.000455	0.0065	1.41	0.0029	7.02
353	0.000473	0.0074	1.41	0.0033	6.84

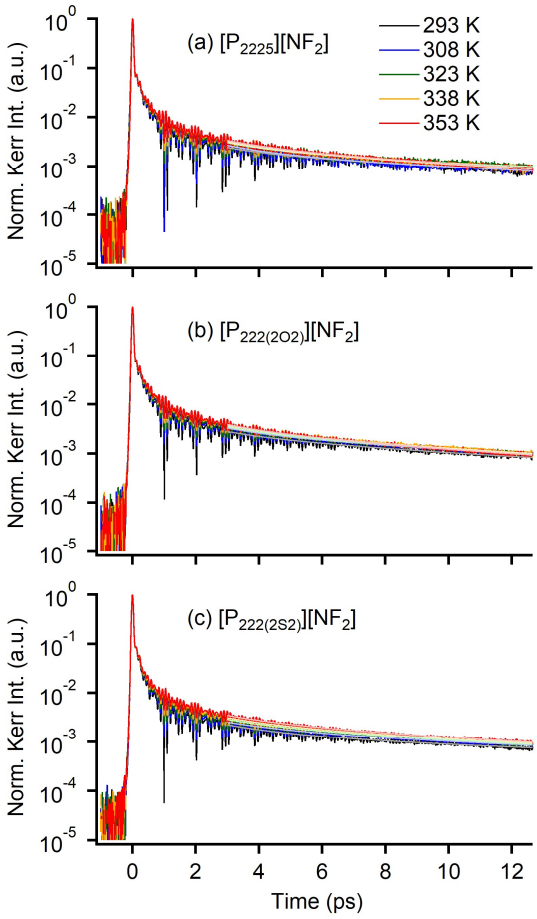

Figure E2. Temperature dependence of normalized Kerr transients for (a) $[P_{2225}][NF_2]$, (b) $[P_{222(2O2)}][NF_2]$, and (c) $[P_{222(2S2)}][NF_2]$. Diexponential fits from 3 to 12 ps are also shown.

E. 2. 2. THz-TDS

In this study, we obtained the THz-TDS spectra from the results of two spectroscopic techniques. One is the photoconductive antenna-based THz-TDS system observing the low-frequency THz-TDS spectra, and the other is the fs laser-induced plasma and air-biased coherent detection-based THz-TDS observing the high-frequency spectra. Figure S2-S4 exhibit the raw spectra of the low-frequency THz-TDS and the high-frequency one. The difference between the spectral intensities of the low-frequency THz-TDS spectrum and those of the high-frequency one at 50 cm^{-1} is less than 10%. Both THz-TDS spectra are obtained from the average of five scanned spectra. The spectra before averaging are shown in Figure S5-S7. The five spectra of the low-frequency THz spectra were in good agreement with each other, but those of the high-frequency THs-TDS spectra varied in intensity. This is because the light source of the THz-TDS based on the fs laser-induced plasma and air-biased coherent detection method has a lower repetition frequency (1 kHz) than that of the THz-TDS based on the photoconductive antenna-based system (78 MHz). To analyze the entire THz-TDS spectra accurately, we multiplied the high-frequency THz-TDS spectra by a factor of 0.960 to 1.097 and obtained the entire THz spectra by patching the low-frequency THz-TDS spectra and the multiplied high-frequency THz-TDS spectra at 50 cm^{-1}. The detailed values of the difference between the spectral intensities of the low-frequency THz-TDS spectrum and the high-frequency one at 50 cm^{-1} and those of how many times the high-frequency THz-TDS spectra are multiplied are listed in Table S5.

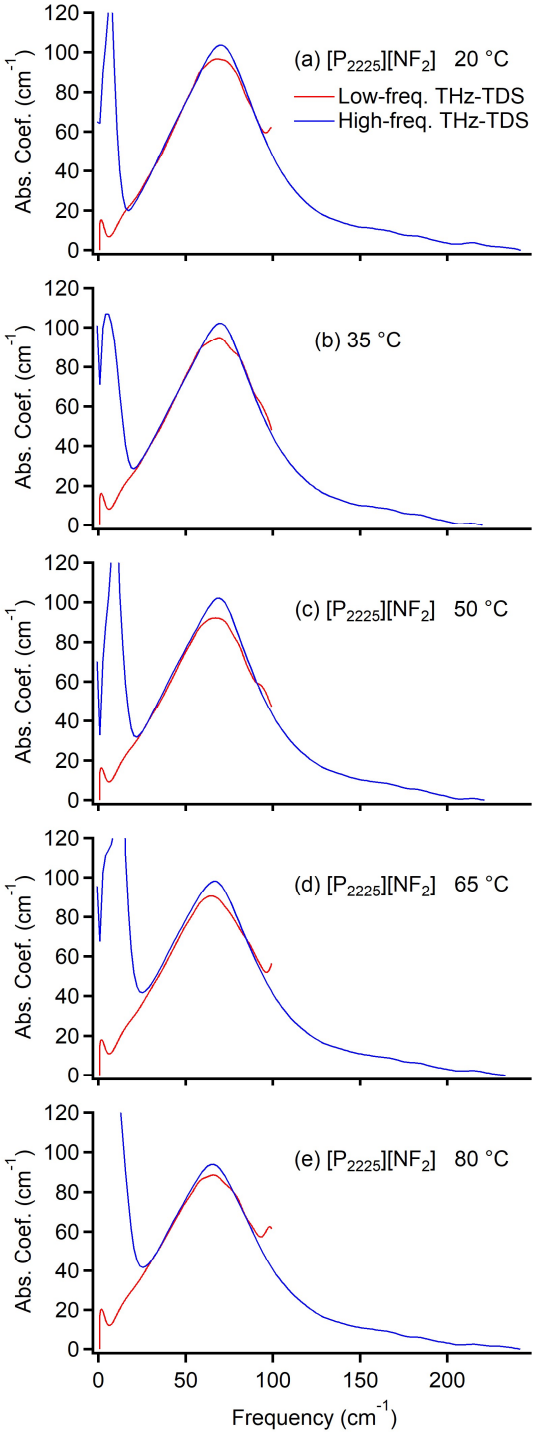

Figure E3. Raw spectra of low-frequency THz-TDS spectra (red lines) and the high-frequency spectra (blue lines) in $[P_{2225}][NF_2]$.

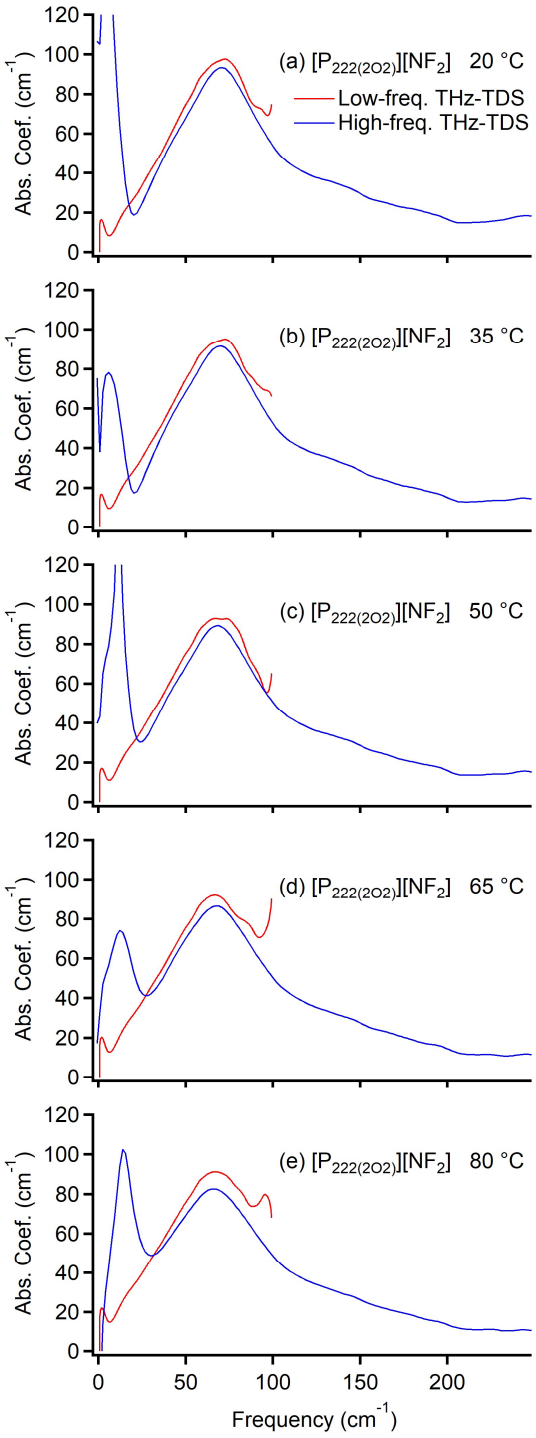

Figure E4. Raw spectra of low-frequency THz-TDS spectra (red lines) and the high-frequency spectra (blue lines) in $[P_{222(2O2)}][NF_2]$.

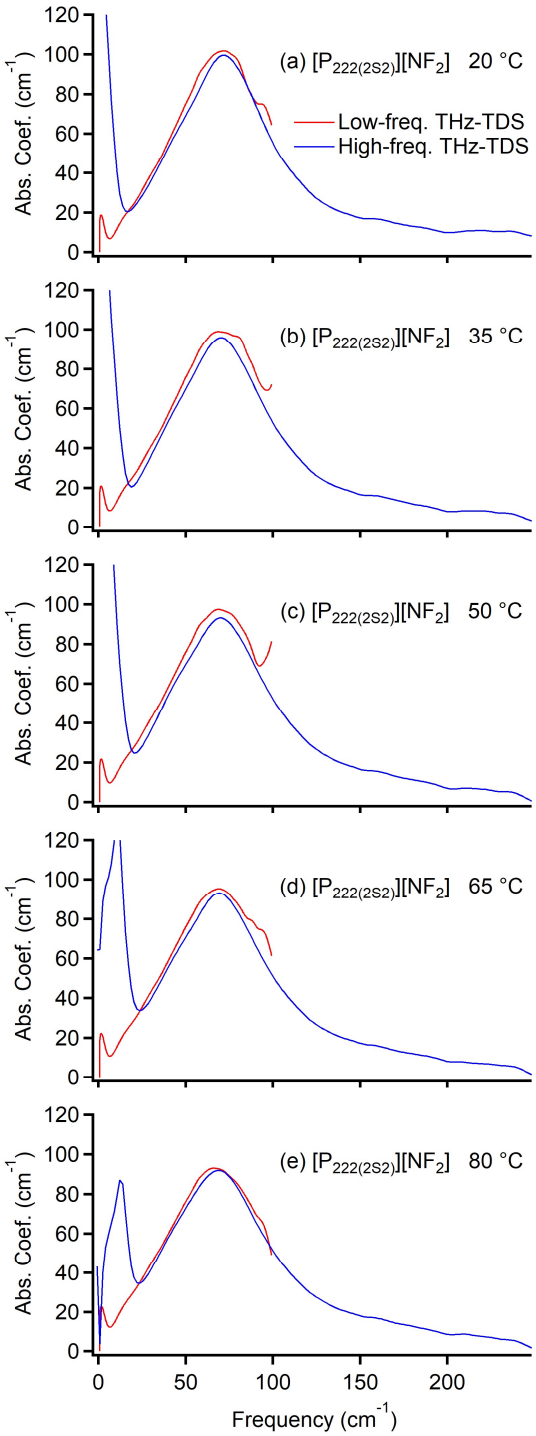

Figure E5. Raw spectra of low-frequency THz-TDS spectra (red lines) and the high-frequency spectra (blue lines) in $[P_{222(2S2)}][NF_2]$.

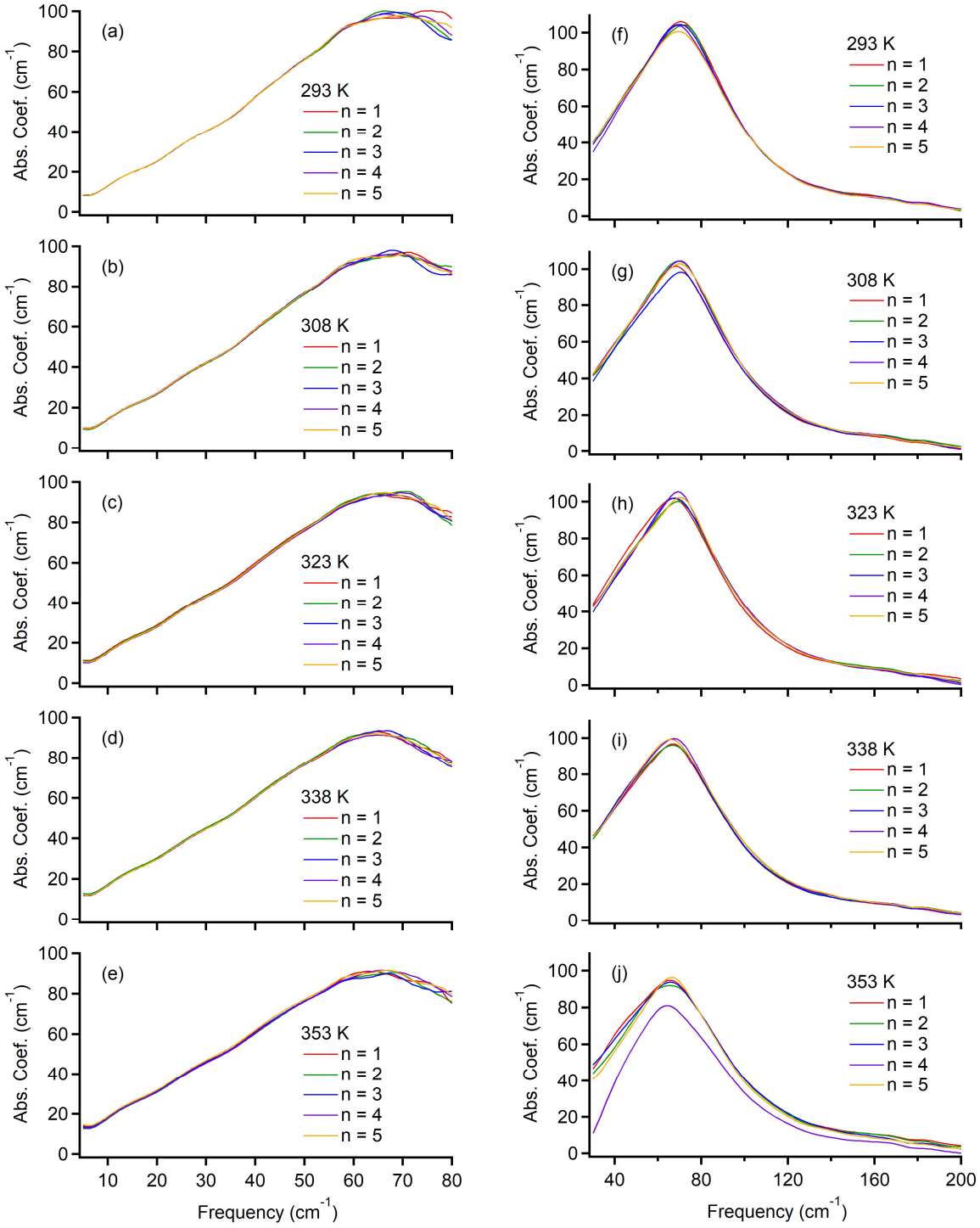

Figure E6. Spectra before averaging of the low-frequency THz-TDS spectra ((a)~(e)) (5–80 cm^{-1}) and the high-frequency spectra ((f)~(j)) (30–200 cm^{-1}) in $[P_{2225}][NF_2]$.

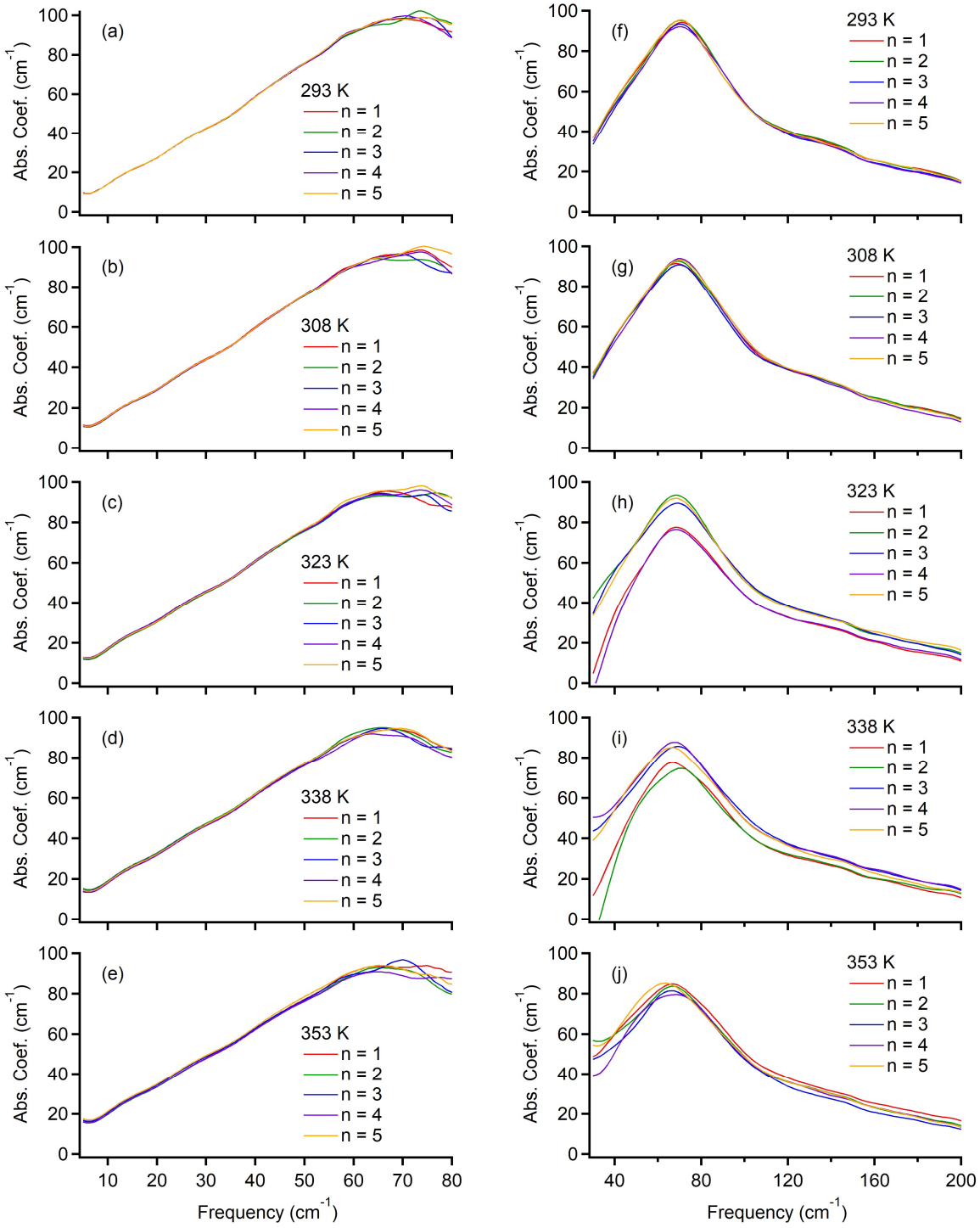

Figure E7. Spectra before averaging of the low-frequency THz-TDS spectra ((a)~(e)) (5–80 cm^{-1}) and the high-frequency spectra ((f)~(j)) (30–200 cm^{-1}) in $[P_{222(2O2)}][NF_2]$.

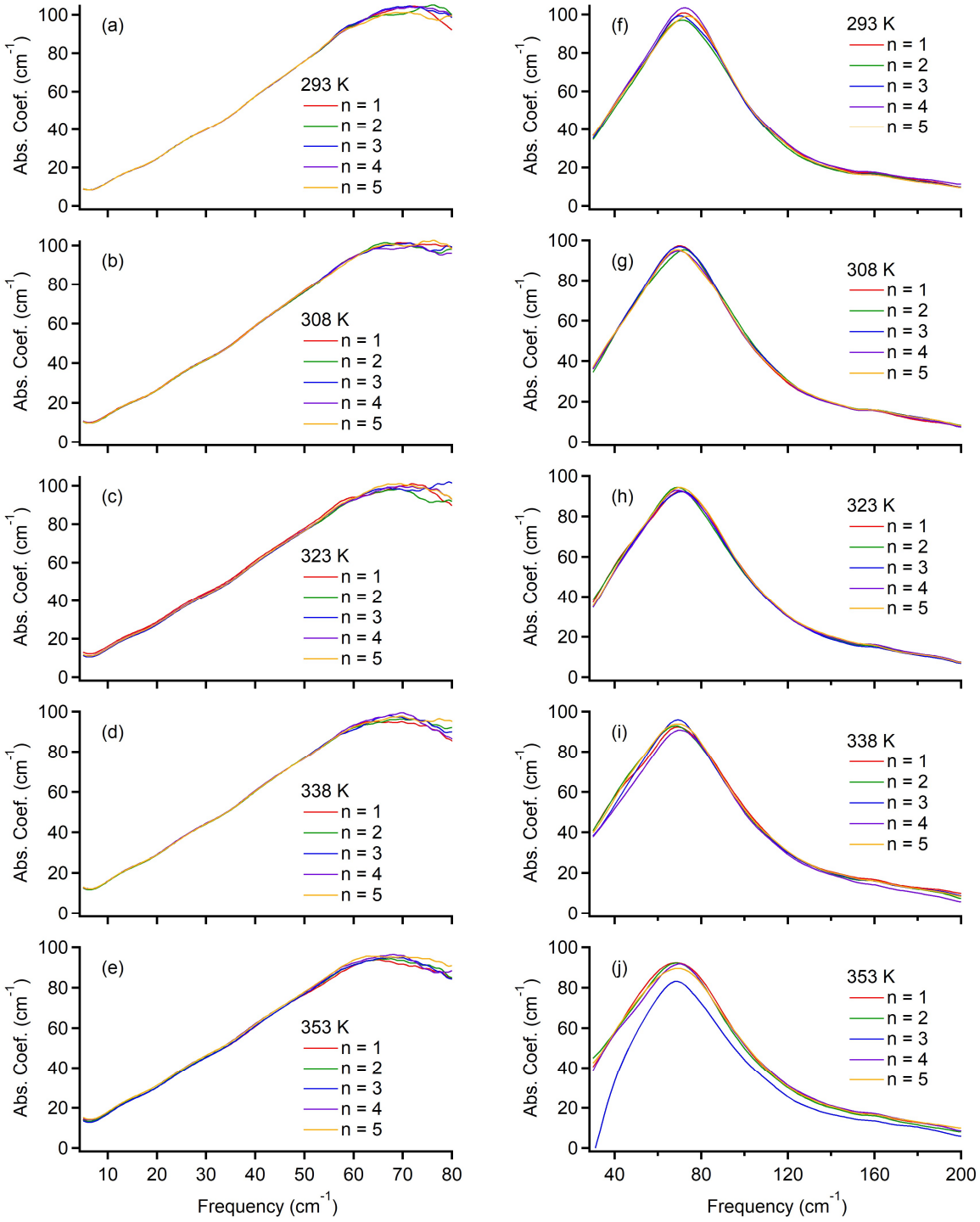

Figure E8. Spectra before averaging of the low-frequency THz-TDS spectra ((a)~(e)) (5–80 cm^{-1}) and the high-frequency spectra ((f)~(j)) (30–200 cm^{-1}) in $[P_{222(2S2)}][NF_2]$.

Table E6. Difference ratio of intensities for the high-frequency spectra against those for the low-frequency spectra at 50 cm^{-1} and factors for patching the high-frequency spectra to the low-frequency spectra.

Temp. (K)	$[P_{2225}][NF_2]$	$[P_{222(2O2)}][NF_2]$	$[P_{222(2S2)}][NF_2]$
	Difference ratio (%)		
293	-0.90	-9.44	-8.42
308	-1.48	-9.09	-8.33
323	1.46	-9.22	-8.55
338	3.26	-7.70	-7.31
353	1.58	-8.96	-4.81
	Factor		
293	1.000	1.097	1.087
308	1.005	1.095	1.087
323	0.980	1.097	1.087
338	0.960	1.077	1.075
353	0.980	1.092	1.045

E. 3. MD Simulations.

E. 3. 1. Polarizability Time Correlation Function (TCF) and Kerr spectra

E. 3. 1. 1. Theoretical Background

The Kerr response for OHD-RIKES with the typical polarization setup is connected with the relaxation of the polarizability anisotropy of the system. Therefore, to investigate it comparing with the experimentally observed Kerr spectra, it is required to calculate the time correlation function (TCF) of off-diagonal elements of the total polarizability of the system.[255] Here, the theoretical background of the polarizability TCF is summarized.

The total polarizability of the system, $\prod(t)$, is represented as the sum of the molecular polarizability, $\prod^{M}(t)$, and the interaction-induced polarizability, $\prod^{II}(t)$, as follows,

$$\prod(t) = \prod^{M}(t) + \prod^{II}(t) \tag{1}$$

where t indicates the time dependence, and subscripts M and II represent the molecular part and the interaction-induced part, respectively. The molecular part is the sum of the polarizability tensors of isolated gas phase molecular polarizability in the laboratory frame,

$$\Pi^{M}(t) = \sum_{i=1}^{N} \alpha_i(t), \tag{2}$$

where N is the number of molecules, and α_i denotes the polarizability tensor of molecule i. The interaction-induced part comprises the modulation of the molecular polarizabilities due to the intermolecular interactions and the contributions from the induced-multipole components. For the computation of the interaction-induced part, we employed the dipole-induced-dipole (DID) model approximation,[255,256] which assumes that the molecular polarizabilities are modulated due to a dipolar coupling and that the influence of higher order multipoles is not considered. Also, it should be noted that the DID model used in this study is a center-center DID model, where it recognizes the polarizability as concentrated in the center of mass of the molecule. The interaction-induced polarizability in the DID approximation is represented as follows,

$$\Pi^{II}(t) = \sum_{i=1}^{N} \sum_{j \neq i}^{N} \alpha_i(t) \cdot T_{ij}(t) \cdot \tilde{\alpha}_j(t), \tag{3}$$

where T_{ij} means the dipole interaction tensor between molecules i and j. $\tilde{\alpha}_i(t)$ is the effective polarizability for molecule i defined by the following equation including the interaction-induced effects,

$$\tilde{\alpha}_i(t) = \alpha_i(t) + \sum_{j \neq i}^{N} \alpha_i(t) \cdot T_{ij}(t) \cdot \tilde{\alpha}_j(t) \cdot \tag{4}$$

Eq 4 can be solved by the calculation procedure which is called the all-orders DID approximation.[256]

The total polarizability of the system, $\prod(t)$, can be reorganized separating it into the isotropic, $\frac{1}{3}\mathrm{Tr}(\prod(t))\boldsymbol{I}$, and anisotropic, $\beta^{\mathrm{M}}(t)$ and $\beta^{\mathrm{II}}(t)$, components as follows,

$$\begin{aligned}\prod(t) &= \frac{1}{3}\mathrm{Tr}(\prod(t))\boldsymbol{I} + \left\{\prod^{\mathrm{M}}(t) - \frac{1}{3}\mathrm{Tr}(\prod^{\mathrm{M}}(t))\boldsymbol{I}\right\} + \left\{\prod^{\mathrm{II}}(t) - \frac{1}{3}\mathrm{Tr}(\prod^{\mathrm{II}}(t))\boldsymbol{I}\right\} \\ &= \frac{1}{3}\mathrm{Tr}(\prod(t))\boldsymbol{I} + \beta^{\mathrm{M}}(t) + \beta^{\mathrm{II}}(t) \end{aligned} \quad (5)$$

where $\boldsymbol{I}$ is the unit tensor, and $\beta^{\mathrm{M}}(t) = \left\{\prod^{\mathrm{M}}(t) - \frac{1}{3}\mathrm{Tr}(\prod^{\mathrm{M}}(t))\boldsymbol{I}\right\}$ and $\beta^{\mathrm{II}}(t) = \left\{\prod^{\mathrm{II}}(t) - \frac{1}{3}\mathrm{Tr}(\prod^{\mathrm{II}}(t))\boldsymbol{I}\right\}$. Therefore, the TCF of the off-diagonal elements of the total polarizability, ϕ, can be rewritten and separated into three parts: a molecular part, ϕ^{mol}, an interaction-induced part, ϕ^{ind}, and a molecular-interaction-induced cross-correlation part, ϕ^{cross}, as follows,

$$\begin{aligned}\phi(t) &= \left\langle \mathrm{Tr}\left[\left(\beta^{\mathrm{M}}(0) + \beta^{\mathrm{II}}(0)\right)\cdot\left(\beta^{\mathrm{M}}(t) + \beta^{\mathrm{II}}(t)\right)\right]\right\rangle \\ &= \left\langle \mathrm{Tr}\left(\beta^{\mathrm{M}}(0)\cdot\beta^{\mathrm{M}}(t)\right)\right\rangle + \left\langle \mathrm{Tr}\left(\beta^{\mathrm{II}}(0)\cdot\beta^{\mathrm{II}}(t)\right)\right\rangle + \left\langle \mathrm{Tr}\left(\beta^{\mathrm{M}}(0)\cdot\beta^{\mathrm{II}}(t)\right)\right\rangle + \left\langle \mathrm{Tr}\left(\beta^{\mathrm{II}}(0)\cdot\beta^{\mathrm{M}}(t)\right)\right\rangle \\ &= \phi^{\mathrm{mol}}(t) + \phi^{\mathrm{ind}}(t) + \phi^{\mathrm{cross}}(t) \end{aligned} \quad (6)$$

where

$$\phi^{\mathrm{mol}}(t) = \left\langle \mathrm{Tr}\left(\beta^{\mathrm{M}}(0)\cdot\beta^{\mathrm{M}}(t)\right)\right\rangle$$

$$\phi^{\mathrm{ind}}(t) = \left\langle \mathrm{Tr}\left(\beta^{\mathrm{II}}(0)\cdot\beta^{\mathrm{II}}(t)\right)\right\rangle$$

$$\phi^{\mathrm{cross}}(t) = \left\langle \mathrm{Tr}\left(\beta^{\mathrm{M}}(0)\cdot\beta^{\mathrm{II}}(t)\right)\right\rangle + \left\langle \mathrm{Tr}\left(\beta^{\mathrm{II}}(0)\cdot\beta^{\mathrm{M}}(t)\right)\right\rangle.$$

The nuclear response function, $R(t)$, due to motion of the nuclei is related to the time derivative of the polarizability TCF, $\phi(t)$,

$$R(t) = -\frac{1}{k_B T}\frac{\partial}{\partial t}\phi(t)\cdot \quad (7)$$

Kerr signal in the frequency domain, $R(\omega)$, is provided by the imaginary part of the Fourier transform of the $R(t)$, and the $R(\omega)$ is represented as, including quantum corrections to the classically obtained spectrum,[139,291]

$$R(\omega) = 2\cdot\frac{1-e^{-\hbar\omega/k_B T}}{1+e^{-\hbar\omega/k_B T}}\int_0^\infty \sin(\omega t)R(t)dt, \quad (8)$$

where $\hbar = h/2\pi$, and h means the Planck constant. With Eq (6), (7) and (8), the $R(\omega)$ can be separated into three components,

$$R(\omega) = R^{\mathrm{mol}}(\omega) + R^{\mathrm{ind}}(\omega) + R^{\mathrm{cross}}(\omega), \tag{9}$$

where $R^{\mathrm{mol}}(\omega)$, $R^{\mathrm{ind}}(\omega)$, and $R^{\mathrm{cross}}(\omega)$ denote Kerr spectra components for the molecular part, the interaction-induced part, and the molecular-interaction-induced cross-correlation part contributions, respectively.

ILs are composed of cation and anion. Therefore, the total polarizability of the system can be decomposed into the cationic and anionic components,[141]

$$\Pi(t) = \Pi^{\mathrm{C(Cation)}}(t) + \Pi^{\mathrm{A(Anion)}}(t). \tag{10}$$

Referring to Eq (1), (2) and (3), the $\Pi^{\mathrm{C}}(t)$ and $\Pi^{\mathrm{A}}(t)$ are represented as follows,

$$\Pi^{\mathrm{C}}(t) = \sum_{k=1} \alpha_k^{\mathrm{C(M)}}(t) + \sum_{k=1} \alpha_k^{\mathrm{C(II)}}(t) \tag{11}$$

$$\Pi^{\mathrm{A}}(t) = \sum_{l=1} \alpha_l^{\mathrm{A(M)}}(t) + \sum_{l=1} \alpha_l^{\mathrm{A(II)}}(t) \tag{12}$$

where the indices k and l go over all cations and anions, respectively. Then, the total polarizability of the system, $\Pi(t)$, can be rewritten in the similar form to eq 5,

$$\begin{aligned}\Pi(t) &= \frac{1}{3}\mathrm{Tr}\left(\Pi^{\mathrm{C}}(t) + \Pi^{\mathrm{A}}(t)\right)\boldsymbol{I} + \left\{\Pi^{\mathrm{C}}(t) - \frac{1}{3}\mathrm{Tr}\left(\Pi^{\mathrm{C}}(t)\right)\boldsymbol{I}\right\} + \left\{\Pi^{\mathrm{A}}(t) - \frac{1}{3}\mathrm{Tr}\left(\Pi^{\mathrm{A}}(t)\right)\boldsymbol{I}\right\} \\ &= \frac{1}{3}\mathrm{Tr}\left(\Pi^{\mathrm{C}}(t) + \Pi^{\mathrm{A}}(t)\right)\boldsymbol{I} + \beta^{C}(t) + \beta^{A}(t),\end{aligned} \tag{13}$$

where $\beta^{\mathrm{C}}(t) = \left\{\Pi^{\mathrm{C}}(t) - \frac{1}{3}\mathrm{Tr}\left(\Pi^{\mathrm{C}}(t)\right)\boldsymbol{I}\right\}$ and $\beta^{\mathrm{A}}(t) = \left\{\Pi^{\mathrm{A}}(t) - \frac{1}{3}\mathrm{Tr}\left(\Pi^{\mathrm{A}}(t)\right)\boldsymbol{I}\right\}$ The polarizability TCF, ϕ, can be rewritten as follows,

$$\begin{aligned}\phi(t) &= \left\langle \mathrm{Tr}\left[\left(\beta^{\mathrm{C}}(0) + \beta^{\mathrm{A}}(0)\right)\cdot\left(\beta^{\mathrm{C}}(t) + \beta^{\mathrm{A}}(t)\right)\right]\right\rangle \\ &= \left\langle \mathrm{Tr}\left(\beta^{\mathrm{C}}(0)\cdot\beta^{\mathrm{C}}(t)\right)\right\rangle + \left\langle \mathrm{Tr}\left(\beta^{\mathrm{A}}(0)\cdot\beta^{\mathrm{A}}(t)\right)\right\rangle + \left\langle \mathrm{Tr}\left(\beta^{\mathrm{C}}(0)\cdot\beta^{\mathrm{A}}(t)\right)\right\rangle + \left\langle \mathrm{Tr}\left(\beta^{\mathrm{A}}(0)\cdot\beta^{\mathrm{C}}(t)\right)\right\rangle \\ &= \phi^{\mathrm{C}}(t) + \phi^{\mathrm{A}}(t) + \phi^{\mathrm{C-A}}(t),\end{aligned} \tag{14}$$

where

$$\phi^{\mathrm{C}}(t) = \left\langle \mathrm{Tr}\left(\beta^{\mathrm{C}}(0)\cdot\beta^{\mathrm{C}}(t)\right)\right\rangle$$

$$\phi^{\mathrm{A}}(t) = \left\langle \mathrm{Tr}\left(\beta^{\mathrm{A}}(0)\cdot\beta^{\mathrm{A}}(t)\right)\right\rangle$$

$$\phi^{\mathrm{C-A}}(t) = \left\langle \mathrm{Tr}\left(\beta^{\mathrm{C}}(0)\cdot\beta^{\mathrm{A}}(t)\right)\right\rangle + \left\langle \mathrm{Tr}\left(\beta^{\mathrm{A}}(0)\cdot\beta^{\mathrm{C}}(t)\right)\right\rangle$$

Corresponding to eq 9, Kerr signal in the frequency domain, $R(\omega)$, is given by three components,

$$R(\omega) = R^{C}(\omega) + R^{A}(\omega) + R^{C\text{-}A}(\omega) \quad (15)$$

where $R^{C}(\omega)$, $R^{A}(\omega)$, and $R^{C\text{-}A}(\omega)$ denote Kerr spectra components for the cation contribution, the anion contribution, and the cation-anion cross-correlation part contribution, respectively.

E. 3. 1. 2. Calculation Details for Polarizability TCF

In Figure S9, the body-fixed coordinate axes we set in cation and anion are shown. For the calculation of gas phase molecular polarizability tensors of cation and anion, we used the Gaussian 09 program package.[254] We employed the DFT/B3LYP level of theory[122,123] with the cc-pVDZ basis sets[292,293] for $[P_{2225}]^{+}$ and $[NF_2]^{-}$.

For the calculation of the molecular polarizability, eq 4 was solved iteratively by the efficient iteration scheme proposed by Kiyohara et al.[294] under the all-orders DID approximation. We also employed the Thole's model[295] in a simplified way for avoiding the unphysical divergence of the polarization in the computation of dipole interaction tensors. In our calculation, we considered the distance and vector between the centers of mass of distinct molecules in the dipole interaction tensor, $T = (\boldsymbol{I} - 3\hat{\boldsymbol{r}}\hat{\boldsymbol{r}})/r^3$, where $\hat{\boldsymbol{r}} = \boldsymbol{r}/r$. Therefore, the range of the attenuation of dipolar interactions at short distances, s, was evaluated with the definition,[295] $s = 1.662(A_iA_j)^{1/6}$, where A_i and A_j denote the molecular polarizabilities set at the centers of mass of molecules i and j, respectively. It should be noted that, only in determining the range of attenuation of dipolar interactions, both the A_i and A_j were taken as isotropic and scalar in our model and that, for the molecular polarizabilities, A_i and A_j, we used 21.460 Å^3 for $[P_{2225}]^{+}$ and 7.5995 Å^3 for $[NF_2]^{-}$, based on the *ab initio* calculations. The dipole interaction tensor we used is given by[295]

$$T = (\boldsymbol{I} - 3\hat{\boldsymbol{r}}\hat{\boldsymbol{r}})/r^3 \quad (r > s) \quad (16)$$

$$T = \left[(4v^3 - 3v^4)\boldsymbol{I} - 3v^4\hat{\boldsymbol{r}}\hat{\boldsymbol{r}}\right]/r^3 \quad (r \le s) \quad (17)$$

where $v = r/s$.

The polarizability TCF, $\phi(t)$, in eq 7 was analyzed by fitting a stretched exponential function to data points, and then, the time derivative of the analytically fitted function $\phi(t)$ was utilized in eq 8 as the nuclear response function, $R(t)$, in order to treat the long-time region of the $R(t)$ and improve the accuracy of the numerical Fourier sine transforms.[296,297]

E. 3. 2. Terahertz Time-Domain Spectroscopy by Molecular Dynamics Simulation

The terahertz spectrum can be computed via the Fourier transform of the ACF of the total dipole moment **M** of the system at time *t*,

$$I(\omega) \propto \int_0^\infty <\boldsymbol{M}(t) \cdot \boldsymbol{M}(0)> \cos(\omega t)\, \mathrm{d}t \tag{18}$$

where *I(ω)* means the spectral density and ω is the vibration frequency. **M**(*t*) is represented as the sum of all the individual dipole moments of the molecules

$$\mathbf{M}(t) = \sum_{i=1}^{n} \boldsymbol{\mu}_i(t) = \sum_{i=1}^{n} e_i \mathbf{x}_i(t) \tag{19}$$

where $\boldsymbol{\mu}_i(t)$ is the dipole moment of the *i*th molecule at time *t*, *n* is the total number of molecules, e_i is the fixed electric charge of the *i*th atom, and $\mathbf{x}_i(t)$ is the position vector of the *i*th atom at time *t*. The IR spectrum can be also calculated with the dipole moment time derivative ACF. [257,259]

$$\left\langle \frac{d\boldsymbol{M}(t)}{dt} \cdot \frac{d\boldsymbol{M}(0)}{dt} \right\rangle = \left\langle \sum_{j=1}^{n} e_j \frac{d\boldsymbol{x}_j(t)}{dt} \cdot \sum_{j=1}^{n} e_j \frac{d\boldsymbol{x}_j(0)}{dt} \right\rangle = \left\langle \sum_{j=1}^{n} e_j \boldsymbol{v}_j(t) \cdot \sum_{j=1}^{n} e_j \boldsymbol{v}_j(0) \right\rangle \tag{20}$$

where $\mathbf{v}_j(t)$ is the position vector of the *j*th atom at time *t*.

$$I(\omega) \propto \int_0^\infty <\sum_{j=1}^{n} e_j \mathbf{v}_j(t) \cdot \sum_{j=1}^{n} e_j \mathbf{v}_j(0)> \cos(\omega t)\, \mathrm{d}t \tag{21}$$

By applying a damping function of a Gaussian type $\exp(-\alpha t^2)$ prior to the Fourier transform calculation, the spectral density is then given as,[257]

$$I(\omega) \propto \int_0^\infty <\sum_{j=1}^{n} e_j \mathbf{v}_j(t) \cdot \sum_{j=1}^{n} e_j \mathbf{v}_j(0)> \exp\left(-\alpha t^2\right) \cos(\omega t)\, \mathrm{d}t \tag{22}$$

By applying a damping function of a Gaussian type $\exp(-\alpha t^2)$ prior to the Fourier transform calculation, the spectral density is then given as $\alpha = 20$.[257]

The absorption cross section, $\alpha(\omega)$, is then[258,259]

$$\alpha(\omega) \propto \omega^2 \int_0^\infty <\sum_{j=1}^{n} e_j \mathbf{v}_j(t) \cdot \sum_{j=1}^{n} e_j \mathbf{v}_j(0)> \exp\left(-\alpha t^2\right) \cos(\omega t)\, \mathrm{d}t \tag{23}$$

Also, we performed the decomposition of the velocity of an atom into translational and rotational components with the following equation[260,261]

$$\left(\frac{d\boldsymbol{r}_i}{dt}\right)_{space} = \left(\frac{d\boldsymbol{r}_i}{dt}\right)_{body} + \Omega \times \boldsymbol{r}_i \tag{24}$$

where the subscripts *space* and *body* mean the velocities observed in the space and body fixed coordinates, and $\boldsymbol{r_i}$ represents the velocity of the *i*th atom. The vector Ω indicates the angular velocity of the molecule which belongs to the *i*th atom. Then, with decomposed components and Eq (24) and (27), we evaluated the contribution of translational and rotational motions to the terahertz spectra we observed.

E. 3. 3. DOS and VACF Profiles

With MD simulation results, we calculated velocity autocorrelation functions (VACFs), $\langle \boldsymbol{v}_i(0) \cdot \boldsymbol{v}_i(t) \rangle$, where $\boldsymbol{v}_i(t)$ is the velocity of *i*-th ionic species, and obtained the vibrational density of states with the Fourier transformation of VACFs. All the DOS spectra are calculated as area normalized spectra,

$$I_{DOS}(\omega) = I(\omega) / \int I(\omega) d\omega \qquad (25)$$

where $I_{DOS}(\omega)$ represents the frequency dependent area normalized DOS intensity and $I(\omega)$ is the calculated DOS from MD simulation. In this study, we calculated the time correlation of the total velocity which includes the velocities of all the atoms in each system (hereafter, denoted as total (anion and cation) DOS), and also, the time correlation functions were calculated for cation and anion species, respectively.

Table E7. Components of the Molecular Polarizability Tensor Elements for $[P_{2225}]^+$ and $[NF_2]^-$ (Units in $Å^3$)

	α_{XX} [a]	α_{XY} [a]	α_{YY} [a]	α_{XZ} [a]	α_{YZ} [a]	α_{ZZ} [a]
$[P_{2225}]^+$	18.451	0.26517	25.060	-0.41077×10^{-10}	-0.10214×10^{-10}	20.870
$[NF_2]^-$	7.7021	-0.18251×10^{-1}	6.0194	−1.2178	0.27858×10^{-1}	9.0769

[a] *X*, *Y*, and *Z* directions are set as shown in Figure S1.

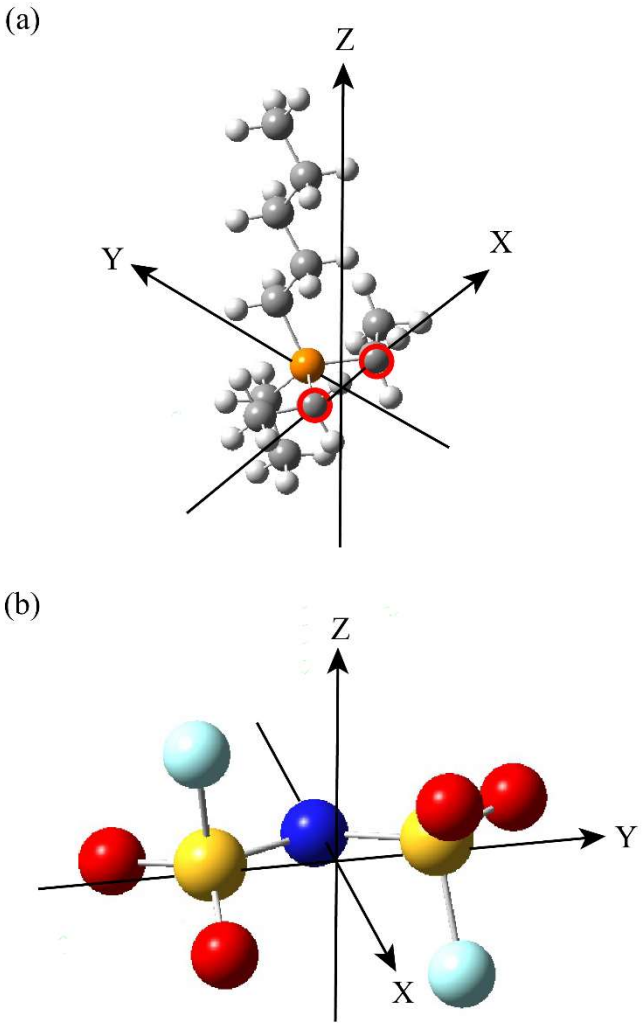

Figure E9. Structures and definitions of body-fixed coordinate axes for the cations and anion of the ILs used in this study: (a) $[P_{2225}]^+$ and (b) $[NF_2]^-$. In $[P_{2225}]^+$, the X direction is along the line connecting two carbon (highlighted with a red colored circle) atoms, and the Y direction is along the line connecting he bisection point between the two highlighted carbon atoms to the phosphorus (orange colored) atom, and is set perpendicular to the X direction. The Z direction is orthogonal to both the X and Y axes. axis. In $[NF_2]^-$, the Y direction is along the line connecting two sulfur (yellow colored) atoms, and the Z direction is set perpendicular to the S−N(blue colored)−S plane and the X direction axis. The X direction is set in the S−N−S plane orthogonal to both the Y and Z axes.

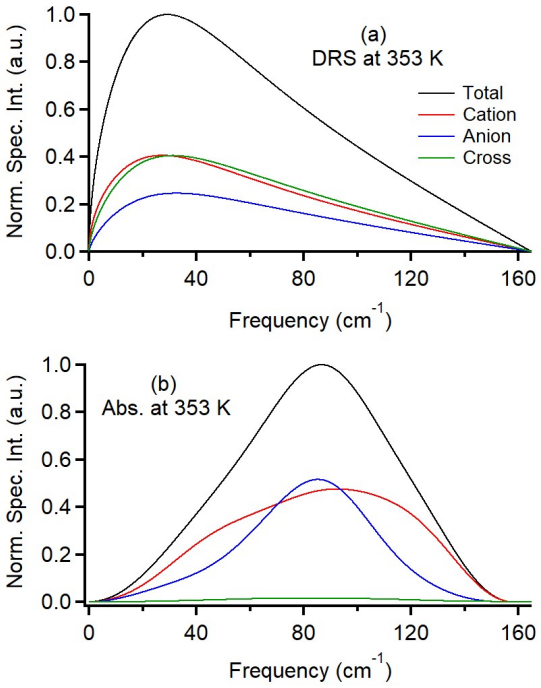

Figure E10. Decomposition analysis results of (a) DRS and (b) ABS of $[P_{2225}][NF_2]$ at 353 K. Black lines denote the total spectra, red lines denote the cation spectra, blue line denotes the anion spectra, and green lines denote the cross-term spectra.

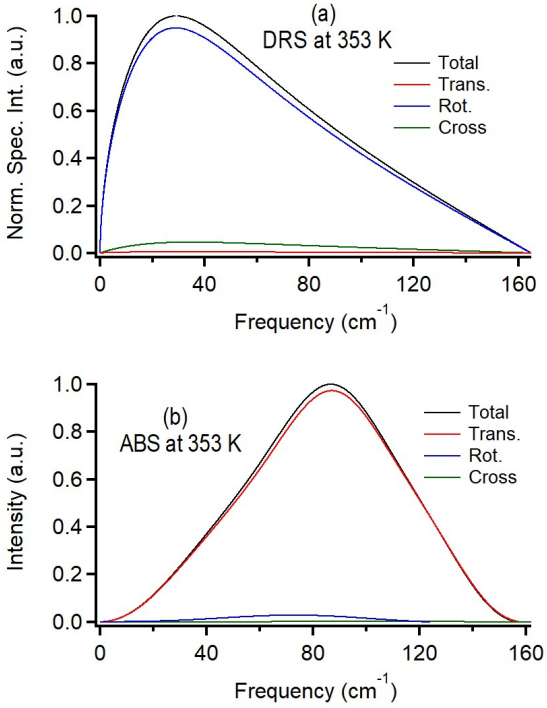

Figure E11. Decomposition analysis results of (a) DRS and (b) ABS of $[P_{2225}][NF_2]$ at 353 K. Black lines denote the total spectra; red lines denote the translational component; blue line denotes the rotational component; green lines denote the cross-term component.

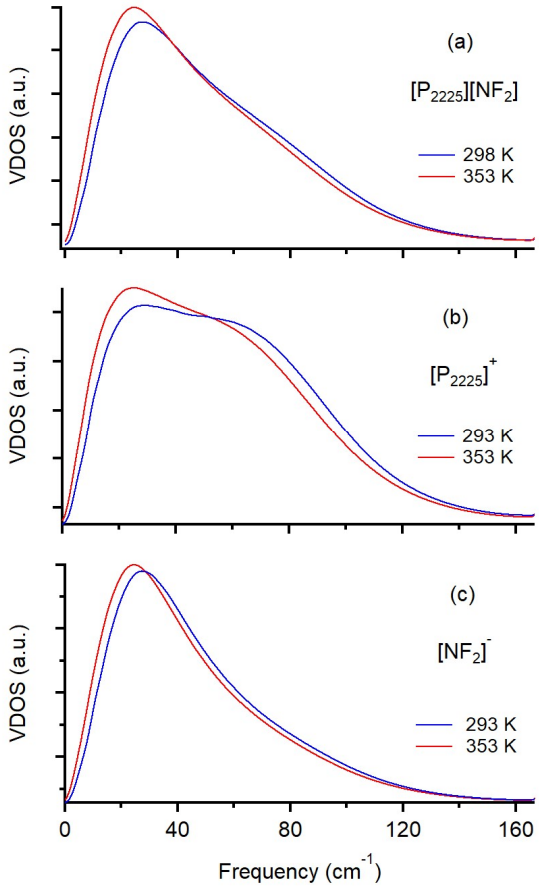

Figure E12. VDOS spectra of (a) $[P_{2225}][NF_2]$, (b) $[P_{2225}]^+$, and (c) $[NF_2]^-$ at 293 K (blue) and 353 K (red).

E. 4. Quantum Chemistry Calculations.

Table E8. Atom coordinates at stable structure calculated by the B3LYP/6-311++G(d,p) levels of theory.

$[P_{2225}]^+$

Center Number	Atomic Number	Atomic Type	Coordinates (Angstroms) X	Y	Z
1	15	0	-1.119206	0.161850	-0.088794
2	6	0	-0.797911	-0.401271	1.630463
3	1	0	0.047500	0.191414	1.990803
4	1	0	-1.669631	-0.087324	2.213099
5	6	0	-0.521817	-1.898678	1.831169
6	1	0	-0.361448	-2.087817	2.894148
7	1	0	-1.355363	-2.524046	1.510475
8	1	0	0.376574	-2.220941	1.303362
9	6	0	-2.840607	-0.233213	-0.588074
10	1	0	-3.013279	0.336733	-1.507370
11	1	0	-3.493940	0.200160	0.174663
12	6	0	-3.175604	-1.716337	-0.807788
13	1	0	-4.203409	-1.796904	-1.165976
14	1	0	-2.531832	-2.179407	-1.557869
15	1	0	-3.106290	-2.294901	0.113846
16	6	0	-0.933251	1.983980	-0.137496
17	1	0	0.109096	2.197502	0.115490
18	1	0	-1.069295	2.281238	-1.182316
19	6	0	-1.884761	2.766410	0.781085
20	1	0	-1.680888	3.833581	0.678515
21	1	0	-2.932729	2.609067	0.519791
22	1	0	-1.746193	2.508499	1.832867
23	6	0	0.014094	-0.591033	-1.321752
24	1	0	-0.508025	-0.476469	-2.278099
25	1	0	0.043477	-1.664954	-1.114091
26	6	0	1.441144	-0.016447	-1.439386
27	1	0	1.394837	1.056311	-1.653139
28	1	0	1.877721	-0.473469	-2.333154
29	6	0	3.804118	0.209182	-0.499224
30	1	0	4.197396	-0.287125	-1.393496
31	1	0	3.787076	1.281332	-0.727854
32	6	0	4.740101	-0.049076	0.684035
33	1	0	4.807463	-1.116868	0.912317
34	1	0	5.750105	0.306065	0.469132
35	1	0	4.395191	0.465022	1.586544
36	6	0	2.370677	-0.277729	-0.248757
37	1	0	2.389947	-1.352667	-0.030756
38	1	0	1.986936	0.213492	0.655324
Rotational constants (GHz):			1.0004647	0.4018945	0.3716337

$[P_{222(2O2)}]^+$

Center Number	Atomic Number	Atomic Type	Coordinates (Angstroms) X	Y	Z

1	15	0	-0.982798	0.170019	-0.110487
2	6	0	-0.489548	-0.393039	1.564549
3	1	0	0.408650	0.177746	1.809316
4	1	0	-1.285679	-0.062833	2.239326
5	6	0	-0.212981	-1.894691	1.727588
6	1	0	0.021283	-2.096538	2.774520
7	1	0	-1.069484	-2.515116	1.459951
8	1	0	0.647493	-2.200192	1.132024
9	6	0	-2.781168	-0.076183	-0.376172
10	1	0	-3.012078	0.421089	-1.324312
11	1	0	-3.290217	0.493629	0.406600
12	6	0	-3.279840	-1.529098	-0.392734
13	1	0	-4.348781	-1.535076	-0.612872
14	1	0	-2.785795	-2.128417	-1.160003
15	1	0	-3.143402	-2.019391	0.571962
16	6	0	-0.632641	1.960615	-0.264418
17	1	0	0.450952	2.061686	-0.162639
18	1	0	-0.889271	2.245669	-1.289735
19	6	0	-1.362538	2.856071	0.748915
20	1	0	-1.067091	3.893698	0.584493
21	1	0	-2.447346	2.805815	0.639408
22	1	0	-1.105120	2.603610	1.779467
23	6	0	-0.093775	-0.736328	-1.437258
24	1	0	-0.667528	-0.605027	-2.359640
25	1	0	-0.130821	-1.797295	-1.179037
26	6	0	1.352775	-0.286898	-1.651314
27	1	0	1.387292	0.698992	-2.136440
28	1	0	1.846294	-0.999322	-2.325163
29	6	0	3.409344	0.009419	-0.476351
30	1	0	3.875644	-0.778923	-1.080131
31	1	0	3.570289	0.967147	-0.988620
32	6	0	3.988399	0.035233	0.922991
33	1	0	3.829208	-0.919026	1.429673
34	1	0	5.064465	0.216779	0.873511
35	1	0	3.540467	0.831791	1.521925
36	8	0	1.994300	-0.247673	-0.392632
Rotational constants (GHz):			1.0018172	0.4775121	0.4369777

$[P_{222(2S2)}]^{+}$

Center Number	Atomic Number	Atomic Type	Coordinates (Angstroms) X	Y	Z
1	15	0	-1.299621	0.193479	-0.096199
2	6	0	-1.056243	-0.388940	1.628386
3	1	0	-0.169991	0.134442	1.995814
4	1	0	-1.914721	-0.008279	2.191092
5	6	0	-0.896383	-1.903579	1.830361
6	1	0	-0.808697	-2.105836	2.899433
7	1	0	-1.750109	-2.471822	1.459038
8	1	0	0.010313	-2.278699	1.353996
9	6	0	-3.054039	0.009131	-0.599685
10	1	0	-3.139848	0.528663	-1.560091
11	1	0	-3.644054	0.584543	0.119514
12	6	0	-3.593274	-1.425014	-0.712376

13	1	0	-4.618183	-1.389503	-1.085812
14	1	0	-3.013559	-2.033393	-1.409362
15	1	0	-3.616482	-1.931074	0.253395
16	6	0	-0.874408	1.972414	-0.182138
17	1	0	0.190922	2.036396	0.05695
18	1	0	-0.991583	2.273842	-1.227976
19	6	0	-1.696183	2.883562	0.743123
20	1	0	-1.351636	3.912347	0.625447
21	1	0	-2.760625	2.867585	0.501980
22	1	0	-1.573273	2.617934	1.794867
23	6	0	-0.279132	-0.732497	-1.318883
24	1	0	-0.808390	-0.638977	-2.272931
25	1	0	-0.318730	-1.788788	-1.040093
26	6	0	1.173758	-0.273848	-1.506652
27	1	0	1.209559	0.762457	-1.850981
28	1	0	1.622820	-0.897050	-2.283146
29	6	0	3.778923	0.192726	-0.528097
30	1	0	4.104250	-0.430296	-1.363606
31	1	0	3.644078	1.216210	-0.884396
32	6	0	4.786228	0.138628	0.616543
33	1	0	4.929257	-0.882646	0.975731
34	1	0	5.752700	0.508931	0.266690
35	1	0	4.473636	0.761430	1.457668
36	16	0	2.143824	-0.442881	0.040392
Rotational constants (GHz):			1.0000916	0.3618575	0.3360789

$[NF_2]^-$

Center Number	Atomic Number	Atomic Type	Coordinates (Angstroms) X	Y	Z
1	7	0	0.000000	0.000000	0.845952
2	16	0	0.000000	1.412292	0.086647
3	8	0	0.122292	2.460860	1.080584
4	8	0	0.764176	1.495806	-1.145669
5	16	0	0.000000	-1.412292	0.086647
6	8	0	-0.122292	-2.460860	1.080584
7	8	0	-0.764176	-1.495806	-1.145669
8	9	0	-1.584147	1.549812	-0.425167
9	9	0	1.584147	-1.549812	-0.425167
Rotational constants (GHz):			2.4614891	0.8613630	0.8442408

Table E 9. Polarizability Tensor Elements α_{ij}, Mean Polarizability α_0, and Polarizability Anisotropy α_{anis} Estimated by DFT Calculations Based on the B3LYP/6-311++G(d,p) Level of Theory.

	α_{xx} (Å^3)	α_{yy} (Å^3)	α_{zz} (Å^3)	α_{xy} (Å^3)	α_{yz} (Å^3)	α_{zx} (Å^3)	α_0 (Å^3)	α_{anis} (Å^3)
$[P_{2225}]^+$	20.367	21.553	24.577	0.059	−0.476	−0.033	22.166	3.851
$[P_{222(2O2)}]^+$	20.023	20.623	22.344	−0.422	0.441	−1.005	20.997	2.916
$[P_{222(2S2)}]^+$	21.784	22.348	26.606	−0.863	1.487	−1.792	23.579	6.273
$[NF_2]^-$	8.152	11.909	9.056	−0.007	0	0	9.706	3.397

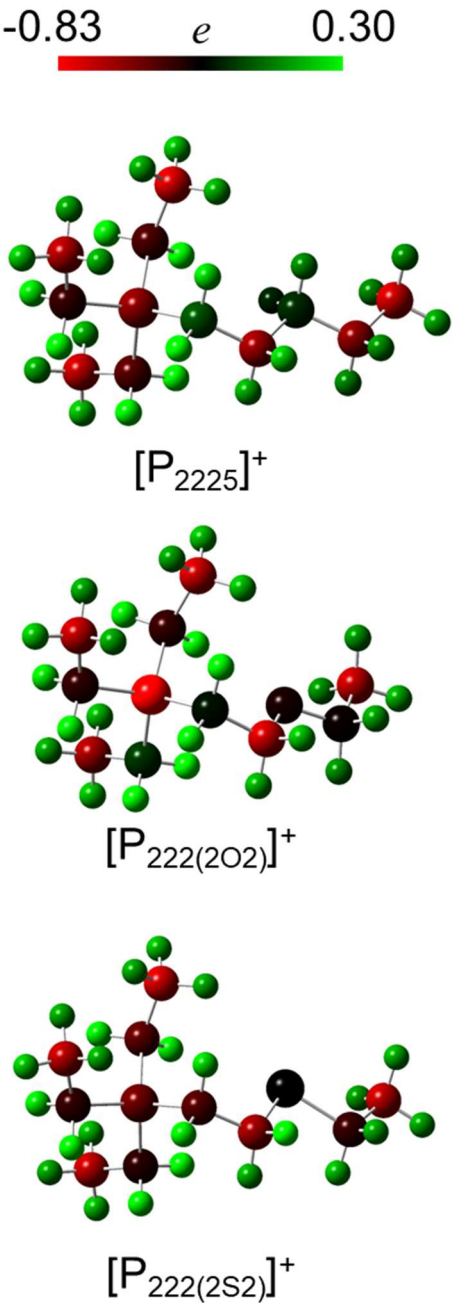

Figure E13. Atom charges of $[P_{2225}]^+$, $[P_{222(2O2)}]^+$, and $[P_{222(2S2)}]^+$.

Acknowledgements

First and foremost, I would like to say thank you to Professor Hideaki Shirota for all you have done for me, which I can't tell you enough about. He patiently taught me not only research techniques but also how to be prepared as a researcher. His coaching and advice were essential to my PhD program. I would like to thank him again.

I am very grateful to Professor Toshiyuki Takamuku at Saga University for his kind encouragement and helpful discussion about the [MOIm][BF_4]/ML mixtures in Chapter III and IV. His advice helped me to consider and understand the [MOIm][BF_4]/ML mixtures more deeply. I would also thank him for critical discussions and comments as a thesis reviewer.

I am very indebted to Dr. Kaoru Ohta at Kobe University who spent a long time on THz-TDS experiment with me and gave me a lot of guidance on the analysis of the THz-TDS spectra. Thanks to him, I was able to obtain the low-frequency THz-TDS spectra that are comparable to the fs-RIKES results in Chapter VI.

I would like to thank Dr. Tateki Ishida at the Institute for Molecular Science for performing MD simulations of the low-Frequency DRS and ABS spectra in Chapter VI. His results of the MD simulations revealed that the types of ions and motions observed in fs-RIKES and THz-TDS are different.

I would like to Professor Keisuke Tominaga at Kobe University for his kind encouragement and helpful discussion about the study in Chapter VI. His valuable comments were very helpful in comparing fs-RIKES and THz-TDS spectra and in comparing liquid properties and spectra of phosphonium-based ILs with different functional groups.

I sincerely thank Dr. Masashi Kawano and Mr. Atsuya Tashiro who performed MD simulation and measured NMR and IR for the [MOIm][BF_4]/ML mixtures in Chapter III and IV, respectively. Their results allowed detailed discussions of the microscopic pictures of the [MOIm][BF_4]/ML mixtures.

I would like to thank Professor Hirofumi Kanoh, Professor Takayoshi Arai, and Professor Takeshi Morita for insightful discussions and comments as the examiners of the degree.

I would also like to express my deepest gratitude to the Shirota lab members who discussed my research and helped me in my research life.

Finally, I would like to thank my parents, grandparents, uncle, and aunt for their support in helping me to have a fruitful doctoral program.

Publication Lists

Original Papers

1) **M. Ando**, M. Kawano, A. Tashiro, Y. Peng, T. Takamuku, H. Shirota, " Exploring the Microscopic Aspects of 1-Methyl-3-octylimidazolium Tetrafluoroborate Mixtures with Formamide, *N*-Methylformamide, and *N*,*N*-Dimethylformamide by Multiple Spectroscopic Techniques and Computations", *Journal of Physical Chemistry B*, American Chemical Society, submitted.

2) **M. Ando**, K. Ohta, T. Ishida, R. Koido, H. Shirota, "Physical Properties and Low-Frequency Polarizability Anisotropy and Dipole Responses of Phosphonium Bis(fluorosulfonyl)amide Ionic Liquids Having Pentyl, Ethoxyethyl, or 2-(Ethylthio)ethyl Group", *Journal of Physical Chemistry B*, American Chemical Society, *J. Phys. Chem. B* **2023**, *127*, 542-556.

【Special issue "Hiro-o Hamaguchi Festschrift"】

3) **M. Ando**, H. Shirota, "Low-Frequency Spectra of 1-Methyl-3-octylimidazolium Tetrafluoroborate Mixtures with Poly(Ethylene Glycol) by Femtosecond Raman-Induced Kerr Effect Spectroscopy", *Journal of Physical Chemistry B*, American Chemical Society, **2021**, *125*, 12006-12019.

【Special issue "Kankan Bhattacharyya Festschrift"】

4) **M. Ando**, M. Kawano, A. Tashiro, T. Takamuku, H. Shirota, "Low-Frequency Spectra of 1-Methyl-3-Octylimidazolium Tetrafluoroborate Mixtures with Methanol, Acetonitrile, and Dimethyl Sulfoxide: A Combined Study of Femtosecond Raman-Induced Kerr Effect Spectroscopy and Molecular Dynamics Simulations", *Journal of Physical Chemistry B*, American Chemical Society, **2020**, *124*, 7857-7871.

【Supplementary Cover Art】

Proceeding

1) **M. Ando**, K. Ohta, T. Ishida, K. Tominaga, H. Shirota, "Low-Frequency Spectra of Phosphonium-based Ionic Liquids Having Pentyl, Ethoxyethyl, or 2-(Ethylthio) Ethyl Group", Proceedings of 16th DAE-BRNS Biennial Trombay Symposium on Radiation & Photochemistry, Ebenezer Printing House, IT-24, 2022.

Other Works

1) T. Takamuku, A. Tashiro, M. Kawano, **M. Ando**, A. Ogawa, K. Sadakane, H. Iwase, H. Shirota, "Anion Effects on the Mixing States of 1-Methyl-3-octylimidazolium Tetrafluoroborate and Bis(trifluoromethylsulfonyl)amide with Methanol, Acetonitrile, and Dimethyl Sulfoxide on the Meso- and Microscopic Scales", *Journal of Physical Chemistry B*, American Chemical Society, **2021**, *125*, 13896-13907.

2) H. Shirota, K. Takahashi, **M. Ando**, S. Kakinuma, "Liquid Properties of Ionic Liquids Based on Phosphonium Cations with (Alkylthio)alkyl Groups", *Journal of Chemical & Engineering Data*, American Chemical Society, **2019**, *64*, 11, 4701-4707.

【Special issue "Celebrating Our High Impact Authors", Supplementary Cover Art】

3)H. Shirota, **M. Ando**, K. Takahashi, S. Kakinuma, "Ultrafast Dynamics in Nonaromatic Cation Based Ionic Liquids: A Femtosecond Raman-Induced Kerr Effect Spectroscopic Study", *Bulletin of the Chemical Society of Japan*, Chemical Society of Japan, **2020**, *93*, 1520-1539.

【Selected Paper】